STRESS ANALYSIS OF OIL LUBRICATED BEARINGS

A thesis presented for the Degree of
Doctor of Philosophy in Mechanical Engineering
in the University of Canterbury,
Christchurch, New Zealand.

by

MAJID LOTFI, B.S.M.E., M.S.M.E.

University of Canterbury,
June 1988.

ACKNOWLEDGEMENTS

I wish to express my sincere appreciation to Professor H. McCallion, my supervisor and the Head of the Mechanical Engineering Department, for his guidance and valuable suggestions throughout this work.

Thanks are also due :

To Profesor L.A. Erasmus for placing the facilities of the Mechanical Engineering Department at my disposal.

To Dr J.S.Smaill for his help and interest in this work.

To Dr A. Thompson and Mrs G.B. Finnegan in the Computer Science Department.

To my colleague, M. Aitken, for sharing some of his experiences in this field.

To Mrs B. Bristowe for her care in the typing of this thesis.

To my wife, Minoo, my children, Vahideh and Morteza, and to my parents, brothers and sister for their constant encouragement and help, which enabled me to finish this work.

TABLE OF CONTENTS

CHAPTER ONE

INTRODUCTION

1.1 REVIEW OF PREVIOUS WORK

Journal bearings are used very widely in industry and transportation and their failures have been a great concern to engineers. The work presented here covers the result of an investigation into the fatigue failures of oil lubricated plain journal bearings.

Fatigue in mechanical elements occurs when the material fails due to repeated variation of stresses which are nominally lower than those needed to cause failure under steady load. A common way to present the results of a fatigue investigation is to plot them on an S–N diagram (i.e. stress vs. number of cycles to failure). As fatigue life also depends upon characteristics of the loading pattern, the state of the material, and the shape of the component being tested, to ensure reliability of a design actual components are tested.

In internal combustion engines, such as diesel engines, the sizes of the big–end bearing of the connecting rods are limited for economic and other reasons. Shorter bearings generate higher oil pressure for given applied loads, therefore the bearing shell, which consists of a very thin layer of soft material bonded to a steel backing, has to withstand high fluctuating stresses. The main research in this field has been aimed at improving bearing materials or at understanding how these bearings operate hydrodynamically. There has been little work done to understand the reasons for fatigue failure in terms of induced stresses.

Blount [1] experimentally investigated design factors influencing the fatigue resistance of journal bearings. His test rig was capable of applying a sinuosoidal variation of loads on bearings. Test results showed that using a very thick rigid housing increased the load carrying capacity of a bearing. This is usually not permissible due to space limitation in I.C. engines. Bearings with a circumferential oil groove in the middle, which were expected to operate on a lower temperature due to better oil flow, were found to run 6 deg^C to 8 deg^C hotter than ungrooved bearings. He reported this to be due to the lower oil film thickness and higher rate of generated heat. He also reported 50% reduction in fatigue life when bearings with .008" diametral clearance were used instead of .004".

Gyde [2] carried out a series of experiments with different mean and amplitude load settings on journal bearings in a test rig, aiming to find a boundary which would separate the failed bearings on an applied load plot. His test results were presented as a set of design curves, which indicated the range of safe combinations of loads (mean, amplitude) for trouble free operation. He reported that in a well aligned journal bearing (i.e. parallel bearing and journal axes) failures should occur in the centre of the bearing length, that is, away from the edges.

Gyde used Roach and Johnson's method [3] to calculate the principal stress distributions. Although this method gave a rough estimate of stresses, which were symmetric about the peak point, it showed that the tangential stresses, which were compressive under the pressurised oil film, became tensile near the edge of the oil film (where the pressure drops to zero). He explained fatigue fracture in journal bearing as being due to variations in these stresses between tension and compression generated by load induced oil film changes, which he believed will take place when oil film cavitation occurs. He also noticed that higher operating temperature or diametral clearance reduces the permissible load amplitude.

McCallion and Ibrahim [4] calculated the stresses in a bimetallic strip of white metal and steel backing subjected to the following types of loading: parabolic variation of pressure on the white metal surface with the steel backing resting on a rigid support; a sinusoidal variation of displacement in the strip due to the housing; raising the strip's temperature uniformly; and lack of support for the shell due to an oil groove in the housing. The computations were performed by using a finite difference representation of the governing differential equations based on plane strain assumption. A successive over relaxation technique was applied in solving the equations for displacement from which the stresses were calculated.

They concluded that housing flexibility and thermal expansion were the most significant factors in raising the stresses, followed by those due to the lack of complete support of the bearing shell due to the presence of oil feed channels. They also found a high shear stress, which occurred at the interface of two metals close to the free edge. This was thought to be important in weakening the metallic bond and causing failure.

Hassan [5] investigated the fatigue cracking in the dynamically loaded journal bearing's of a test rig. To calculate the pressure distribution, he used the program developed by Lloyd and McCallion [6]. Hassan showed that cracks were initiated at the surface of a bearing and then propagated toward the interface. The metallic bond at the interface was so strong that some cracks continued to propagate into the steel backing. Hassan related the circumferential position of failure to some oil film parameters, like maximum $\frac{dp}{dx}$, $P\ \frac{dp}{dx}$ and the axial position of failure to maximum $P\ \frac{dp}{dz}$, but he gave no scientific reason such as stress calculation for these correlations.

Blundell [7] investigated experimentally the fatigue failure of journal bearings and reported the position and time of failure of bearing shells subjected to a wide variety of loading patterns. He then used the computer program

developed by Lloyd and McCallion to generate the variation in the pressure distributions with time due to each loading pattern. These pressure distributions were taken as the input loads to his finite element stress analysis. Unfortuantely, Blundell's work concentrated on analysing the shear stress at the interface between the two metals, which has been proved by Hassan not to be the initial location of failures. His S–N diagram (stress vs. number of cycles to failure) for the shear stresses resulted in some scattered points on the diagram. Blundell also investigated the thermal stresses induced in the bearing shell and showed that among the principal thermal stresses the radial stresses were significant but still very low relative to the radial stresses due to the oil pressure at the surface. He found that the tangential stresses due to thermal expansion were negligible.

Martin, Garner and Adams [8] reported the result of stress analysis of Gyde's experimental data. They applied the mobility method, which is based on the short bearing theory, to find the approximate shape of pressure distribution curves. Their finite element stress analyses were carried out on a flat geometry as a rough approximation to a circular bearing shell. They came to the conclusion that tensile stresses with sufficient magnitude to cause fatigue failure were produced in the bearing shell. They reported a close correlation between the position of maximum tensile stress and the point of failure.

1.2 SCOPE OF THE DISSERTATION

This work covers an investigation of stresses produced in dynamically loaded journal bearings of two different test rigs. The results of a detailed study of all the stresses at different depths produced in a circular geometry representing the bearing shell are discussed. A finite difference program developed by Lloyd and McCallion was modified and used to generate the centreline oil pressure

distributions. Finite element stress analysis codes from the work of Hinton [21] were chosen and modified to enable the program to work in both polar and cartesian form (i.e. for computing the stresses in the radial and tangential directions due to centreline pressure distributions or the stresses in axial direction due to parabolic variation of pressure).

Sensitivity of journal bearing performance to some input load parameters, which changes the oil pressure distribution and affects the stresses induced in the bearing shell, are investigated. Numerical simulations of experimental work of other researchers are performed. Different types of stresses induced in the white metal layer were investigated and the one responsible for the failure was determined. Mean and amplitude values of stresses are used in plotting the Modified Goodman Diagram. The stress versus number of cycles to failure (S–N diagram) are plotted. The difference between the time variation of stresses at the point of failure for cases in which the direction of the input load locus is the same as or opposite to the shaft rotation are studied in detail. A crack closure model capable of estimating the stresses at the tip of a surface crack filled with oil is developed and used to relate the fatigue stresses on the bearing shell to the stresses at the tip of a surface crack during its closure. The effects which this model has on the S–N diagram, for a parallel and V–shaped crack assumptions, are studied.

Chapter Two presents the hydrodynamic theory of lubrication and attempts to solve the Reynolds' equation including the finite difference method of Lloyd and McCallion which is the basis of all the calculation in this work.

Chapter Three explains the modification made to the Lloyd and McCallion program, and the finite element program including how it works in both cartesian and polar forms. Extrapolation, Interpolation, Automatic mesh generating, and some plotting routines are also discussed.

Chapter Four shows how the variation of parameters such as temperature, diametral clearance, bearing land length, and the direction of rotation of input load affects the pressure distribution and eccentricity locus. It also covers the sensitivity of results to slight variation in input load and discusses the type of stress responsible for the failure of a bearing.

In Chapter Five, the results of the numerical simulations of the experimental tests of other workers, performed with the help of the bearing performance program and the finite element program (Chapter Three), are explained. Some stress distributions and scattering of the results on the S–N diagram which persuaded us to study crack closure are discussed.

Chapter Six explains the finite element stress analysis of a crack filled with oil under the action of surface stresses (crack closure model). The effects which this model has in increasing the stresses at the tip of a crack, by applying it to the results obtained from numerical simulation of Blundell's and Gyde's work and observing the changes which it brings to the S–N diagram and the sensitivity of the final results to small variation of input load data are discussed.

Finally, a brief summary and the conclusions are discussed in Chapter Seven.

CHAPTER TWO

HYDRODYNAMIC THEORY OF LUBRICATION

Hydrodynamic theory of lubrication originated by Beauchamp Tower [9] who was doing experiments on the railroad journal bearings to determine their coefficient of friction. He drilled a hole at the top of a bearing to pour in the lubricant, but he noticed that oil flowed out when the journal was rotated. He tried to stop the oil flowing out of the bearing by inserting a cork but it was forced out so he measured the pressure with a gauge and was surprised to find that the pressure was more than twice the load per projected area on the bearing, but he had no explanation for this. He also noticed that the pressure had a parabolic distribution across the bearing. Later, Osborne Reynold [10], who was interested in Tower's work, found a mathematical relation between the friction, the pressure and the velocity. He pointed out that since the journal's diameter was less than the bearing's diameter, they were not concentric. This would give rise to a wedged–shaped oil film. The above discovery was represented by an equation known as the Reynolds' equation which was restricted to isoviscous, incompressible fluids. But today, this name is applied very loosely to any equation relating to hydrodynamic lubrication.

2.1 A SIMPLE EXPLANATION OF THE REYNOLDS' EQUATION

In a full journal bearing under the action of rotation the journal pumps the lubricant around the bearing. Newton's law of viscous flow states that the shear

stress in the fluid is proportional to the rate of change of velocity with respect to y.

$$\tau = \frac{F}{A} = \mu \frac{\partial u}{\partial y} \tag{2.1}$$

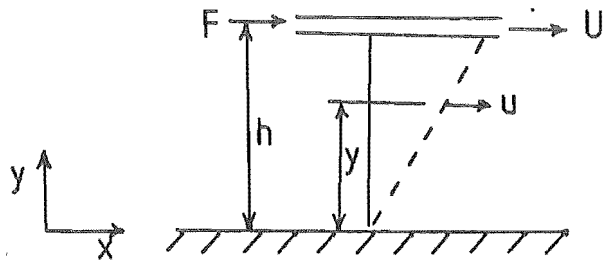

Fig. 2.1

where μ is the absolute viscosity of fluid and u is its velocity at x,y coordinates.

We now consider a fluid element Fig. 2.2 with the dimensions dx, dy, dz and sum the normal forces due to the pressure which act on its vertical sides and shear forces which act on its horizontal sides.

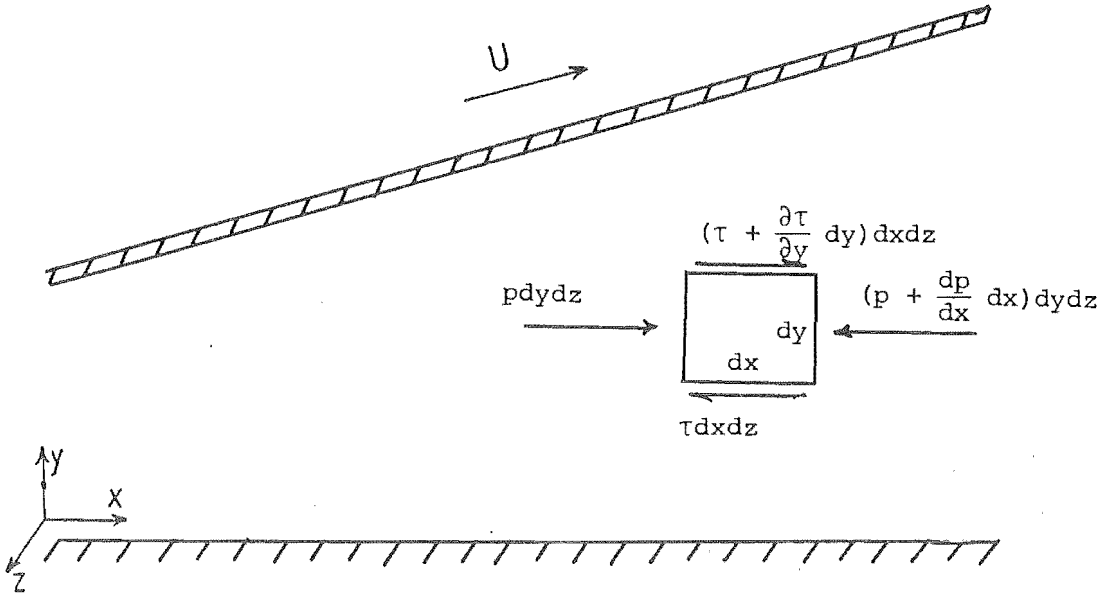

Fig. 2.2

$$F = (p + \frac{dp}{dx}dx)\, dydz - pdydz + \tau dxdz - (\tau + \frac{\partial \tau}{\partial y}dy)dxdz = 0 \quad . \tag{2.2}$$

This reduces to

$$\frac{dp}{dx} = \frac{\partial \tau}{\partial y} \tag{2.3}$$

substituting for τ from Equation (2.1)

$$\frac{dp}{dx} = \mu \frac{\partial^2 u}{\partial y^2} \tag{2.4}$$

integrating this equation with respect to y and using the boundary conditions

$$@\ y = 0 \qquad u = 0$$

$$@\ y = h \qquad u = U$$

$$u = \frac{U}{h} y + \frac{1}{2\mu} \frac{dp}{dx}(y^2 - hy) = Q_1 + Q_2 \tag{2.5}$$

Equation (2.5) gives the velocity of lubricant as the superposition of a parabolic and linear distribution at a particular $\frac{dp}{dx}$ and y.

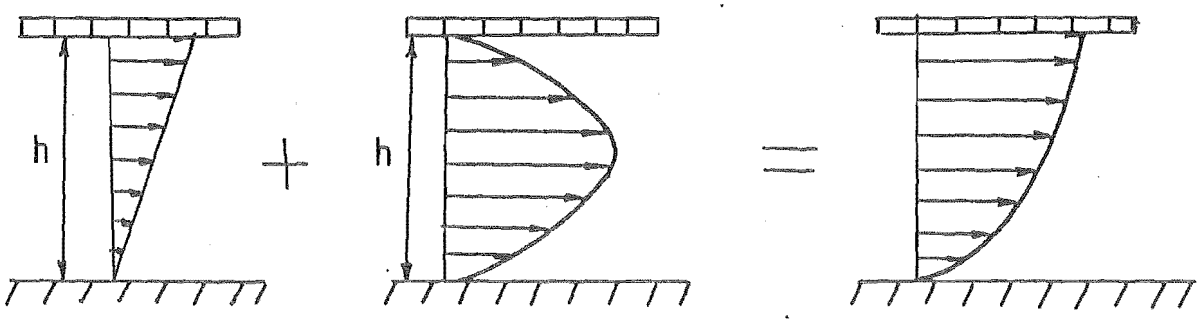

Fig. 2.3

By integrating Equation 2.5 with respect to y, the volume of lubricant flowing in x direction Q_x is obtained.

$$Q_x = Q_{1x} + Q_{2x} = \frac{Uh}{2} - \frac{h^3}{12\mu} \frac{dp}{dx} \tag{2.6}$$

Similarly the volume of lubricant flowing in z direction Q_z is obtained as

$$Q_z = Q_{2z} = -\frac{h^3}{12\mu} \frac{dp}{dz} \quad . \tag{2.7}$$

Equating the flow rate to the rate of change of prism volume as given in Fig. 2.4 relates the pressure and position of any point inside the lubricant film by Equation (2.8) which is known as the Reynolds' equation.

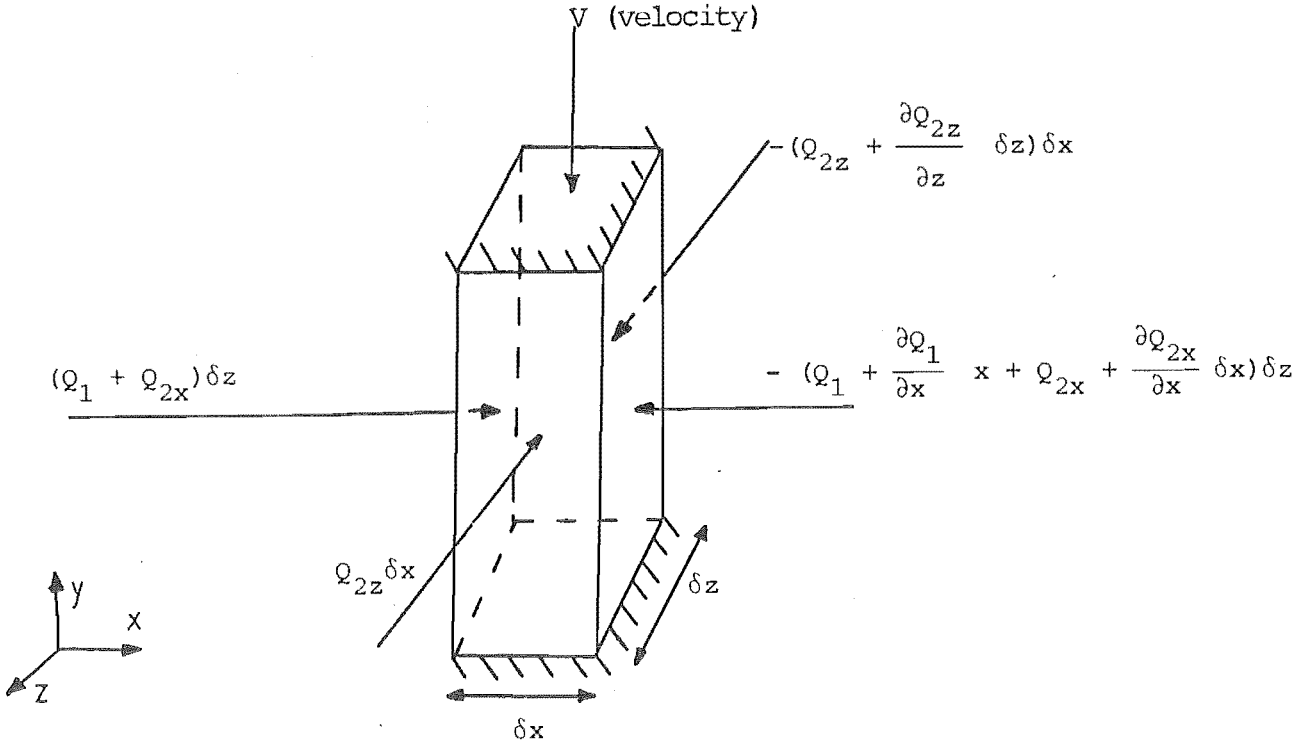

Fig. 2.4

$$\frac{\partial}{\partial x}\left(\frac{h^3}{\mu} \cdot \frac{\partial p}{\partial x}\right) + \frac{\partial}{\partial z}\left(\frac{h^3}{\mu} \cdot \frac{\partial p}{\partial z}\right) = 6U \frac{\partial h}{\partial x} - 12V \tag{2.8}$$

2.1.1 Boundary Conditions

Solutions to the Reynolds' equation are boundary value dependent, and the "true" boundary conditions are still a subject of research. The following approximations have been used by previous workers.

In 1904 Sommerfield [11] gave the first closed form solution to the one dimensional Reynolds' equation, which is for an infinitely long bearing (neglecting the axial pressure flow). He assumed a continuous 360^0 oil flow, that is, no oil film disruption. This gave unrealistic negative pressures. In the next important development, Swift [12] developing Reynolds' work for an infinitely long bearing, proposed a zero derivative for the pressure as the boundary condition at the oil film breakdown boundary.

The development of relaxation methods by Southwell [13] in 1940 and their application by Christopherson [14] paved the way for the numerical solutions of the lubrication problems. In 1957 Jackobson and Floberg [15] published a theoretical analysis of oil film disruption by supporting the zero pressure gradient at breakdown boundary. Hornell and McCallion [16] in 1963 applied the above boundary conditions to the numerical analysis of a boundary for a bearing with a circumferential oil groove.

Gumbel and Everling [17] gave an alternative approximation by proposing that the Sommerfield conditions should be assumed in finding a preliminary solution and that the final solution is obtained by ignoring the negative pressures of the preliminary solution. The above boundary condition which is simple to apply and gives results of acceptable accuracy was used by Lloyd and McCallion [18]. This procedure has been used as the basis of all the calculation in this work.

2.2 LLOYD AND McCALLION'S APPROACH IN SOLVING THE REYNOLDS' EQUATION

It is usual to consider both the tangential and the normal surface motion to be confined to the journal only as shown in Fig. 2.5a. During the motion, the velocity v which causes a change of prism volume as in Fig. 2.4 is given by equation

$$v = -U\frac{\partial h}{\partial x} + v_0 \tag{2.9}$$

v_0 is due to the journal's radial velocity. After substituting the above and assuming the journal and bearing centrelines to be parallel and the viscosity to be constant, the Reynolds' equation becomes

$$\frac{\partial}{\partial x}(h^3\frac{\partial p}{\partial x}) + h^3\frac{\partial^2 P}{\partial z^2} = 6\eta\left[U\frac{\partial h}{\partial x} - 2v_0\right] \tag{2.10}$$

considering Fig. 2.5b, the film thickness h may be related to the eccentricity e and its angular position x as

$$(R + c)^2 = (R + h)^2 + e^2 - 2e\,(R + h)\cos(\frac{x}{R}) \tag{2.11}$$

since c^2, h^2, e^2 and eh are small compared to the rest, they are neglected, giving

$$h = c + e\cos(\frac{x}{R}) \tag{2.12}$$

U, v_0 and x may be related to the angular velocity ω, to the rate of change of distance between centres $\frac{de}{dt}$ and to the angular velocity of the line of centres $\frac{d\phi}{dt}$

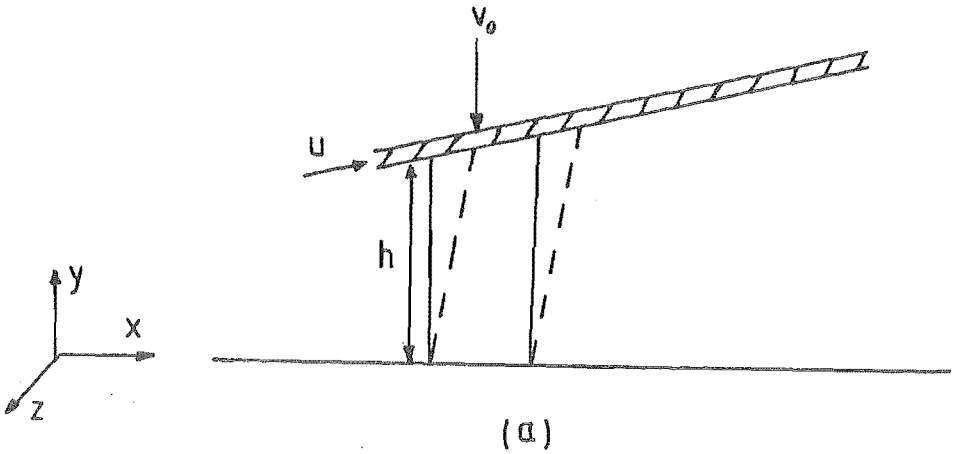

(a)

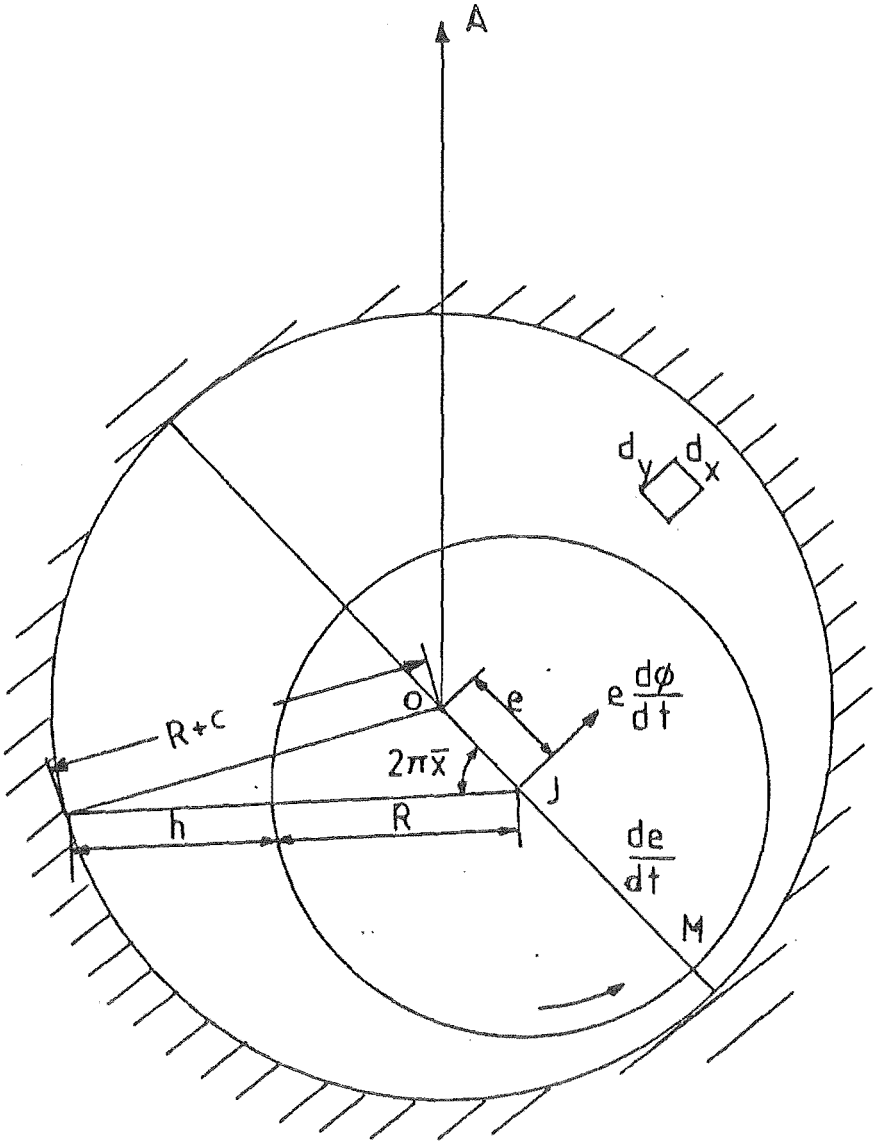

(b)

Fig. 2.5

$$U = R\omega - e\frac{d\phi}{dt}\cos 2\pi\bar{x} + \frac{de}{dt}\sin 2\pi\bar{x} \simeq R\omega \tag{2.13}$$

$$v_0 = -e\frac{d\phi}{dt}\sin 2\pi\bar{x} - \frac{de}{dt}\cos 2\pi\bar{x} \tag{2.14}$$

By substituting (2.13), (2.14) into the Reynolds' equation gives

$$\frac{\partial}{\partial x}(h^3\frac{\partial p}{\partial x}) + h^3\frac{\partial^2 p}{\partial z^2} = 6\eta\Big\{-e\sin(\frac{x}{R})[\omega - 2\frac{d\phi}{dt}] + 2\frac{de}{dt}\cos(\frac{x}{R})\Big\}. \tag{2.15}$$

The above equation may be made non–dimensional by assuming

$$\begin{aligned} &\bar{x} = x/(2\pi R) && \bar{z} = z/L && \epsilon = \frac{e}{c} \\ &P = p/[\eta\omega(\frac{R}{c})^2] && H = h/c \\ &b = 1-2\frac{d\phi}{dt}/\omega && b' = \frac{d\epsilon}{dt}/\omega \end{aligned} \tag{2.16}$$

Thus

$$\frac{\partial}{\partial\bar{x}}(H^3\frac{\partial P}{\partial\bar{x}}) + (\frac{\pi D}{L})^2 H^3\frac{\partial^2 P}{\partial\bar{z}^2} = 24\pi^2[-b\epsilon\sin 2\pi\bar{x} + 2b'\cos 2\pi\bar{x}] \tag{2.17}$$

The first term on the right hand side of this equation is due to the wedge film effect which include the steady rotation of journal plus the tangential motion of its centre, while the second term is due to the radial movement of the journal centre that is the squeeze film effect. In Section 2.2.3 it will be explained how the finite difference method is used to solve the above equation by treating the wedge and squeeze effect separately.

2.2.1 Approximations and Limitations of the Program

To analyse the performance of the journal bearing under full dynamic loading, a computer program developed by Lloyd, McCallion [6] was used. But, in order to prepare the program for a more accurate stress analysis, some modifications were required as explained in Chapter Three. The program has been successfully tested and used over a period of years by Lloyd [6], Patrick [19], Hassan [5], and Blundell [7].

The following assumptions were made by Lloyd and McCallion to make the calculations simpler and more economical but of course they limit the applicability of the program.

(a) Reynolds' assumptions in deriving his equation which are –

- The fluid is isoviscous and incompressible.
- The fluid flow is Newtonian and laminar.
- The fluid thickness is very small when compared with the diameter of bearing. This allows surface curvature and change in pressure across the oil film to be neglected. Velocity of fluid perpendicular to the surface is negligible when compared with the velocity parallel to it.
- The inertia force of the fluid may be neglected.
- There is no slip. This requires that the moving surface and the fluid in contact with it have the same velocity.

(b) Both the journal and bearing surfaces are assumed to remain rigid circular cylinders. This neglects any kind of deformation of them during the operation.

(c) Journal and bearing remain perfectly aligned during the operation.

(d) Since journal's acceleration relative to the bearing is very small, the corresponding inertia forces are negligible.

(e) All the negative pressures are taken to be zero.

(f) The oil feed to the bearing is by a centre circumferential groove or else it is ignored.

(g) Length to diameter ratio of the bearing, L/D should remain below 0.75.

2.2.2 A Brief Description of the Program

The main object of the program was to calculate the path in time of an oil lubricated journal relative to its bearing under full dynamic loading. A finite difference assumption of Reynolds' equation was solved iteratively for both wedge and squeeze film terms separately, assuming no film disruption and no feed pressure. This gives symmetries in both circumferential and axial directions at the point of minimum film thickness. Therefore each bearing side was divided into four equal parts reducing the number of meshes to a quarter (16 x 4). Computational time was reduced accordingly. Fig. 2.6 shows the block diagram of the program logic. To calculate the journal centre locus, an arbitrary journal centre position and velocity was chosen. Wedge and squeeze film pressure distributions were calculated at various carefully spaced eccentricity ratios by the Gauss–Siedel over relaxation technique. The total pressure was then found and summed in both circumferential and axial directions to give the oil film force F on the journal centre. The radial and tangential components of the above internal forces F_r, F_t must always balance the two fixed A & B components of the applied external force P_a, P_b as shown in Fig. 2.6 by Equation (2.18).

$$P_a \cos \phi + P_b \sin \phi + F_r = 0$$

$$-P_a \sin \phi + P_b \cos \phi - F_t = 0 \qquad (2.18)$$

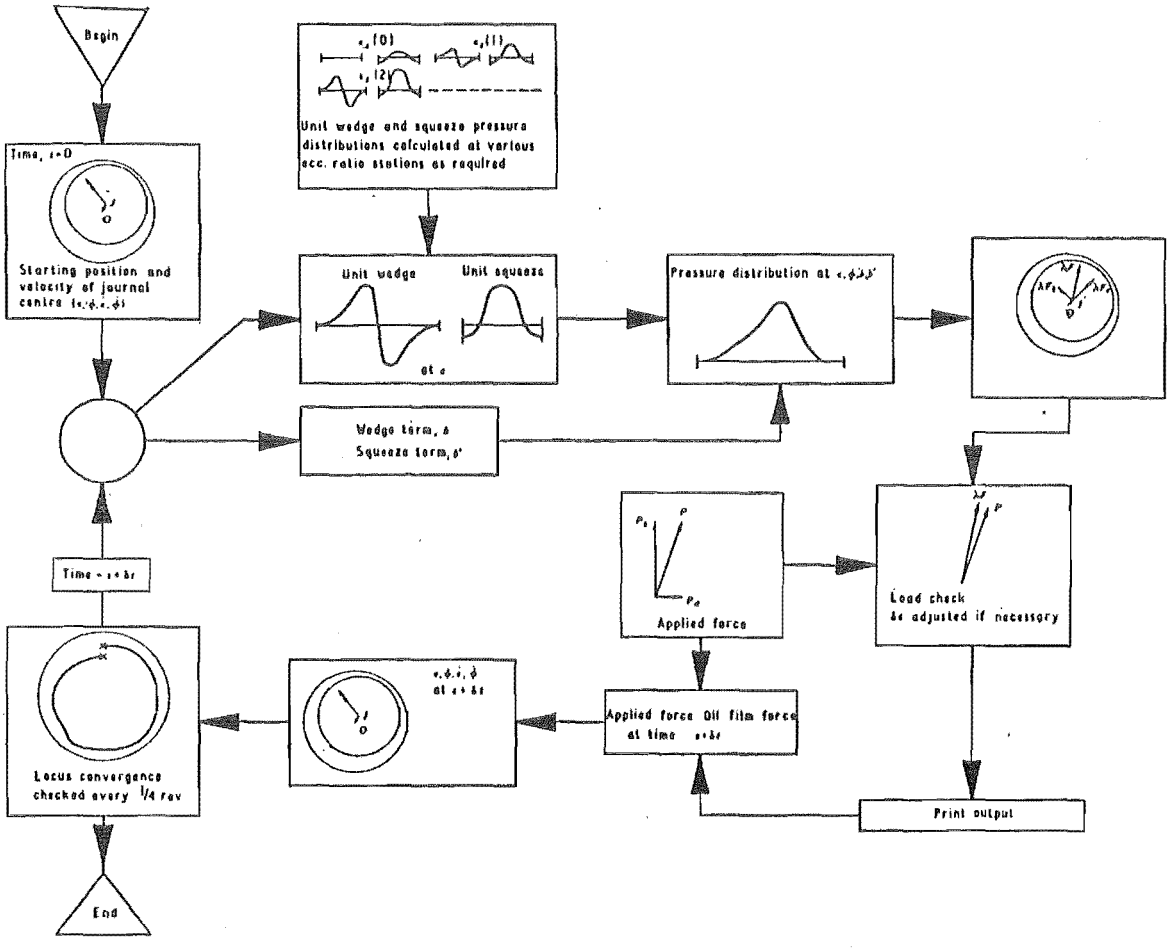

Block diagram of the bearing analysis program

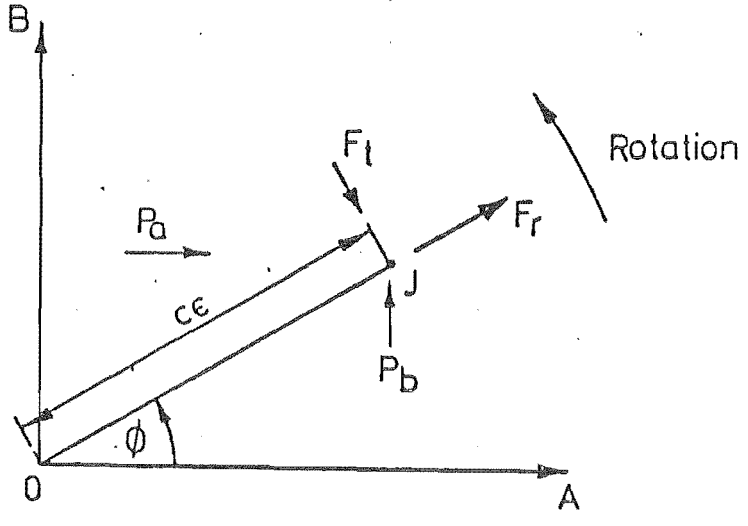

The system of axes

(after Lloyd and McCallion [6])

Fig. 2.6

Since F_r,F_t are functions of ϵ, $\frac{d\epsilon}{dt}$, $\frac{d\phi}{dt}$, the above equation relates the external load P_a,P_b to the journal centre position and velocity which is the basis of the locus prediction. The accuracy of solution on each step was checked by balancing the applied load and calculated oil film force to within 1% difference. Otherwise, the time step length was halved or doubled.

CHAPTER THREE

MODIFIED LLOYD AND FINITE ELEMENT PROGRAMS

In this chapter, some modification to the Lloyd and McCallion program for calculating centreline pressure distribution and the Finite Element program for calculating the stresses are explained. Extrapolation, interpolation, and plotting routines are discussed.

3.1 MODIFICATION OF THE LLOYD'S PROGRAM

3.1.1 Constant Graded Meshes

Since the dynamically loaded journal bearing operates at a high eccentricity ratio, Lloyd [18] decided to have a high density of meshes near the point of minimum film thickness. This is close to where the lubricant film pressure is generated. He used the following relation to calculate the spacing between the graded meshes in the circumferential direction, which becomes finer as it gets closer to the point of minimum film thickness (as i increases)

$$\Delta x_i = [1 + c\epsilon \cos \frac{\pi(i-1)}{(m/2-1)}]/m$$

ϵ is the eccentricity ratio, c is an arbitrary constant and m is the number of meshes in the circumferential direction. As the shaft rotates the eccentricity ratio ϵ and consequently the meshes spacing Δx_i changes. Since calculation of stiffness matrix $|K|$ in the finite element method is dependent on the mesh geometry, it is very advantageous to keep the grading of a very finely graded

mesh constant, as time and ϵ changes, but rotate it with the shaft in such a way that the finest mesh is always located at the position of minimum film thickness as it is shown in Fig. 3.1. This gives very accurate oil film results but its main advantage is that the stiffness matrix for the stress analysis of the bearing needs to be formed only once. This is very economical when stresses under many loading conditions are required, as in this work.

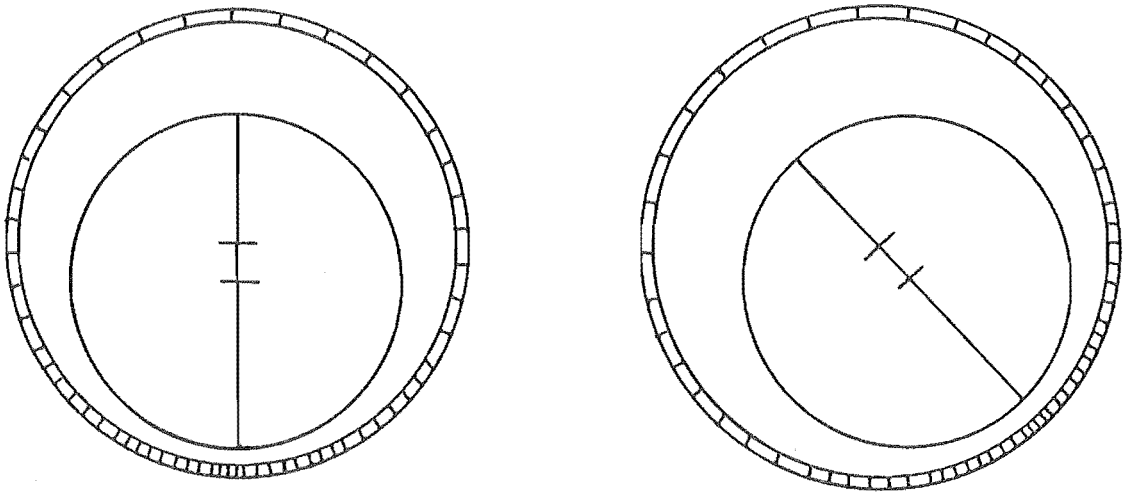

Fig. 3.1

To prevent the possible loss of accuracy involved in the above decision, it was decided to increase the number of meshes in the circumferential direction from 32 which was suggested by Lloyd to 112. This enabled us to have extremely fine meshes (1^{o} spacing) in the critical section between the peak pressure and the minimum oil film. Fig. 3.2 shows the finely graded mesh which was used in both modified Lloyd and finite element programs. Table 3.1 gives a list of spacings between the meshes.

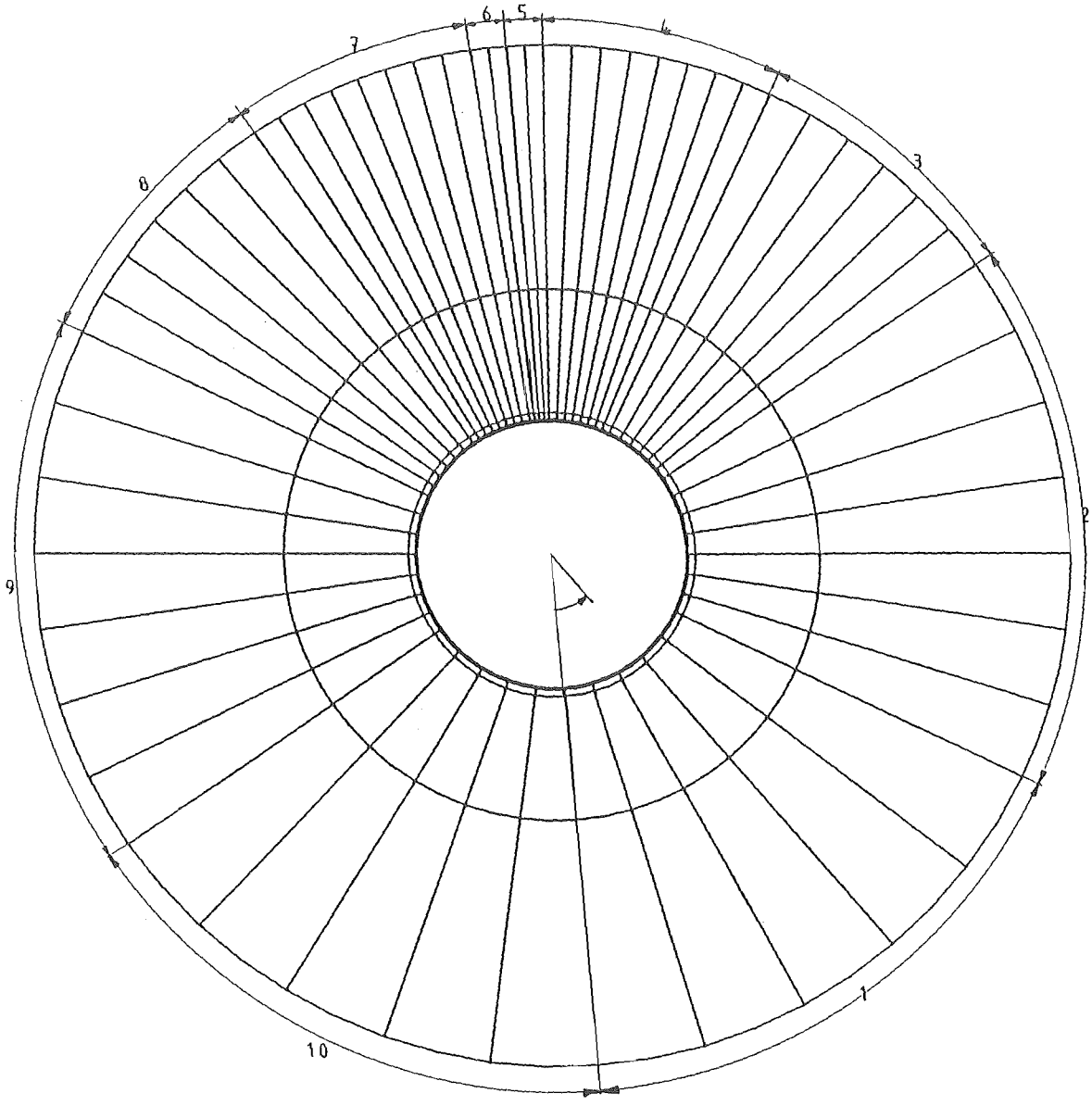

Radial and circumferential mesh gradings

Fig.3.2

Region	Angle (Deg)	Angular space (Deg/node)
1	0 — 60	6
2	60 — 120	4.286
3	120 — 150	2.5
4	150 — 176	1.625
5	176 — 180	1.
6–10	180 — 360	symmetric

Table 3.1

3.1.2 Input Load Data

The dynamic input load in Blundell's [7] experiments were generated by four digitally controlled hydraulic rams. The resulting local locus shown in Fig. 3.3a were not smooth curves. To generate a similar load diagram (Fig. 3.3b) to calculate the input load data for the Lloyd program, the two sinusoidal functions (3.1), (3.2) were used.

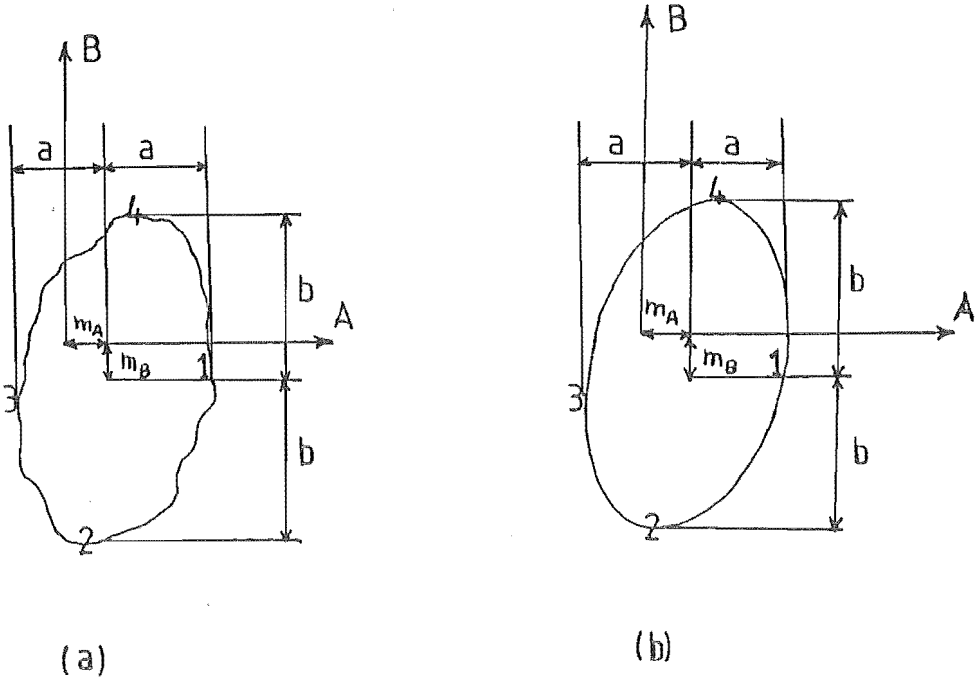

(a) (b)

Fig. 3.3

$$F_{A_{(t)}} = a_A \cos(\omega t) + m_A \tag{3.1}$$

$$F_{B_{(t)}} = a_B \sin(\omega t + \phi) + m_B \tag{3.2}$$

$F_{A_{(t)}}$, $F_{B_{(t)}}$ are the A & B components of force F at different instants of time, while a_A , m_A and a_B , m_B are the amplitude and mean loads on the A & B axes respectively. ϕ is the phase angle (time lag between the operation of the two pistons). To simulate Blundell's experiments, amplitude and mean load values a_A, a_B, m_A, m_B for each individual test were carefully measured from his load diagrams, similar to Fig. 3.3a. Different values for ϕ were tried to make the load diagram as close as possible to those from the experiments.

3.1.3 Pressure Distribution

Subroutine peak in the program was also modified to store the centreline oil pressure and its angular position at different instants of time, as two dimensional arrays. These were then used by the finite element program to calculate the stresses.

3.1.4 Plotting the Results

A plotting subroutine was written to present the input load data, eccentricity ratio and pressure distribution at different instants of time. NCAR plotting library [20] was used here. Fig. 3.4a,b show the input load and the eccentricity loci. Points 1, 2, 3, 4 corresponds to the four equal intervals of time

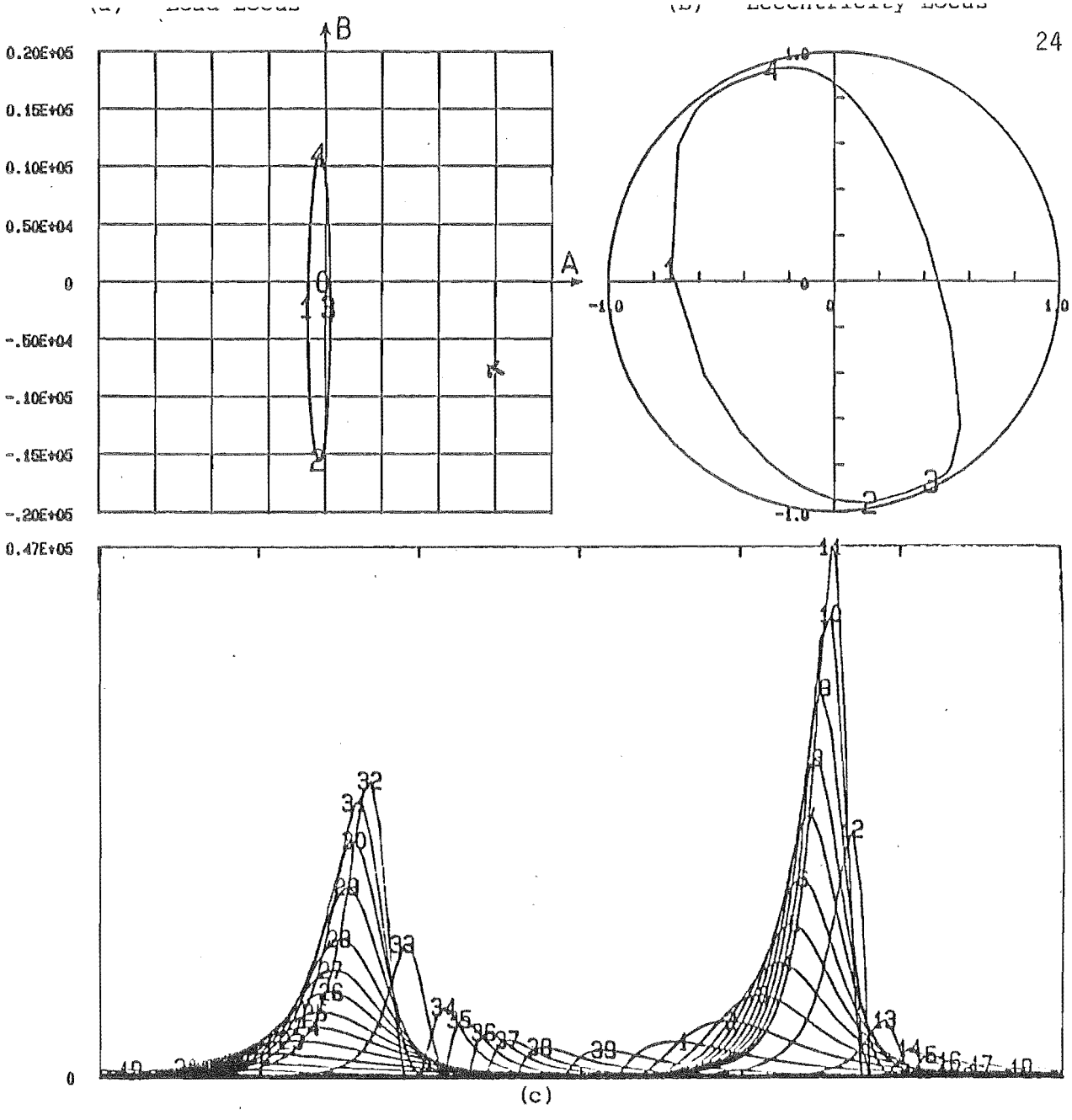

TEST NO 505 CO ROTATIONAL LOAD, 1 LAND BEARING

Operating temperature	=	48.3°C
Diametral clearance	=	.0033"
Bearing land length	=	1.16"
Rotational speed	=	1050 RPM
Load amplitude (A Axis)	=	1000 LbF
Load Amplitude (B Axis)	=	13280 LbF
Mean load (A Axis)	=	- 500 LbF
Mean load (B Axis)	=	- 2200 LbF
Phase angle	=	0°

Fig3.4

in a complete revolution of the shaft. Fig. 3.4c shows the centreline pressure distribution at different instants of time in that shaft revolution. Points 1, 2,.....39 indicates the peak of each pressure curve.

3.2 FINITE ELEMENT METHOD (FEM)

For computing the stresses produced in the bearing due to the oil pressure, the finite element method was used. Since the geometry of the bearing, loads on it and the required deflections and stresses were all in polar form (radial, tangential), codes from the work of Hinton [21] were chosen and modified to enable the program to work in both polar and Cartesian form (i.e. for computing the stresses in the radial and tangential directions due to the centreline pressure distribution or the stresses in the axial direction due to the parabolic variation of pressure). An automatic mesh generating program was also written. Major changes were made in the methods Hinton used for data handling and to enable the program to handle multiple loading cases.

3.2.1 FEM in Cartesian Form

The displacements at any point within a two dimensional element of the general shape shown in Fig. 3.5 may be represented by

$$u(\xi,\eta) = \sum_{i=1}^{n} N_i(\xi,\eta) \cdot u_i \qquad (3.3a)$$

$$v(\xi,\eta) = \sum_{i=1}^{n} N_i(\xi,\eta) \cdot v_i \qquad (3.3b)$$

where u_i , v_i are the x,y components of the displacements at any nodal point i. N_i known as the shape functions depend on local coordinates (ξ,η).

The coordinates x and y at any point i inside the element domain can be described similarly as

$$x(\xi,\eta) = \sum_{i=1}^{8} N'_i(\xi,\eta) \cdot x_i \tag{3.4a}$$

$$y(\xi,\eta) = \sum_{i=1}^{8} N'_i(\xi,\eta) \cdot y_i \tag{3.4b}$$

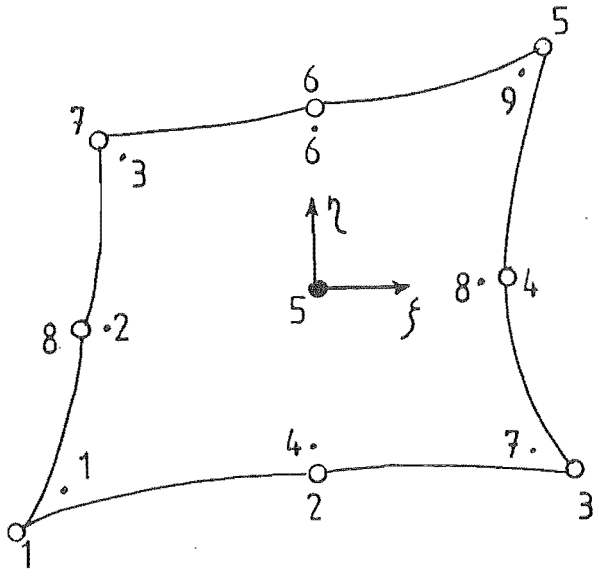

Fig. 3.5

It may be assumed that both the displacement and the coordinates may be represented by the same shape function (i.e. N_i and N'_i are identical). The element are then called isoparametric. The two dimensional quadratic shape

function for this element are

$$
\begin{aligned}
N_1(\xi,\eta) &= -\tfrac{1}{4}\,(1-\xi)\,(1-\eta)\,(1+\xi+\eta) \\
N_2(\xi,\eta) &= \tfrac{1}{2}\,(1-\xi^2)\,(1-\eta) \\
N_3(\xi,\eta) &= \tfrac{1}{4}\,(1+\xi)\,(1-\eta)\,(\xi-\eta-1) \\
N_4(\xi,\eta) &= \tfrac{1}{2}\,(1+\xi)\,(1-\eta^2) \\
N_5(\xi,\eta) &= \tfrac{1}{4}\,(1+\xi)\,(1+\eta)\,(\xi+\eta-1) \\
N_6(\xi,\eta) &= \tfrac{1}{2}\,(1-\xi^2)\,(1+\eta) \\
N_7(\xi,\eta) &= \tfrac{1}{4}\,(1-\xi)\,(1+\eta)\,(-\xi+\eta-1) \\
N_8(\xi,\eta) &= \tfrac{1}{2}\,(1-\xi)\,(1-\eta^2)
\end{aligned}
\tag{3.5}
$$

in order to compute the displacement and the stresses, the stiffness matrix $|K|^e$ for each element had to be determined. This was done by integrating (3.6) over the element's area (A_e)

$$
|K|^e = \int_{Ae} |B|^T |D|\,|B|\,dA \tag{3.6}
$$

The strain matrix $|B|$ relates the strain and displacement at Gauss points within each element (sampling points 1,.....,9 for integration) as shown in Fig. 3.5

$$\epsilon = \sum_{i=1}^{n} B_i \delta_i \tag{3.7}$$

B_i is the derivatives of the shape functions with respect to the global coordinates x,y

$$B_i = \begin{vmatrix} \frac{\partial N_i}{\partial x} & 0 \\ 0 & \frac{\partial N_i}{\partial} \\ \frac{\partial N_i}{\partial y} & \frac{\partial N_i}{\partial y} \end{vmatrix} \tag{3.8}$$

The derivatives of a function $f(\xi,\eta)$ within an element with respect to its local coordinates ξ,η are

$$\frac{\partial f}{\partial \xi}(\xi,\eta) = \sum_{i=1}^{8} \frac{\partial N_i}{\partial \xi} \cdot f_i \tag{3.9}$$

where f_i are the displacements u,v or coordinates x,y. But as mentioned earlier, its derivative has to be determined in the global coordinate system x,y namely $\frac{\partial f}{\partial x}, \frac{\partial f}{\partial y}$. This can be done by taking the inverse of Jacobian matrix $J(\xi,\eta)$ and applying the chain rule

$$J = \begin{vmatrix} \frac{\partial x}{\partial \xi} & \frac{\partial y}{\partial \xi} \\ \frac{\partial x}{\partial \eta} & \frac{\partial y}{\partial \eta} \end{vmatrix} \quad \sum_{i=1}^{8} \quad \begin{vmatrix} \frac{\partial N}{\partial \xi} & x_i & \frac{\partial N_i}{\partial \xi} & y_i \\ \frac{\partial N}{\partial \eta} & x_i & \frac{\partial N_i}{\partial \eta} & y_i \end{vmatrix} \tag{3.10}$$

$$|J|^{-1} = \begin{vmatrix} \frac{\partial \xi}{\partial x} & \frac{\partial \eta}{\partial x} \\ \frac{\partial \xi}{\partial y} & \frac{\partial \eta}{\partial y} \end{vmatrix} = \frac{1}{\det\ J} \begin{vmatrix} \frac{\partial y}{\partial \eta} & -\frac{\partial y}{\partial \xi} \\ -\frac{\partial x}{\partial \eta} & \frac{\partial x}{\partial \xi} \end{vmatrix} \tag{3.11}$$

The Cartesian derivative of the function is

$$\begin{vmatrix} \frac{\partial f}{\partial x} \\ \frac{\partial f}{\partial y} \end{vmatrix} = \begin{vmatrix} \frac{\partial \xi}{\partial x} & \frac{\partial \eta}{\partial x} \\ \frac{\partial \xi}{\partial y} & \frac{\partial \eta}{\partial y} \end{vmatrix} \begin{vmatrix} \frac{\partial f}{\partial \xi} \\ \frac{\partial f}{\partial \eta} \end{vmatrix} \tag{3.12}$$

By substituting N for f, the required terms in (3.8) namely $\frac{\partial N}{\partial x}$, $\frac{\partial N}{\partial y}$ are found.

$$\begin{vmatrix} \frac{\partial N}{\partial x} \\ \frac{\partial N}{\partial y} \end{vmatrix} = \begin{vmatrix} \frac{\partial \xi}{\partial x} & \frac{\partial \eta}{\partial x} \\ \frac{\partial \xi}{\partial y} & \frac{\partial \eta}{\partial y} \end{vmatrix} \begin{vmatrix} \frac{\partial N}{\partial \xi} \\ \frac{\partial N}{\partial \eta} \end{vmatrix} \tag{3.13}$$

Having evaluated B_i, the element stiffness $|K|$, displacement $|\delta|$ and stresses $|\sigma|$ may be computed in Cartesian coordinate system.

3.2.2 FEM in Polar Form

Displacements in polar coordinates u′, v′, are determined from the Cartesian form by using the transformation matrix $|T|$

$$|T| = \begin{vmatrix} \cos\theta & -\sin\Theta \\ \sin\Theta & \cos\Theta \end{vmatrix} \tag{3.14}$$

The polar components of nodal forces and displacements are related to the Cartesian components by

$$\begin{vmatrix} P_x \\ P_y \end{vmatrix}' = \begin{vmatrix} T \end{vmatrix}^T \begin{vmatrix} P_x \\ P_y \end{vmatrix} \tag{3.15}$$

$$\begin{vmatrix} u \\ v \end{vmatrix} = \begin{vmatrix} T \end{vmatrix} \begin{vmatrix} u \\ v \end{vmatrix}' \tag{3.16}$$

nodal forces and displacements are related to each other by the 2 x 2 submatrix K_{ij}.

$$\begin{vmatrix} P_{x_i} \\ P_{y_i} \end{vmatrix} = \begin{vmatrix} K_{ij} \end{vmatrix} \begin{vmatrix} u_j \\ v_j \end{vmatrix} \tag{3.17}$$

By substituting (3.15), (3.16) in (3.17), an equivalent expression for nodal forces and displacements in the polar coordinate system is obtained.

$$\begin{vmatrix} P_{x_i} \\ P_{y_i} \end{vmatrix}' = \begin{vmatrix} K'_{ij} \end{vmatrix} \begin{vmatrix} u_j \\ v_j \end{vmatrix}' \tag{3.18}$$

where

$$\begin{vmatrix} K'_{ij} \end{vmatrix} = \begin{vmatrix} T \end{vmatrix}^T \begin{vmatrix} K_{ij} \end{vmatrix} \begin{vmatrix} T \end{vmatrix} \tag{3.19}$$

To obtain the displacements in polar coordinates, the stiffness and nodal forces of each element's has to be transformed according to (3.19) and (3.15).

Since the strain displacement relationship in the finite element approximation can be written as

$$\epsilon = [B_1,....,B_8]\delta^e \quad . \tag{3.20}$$

The stresses at any point inside the element may be expressed as

$$\sigma = DB\delta^e \quad . \tag{3.21}$$

D is the property matrix and σ, B, δ^e are the stresses, strain, displacement matrices in polar form.

The strain matrix in polar coordinates may be expressed as

$$B_i = \begin{vmatrix} \frac{\partial N}{\partial r} & 0 \\ \frac{N_i}{r} & \frac{1}{r}\frac{\partial N}{\partial \theta} \\ \frac{1}{r}\frac{\partial N}{\partial \theta} & \frac{\partial N_i}{\partial r} - \frac{N_i}{r} \end{vmatrix} \tag{3.22}$$

The polar derivatives of the shape functions $\frac{\partial N}{\partial r}$, $\frac{\partial N}{\partial \theta}$ were determined by using Cartesian derivatives of shape functions and the chain rule as follows

$$\frac{\partial N}{\partial r} = \frac{\partial N}{\partial x}\frac{\partial x}{\partial r} + \frac{\partial N}{\partial y}\frac{\partial y}{\partial r} \tag{3.23a}$$

$$\frac{\partial N}{\partial \Gamma} = \frac{\partial N}{\partial x}\frac{\partial x}{\partial \Gamma} + \frac{\partial N}{\partial y}\frac{\partial y}{\partial \Gamma} \tag{3.23b}$$

where

$$\frac{\partial x}{\partial r} = \cos\theta \qquad \frac{\partial y}{\partial r} = \sin\theta$$
$$\frac{\partial y}{\partial T} = \cos\theta \qquad \frac{\partial x}{\partial T} = -\sin\theta \tag{3.24}$$
$$\frac{\partial N}{\partial T} = \frac{1}{R}\frac{\partial N}{\partial \theta}.$$

Thus

$$\begin{vmatrix} \frac{\partial N}{\partial r} \\ \\ \frac{\partial N}{\partial \theta} \end{vmatrix} = \begin{vmatrix} \frac{\partial N}{\partial x} & \frac{\partial N}{\partial y} \\ \\ \frac{\partial N}{x} & \frac{\partial N}{y} \end{vmatrix} \begin{vmatrix} \cos\theta & -R\sin\theta \\ \\ \sin\theta & R\cos\theta \end{vmatrix} \tag{3.25}$$

r and θ are the radius and the angle of each Gauss point.

The above procedure enabled the program to compute the displacement and stresses for both circular and rectangular geometries (i.e. in circumferential direction due to centreline oil pressure or in axial direction due to parabolic type of oil distribution). The resultant stresses in circular geometry are obviously in polar form which is very advantageous.

3.2.3 Data Handling

Data preparation is a major part of any finite element analysis. It would therefore be extremely advantageous to be able to generate the data automatically, both in the saving of time and in the reduction of the possibility of errors. The numbering of the nodes (element topology) and the calculating of their coordinates and angular positions were done automatically by a computer program written for the purpose. It required only the data to describe the geometry of the system and the sizes of its elements. The data generated by the

program was checked by the plotting routine. Fig. 3.2 shows how the 280–elements (56 x 5) were graded in both circumferential and radial directions. The 56 elements in circumferential directions were graded according to Table 3.1. In the radial direction there were two elements in the white metal, one element in the steel backing and two elements in the thick housing sections. These required a total of 952 nodes to represent the structure. A second group of data specified the control parameters such as the number of nodes, number of elements, constrained nodes and material properties which were all prepared manually. The centreline oil pressures and their nodal angular positions computed for each instant of time of the dynamic loading cycle was the third major group of data. These were prepared by the modified Lloyd program (Chapter 3) and were stored on the disc file.

3.3 EXTRAPOLATION, INTERPOLATION AND THE PLOTTING ROUTINE

The finite element method which was explained in Section 3.2 outputs the stresses at (3 x 3) Gauss points of each element. These are not equally spaced around the bearing so values at equally spaced fixed points around the bearing had to be found. Some plotting routines were also written to present the stresses graphically.

3.3.1 Extrapolation

In a numerical integration scheme such as FEM, experience has shown that Gauss points are the best locations to compute the stresses. Nodal points which are the most useful points for the output, appear to be the worst points. This is

because the Gauss points are the sampling points for all the integration steps. It is also well known that interpolation functions behave badly near the extremities of the interpolation region. Therefore the stresses were computed at the Gauss points (i = 1′,....,9′ of Fig. 3.6) and were extrapolated to the corner nodes (J = 1, 3, 5, 7) using the Lagrangian functions N_1,...,N_9 in (3.27)

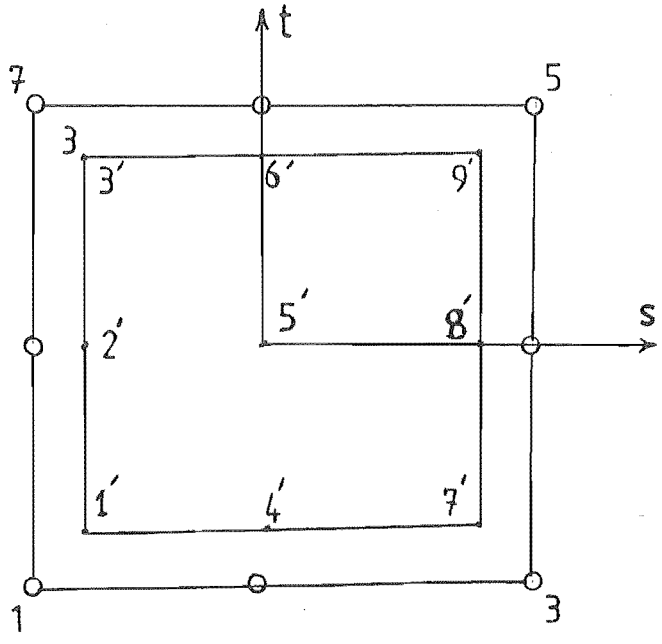

Fig. 3.6

$$
\begin{aligned}
N_1 &= \tfrac{1}{4}\,st(1-s)\,(1-t)\\
N_2 &= -\tfrac{1}{2}\,s(1-s)\,(1-t^2)\\
N_3 &= -\tfrac{1}{4}\,st(1-s)\,(1+t)\\
N_4 &= -\tfrac{1}{2}\,t(1-t)\,(1-s^2)\\
N_5 &= (1-s^2)\,(1-t^2)\\
N_6 &= \tfrac{1}{2}\,t(1+t)\,(1-s^2)\\
N_7 &= -\tfrac{1}{4}\,st(1+s)\,(1-t)\\
N_8 &= \tfrac{1}{2}\,s(1+s)\,(1-t^2)\\
N_9 &= \tfrac{1}{4}\,st(1+s)\,(1+t)
\end{aligned}
\qquad (3.26)
$$

$$
\sigma_j = \sum_{i=1'}^{9'} N_i \sigma_i \qquad (3.27)
$$

The above technique resulted in several values of stresses at each node, one from each element. The values from all the elements sharing a node were averaged.

3.3.2 Interpolation

As explained earlier in Section 3.1.1, the graded meshes for the oil film calculations rotated with the shaft in such a way that the position of the finest mesh point region always coincided with the location of minimum film thickness. This allocates the maximum number of elements to the critical region between the peak pressure and the line of centres which obviously also result in a much more accurate stress analysis. But the stresses should be interpolated to some fixed points in space.

In Fig. 3.7, x_1', x_2' are the angular positions of the rotating graded meshes J to which the stresses were extrapolated (Section 3.3.1). x_1, x_2,... are the angular positions of the fixed equally spaced points K which the stresses should be interpolated to.

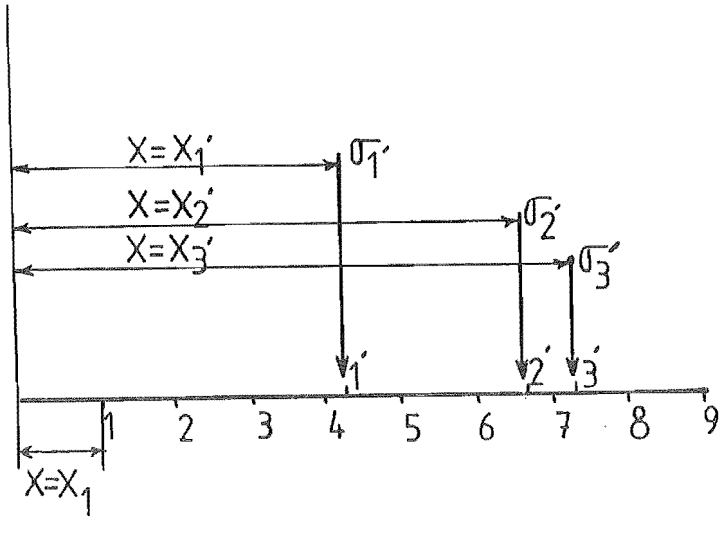

Fig. 3.7

Linear shape functions N_1', N_2' were chosen for this purpose.

$$N_1' = a_1 x + b_1 \tag{3.28a}$$

$$N_2' = a_2 x + b_2 \tag{3.28b}$$

where a_1, a_2, b_1, b_2 are

$$a_1 = \frac{1}{(x_1' - x_2')} \quad , \quad b_1 = \frac{- x_2'}{(x_1' - x_2')}$$

$$a_2 = \frac{- 1}{(x_1' - x_2')} \quad , \quad b_2 = \frac{x_1'}{(x_1' - x_2')} \tag{3.29}$$

The stresses were then calculated from

$$\sigma_K = \sum_{j=1}^{2} N_j' \sigma_j \tag{3.30}$$

3.3.3 Plotting Routines

Fig. 3.9 shows a typical plot of stresses for Blundell's Test No. 5 at a particular instant of time (when the peak pressure is maximum). Fig. 3.9a presents the centreline pressure, the radial stresses and the tangential stresses at the surface of bearing while Fig. 3.9b shows the surface displacement (dotted line). The middle circle indicates the bearing's surface before distortion. To show the amount of distortion simply, the solid–line circle was plotted with a radius equal to bearing clearance. As shown, the position of maximum distortion

is in the region of 270^{O} which corresponds to the position of peak pressure of Fig. 3.9a. Fig. 3.10 shows the contour plots of the three main stresses σ_r, σ_θ, $\tau_{r\theta}$ which were stored in rectangular arrays (a x b). It should be noted that (a) is the number of equally spaced points in circumferential direction (3^{O} a part). (b) is the number of graded points in the radial direction (Fig. 3.8). (INT) is the interval between the contour lines in the white metal region, while (H), (L) and (ANGLE) represent highest, lowest values of stresses and their corresponding angular position in the white metal layer only. Positive and negative signs indicate tensile and compressive stresses respectively. Similar plotting routines were used to contour plot the maximum principal, maximum shear and maximum distortion energy stresses. These are explained in Section 4.3.

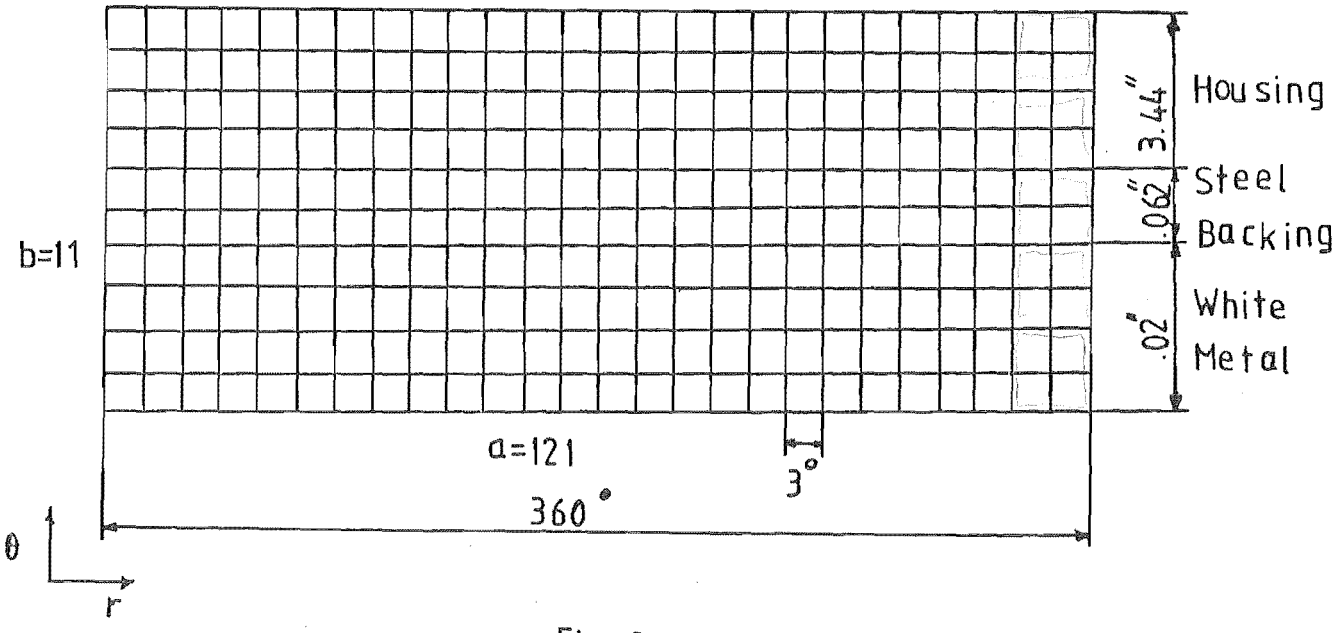

Fig. 3.8

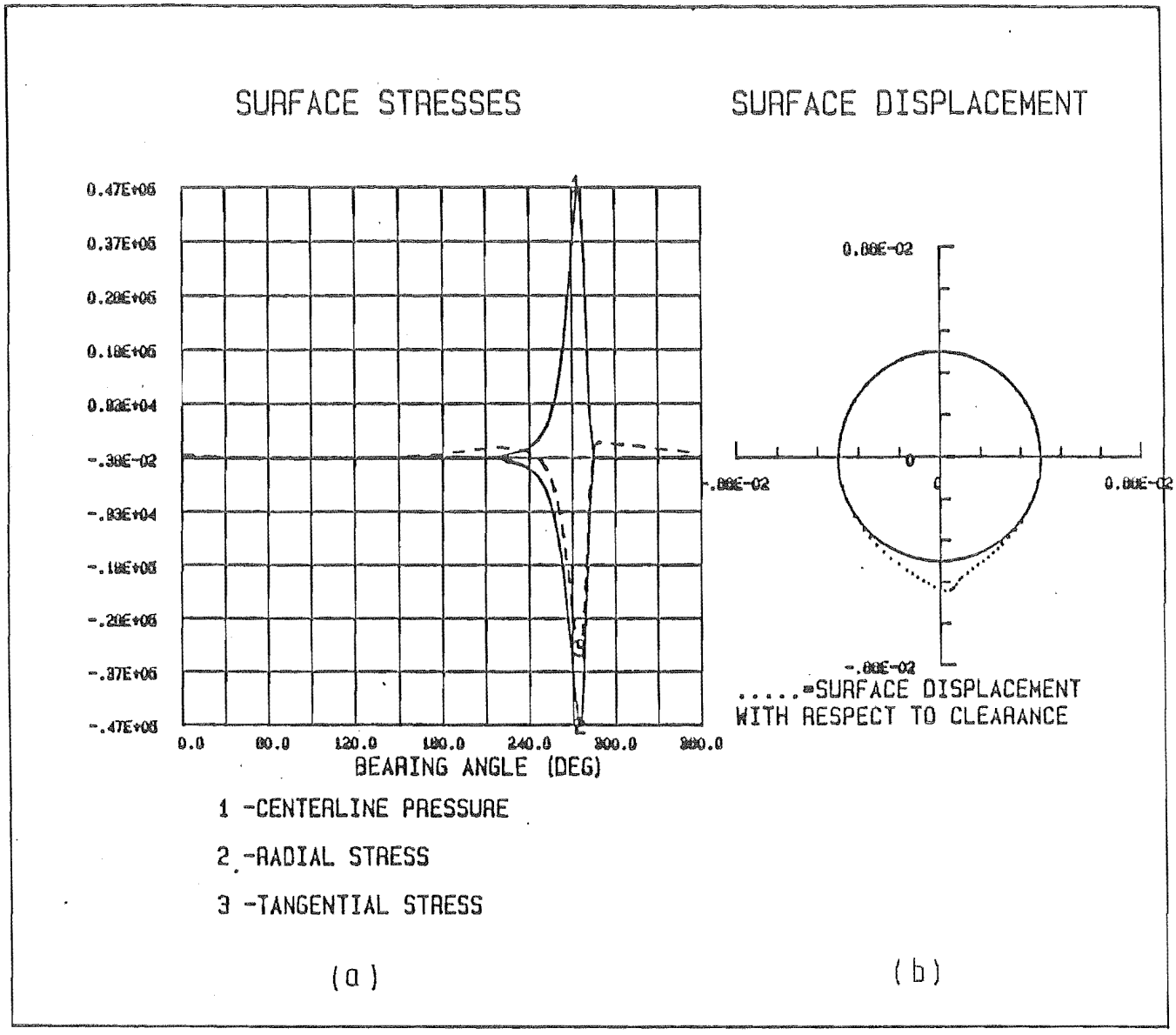

JOURNAL POSITION = 99.5 DEGREE

TEST NO 505 CO ROTATIONAL LOAD , 1 LAND BEARING

Fig 3.9

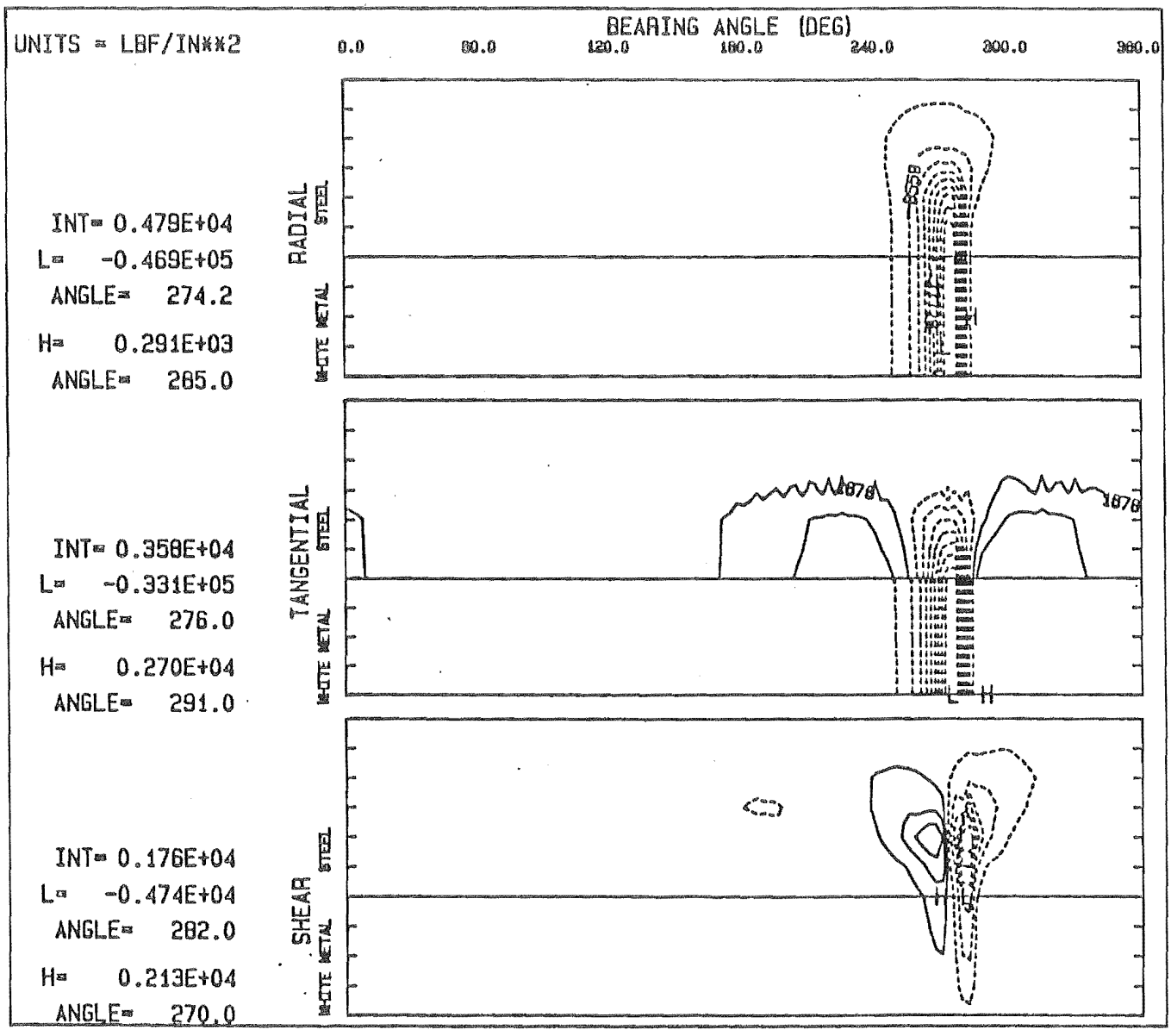

CONTOUR PLOT OF DIFFERENT STRESSES , JOURNAL POSITION = 99.5 DEGS, PL=TASV2
H, L=HIGH, LOW IN WHITE METAL, INT=INTERVAL DASHED LINES ARE NEGATIVE
TEST NO 505 CO ROTATIONAL LOAD . 1 LAND BEARING

Fig 3.10

CHAPTER FOUR

SENSITIVITY TESTS AND SOME STRESS DISTRIBUTIONS

In this chapter the sensitivity of journal bearing performance to some input load parameters such as operating temperature, diametral clearance, bearing's land length, load amplitude and mean load are explained. Some stress distributions are also discussed.

4.1 INPUT PARAMETERS

There are some important parameters such as operating temperature, diametral clearance and bearing land length which have influence on the performance of the journal bearing. Since there always exists some type of error during the actual experiment or in its numerical reconstruction, it was decided to run some sensitivity tests on these important parameters. This will evaluate the range of any possible error associated with the recording of experimental data or in the assumptions made in its numerical reconstruction. In the following sections, the effect of some variation of the input parameters on the centreline pressure and eccentricity ratio are explained. Blundell's [7] Test No. 5 (named 505 in here), for which he had reported most of his results, was chosen for the following sensitivity tests.

4.1.1 Temperature

Operating temperature is one of the important parameters affecting the design of a journal bearing. Since different points on the bearing's surface have different temperatures which vary as the shaft rotates, the oil viscosity varies

continuously. So it is very important to make an appropriate decision in choosing the operating temperature in the numerical simulation. Over the past years, people have made different decisions regarding this point. The majority of them have used the outlet oil temperature as the operating temperature. A comparison of Figs. 4.1 and 4.2 indicates how much the eccentricity locus and pressure curves change due to a 22^{o}C increase in operating temperature. Maximum peak pressure increases by 38%. Fig. 4.3 gives a plot of variation of peak pressure and eccentricity ratio with respect to temperature. To make the analysis simple, an isoviscous system was assumed and the outlet oil temperature which is measured directly was taken as the operating temperature. Blundell reported a variation of 47.1^{o}C to 51.4^{o}C in the outlet oil temperature of his experiments. Therefore an average value of 48.3^{o}C was taken in numerical reconstruction of all his tests. Fig. 4.3 shows that there is a negligible change in pressure due to using this average temperature instead of the maximum of 51.4^{o}C.

4.1.2 Diametral Clearance

The other important factor which influences the performance of a journal bearing is the diametral clearance. A comparison of Figs. 4.1 and 4.4 shows that a higher diametral clearance (.0050") increases the maximum peak pressure by 40%. Fig. 4.5 gives plots of peak pressure and journal position with respect to diametral clearance. Blundell had reported a variation of .0031 to .0036 (inch) in the measured diametral clearance. This gives an average value of .00335" which was used in reconstruction of his experiments.

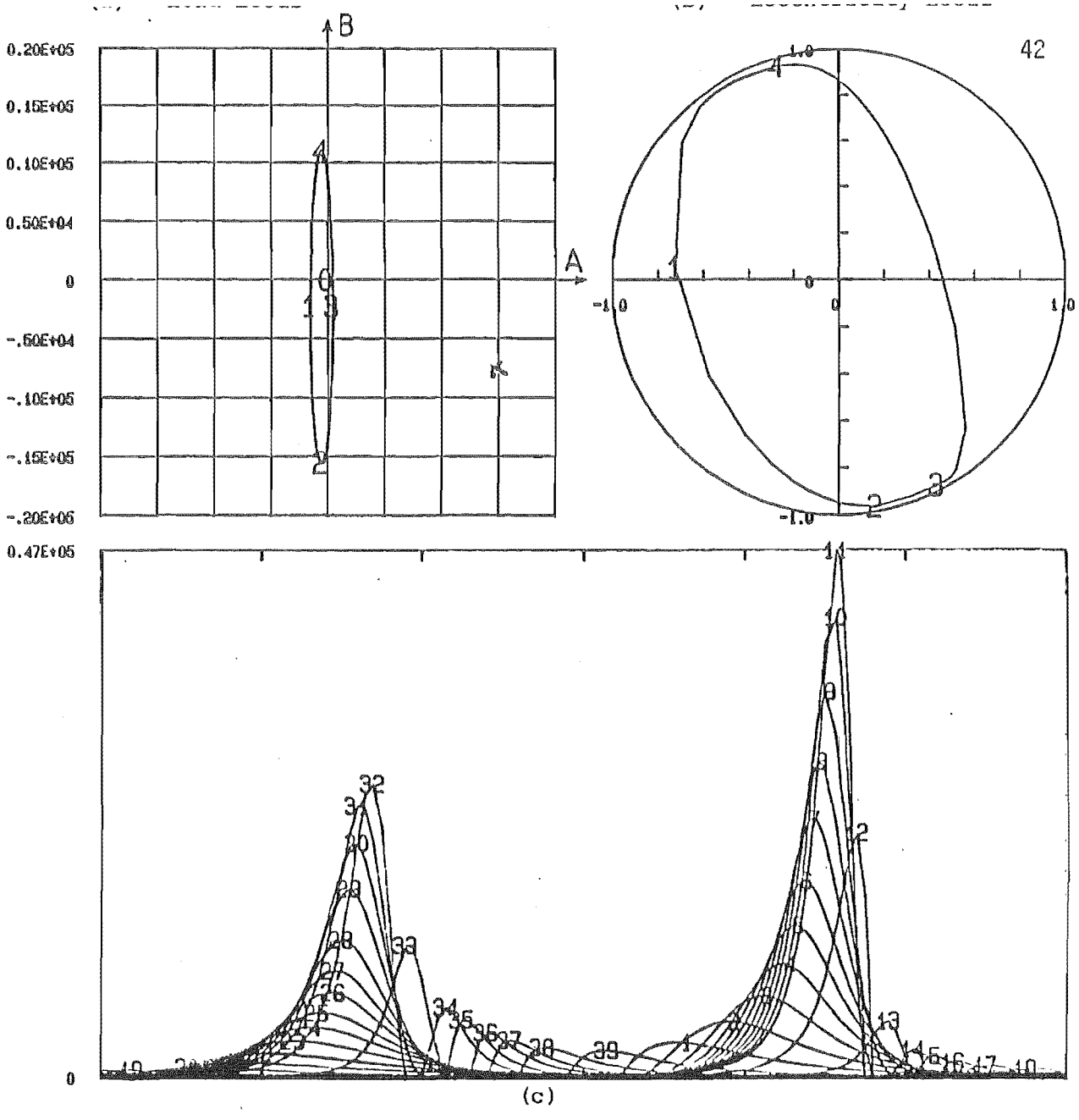

TEST NO 505 CO ROTATIONAL LOAD, 1 LAND BEARING

Operating temperature	=	48.3°C
Diametral clearance	=	.0033"
Bearing land length	=	1.16"
Rotational speed	=	1050 RPM
Load amplitude (A Axis)	=	1000 LbF
Load Amplitude (B Axis)	=	13280 LbF
Mean load (A Axis)	=	- 500 LbF
Mean load (B Axis)	=	- 2200 LbF
Phase angle	=	0°

Fig.4.1

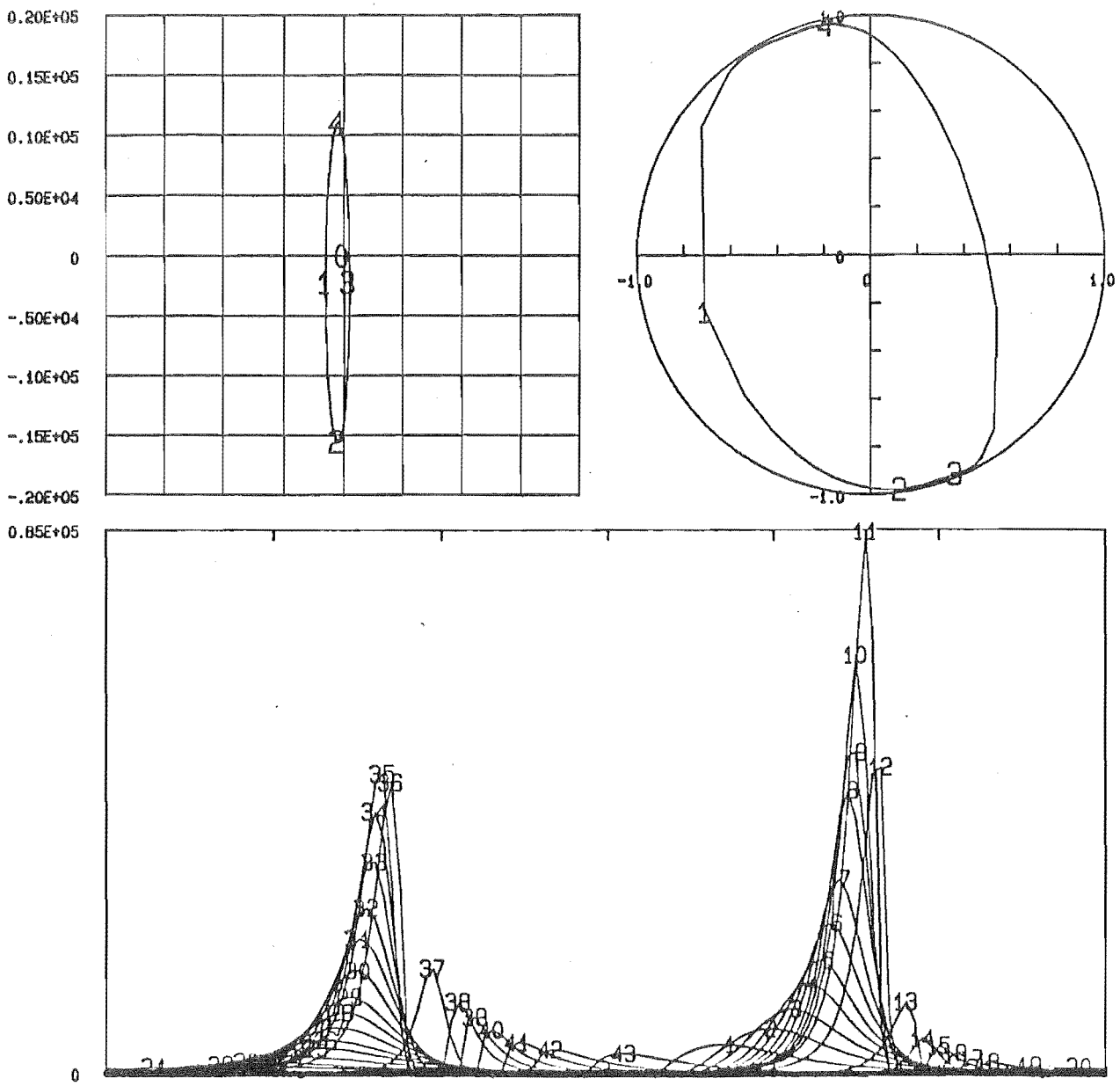

TEST NO 505 COROTATIONAL LOAD , I LAND BEARING , (TEMP = 70 C)

Fig.4.2

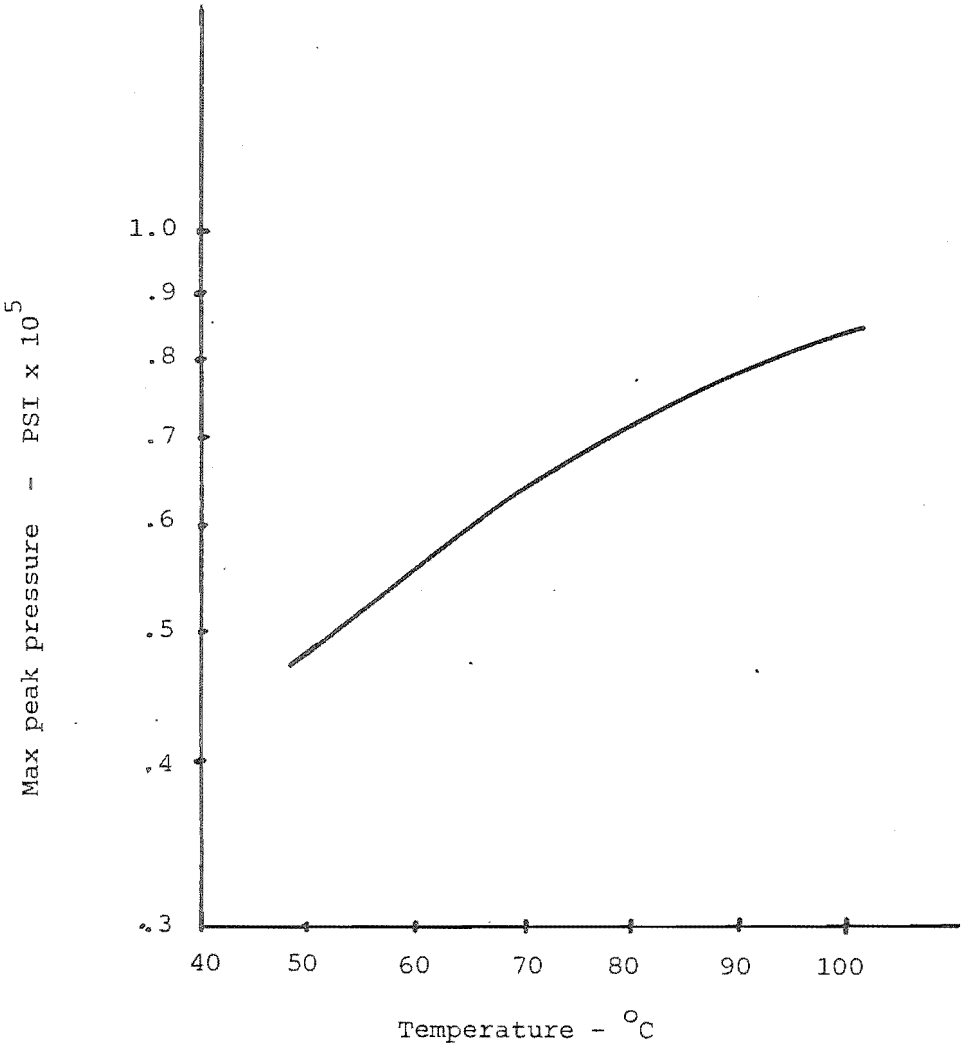
Max peak pressure - PSI x 10^5
1.0
.9
.8
.7
.6
.5
.4
.3
40
50
60
70
80
90
100
Temperature - °C

(a)

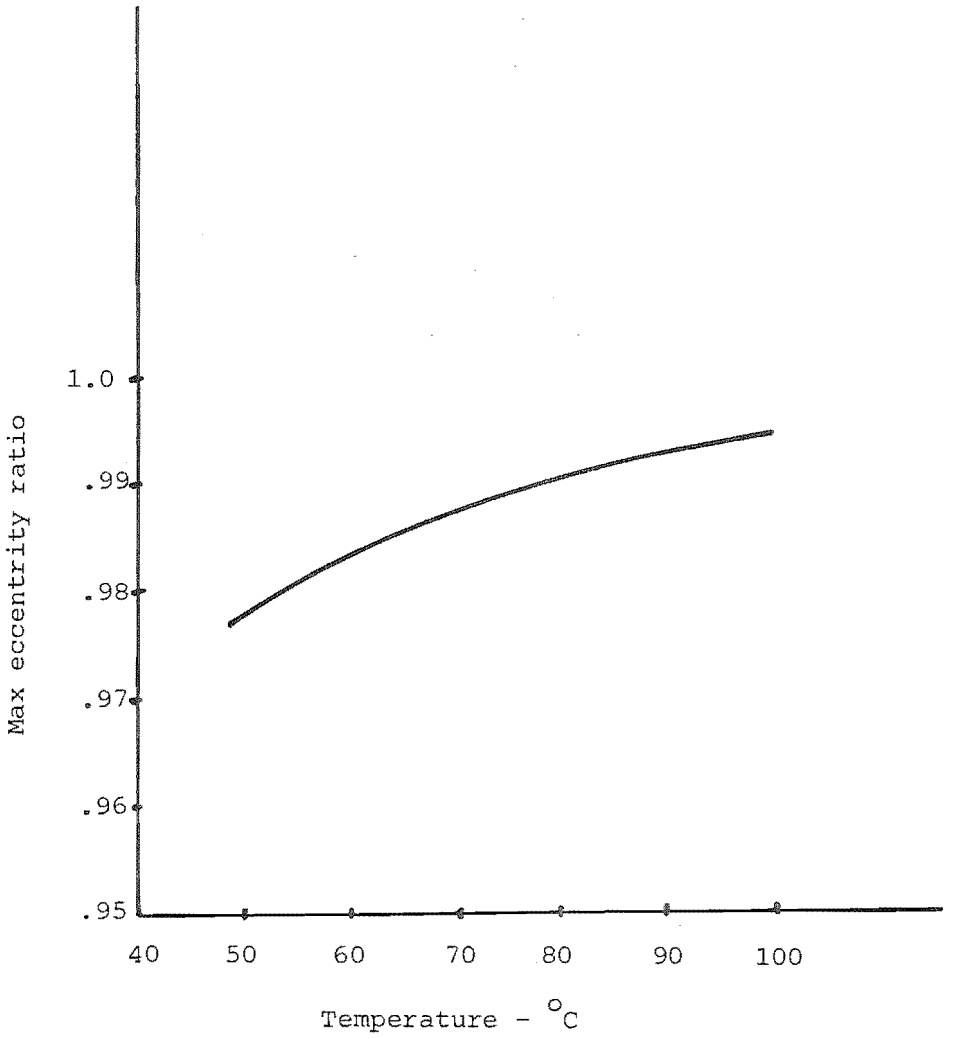
Max eccentrity ratio
1.0
.99
.98
.97
.96
.95
40
50
60
70
80
90
100
Temperature - °C

(b)

Fig. 4.3

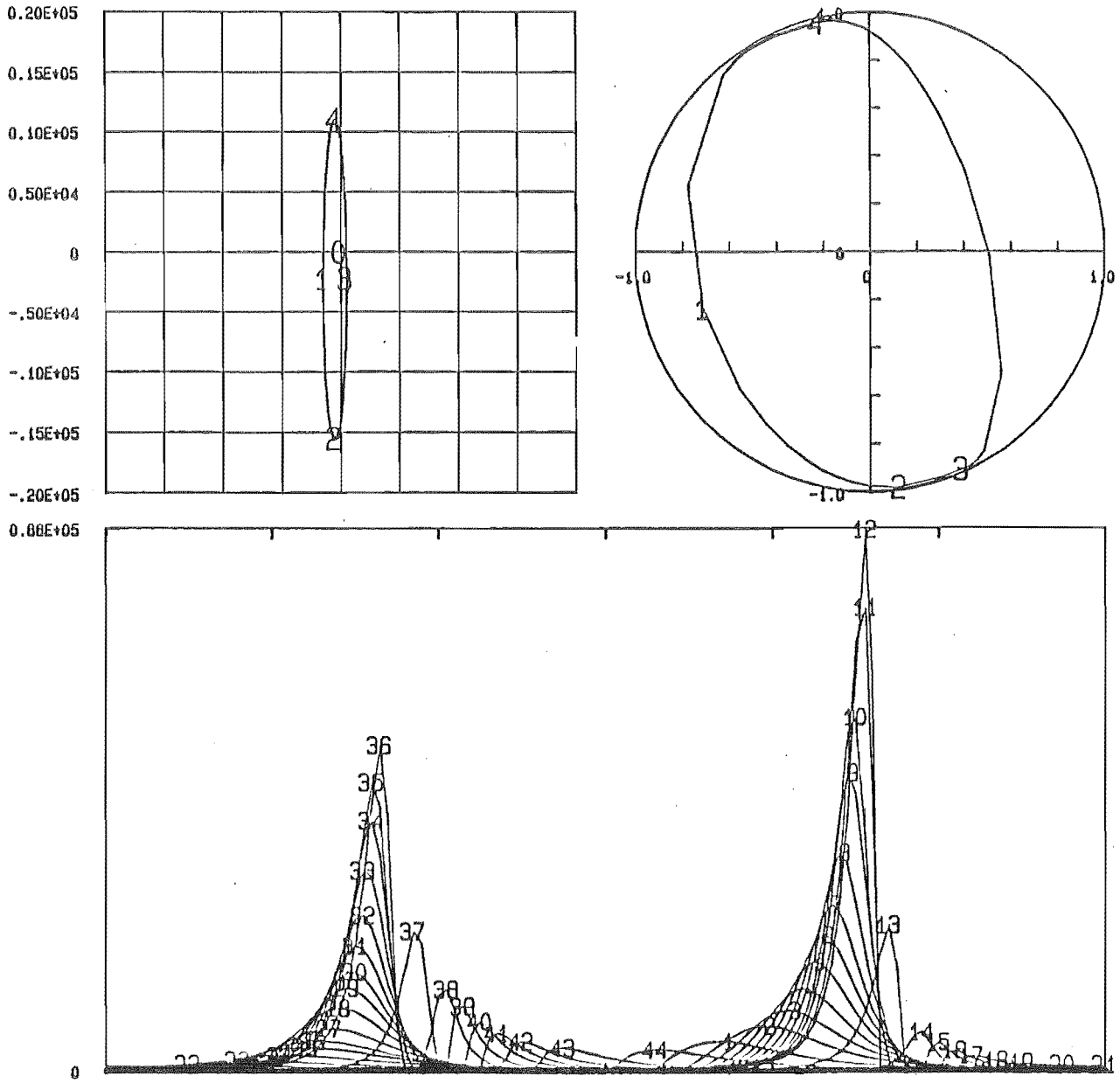

TEST NO 505 CO ROTATIONAL LOAD, 1 LAND BEARING, (DIAMETRAL CLEARANCE=.0050 IN)

Fig. 4.4

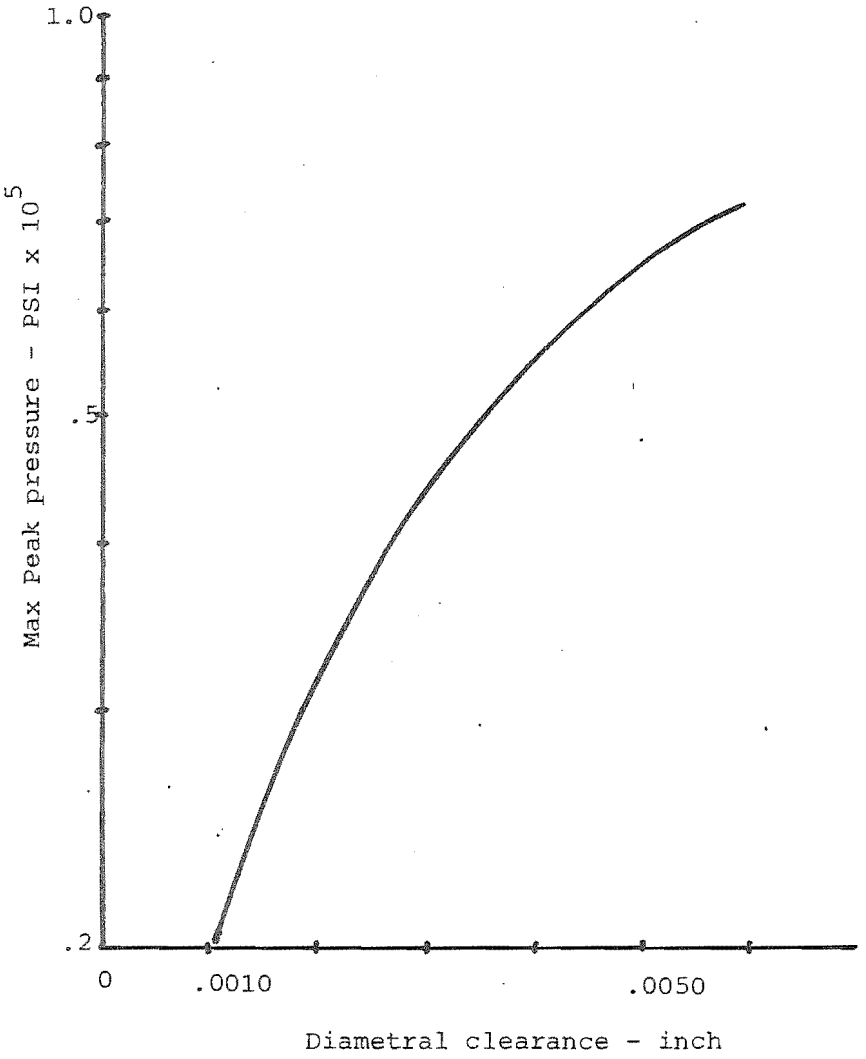
1.0
.5
.2
Max Peak pressure - PSI x 10^5
0
.0010
.0050
Diametral clearance - inch

(a)

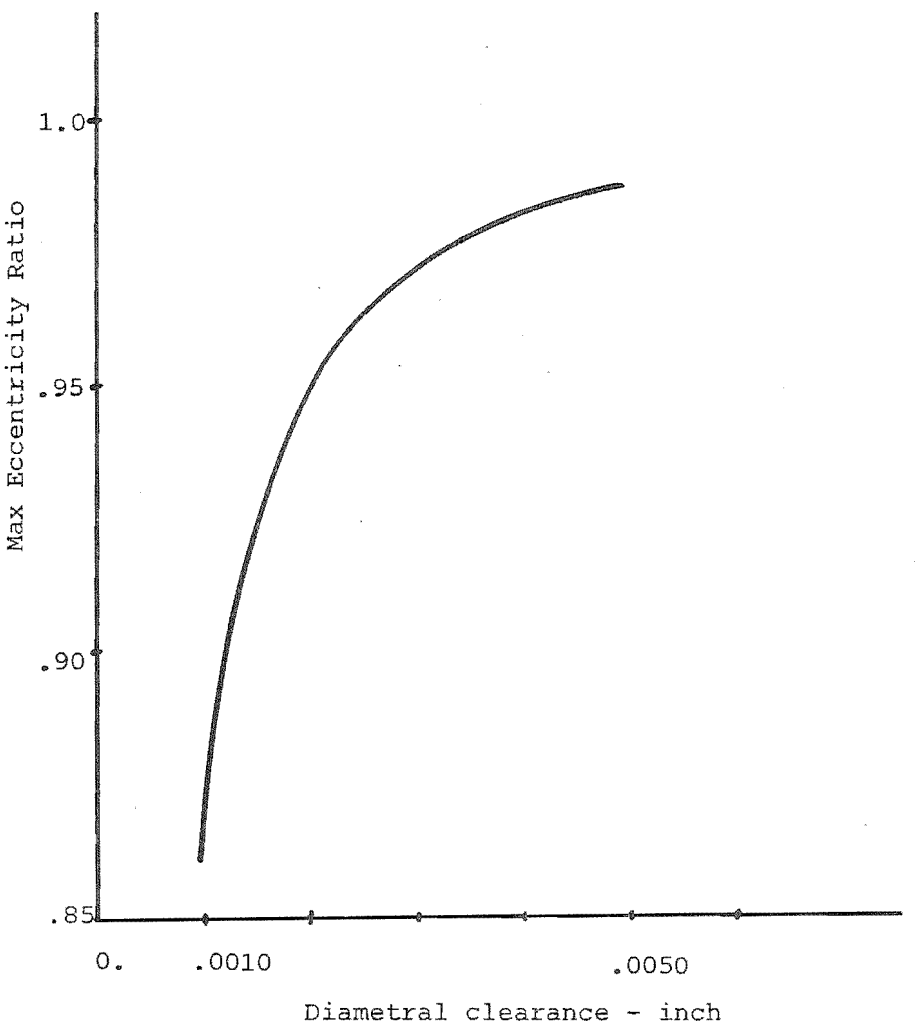
1.0
.95
.90
.85
Max Eccentricity Ratio
0.
.0010
.0050
Diametral clearance - inch

(b)

Fig. 4.5

4.1.3 Bearing Land Length

Blundell used both ungrooved bearings (one land) and bearings with circumferential oil grooves in the middle (two lands), in his experiments. His one land bearings were 1.16" in length while the grooved ones had two 0.5" length lands. Fig. 4.7 shows the eccentricity locus and the pressure curves for a 0.7" length one land bearing. This may be compared with Fig. 4.1 which is for a 1.16" length bearing. Fig. 4.8 shows how the increase in land length decreases the maximum eccentricity ratio and peak pressure in both type of bearings. It also shows that for the same input loads the grooved bearing generates a much higher pressure than the ungrooved bearing. This was because of the input force which in the two land case had to be balanced by two narrower but peakier parabolas (Fig. 3.9).

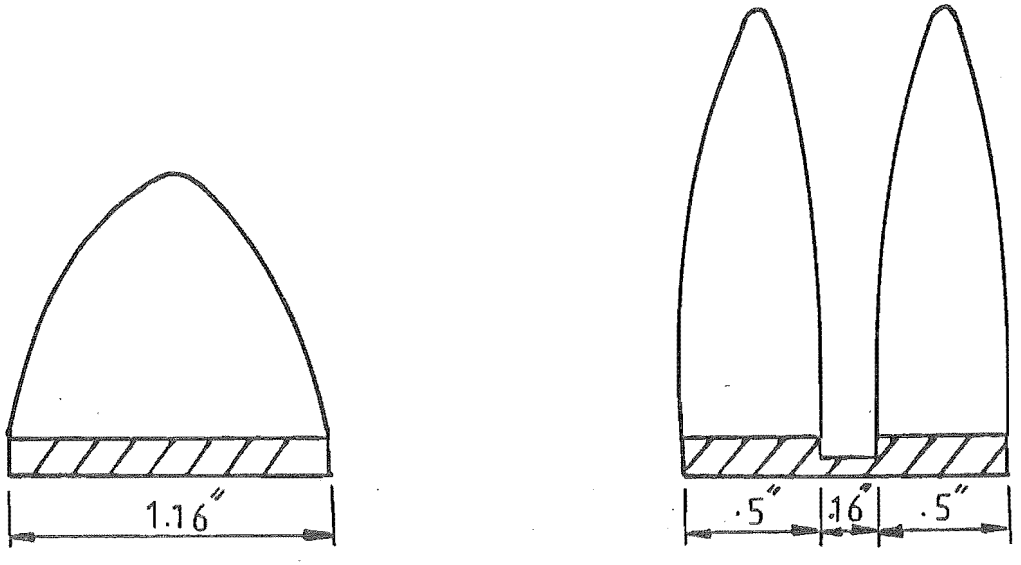

Fig. 4.6

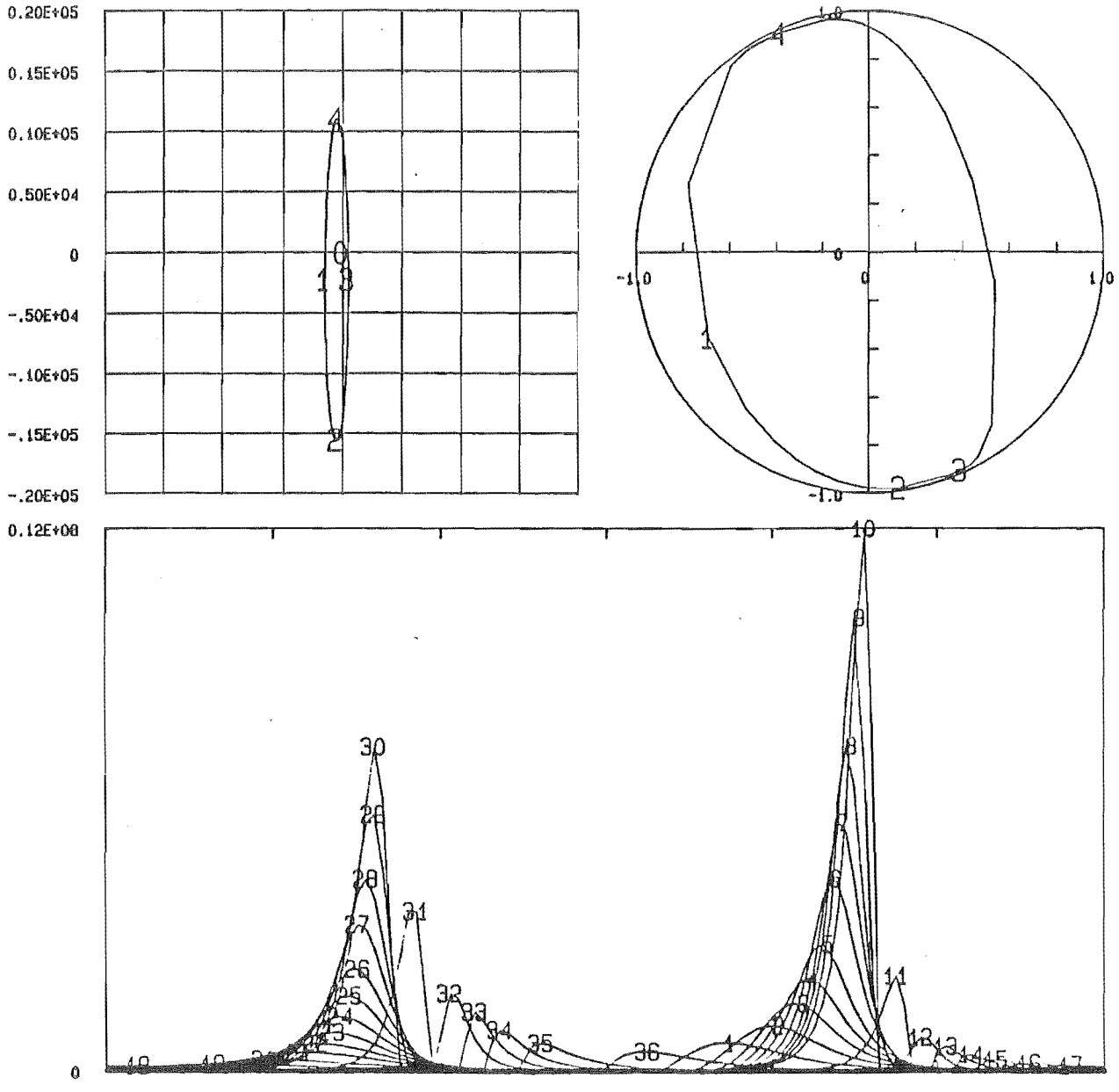
0.20E+05
0.15E+05
0.10E+05
0.50E+04
0
-.50E+04
-.10E+05
-.15E+05
-.20E+05
0.12E+08
0
-1.0
1.0
TEST NO 505 CO ROTATIONAL LOAD, 1 LAND BEARING , (LAND LENGTH = 0.7 IN)

Fig. 4.7

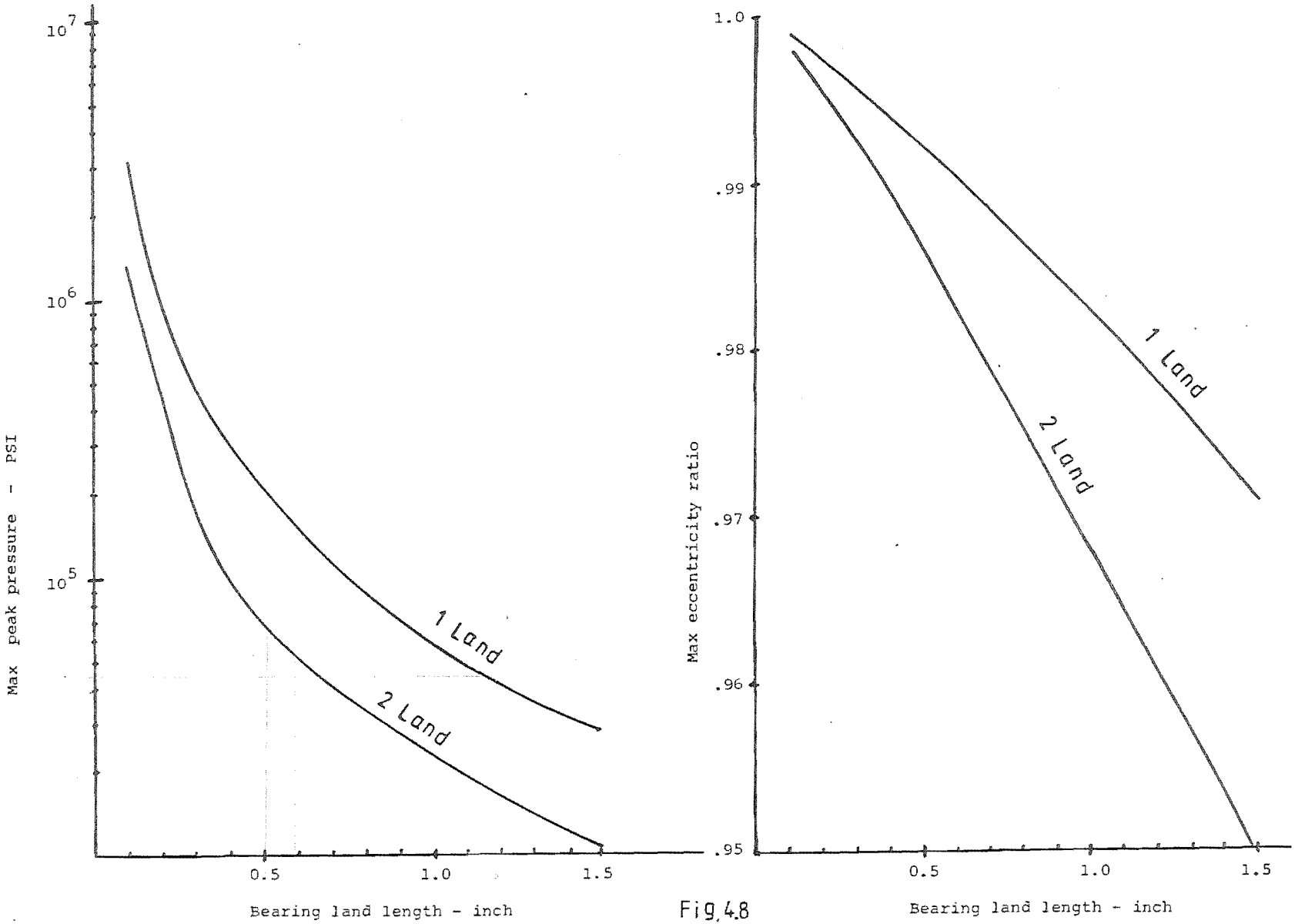
Max peak pressure - PSI
10^7
10^6
10^5
1 Land
2 Land
0.5
1.0
1.5
Bearing land length - inch
Max eccentricity ratio
1.0
.99
.98
.97
.96
.95
1 Land
2 Land
0.5
1.0
1.5
Bearing land length - inch

Fig 4.8

4.1.4 Surface Distortion

As it was mentioned in Chapter Two, the Lloyd program [6] assumes the bearing surface to remain circular. However, Allen [22] showed that the surface distortion has some effect on the centreline pressure distribution. Fig. 4.9 shows how this reduces the peak pressure in a connecting rod bearing by making the pressure curve less steep. The connecting rod had a thickness–radius ratio of 0.33 which was lower than the Blundell's case which had a thicker housing, giving him a 0.9 thickness–radius ratio.

4.2 LOAD LOCUS

Blundell selected a wide variety of input load patterns in his experiments (Chapter Five). They had different amplitude and mean loads in both directions of application of pistons A and B. There was also an angular phase difference between the operation of the two pistons in some of the tests which caused their input load diagrams to turn slightly (clockwise or anticlockwise).

Since Blundell had reported a maximum uncontrollable fluctuation of ± 600 LbF on his input load diagrams, and there were also some differences between the actual load diagram and those simulated theoretically (Fig. 3.3), it was decided to check the sensitivity of oil pressure to some variation of mean load, load amplitude and the phase angle. Again Test No. 5 of Blundell (named 505 in here) was chosen for the following sensitivity tests.

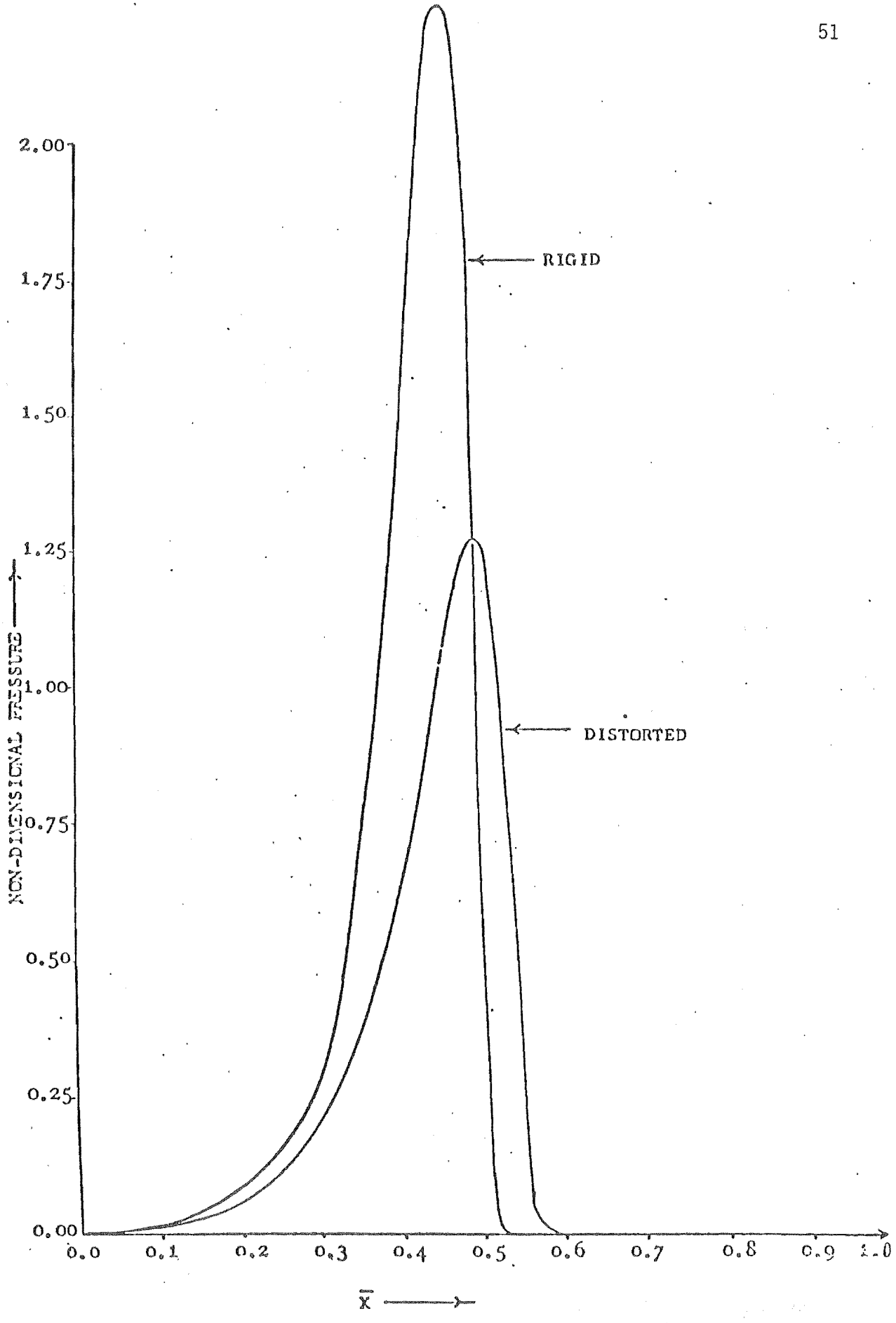

(after Allen [22])

Fig. 4.9

4.2.1 Load amplitude

Fig. 4.10a shows a typical input load diagram with different load amplitude (a and b) in the A and B directions. An increase in the load amplitude of piston B changes the load locus especially in the 90^{O} and 270^{O} regions. Since the maximum peak pressure is in the 270^{O} region, it will increase considerably, while the pressure in $0^{O}$and 180^{O} will not be affected.

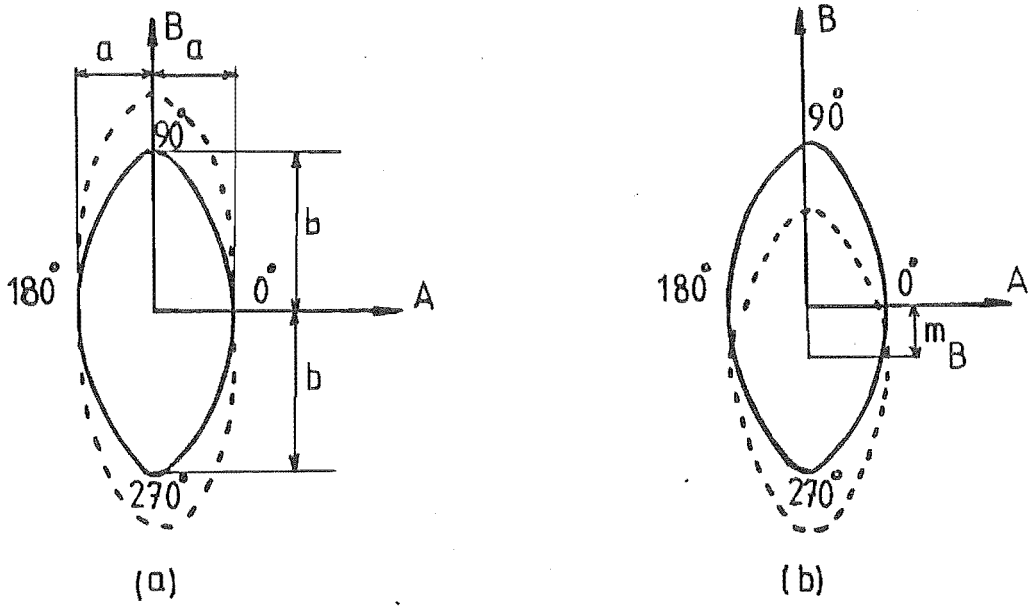

Fig. 4.10

The same thing will happen to the A axis if the load amplitude in that axis (a) changes. On Fig. 4.13a, the effect of variation of load amplitude (b) on the maximum peak pressure has been plotted. A comparison of Figs. 4.1 and 4.11 shows how the pressure curves and eccentricity locus changes with a 2500 LbF increase in load amplitude. Fig. 4.13a indicates a 3.2% increase of peak pressure

due to the 600 LbF fluctuation of input load reported by Blundell, which is negligible.

4.2.2 Mean Load

Fig. 4.10b shows how a mean load increase in B direction shifts the load locus which obviously increases the maximum peak pressure. On Fig. 4.13b the effect of variation of mean load on maximum peak pressure has been plotted. A comparison of Figs. 4.1 and 4.12 shows how the eccentricity locus and pressure curves changes with a 3500 LbF increase in mean load. Fig. 4.13b indicates a 4% increase in peak pressure due to the 600 LbF fluctuation of input load reported by Blundell, which is negligible. However, a test showed that a 600 LbF shift of mean load in A direction (i.e. –500 LbF to 100 LbF) shifts the angular position of peak pressure by 4^{O} (i.e. 274.2 to 278.1), whereas the maximum peak pressure remains constant (Fig. 4.14). This indicates how sensitive the position of peak pressure is to slight fluctuation of load in the A direction.

4.2.3 Phase Angle ϕ

If there is no time lag between the operation of the two pistons A and B (i.e. $\phi = 0$ in (3.1),(3.2)), then the load locus would appear symmetric about the B axis (Fig. 4.15b). Inserting a positive or negative value for ϕ in (3.1), (3.2) causes the load locus to turn clockwise (Fig. 4.15a) or anticlockwise (Fig. 4.15c), which also rotates the position of maximum peak pressure.

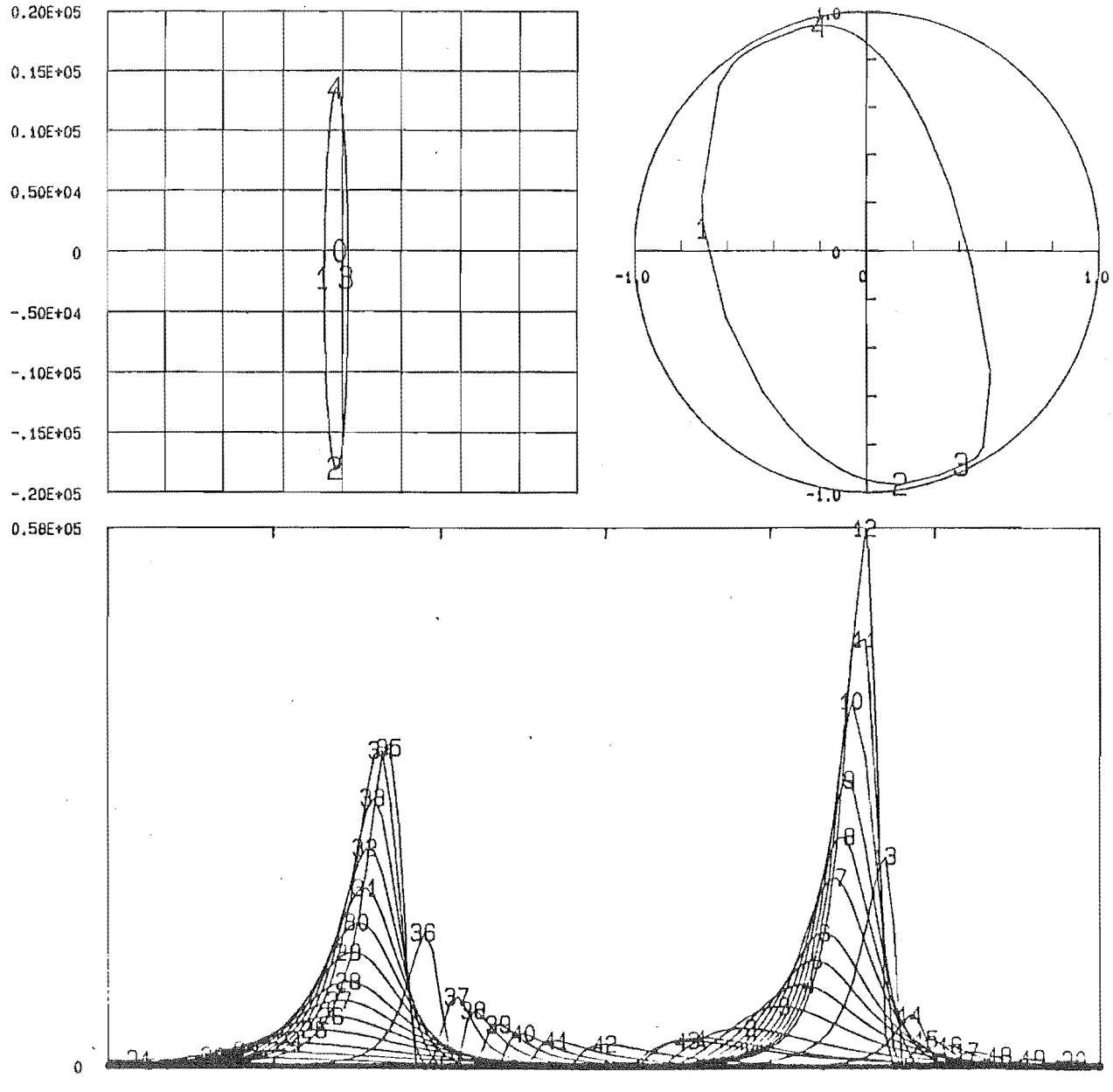

TEST NO 505 CO ROTATIONAL LOAD, 1 LAND BEARING, (LOAD AMPLITUDE (B-AXIS) =15780

Fig.4.11

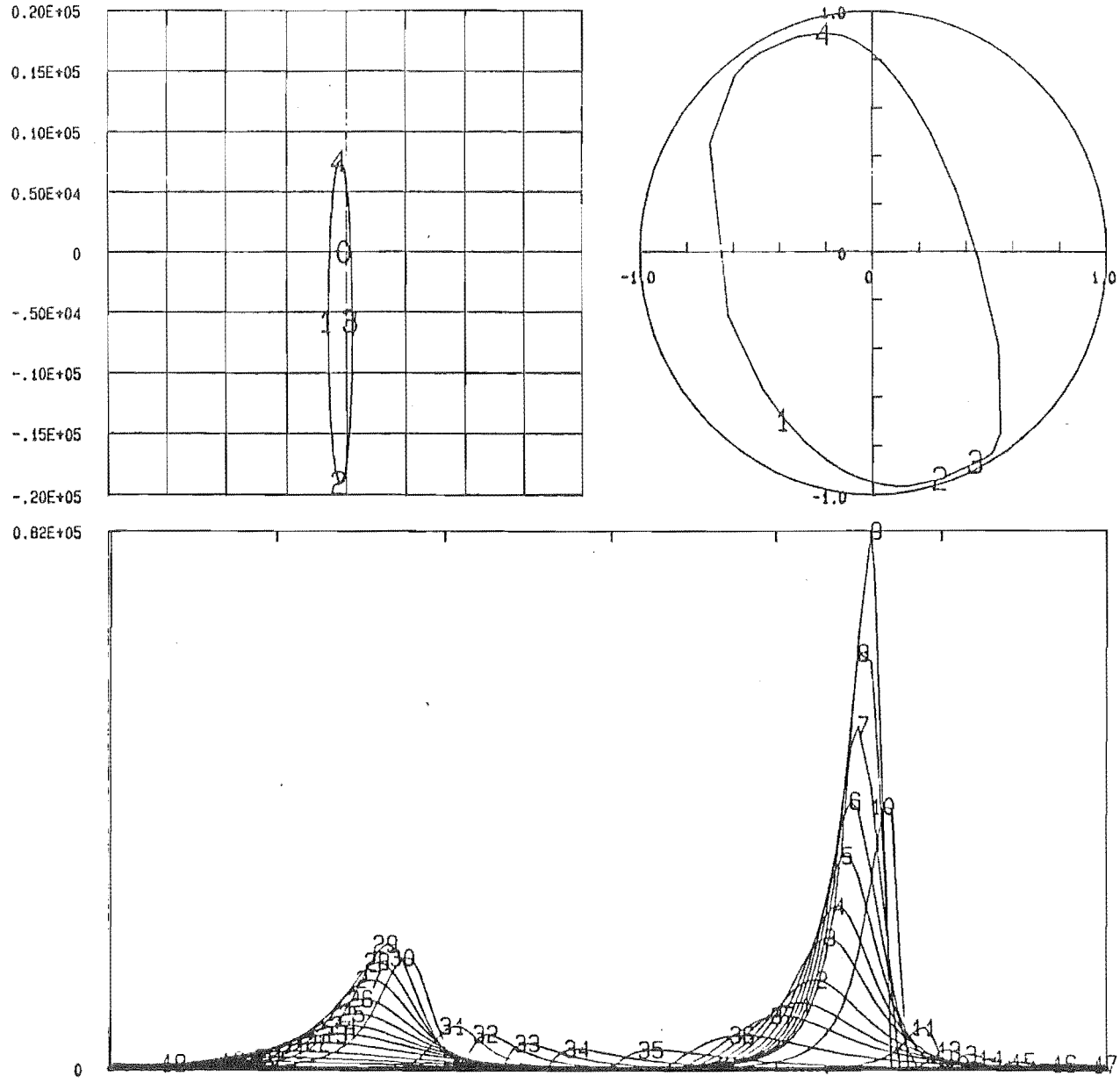

TEST NO 505 CO ROTATIONAL LOAD, 1 LAND BEARING , (MEAN LOAD (B-AXIS) =-5700)

Fig.4.12

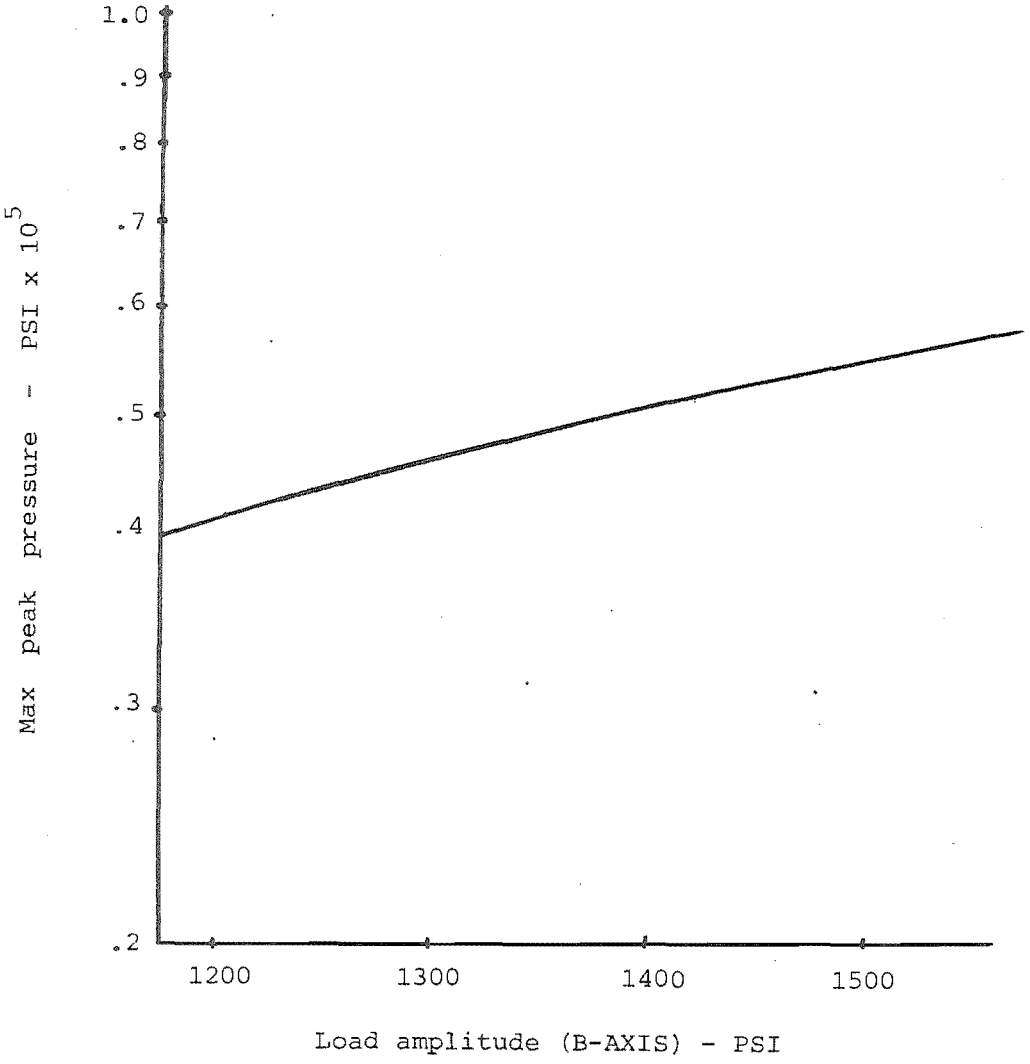
1.0
.9
.8
.7
.6
.5
.4
.3
.2
Max peak pressure - PSI x 10^5
1200
1300
1400
1500
Load amplitude (B-AXIS) - PSI

(a)

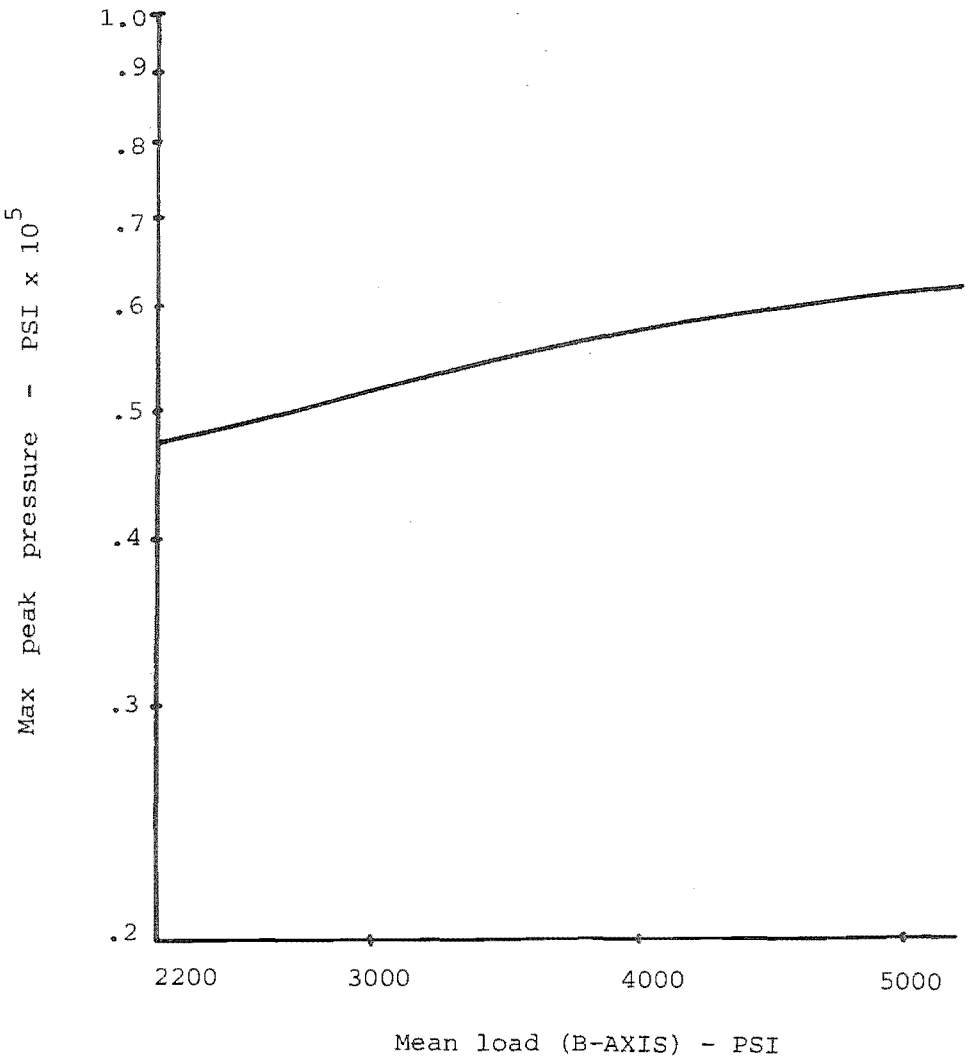
1.0
.9
.8
.7
.6
.5
.4
.3
.2
Max peak pressure - PSI x 10^5
2200
3000
4000
5000
Mean load (B-AXIS) - PSI

(b)

Fig. 4.13

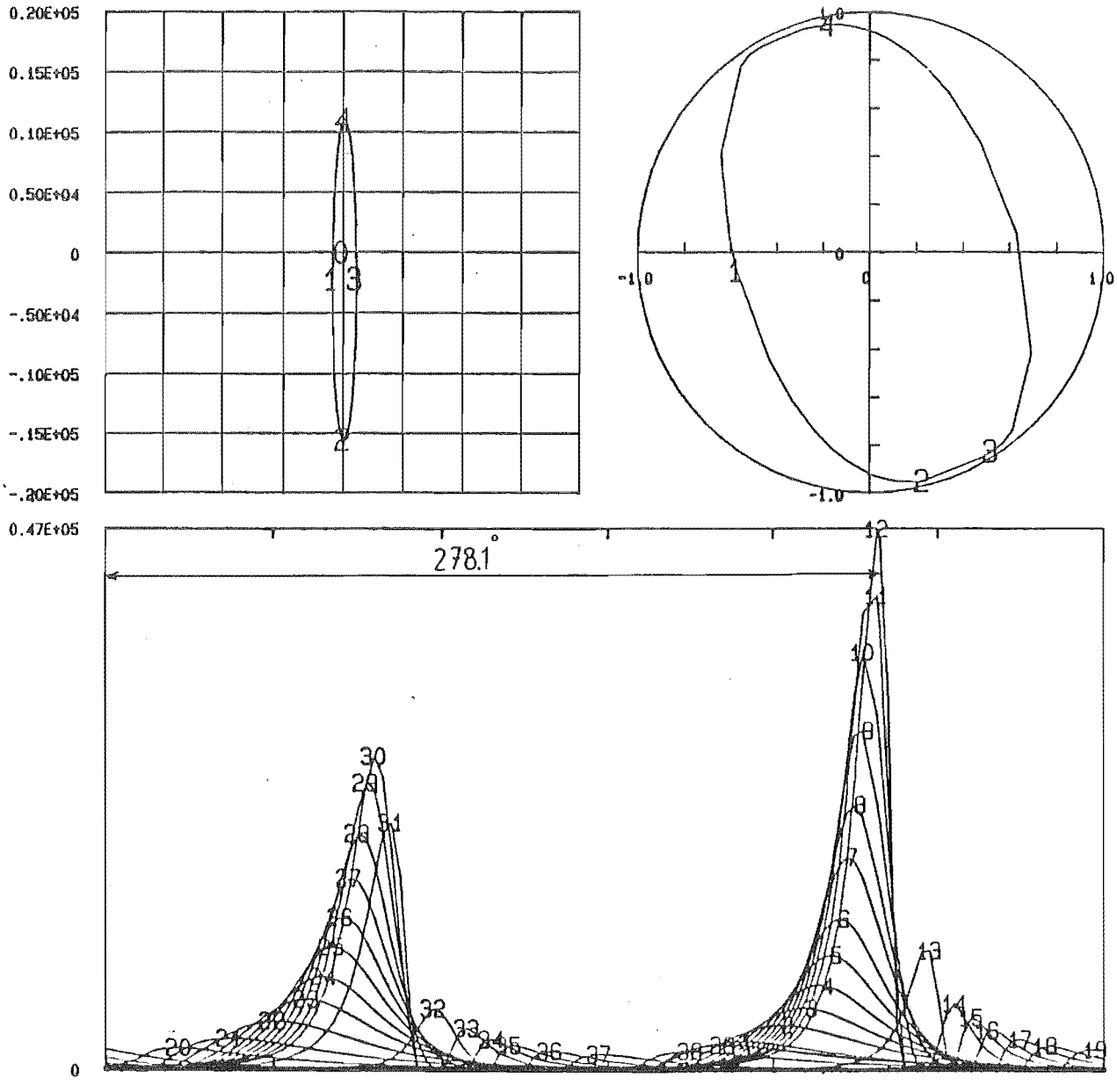

TEST NO 505 CO ROTATIONAL LOAD, 1 LAND BEARING, (MEAN LOAD (A-AXIS) =100)

Fig 4.14

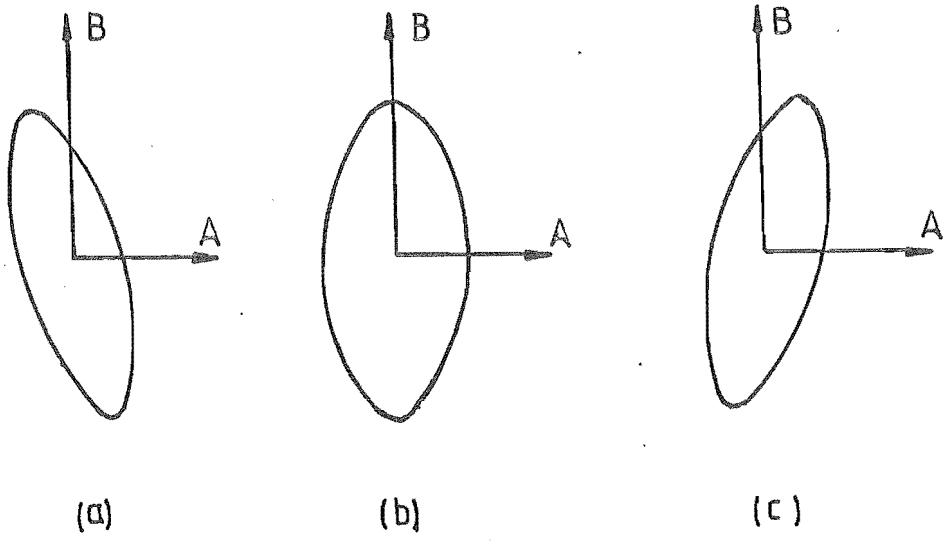

Fig. 4.15

The amount of rotation of load locus also depends on the load amplitude ratios (b/a). Fig. 4.16a has a lower amplitude ratio than Fig. 4.16b, therefore a 90^{O} phase angle causes only 20^{O} rotation of load locus compared to 45^{O} for Fig. 4.16b. Test 505 had a low amplitude ratio of .075, therefore a 20^{O} phase angle has a negligible effect on it while Test 504 (Chapter Five) has a .22 amplitude ratio and a 20^{O} phase angle rotates its peak pressure position by 4.5^{O} (i.e. 278.3^{O} to 282.8^{O})

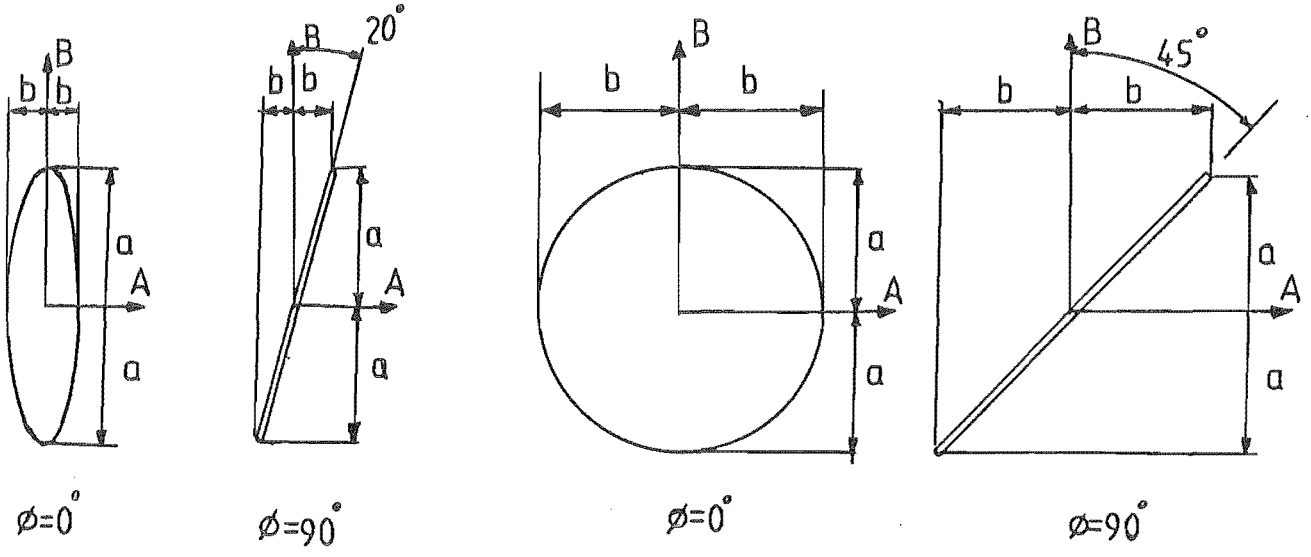

ø=0° ø=90° ø=0° ø=90°

$\frac{b}{a}=.2$ $\frac{b}{a}=1$

(a) (b)

Fig. 4.16

4.2.4 Mean–Amplitude Ratio

In a journal bearing which is under a sinusoidal type of loading, Fig. 4.17, it is possible to have four groups of load diagrams by changing the mean and amplitude loa setting. All four load loci shown in Fig. 4.18 have the same amplitude but different magnitude of mean loads. Fig. 4.18 shows that by increasing the mean load, the load locus gradually moves to one side of A axis which obviously shifts the eccentricity locus to one side of bearing centre. Fig. 4.19 shows that as the mean load increases, all the oil pressure curves shift to one side of the bearing. If the mean load becomes very large compared to the load amplitude, the load diagram and eccentricity locus would appear as a point and all the pressure curves will coincide on a single curve.

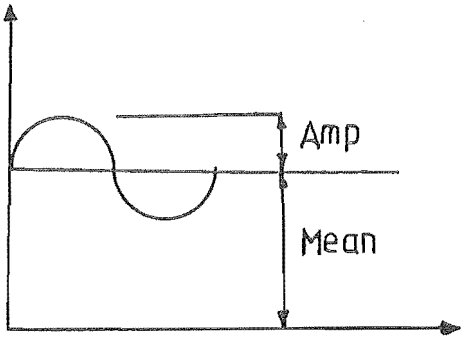

Fig . 4 .17

4.2.5 Direction of Load Locus

Changing the direction of input load diagrams also affects the performance of journal bearing. Blundell tested his bearings with both a co–rotational load (i.e. direction of load rotation was the same as that of the shaft rotation) and an anti–rotational load (i.e. direction of load rotation was opposite to that of shaft rotation). A comparison of Figs. 4.1 and 4.20 shows how this change of direction reduces the peak pressure and the eccentricity ratio. Later on, in Chapter Five,

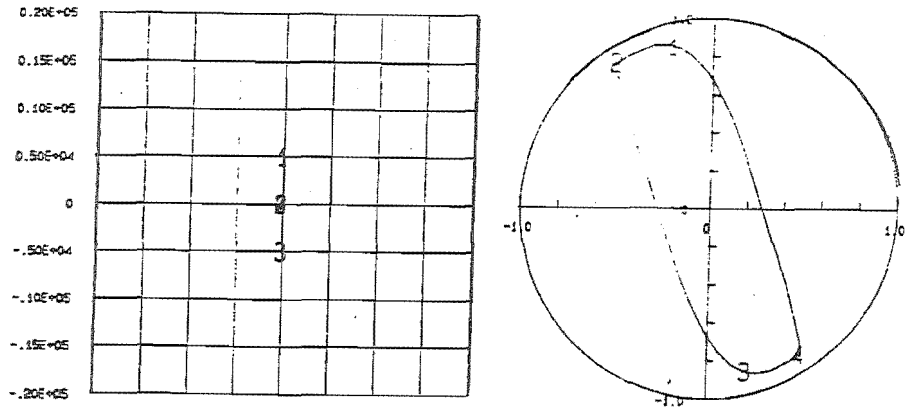

MEAN/AMP TEST , CO ROTATIONAL LOAD, 1 LAND BEARING , MEAN=0. , AMP=5000.

(a)

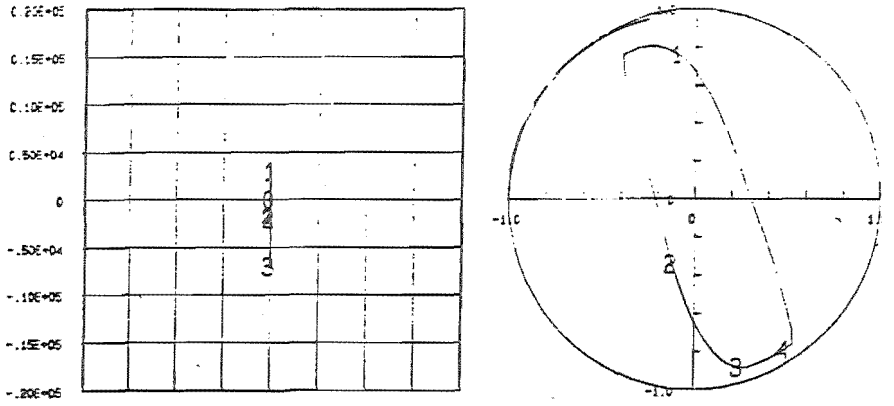

MEAN/AMP TEST , CO ROTATIONAL LOAD, 1 LAND BEARING , MEAN=2000. , AMP=5000

(b)

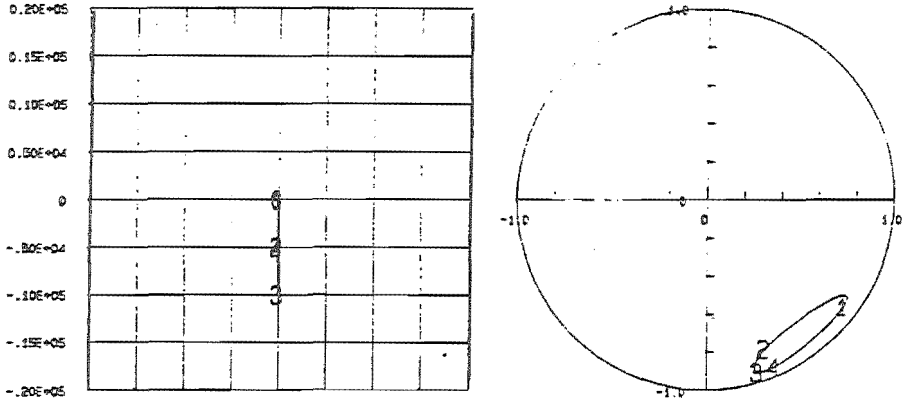

MEAN/AMP TEST , CO ROTATIONAL LOAD, 1 LAND BEARING , MEAN=5000. , AMP=5000.

(c)

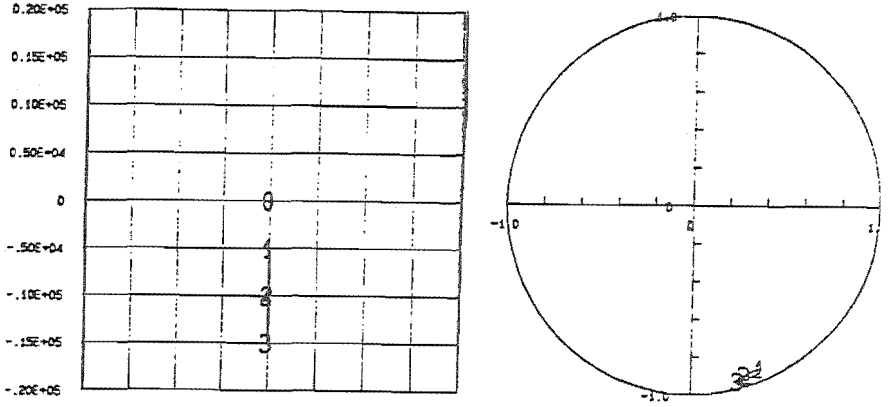

MEAN/AMP TEST , CO ROTATIONAL LOAD, 1 LAND BEARING , MEAN=10000. , AMP=5000.

(d)

Fig.4.18

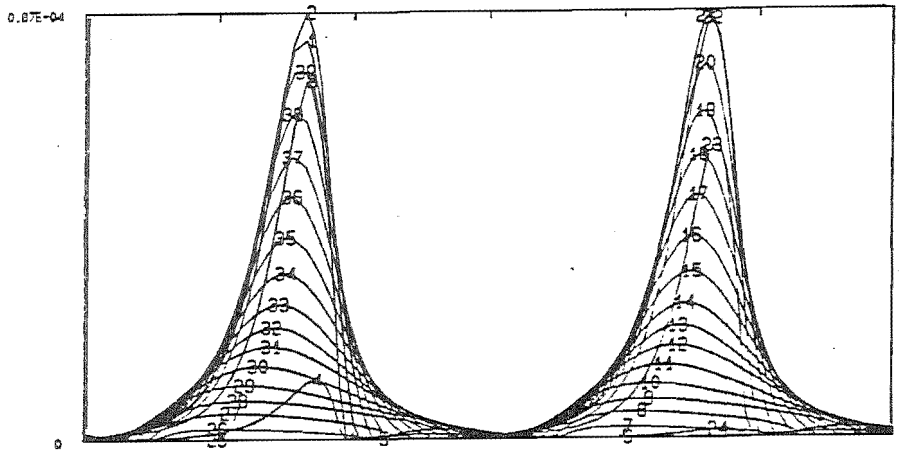

MEAN/AMP TEST , CO ROTATIONAL LOAD, 1 LAND BEARING , MEAN=0. , AMP=5000.

(a)

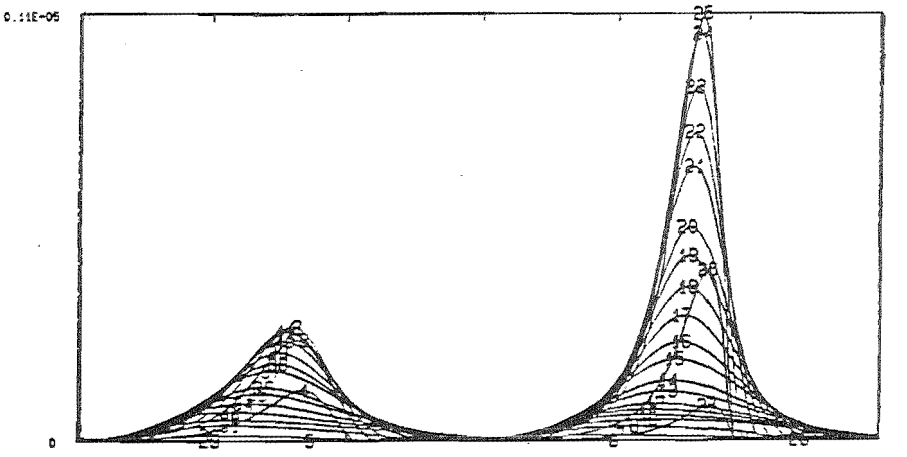

MEAN/AMP TEST , CO ROTATIONAL LOAD, 1 LAND BEARING , MEAN=2000. , AMP=5000.

(b)

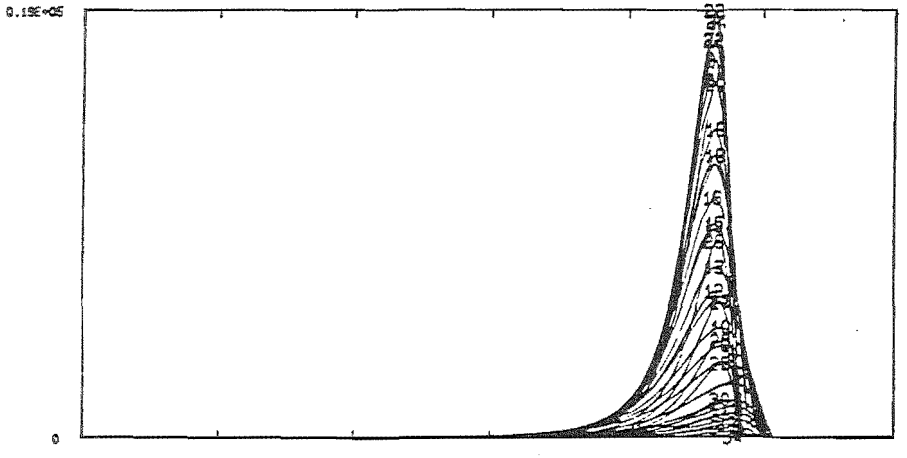

MEAN/AMP TEST , CO ROTATIONAL LOAD, 1 LAND BEARING , MEAN=5000. , AMP=5000.

(c)

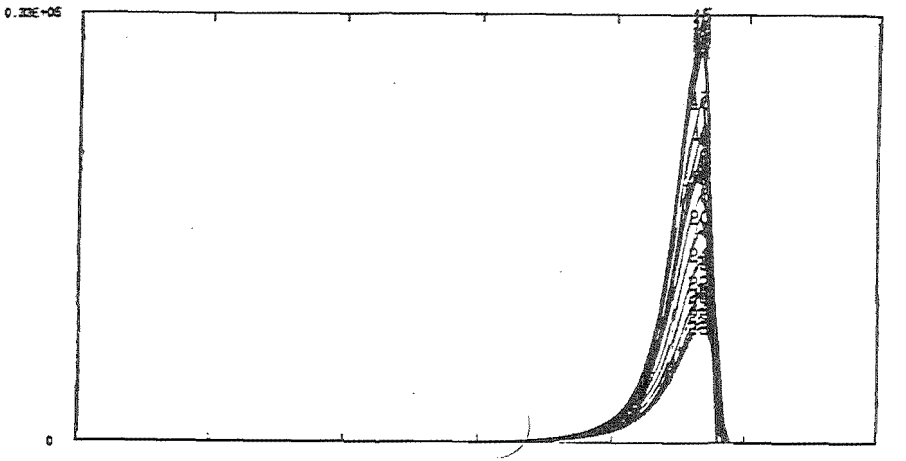

MEAN/AMP TEST , CO ROTATIONAL LOAD, 1 LAND BEARING , MEAN=10000. , AMP=5000.

(d)

Fig 4.19

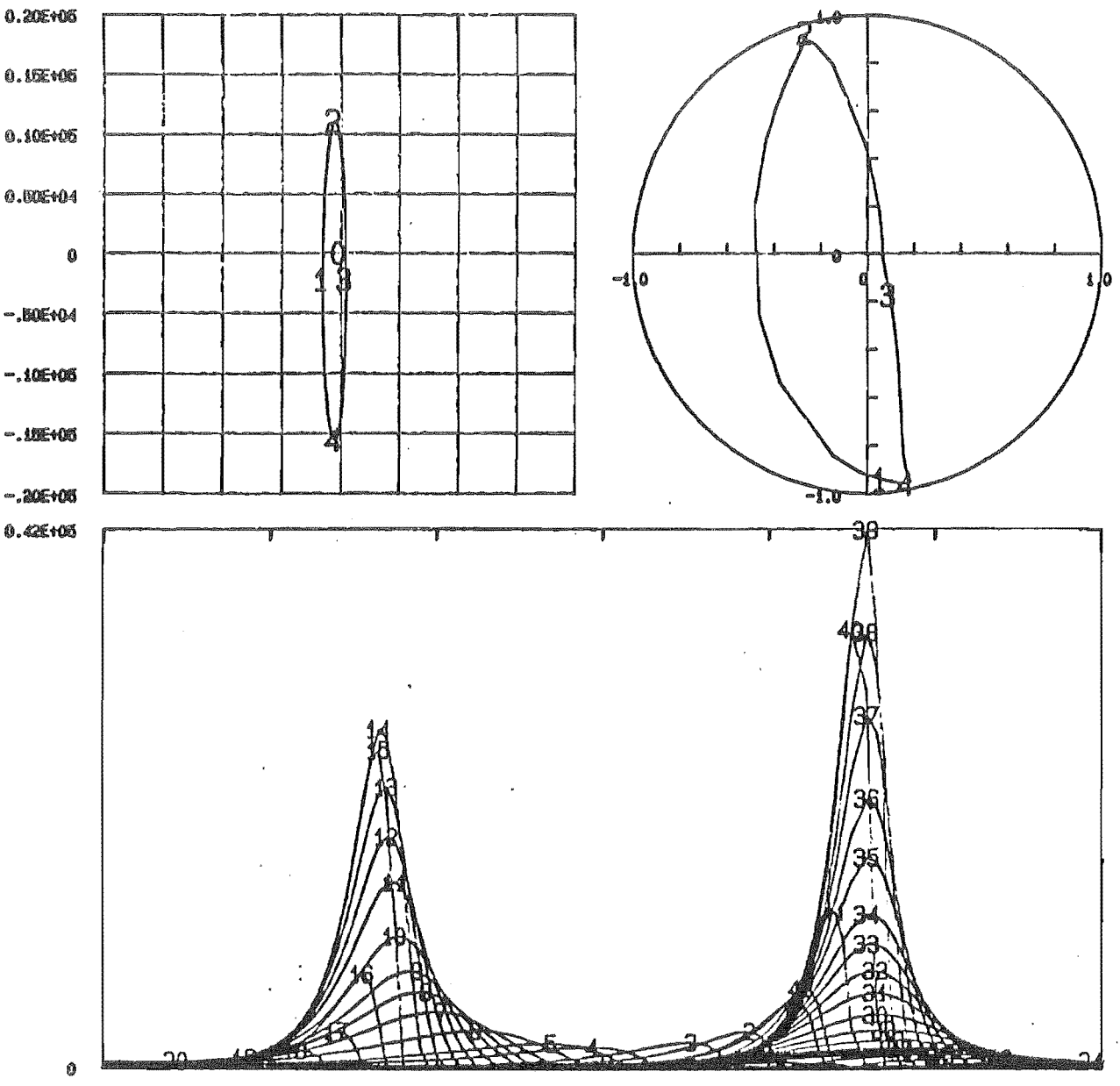
0.20E+05
0.15E+05
0.10E+05
0.00E+04
0
-.50E+04
-.10E+05
-.15E+05
-.20E+05
0.42E+05
0
1.0
-1.0
TEST NO 505 1 LAND BEARING
(ANTI ROTATIONAL)

Fig.4.20

it will be shown how this also affected the time history of stresses in a way that persuaded us to study it in more detail.

4.3 SOME STRESS DISTRIBUTIONS

To verify the validity of the FEM, interpolation and plotting programs, it was decided to test them against the stress distributions reported by the Ibrahim and McCallion [4] of a bimetallic strip (white metal bonded to steel backing) which was supported on a completely rigid surface (Fig. 4.21).

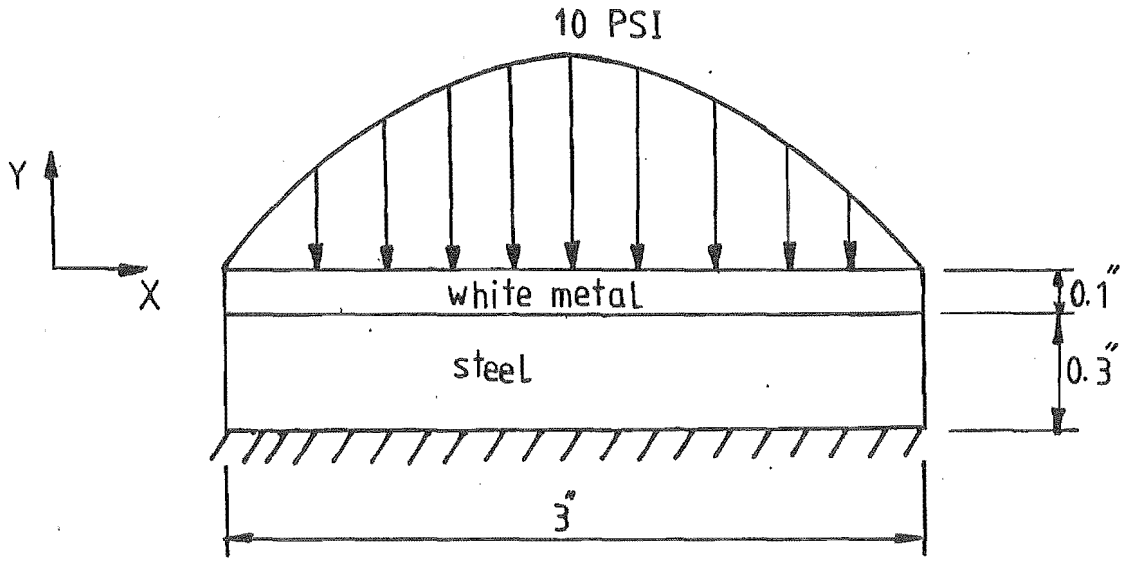

Fig. 4.21

The white metal surface was subjected to a fluid pressure of peak 10 LbF/in^2 which varied parabolically with x. The material properties of the two metals are listed in Table 4.1. Fig. 4.22 shows the contour plot of the stresses. It should be

noted that the bearing length was divided into 360 divisions. Therefore, 0, 180, 24, 336 positions shown on the plot are with respect to those divisions.

	Young modulus (PSI)	Poisson ratio
white metal	4×10^6	0.4
steel	30×10^6	0.3

Table 4.1

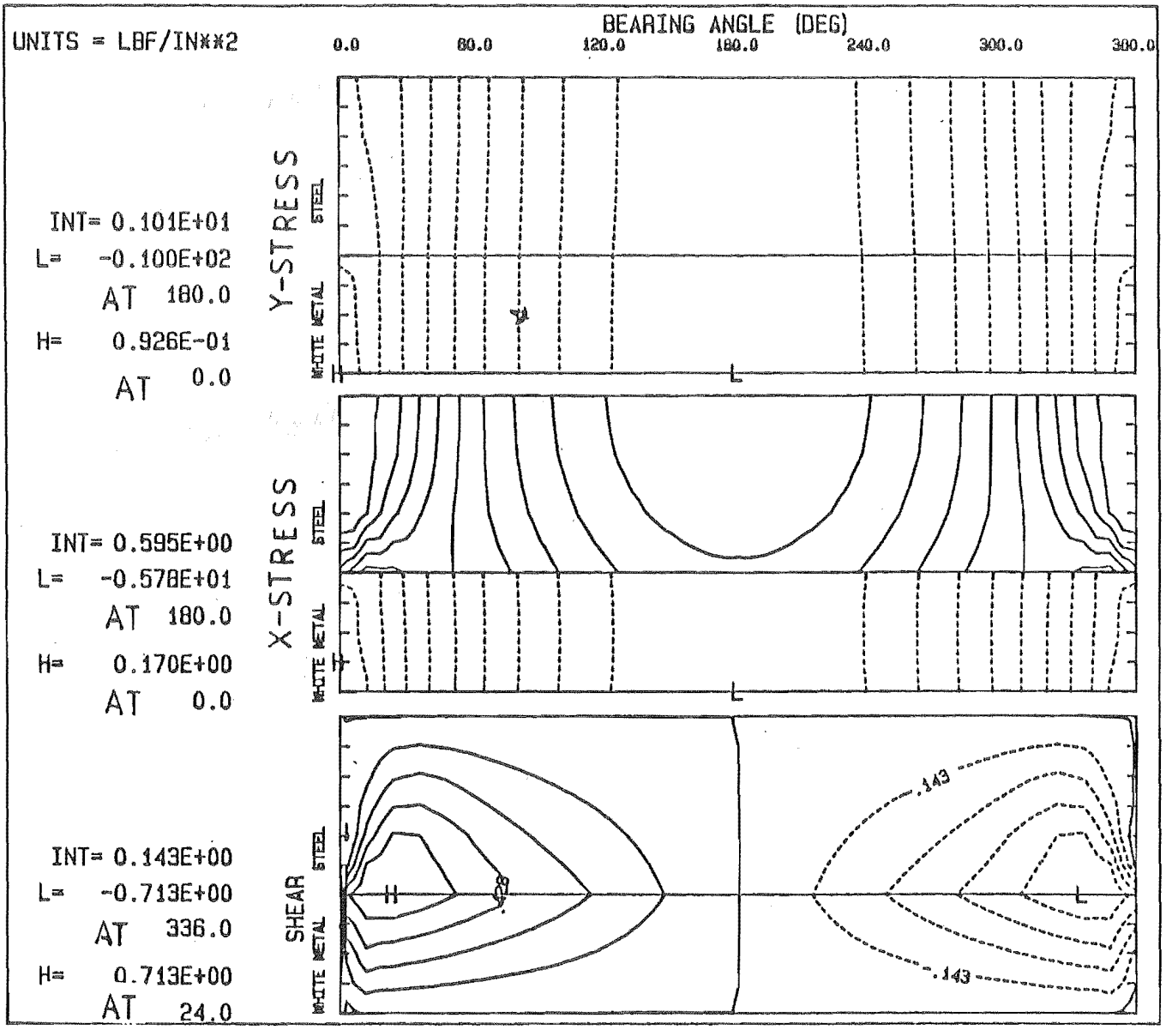

CONTOUR PLOT OF DIFFERENT STRESSES , JOURNAL POSITION = 0.0 DEGS, PL=TASV2
H, L=HIGH, LOW IN WHITE METAL, INT=INTERVAL DASHED LINES ARE NEGATIVE
MCCALLLION , IBRAHIM PARABOLIC LOAD = 10 PSI

Fig. 4.22

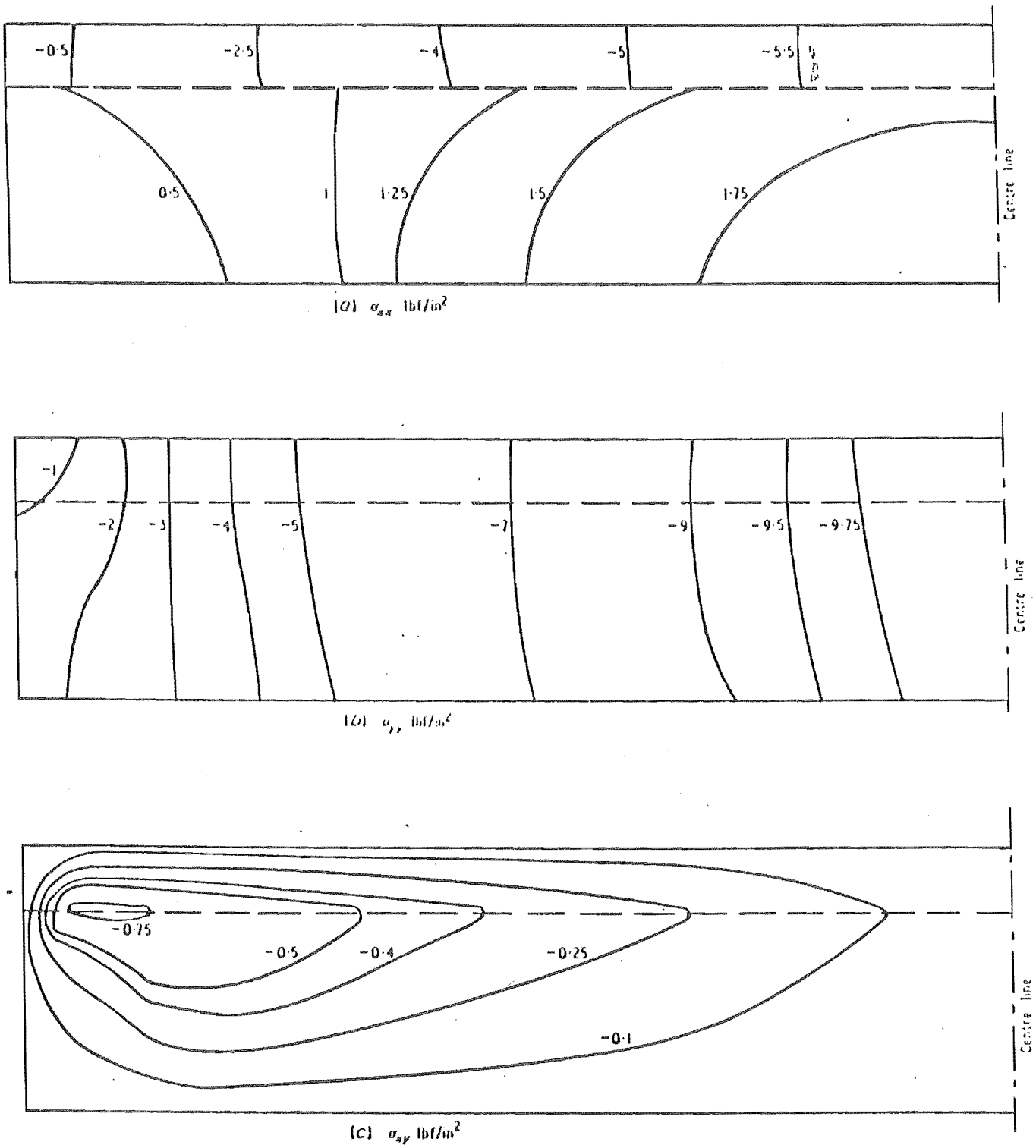

Fig.4.23

(after Ibrahim and McCallion [4])

The computed results were in close agreement with those reported by McCallion and Ibrahim (Fig. 4.23). It showed that the direct stresses σ_{xx} , σ_{yy} were very uniform in the white metal layer. At the interface, the σ_{xx} were discontinuous. This was due to the fact that although both metals underwent the same strain, but their material properties were different. The white metal layer was restrained by the steel backing while it was under compression due to the load. The shear stress τ_{xy} has its maximum value on the interface closer to the free edge. Later on in this section it will be explained how the maximum shear and maximum distortion energy stress (von mises) for the above geometry will reach their maximum value under the peak pressure (Fig. 4.42).

As a first step toward fatigue stress analysis, it was decided to investigate each one of the six stresses listed in Table 4.2 as a possible fatigue stress. To do this, the magnitude and angular position of the above stresses at different depth in the white metal layer were needed. This involved going through a lot of data generated for different instants of time. The plotting routines written for this purpose and explained in Section 3.3.3, helped to reduce the time and effort of this task. It could plot any one of the six stresses, at any instant of time with respect to bearing angle as a curve (Fig. 4.24) or contour plot (Fig. 4.25). It could also plot the complete history of stresses for a full dynamic load cycle (Chapter Five).

No.	Stress
1	Radial
2	Tangential
3	Shear
4	Maximum Principal
5	Maximum Shear
6	Maximum Distortion Energy

Table 4.2

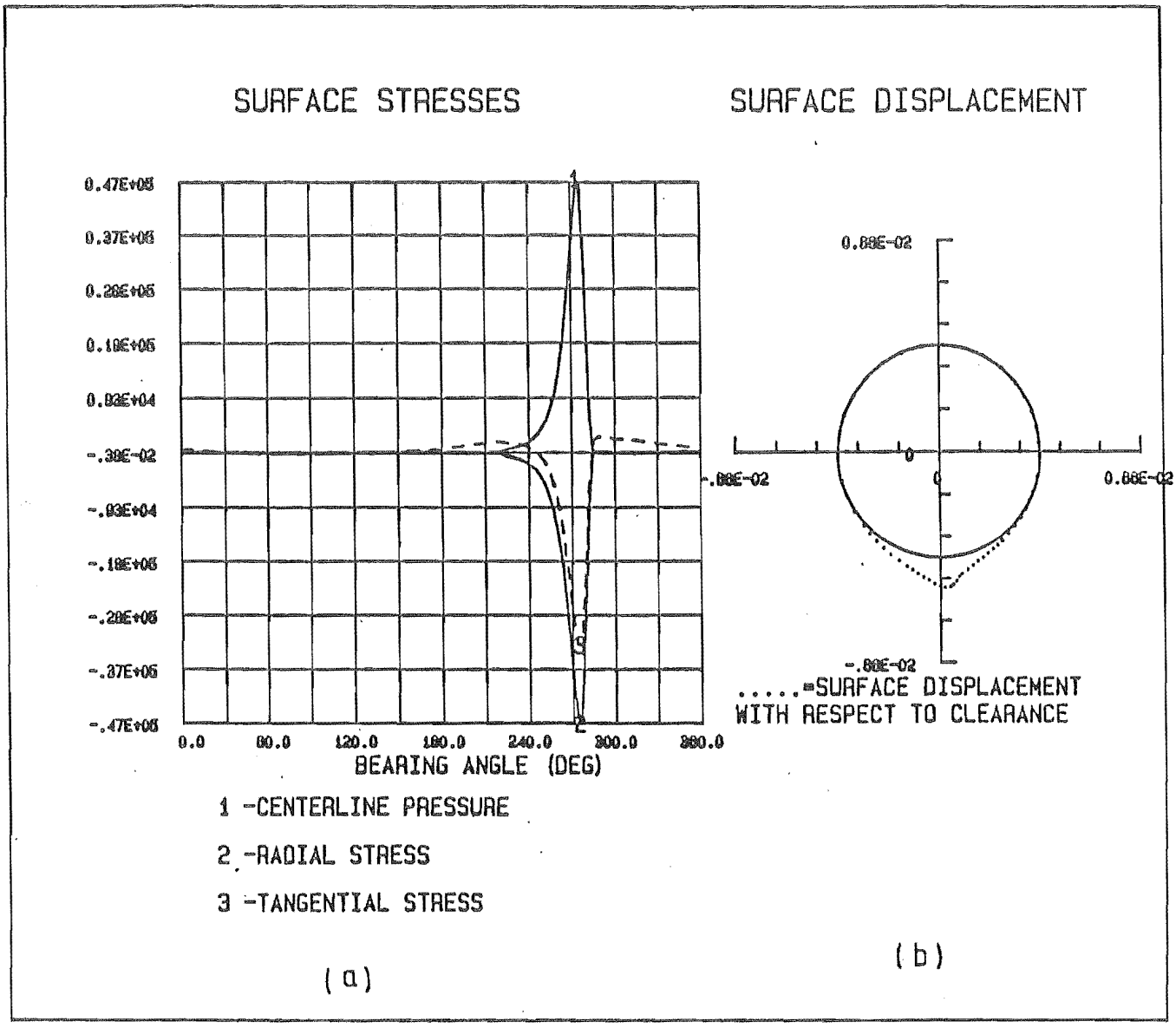

JOURNAL POSITION = 99.5 DEGREE

TEST NO 505 CO ROTATIONAL LOAD , 1 LAND BEARING

Fig.4.24

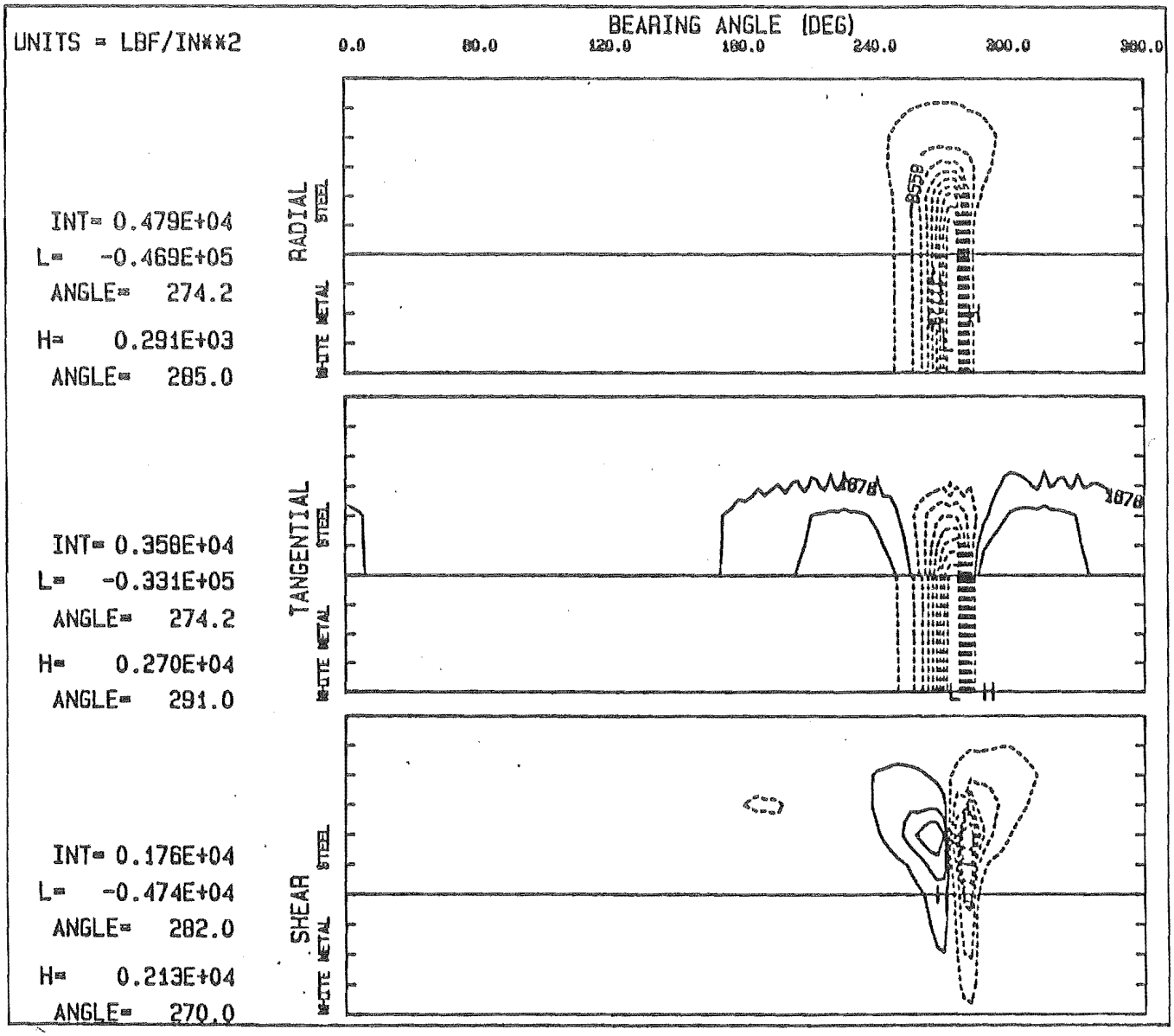

CONTOUR PLOT OF DIFFERENT STRESSES , JOURNAL POSITION = 99.5 DEGS, PL=TASV2
H, L=HIGH, LOW IN WHITE METAL, INT=INTERVAL DASHED LINES ARE NEGATIVE
TEST NO 505 CO ROTATIONAL LOAD , 1 LAND BEARING

Fig.4.25

To compute the stresses, a FEM mesh as shown in Fig. 3.6, which had two elements in white metal, one element in steel backing and two elements in the housing sections, was used. All the nodes on the outer surface of the housing were constrained radially. However, because the housing was very thick, the outside boundary conditions did not have any effect on the surface stress. This may be seen in a comparison of Fig. 4.25 (constrained radially) and Fig. 4.26 which was constrained both radially and tangentially. From the FEM program, the three stresses in the rθ plane, namely σ_r, σ_θ, $\tau_{r\theta}$ were obtained (Figs. 4.24 and 4.25). There was no shear force at the surface. The radial stress had the same magnitude as the applied pressure but in compression. This meant the FEM program had satisfied the surface boundary conditions. The tangential stress was negative under the peak pressure while it was positive near the two edges of the curve with its maximum value closer to the higher slope side. The positive tangential stress was found to be related to the thick housing section. This may be seen when Figs. 4.24 and 4.25 and Fig. 4.27 are compared. Fig. 4.27 shows the contour plot of σ_r, σ_θ, $\tau_{r\theta}$ stresses in a system consisting of white metal and steel backing supported in a rigid housing; that is, the outer surface of steel backing was constrained radially. Fig. 4.27 shows no positive tangential surface stress. The compressive tangential stress under the peak load and the surface displacement were considerably lower. This shows the importance of the bending effect due to the outer shell (the housing), which could be even greater with a connecting rod housing.

The two principal stresses in the rθ plane σ_1, σ_2 and the third principal stress perpendicular to them σ_3 were calculated according to (4.1 a,b,c).

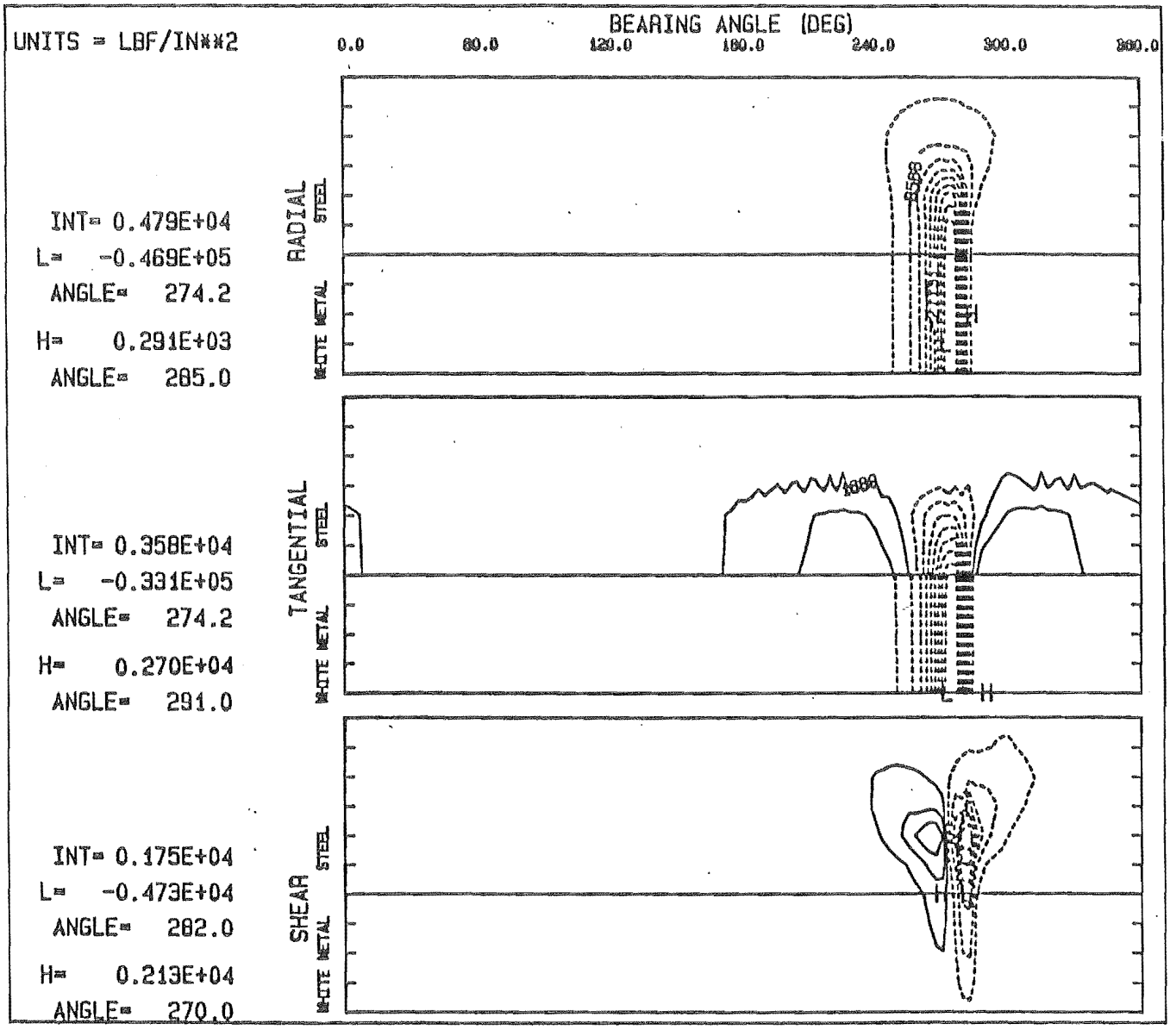

CONTOUR PLOT OF DIFFERENT STRESSES , JOURNAL POSITION = 99.5 DEGS. PL=TASV2
H, L=HIGH, LOW IN WHITE METAL, INT=INTERVAL DASHED LINES ARE NEGATIVE
TEST NO 505 COROTATIONAL LOAD , I LAND BEARING (FULLY CONSTRAINED ON BACK)

Fig.426

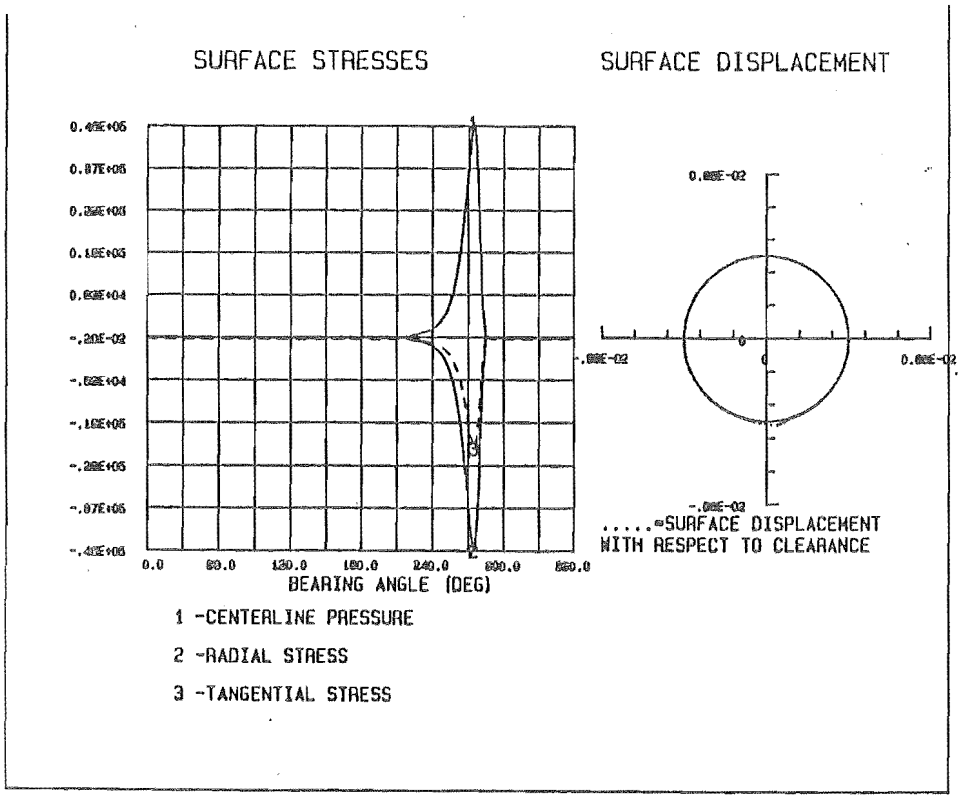

JOURNAL POSITION = 99.5 DEGREE

TEST NO 505 COROTATIONAL LOAD , I LAND BEARING , (BEARING SHELL ONLY)

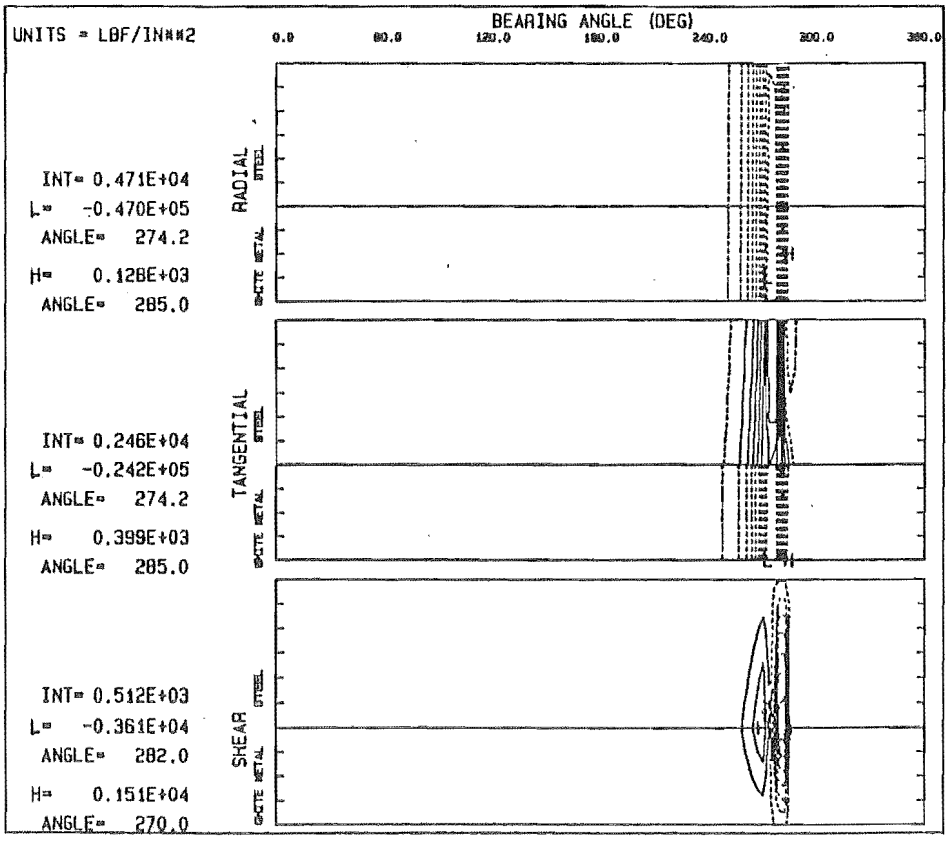

CONTOUR PLOT OF DIFFERENT STRESSES , JOURNAL POSITION = 99.5 DEGS, PL=TASV2

H, L=HIGH, LOW IN WHITE METAL, INT=INTERVAL DASHED LINES ARE NEGATIVE

TEST NO 505 COROTATIONAL LOAD , I LAND BEARING , (BEARING SHELL ONLY)

Fig.4.27

$$\sigma_1 = \frac{\sigma_r + \sigma_\theta}{2} + \left[\frac{(\sigma_r - \sigma_\theta)^2}{4} + \tau^2_{r\theta}\right]^{\frac{1}{2}} \tag{4.1a}$$

$$\sigma_2 = \frac{\sigma_r + \sigma_\theta}{2} - \left[\frac{(\sigma_r - \sigma_\theta)^2}{4} + \tau^2_{r\theta}\right]^{\frac{1}{2}} \tag{4.1b}$$

$$\sigma_3 = \mu(\sigma_r + \sigma_\theta) \tag{4.1c}$$

The positive sign was taken as tension while the negative was compression. Since there was no shear force on the surface of white metal, the tangential and radial stresses were the two principal stresses (maximum and minimum) in this plane. Equation (4.1c) indicates that σ_3 was dependent on Poisson ratio ($\mu = .4$) and the other two principal stresses σ_1, σ_2. Since the radial stress is very small or zero in the positive tangential stress region, Equation (4.1c) gives a value of about .4 times the tangential stress for the axial stress σ_3. But in the peak pressure region, the radial stress has its peak magnitude. This indicates that σ_3 has an equivalent or slightly higher value than the tangential stress. These are shown very clearly in the Mohr circle diagrams of Fig. 4.28.

Equations (4.2 a,b,c) may now be used to calculate the three maximum shear stresses in the rθ, rz and θz planes.

$$\tau_{r\theta\,\max} = \frac{\sigma_1 - \sigma_2}{2} \tag{4.2a}$$

$$\tau_{rz\,\max} = \frac{\sigma_2 - \sigma_3}{2} \tag{4.2b}$$

$$\tau_{\theta z\,\max} = \frac{\sigma_1 - \sigma_3}{2} \tag{4.2c}$$

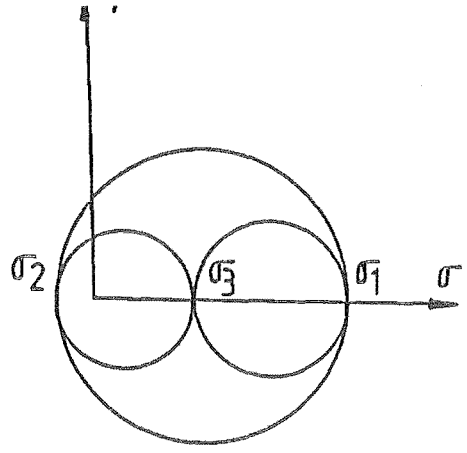

Positive tangential stress region

(a)

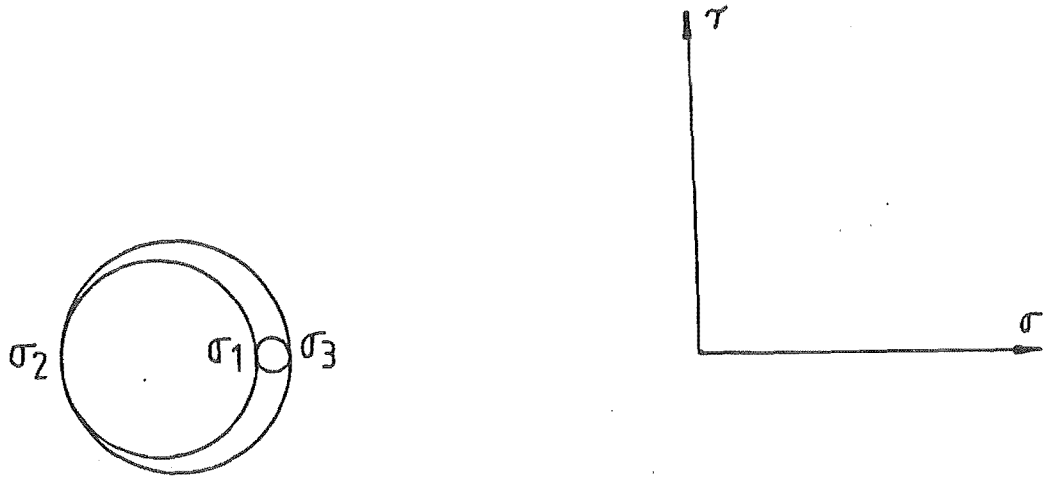

Peak pressure region

(b)

Fig. 4.28

As it is shown in Fig. 4.28a, σ_1, σ_2 which lay in the rθ plane make the largest Mohr circle which obviously indicates that the highest maximum shear streess of that region is in the rθ plane. Fig. 4.28b shows that σ_2, σ_3 stresses which lay in the rz plane make a circle which is slightly larger than the one made by σ_2, σ_1 of rθ plane, so the maximum shear stress in the rz plane is the highest of the three in that region.

Since the white metal layer was very thin compared to the steel backing and the housing, the variation of the σ_r and σ_θ in the radial direction throughout this thin layer was negligible. There was no shear stress on the surface but its magnitude increased to a maximum of about 10% of peak pressure at the interface between the two metals. Therefore, according to (4.1 a,b), the two principal stresses σ_1, σ_2 will not vary much in the radial direction, that is, they remain almost constant (similar to the σ_θ and σ_r). The maximum distortion energy stress (von mises) was also calculated for the white metal, steel backing, and the housing sections. Equation (4.3) was used for this purpose

$$\sigma' = [((\sigma_1 - \sigma_2)^2 + (\sigma_2 - \sigma_3)^2 + (\sigma_3 - \sigma_1)^2)/2]^{\frac{1}{2}} \tag{4.3}$$

Results of numerical reconstruction of Blundell's and of Gyde's work are explained in the next chapter. Figs. 4.24, 4.25 and 4.29–4.42 show the surface stresses, surface displacement and contour plots of the six mentioned stresses for Blundell's experiments 1–7. They were tested on the one land bearings with the direction of load rotation opposite to that of the shaft rotation. Maximum shear and maximum distortion energy stresses had similar contour plots. They were uniform in the white metal layer with their maximum values under the peak pressure. As shown in the Tables 5.5 and 5.6 of Chapter Five, the angular position of failures for different tests (i.e. 288^O for Test No. 5 of Blundell, which

was named 505 in here, and approximately 290^{O} for Gyde's Tests) were away from the position of maximum peak pressure (i.e. 274.2 for Test 505 and 277.5^{O} for Test 730) and were closer to the angular position of maximum tangential stress. Therefore the maximum tangential stress σ_{θ} was chosen for further consideration (Chapters Five and Six).

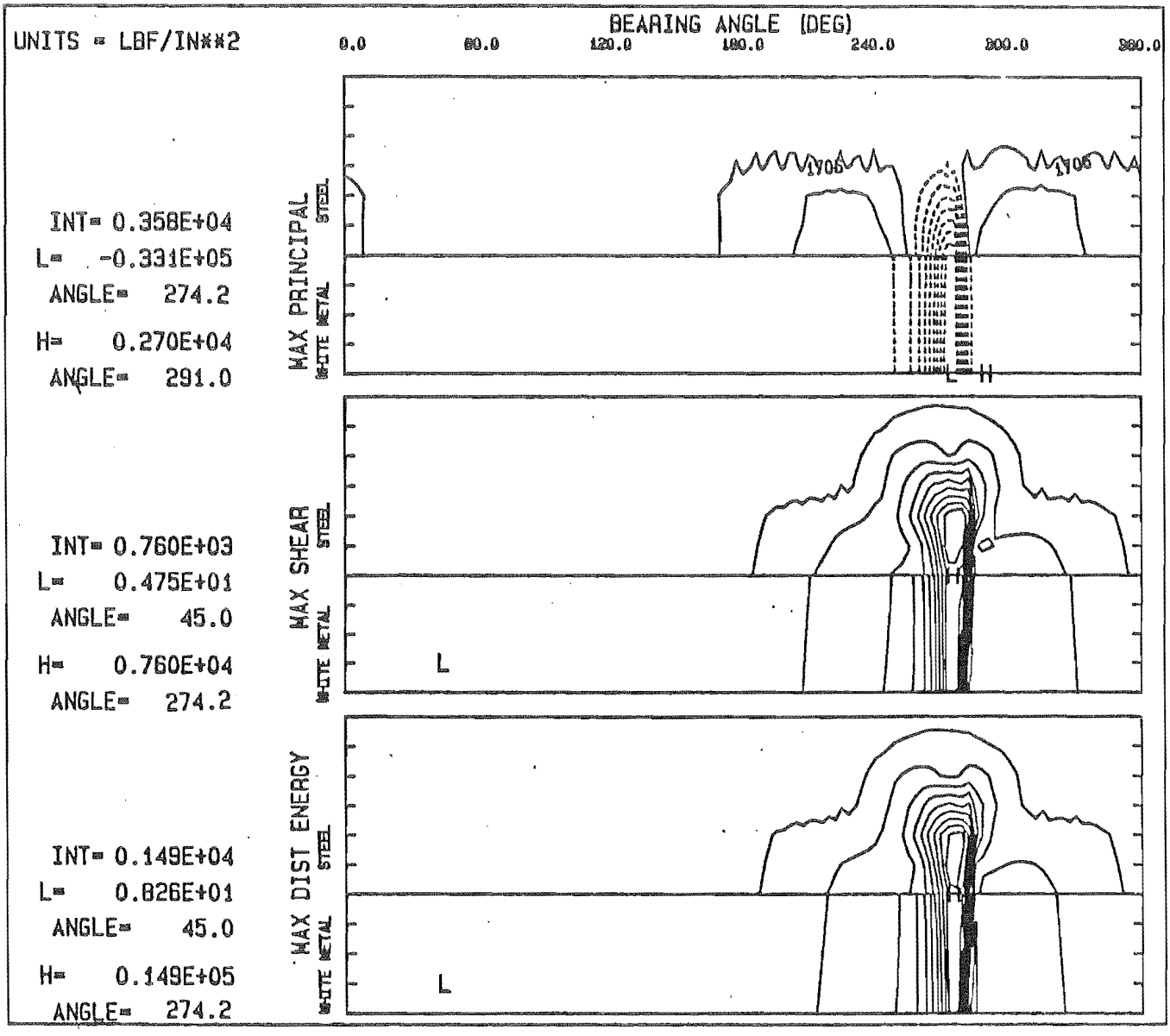

CONTOUR PLOT OF DIFFERENT STRESSES , JOURNAL POSITION = 99.5 DEGS, PL=TASV3
H, L=HIGH, LOW IN WHITE METAL, INT=INTERVAL DASHED LINES ARE NEGATIVE
TEST NO 505 CO ROTATIONAL LOAD , 1 LAND BEARING

Fig 4.29

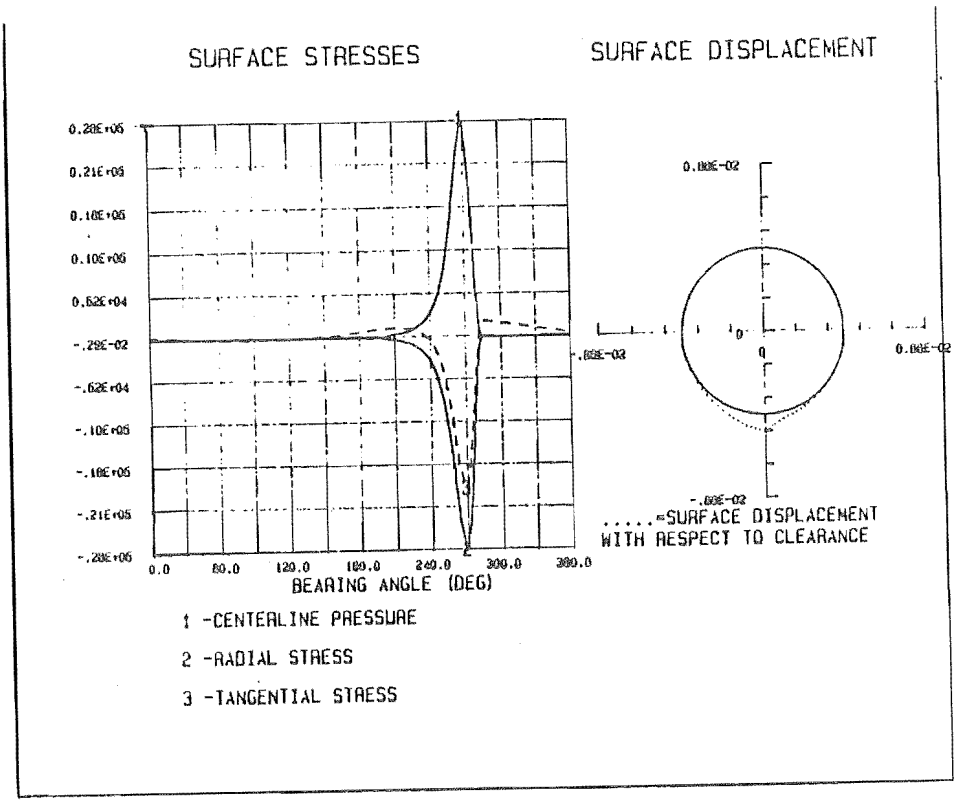

JOURNAL POSITION = 25.5 DEGREE

TEST NO 501 CO ROTATIONAL LOAD, 1 LAND BEARING

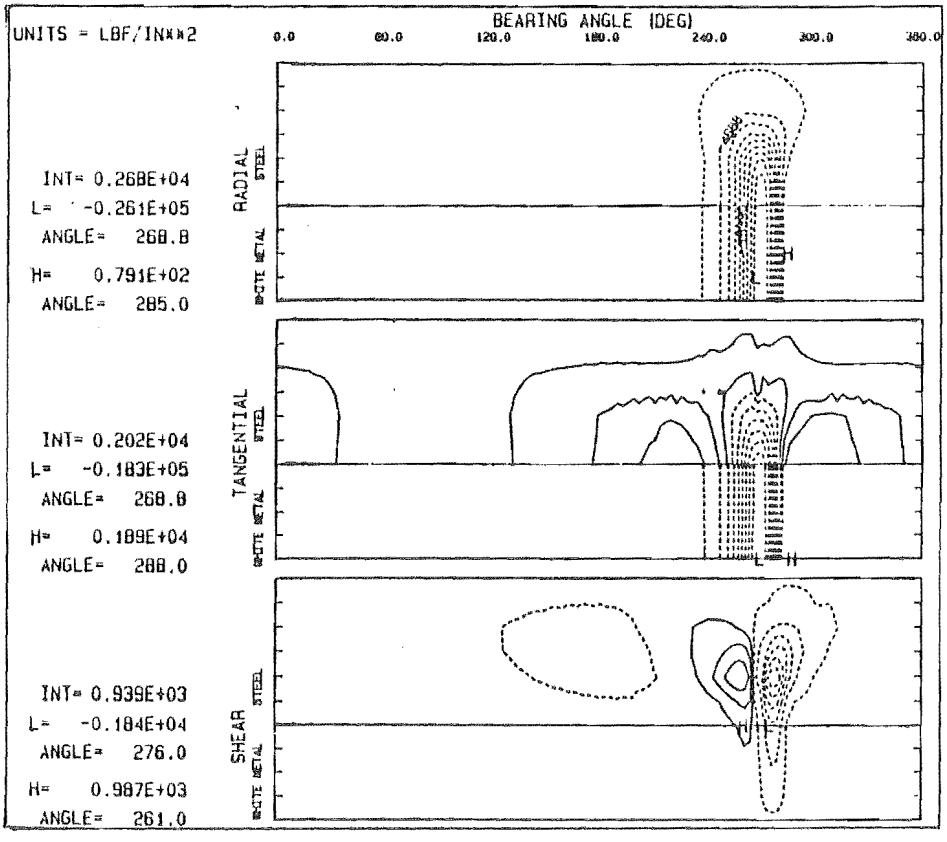

CONTOUR PLOT OF DIFFERENT STRESSES , JOURNAL POSITION = 25.5 DEGS, PL=TASV2
H, L=HIGH, LOW IN WHITE METAL, INT=INTERVAL DASHED LINES ARE NEGATIVE
TEST NO 501 CO ROTATIONAL LOAD, 1 LAND BEARING

Fig 4.30

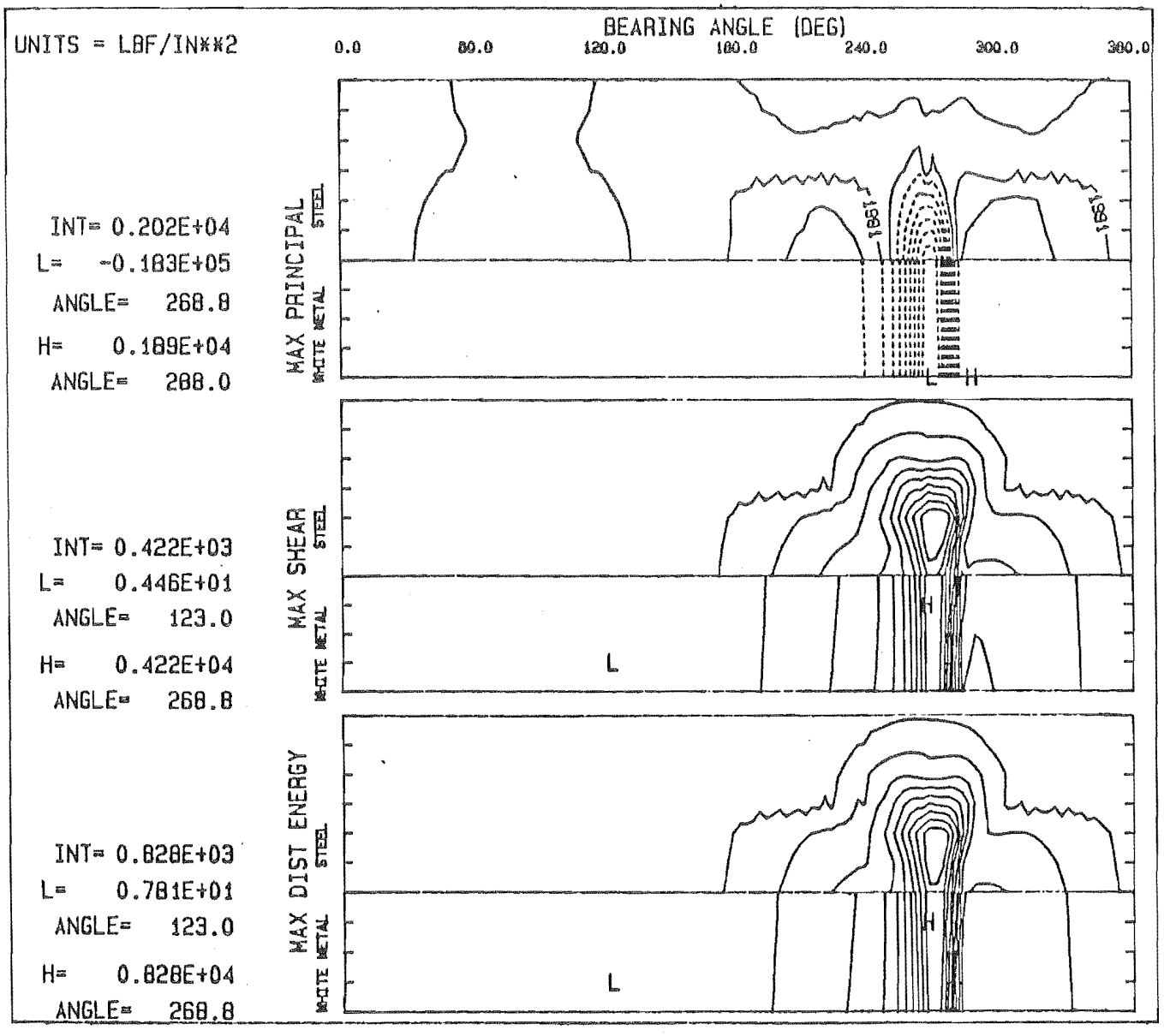

CONTOUR PLOT OF DIFFERENT STRESSES , JOURNAL POSITION = 25.5 DEGS, PL=TASV3
H, L=HIGH, LOW IN WHITE METAL, INT=INTERVAL DASHED LINES ARE NEGATIVE
TEST NO 501 CO ROTATIONAL LOAD, 1 LAND BEARING

Fig 4.31

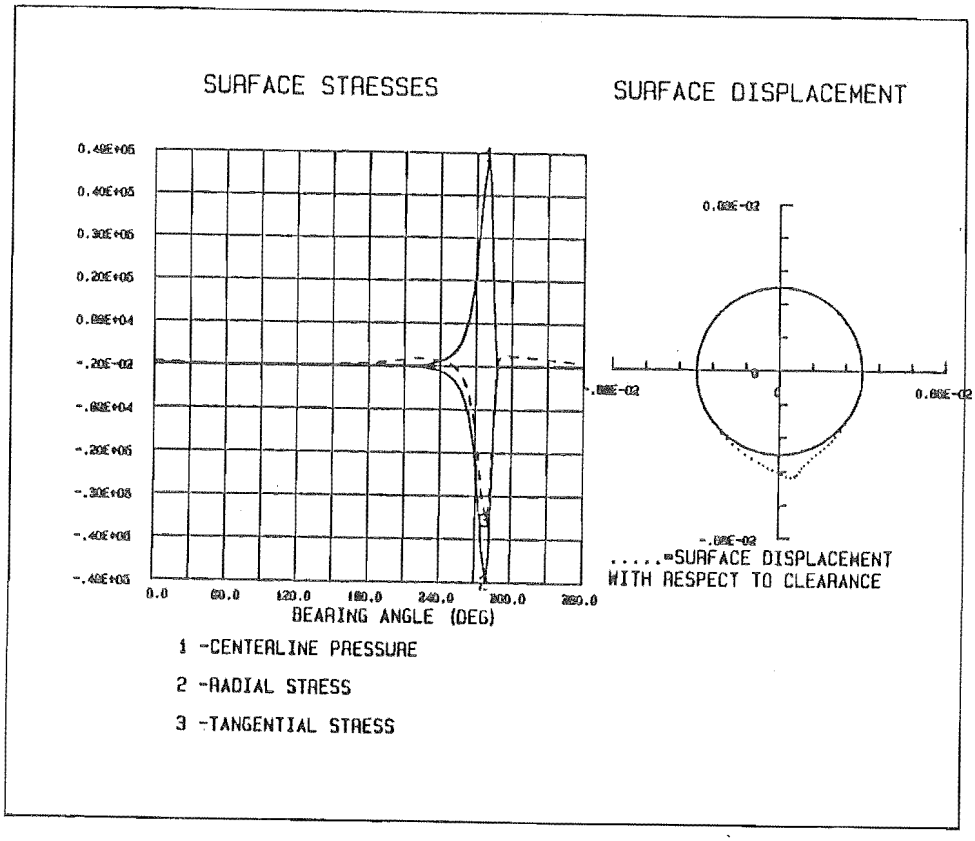

JOURNAL POSITION = 90.0 DEGREE

TEST NO 502 CO ROTATIONAL LOAD, 1 LAND BEARING

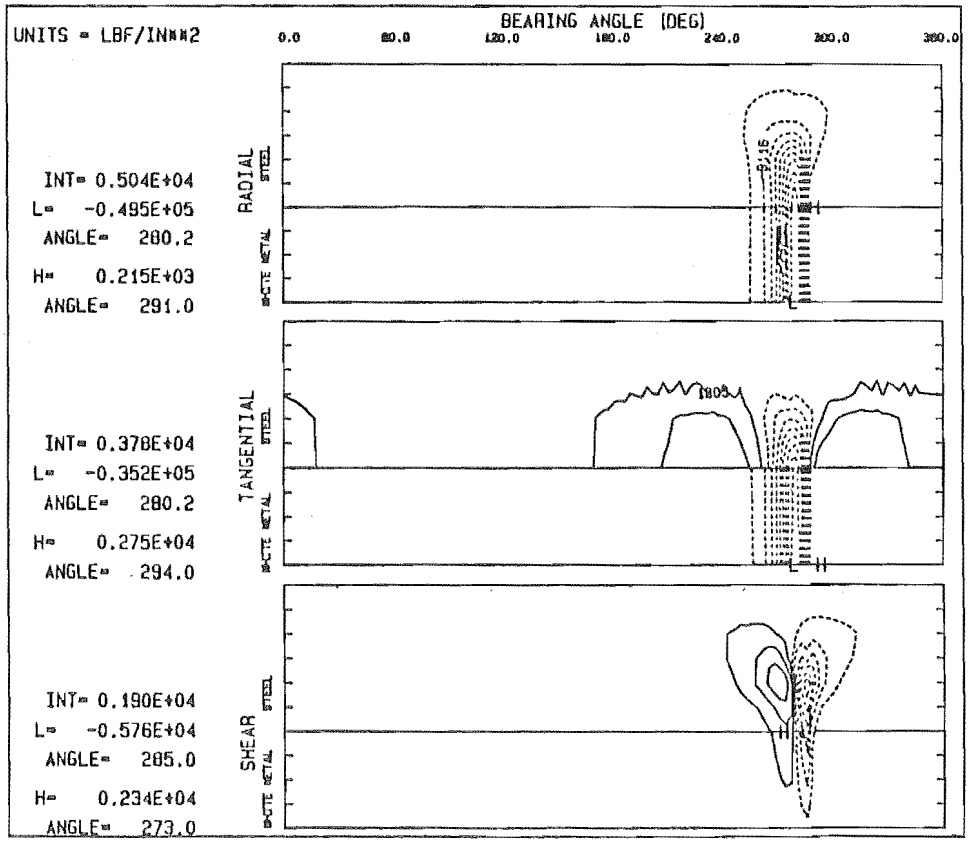

CONTOUR PLOT OF DIFFERENT STRESSES , JOURNAL POSITION = 90.0 DEGS, PL=TASV2
H, L=HIGH, LOW IN WHITE METAL, INT=INTERVAL DASHED LINES ARE NEGATIVE
TEST NO 502 CO ROTATIONAL LOAD, 1 LAND BEARING

Fig4.32

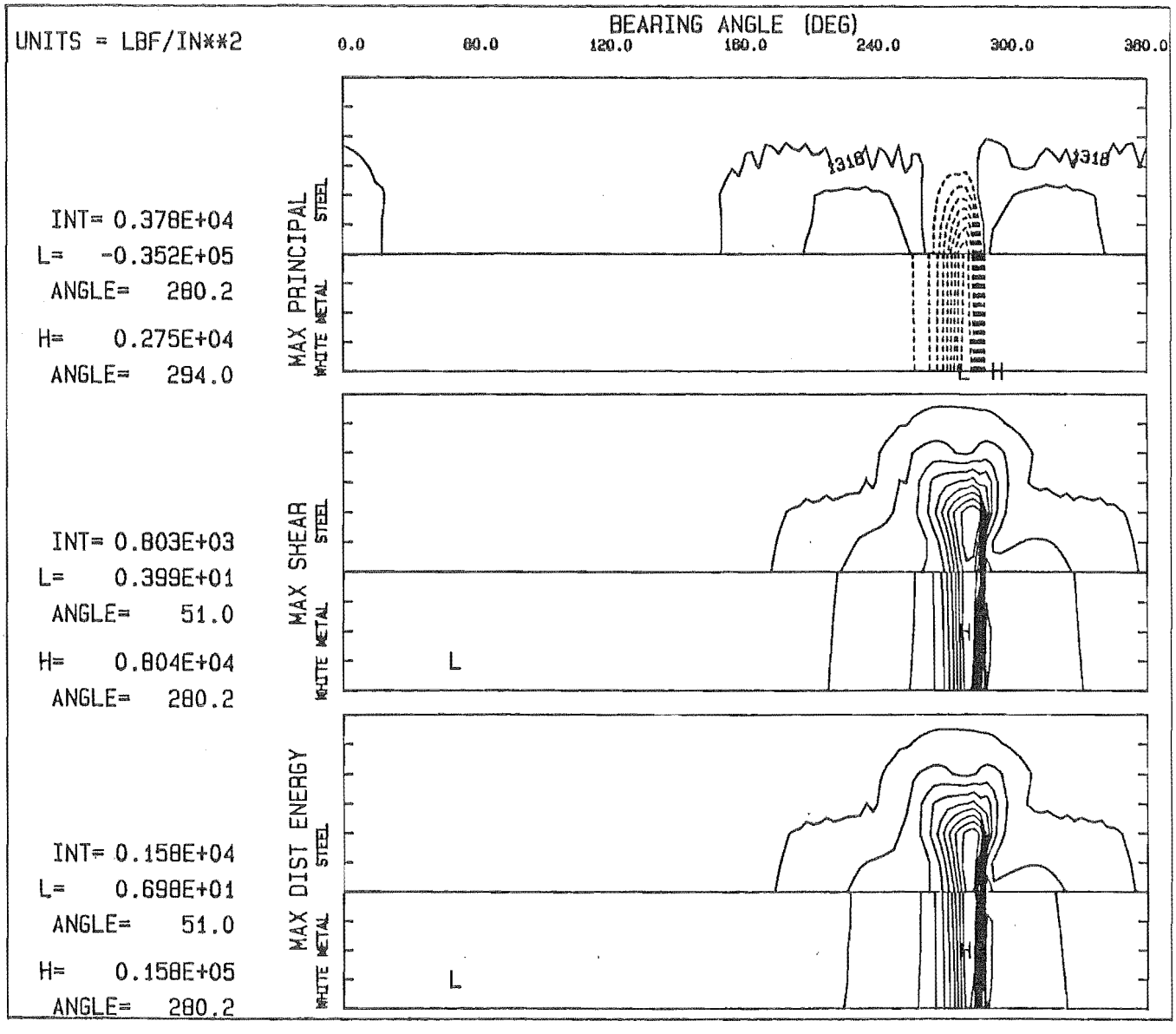

CONTOUR PLOT OF DIFFERENT STRESSES , JOURNAL POSITION = 90.0 DEGS, PL=TASV3
H, L=HIGH, LOW IN WHITE METAL, INT=INTERVAL DASHED LINES ARE NEGATIVE
TEST NO 502 CO ROTATIONAL LOAD, 1 LAND BEARING

Fig.4.33

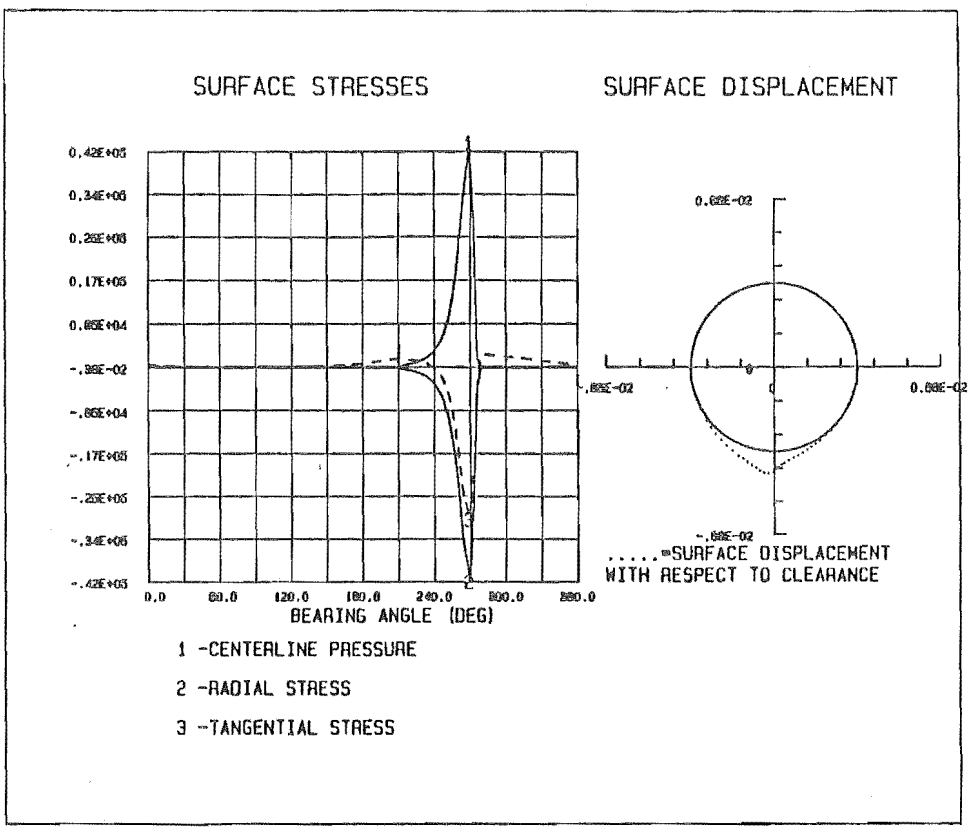

JOURNAL POSITION = 38.5 DEGREE

TEST NO 503 CO ROTATIONAL LOAD, 1 LAND BEARING

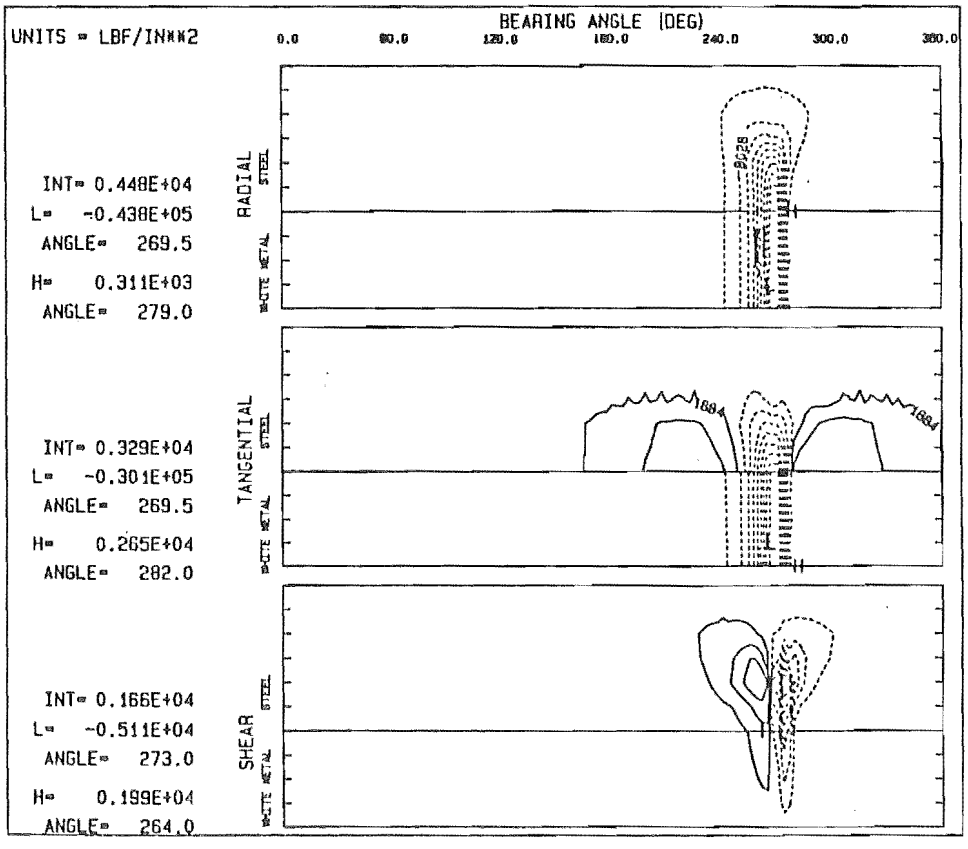

CONTOUR PLOT OF DIFFERENT STRESSES , JOURNAL POSITION = 38.5 DEGS, PL=TASV2
H, L=HIGH, LOW IN WHITE METAL, INT=INTERVAL DASHED LINES ARE NEGATIVE
TEST NO 503 CO ROTATIONAL LOAD, 1 LAND BEARING

Fig.434

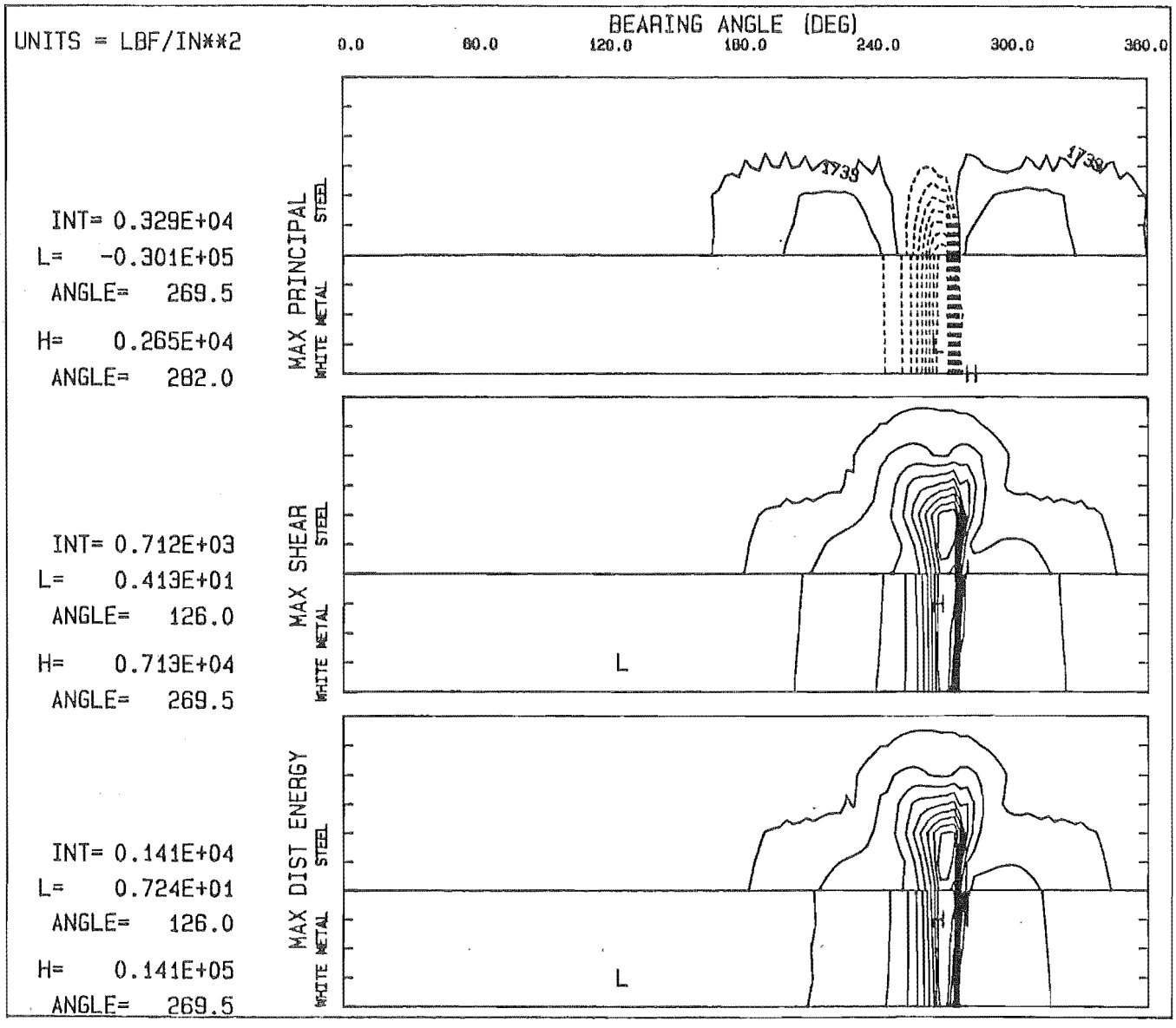

CONTOUR PLOT OF DIFFERENT STRESSES , JOURNAL POSITION = 38.5 DEGS, PL=TASV3
H, L=HIGH, LOW IN WHITE METAL, INT=INTERVAL DASHED LINES ARE NEGATIVE
TEST NO 503 CO ROTATIONAL LOAD, 1 LAND BEARING

Fig4.35

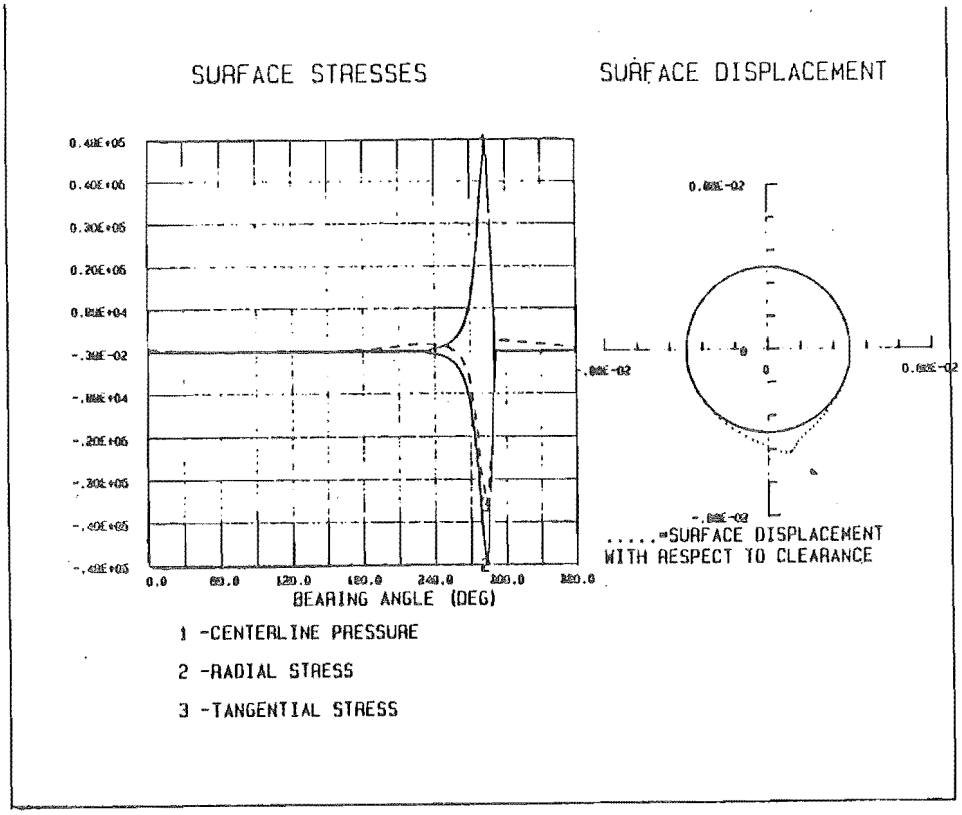

JOURNAL POSITION = 128.8 DEGREE

TEST NO 504 CO ROTATIONAL LOAD, 1 LAND BEARING

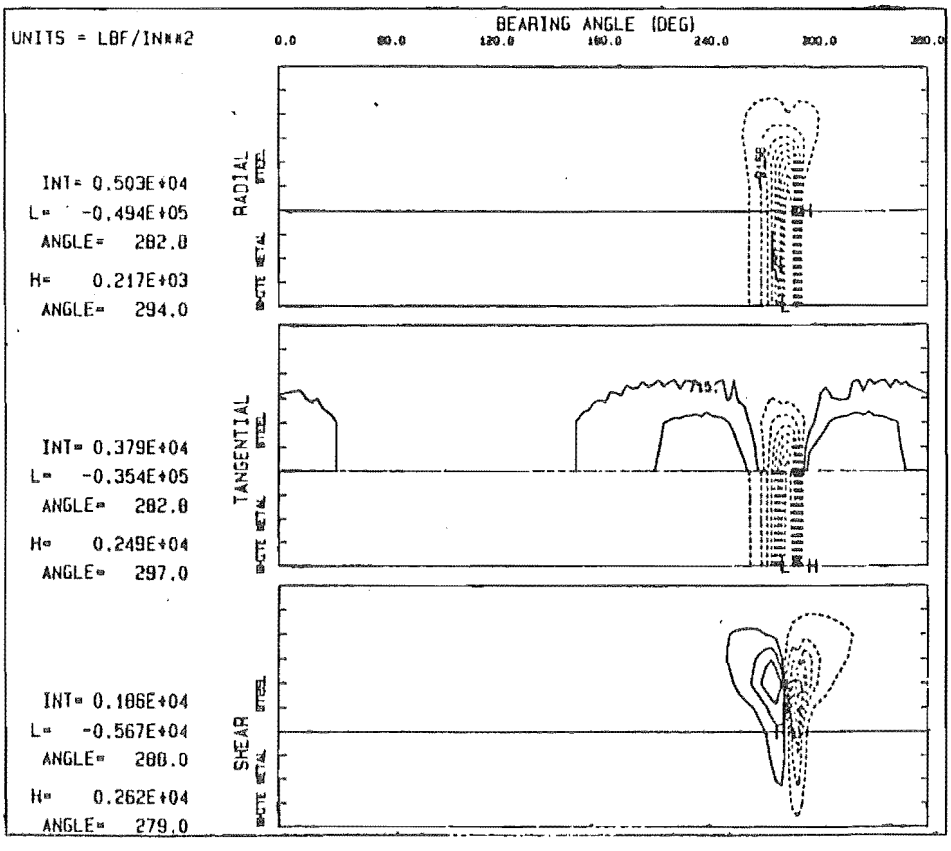

CONTOUR PLOT OF DIFFERENT STRESSES , JOURNAL POSITION = 128.8 DEGS, PL=TASV2

H, L=HIGH, LOW IN WHITE METAL, INT=INTERVAL DASHED LINES ARE NEGATIVE

TEST NO 504 CO ROTATIONAL LOAD, 1 LAND BEARING

Fig.4.36

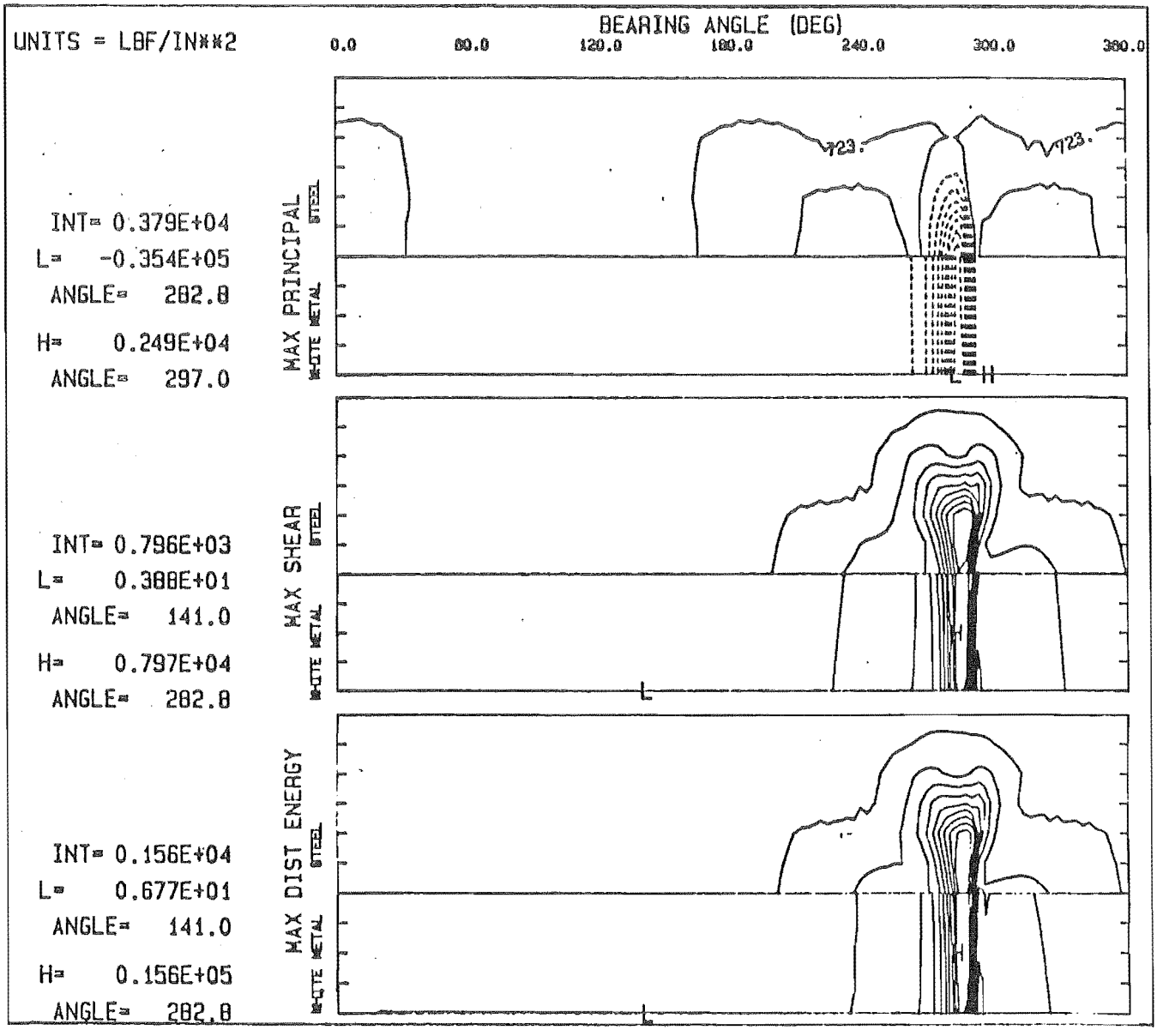

CONTOUR PLOT OF DIFFERENT STRESSES , JOURNAL POSITION = 120.0 DEGS, PL=TASV3
H, L=HIGH, LOW IN WHITE METAL, INT=INTERVAL DASHED LINES ARE NEGATIVE
TEST NO 504 CO ROTATIONAL LOAD, 1 LAND BEARING

Fig.4.37

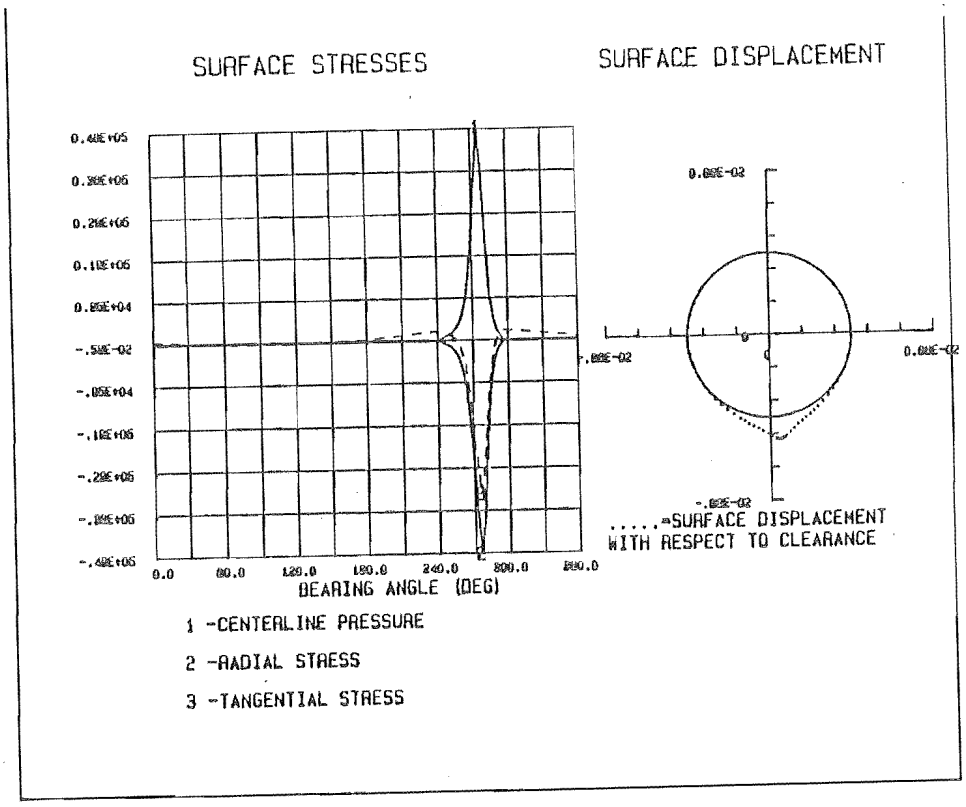

JOURNAL POSITION = 100.0 DEGREE

TEST NO 506 CO ROTATIONAL LOAD, 1 LAND BEARING

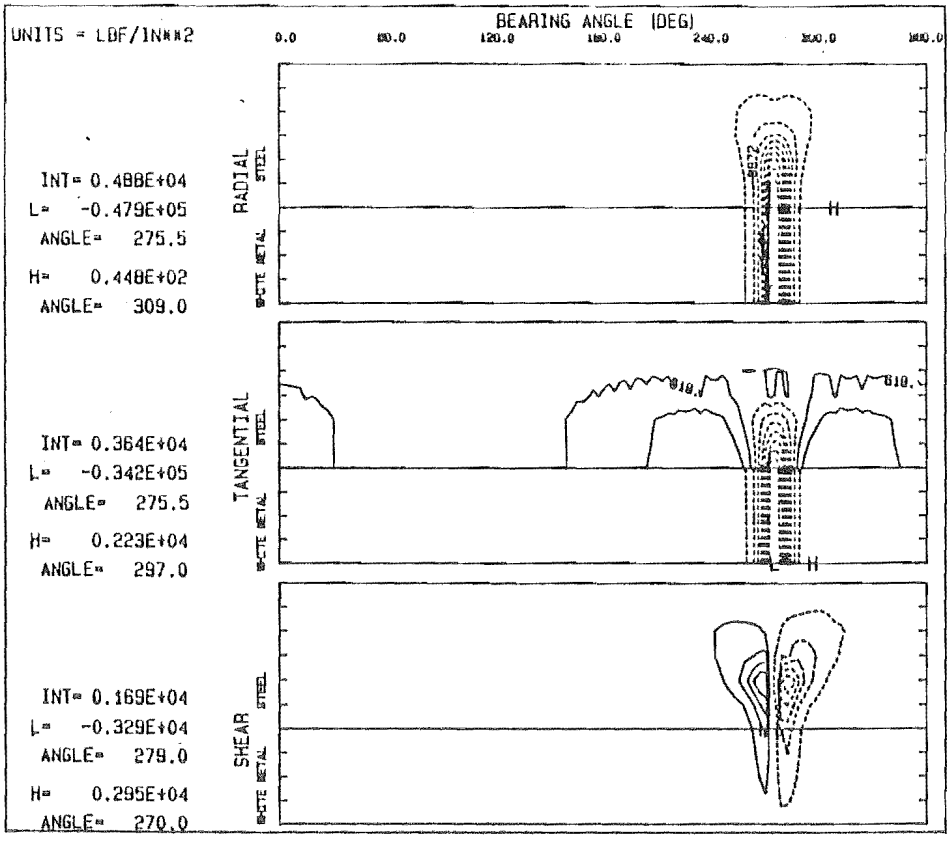

CONTOUR PLOT OF DIFFERENT STRESSES , JOURNAL POSITION = 100.0 DEGS, PL=TASV2
H, L=HIGH, LOW IN WHITE METAL, INT=INTERVAL DASHED LINES ARE NEGATIVE
TEST NO 506 CO ROTATIONAL LOAD, 1 LAND BEARING

Fig.438

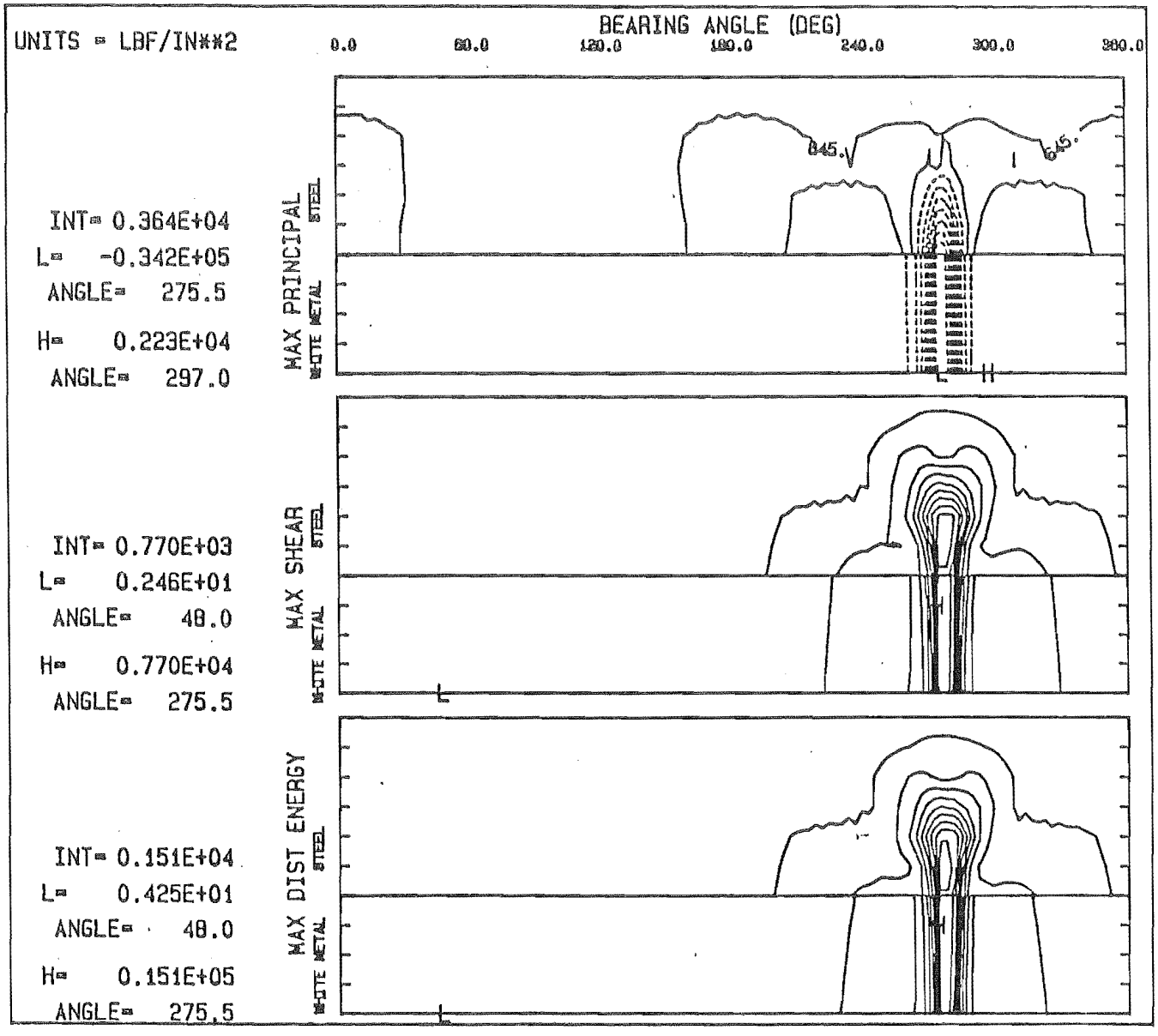

CONTOUR PLOT OF DIFFERENT STRESSES , JOURNAL POSITION = 100.8 DEGS, PL=TASV3
H, L=HIGH, LOW IN WHITE METAL, INT=INTERVAL DASHED LINES ARE NEGATIVE
TEST NO 506 CO ROTATIONAL LOAD, 1 LAND BEARING

Fig.4.39

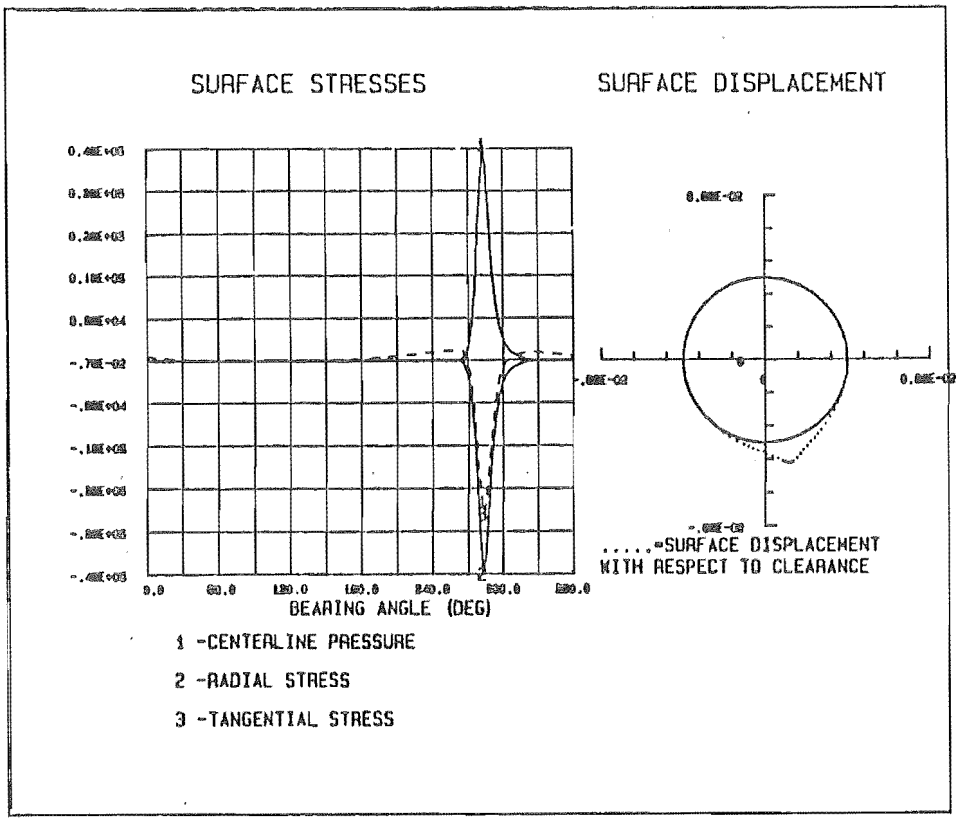

JOURNAL POSITION = 114.6 DEGREE

TEST NO 507 CO ROTATIONAL LOAD, 1 LAND BEARING

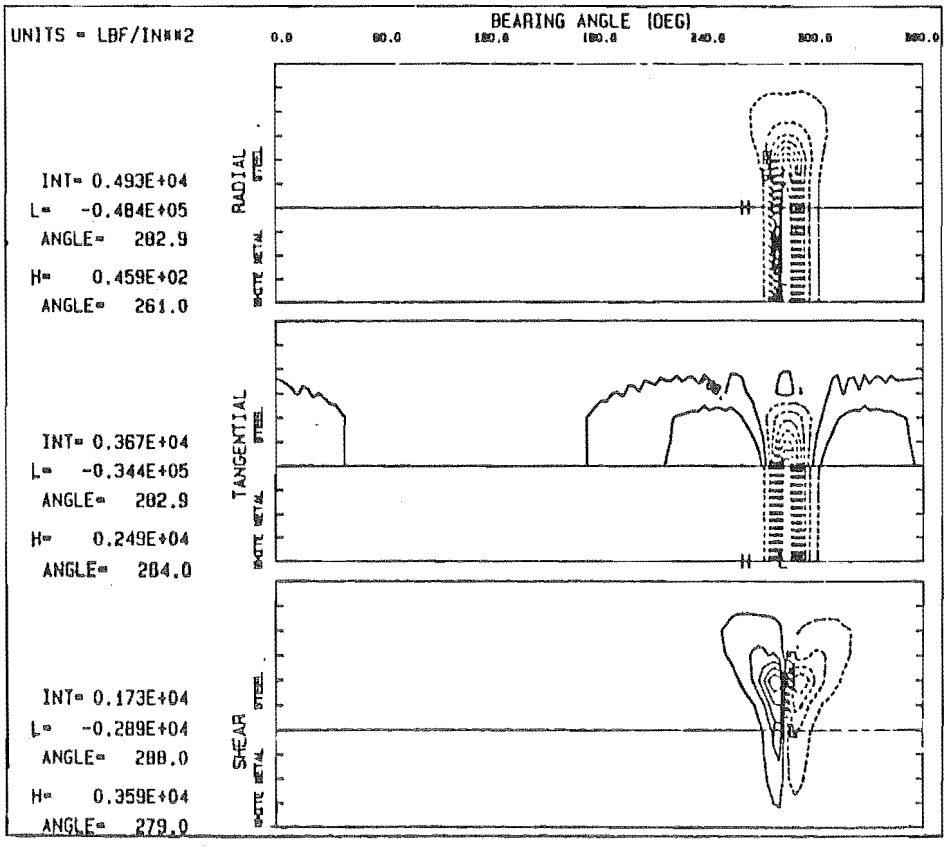

CONTOUR PLOT OF DIFFERENT STRESSES , JOURNAL POSITION = 114.6 DEGS, PL=TASV2
H, L=HIGH, LOW IN WHITE METAL, INT=INTERVAL DASHED LINES ARE NEGATIVE
TEST NO 507 CO ROTATIONAL LOAD, 1 LAND BEARING

Fig.4.40

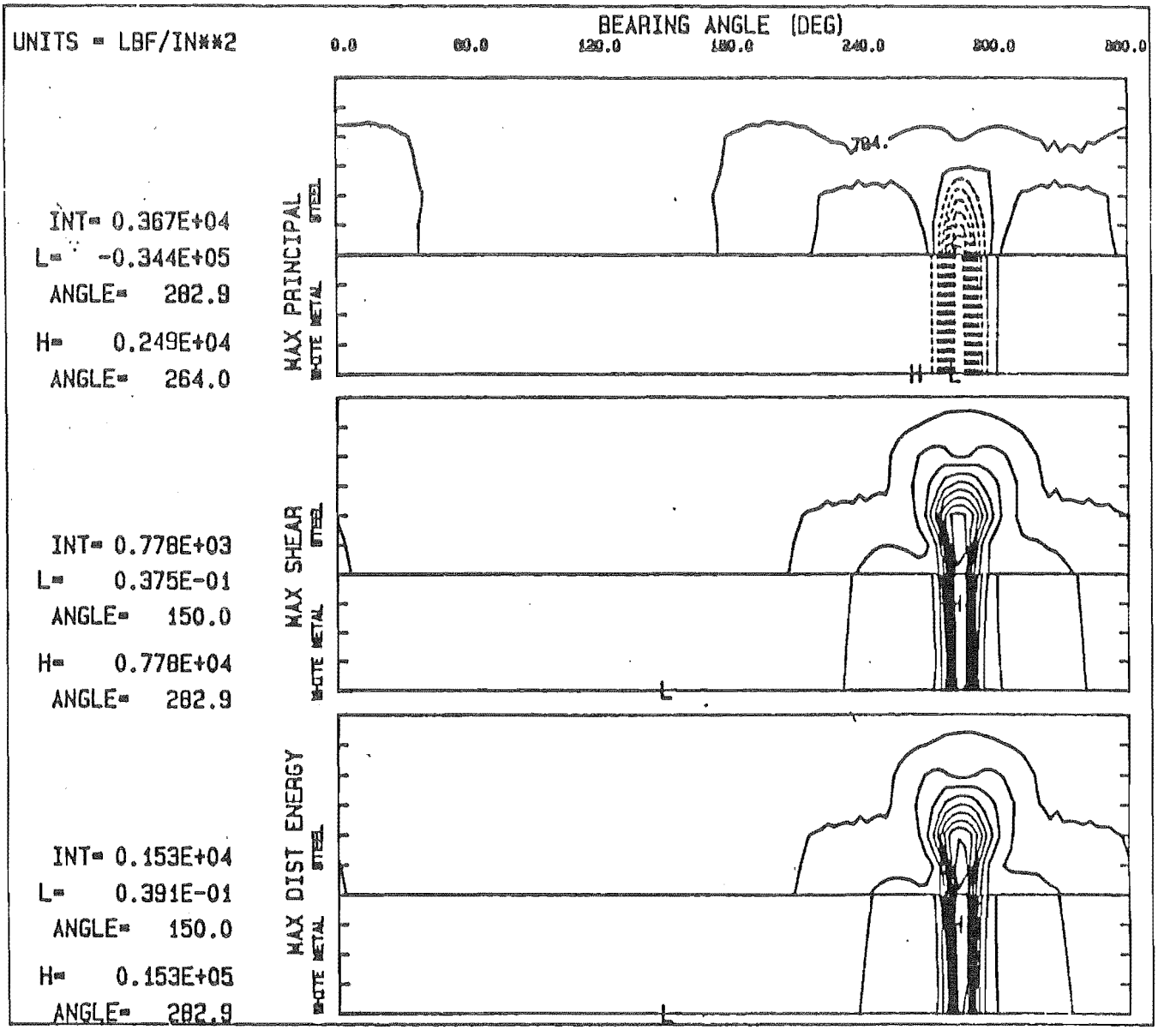

CONTOUR PLOT OF DIFFERENT STRESSES , JOURNAL POSITION = 114.8 DEGS, PL=TASV3
H, L=HIGH, LOW IN WHITE METAL, INT=INTERVAL DASHED LINES ARE NEGATIVE
TEST NO 507 CO ROTATIONAL LOAD, 1 LAND BEARING

Fig. 4.41

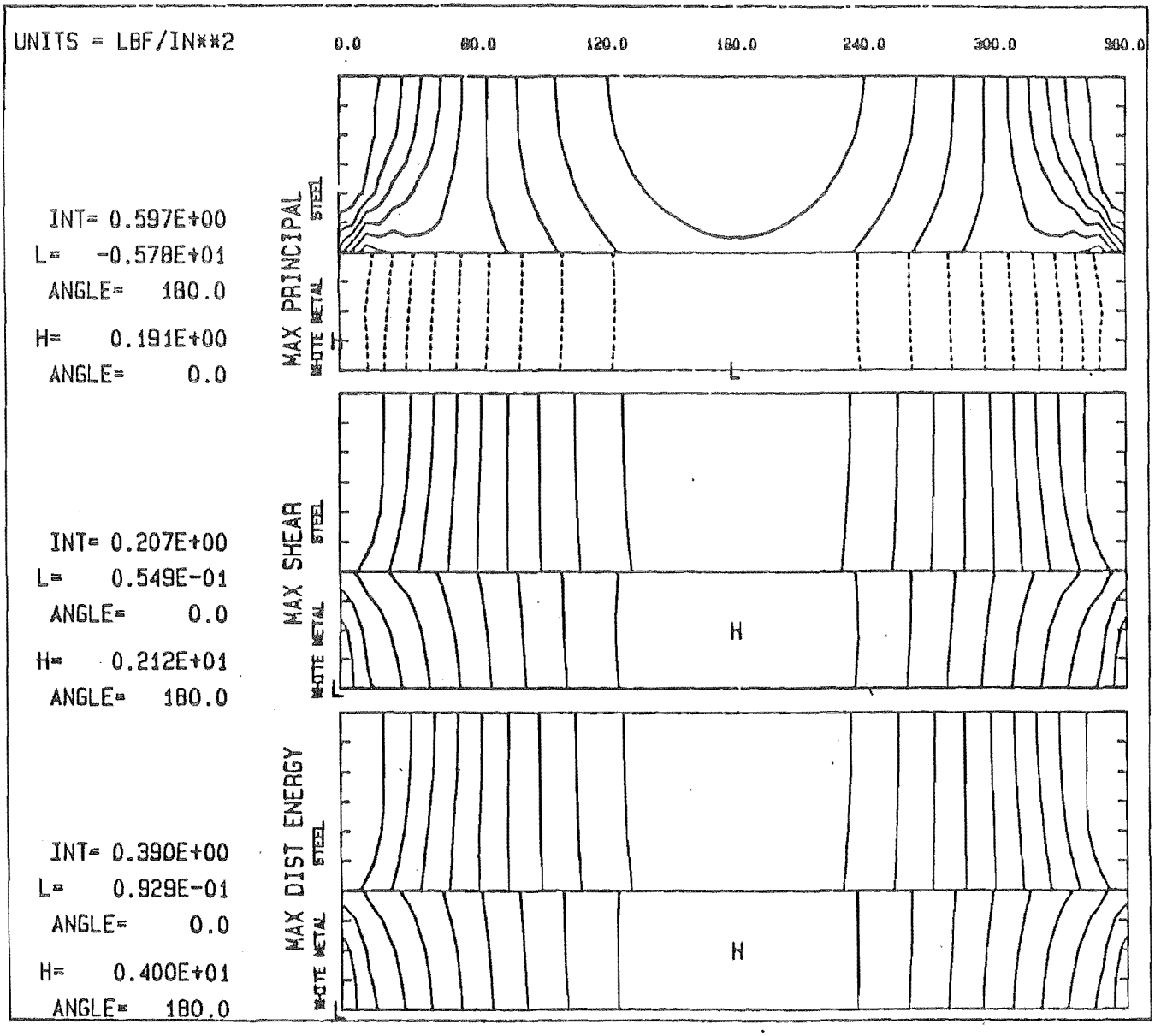

CONTOUR PLOT OF DIFFERENT STRESSES

H, L=HIGH, LOW IN WHITE METAL, INT=INTERVAL DASHED LINES ARE NEGATIVE

Fig.4.42

CHAPTER FIVE

SIMULATION OF EXPERIMENTAL WORK AND STRESS ANALYSIS

In this chapter, the results of the numerical analysis performed with the help of the bearing performance and the finite element programs (Chapter Three) in simulating the experimental work of Blundell [7] and Gyde [2] are explained. Blundell's work gave useful information such as the angular position of failure and the time taken to failure, for each bearing. Failure position was used to infer the type of stress causing the failure, while the time to failure was used in plotting the S–N diagram (stress versus number of cycles to failure). Blundell used a bearing testing machine which was designed to apply varying load on two orthogonal axes. Gyde's machine was simpler and could only apply a varying load on one axis. These machines are very advantageous for testing the bearings since they could exclude undesirable parameters such as oil contamination, combustion products, engine heat and etc. They are also cheaper and easier to operate than engines.

5.1 BLUNDELL'S EXPERIMENTS, INPUT DATA

5.1.1 Blundell's Experiments

Blundell's testing machine was designed by H.D. Rees [23] at Nottingham University. The machine consisted of a 2.4567" steel shaft (shown in Fig. 5.1), supported on two bearings in a rigid housing and frame. The test bearing, which had the same dimension as the supporting bearings, was also held in a very rigid housing (9.0" O.D as shown in Fig. 4.2), positioned mid–way between them.

The reason behind choosing this comparatively large diameter housing was to prevent its bending, which was thought to be an important factor in causing failure. The input loads on the test rig were applied through four (90^{O} apart) pistons moving inside four hydraulic actuators. These pistons were exerting forces on the spherical loading pads which were in contact with the housing's outer surface as shown in Fig. 5.2. The housing was allowed linear rigid body movments only, that it was not allowed to rotate. The applied load from each hydraulic actuator was measured by a pressure transducer mounted on it. The load control system operated two servo valves, each controlling the input load of an axis. A positive current to each valve caused the pressure to increase in the positive and decrease in the negative actuator of that axis. Sinusoidal variations of load could be programmed for each axis. Fig. 5.3 shows the above load variation on each of the axes and the effect of addition of mean load on them. Therefore, by changing the load amplitude on the two axes, it was possible to generate straight line, elliptical and circular load diagrams shown in Fig. 5.4

The resultant load diagram was used in the present work as input to the bearing performance program (Chapter Three) to generate the centreline oil pressure at different time steps.

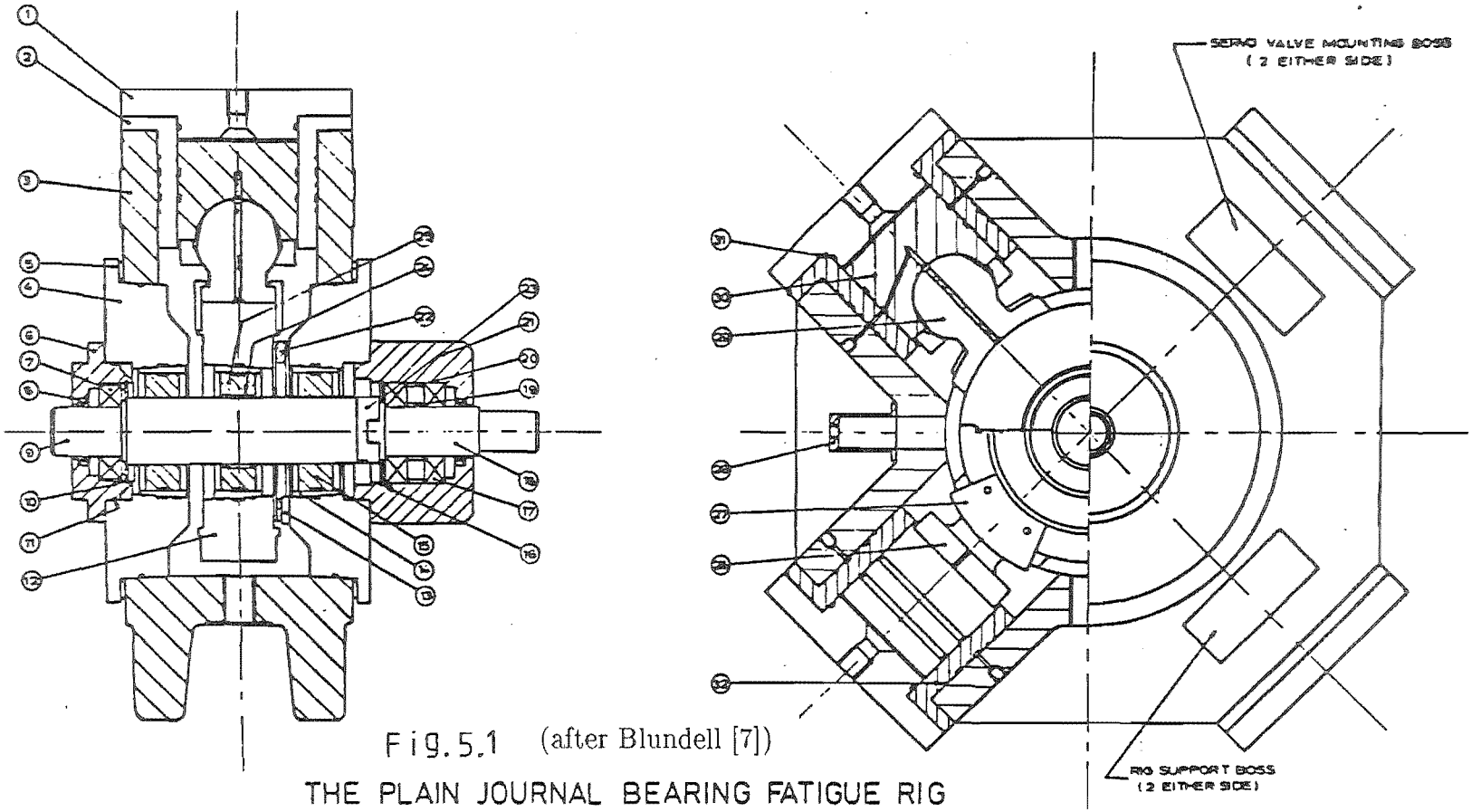

Fig. 5.1 (after Blundell [7])

THE PLAIN JOURNAL BEARING FATIGUE RIG

1. CYLINDER HEAD
2. CYLINDER LINER
3. RIG MAIN BODY
4. END PLATE
5. SPACER
6. SMALL BEARING HOUSING
7. BALL BEARING
9. SHAFT
10. RETAINER & WASHER
11. O RING SEAL
12. TEST BEARING HOUSING
13. STATIC DOG
14. BEARING TAPER RING
15. SUPPORT BEARING
17. BALL BEARING
18. STUB SHAFT
19. SPACER
20. SPACER
21. STUB SHAFT HOUSING
22. ANTI-ROTATION RING
23. OLDHAM COUPLING
25. TEST BEARING SUPPORT RING
26. OIL SUPPLY HOUSING
27. PAD CLAMP
28. SPHERE CLAMP
29. SPHERICAL LOADING PAD
30. PISTON
31. O RING SEAL

Scale :- Approx. $\frac{1}{5}$

NDR
Nov. 76

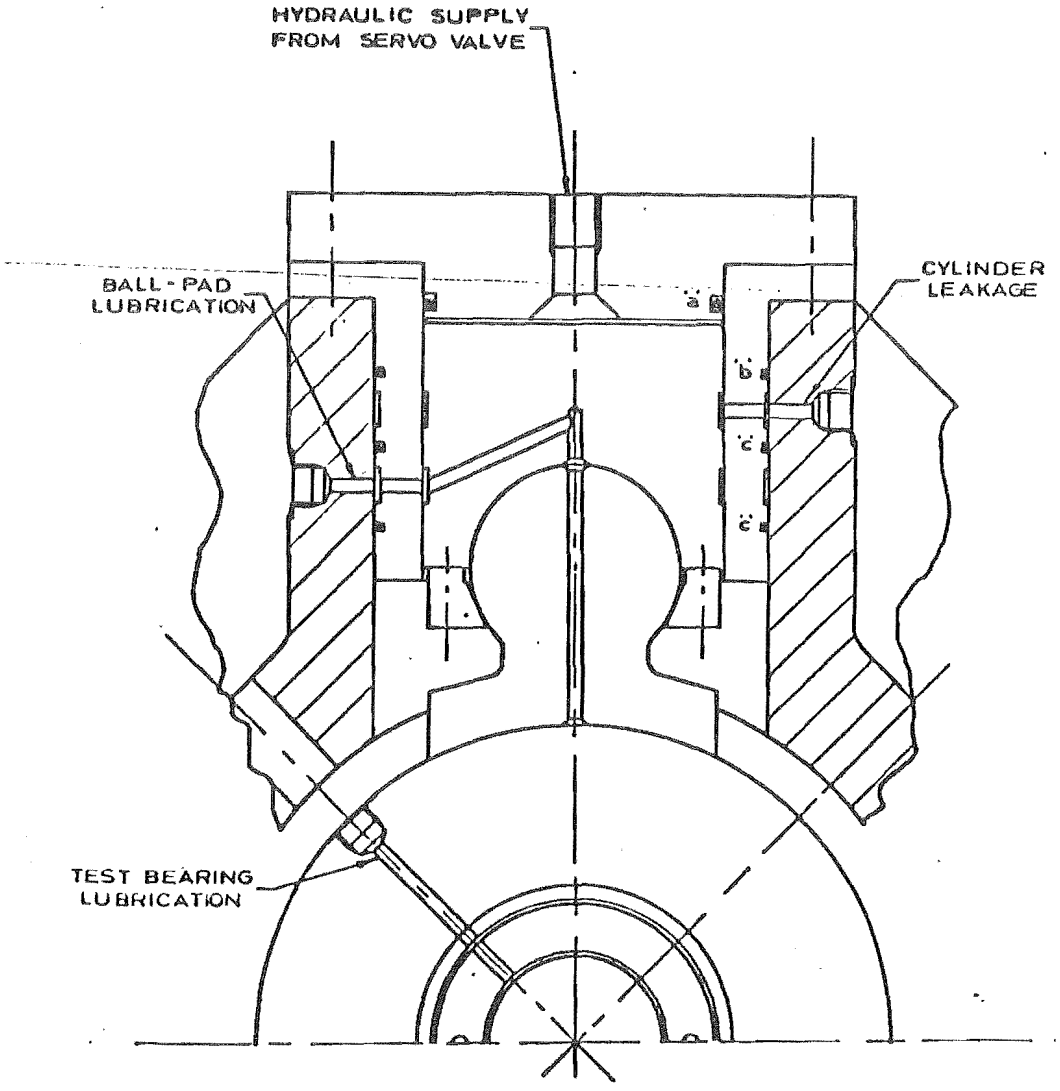

Fig.5.2

(after Blundell [7])

SECTION THROUGH HYDRAULIC ACTUATOR

Scale: x0·4

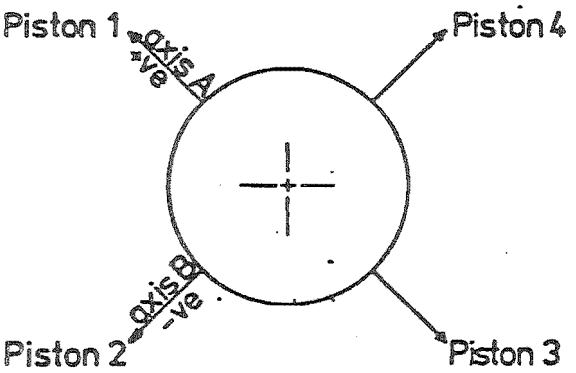

	BASIC SIGNAL	INCREASE BIAS AXIS A	INCREASE BIAS AXIS B	INCREASE AMPLITUDE AXIS A	INCREASE AMPLITUDE AXIS B
SIGNAL AXIS A					
SIGNAL AXIS B					
RESULTANT LOAD LOCUS					

Fig. 5.3 Effect of bias and amplitude controls on load locus

(after Blundell [7])

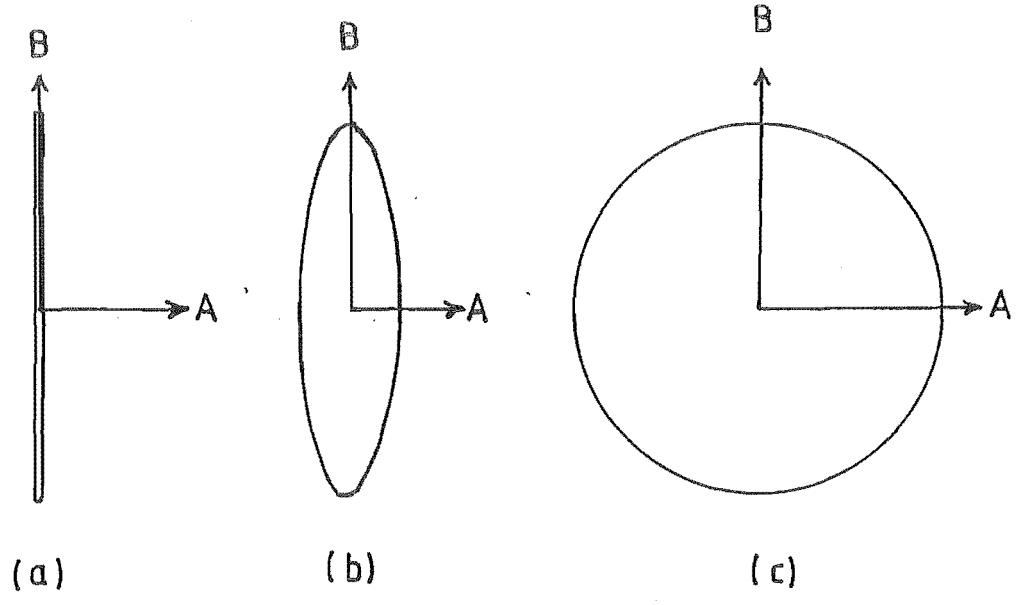

Fig.5.4

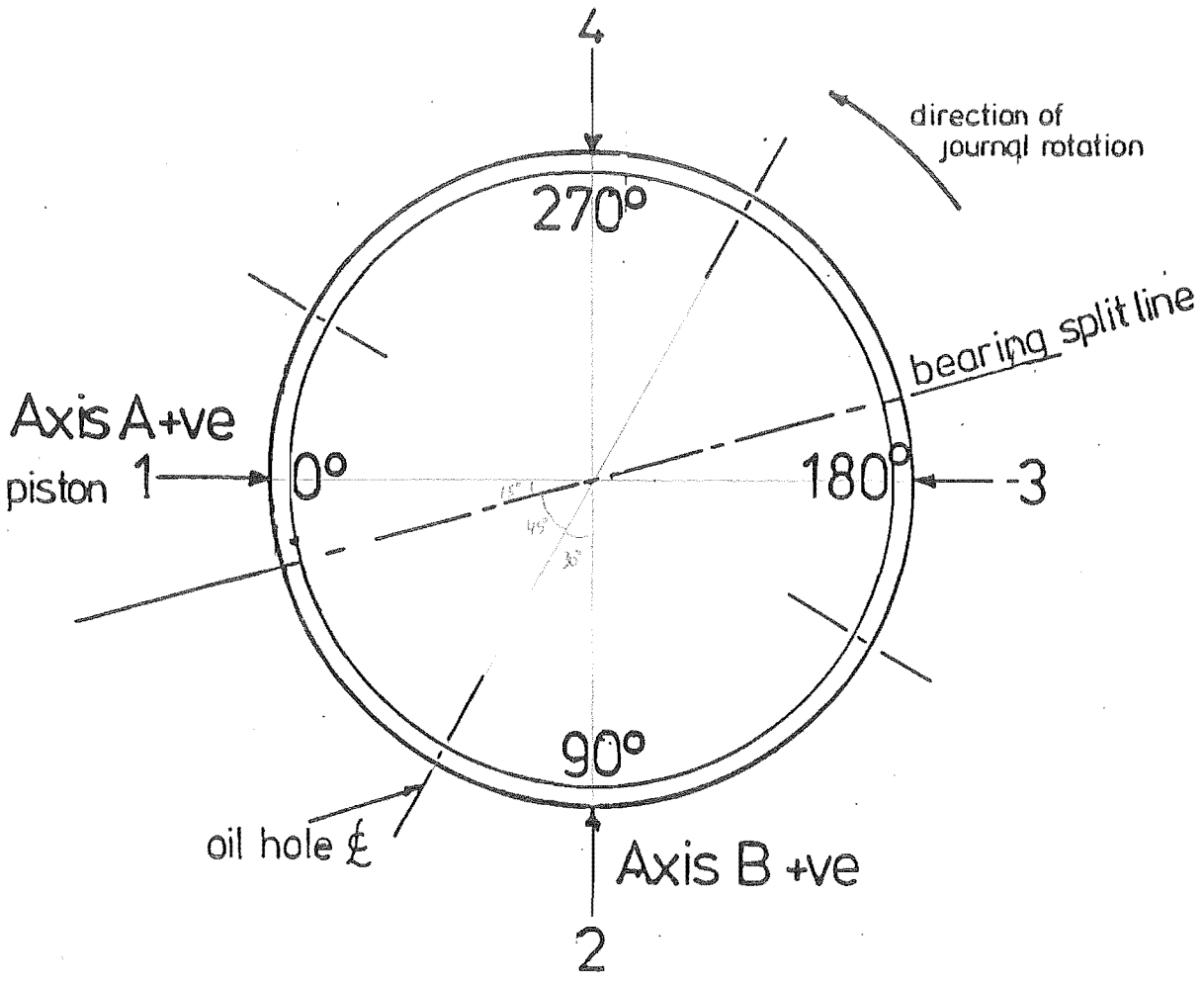

Fig.5.5 - Relative Bearing Geometry

(after Blundell [7])

→ See pg. 151 and Fig 8.4 of [7]

Blundell repeated his tests for each load pattern a number of times and for each set of these tests he left the machine to operate for an initial six hours period during which six data recordings of the input load were made. At the end of this time the machine was turned off and the test bearing was inspected, using an intrascope, for visible cracks. If none were found, further inspections were made every three hours until the first crack was detected. The total running time was recorded as the time to failure for that initial test. In any subsequent test of the set with the same applied load pattern, the first inspection was made at the longest recorded inspection time before failure of the initial test, and the following inspections were made every one hour until the first crack was visible. In these tests, the bearing halves were positioned as shown in Fig. 5.5 so that the angle of failure would fall in the middle of a bearing half, that is, away from a split line.

Blundell basically selected seven load patterns, their approximate shapes being given in Figs. 5.6–5.12. A mean load in the direction of piston No.4 (–B axis) encouraged the failure to fall in that region. A similar set of seven experiments using approximately the same input loads but with the shaft rotating in a direction opposite to that of the load (antirotational) were also tested. Their results are shown in Figs. 5.13–5.19. The above tests were performed on plain bearings (1 land type). In a similar series of experiments, bearings with a circumferential oil groove in the middle (2 land type) were also tested. Plots of results from their numerical reconstruction are shown in Figs. 5.20–5.33. They include the input load and eccentricity ratio locus and pressure curves obtained from the bearing performance program and the tangential stress curves on the surface and its variation at the maximum point with respect to time. Variation of surface pressure at this point was also plotted on the same frame but to a

different scale (same as that on pressure curves plot). Blundell's experiment resulted in a total of 28 different test cases. Each case was tested up to three times in which a maximum fluctuation of ±600 LbF in the average peak load of 15900 LbF was permitted. Results of the tests with larger load fluctuations were ignored. Fig. 3.3 shows that the experimental load diagrams were not as smooth as those constructed from sinusoidal functions. This was due to hysteresis in the testing system.

5.1.2 Input Data

For the numerical reconstruction of Blundell's experiments, the required input data were divided into three groups:

a – The input load data needed to generate the A and B coordinates of forces exerting on the bearing at every 5^{O} rotation of shaft.

b – The data required to run the bearing performance program.

c – The data required by the FEM program to calculate the stresses.

The first group of data included the mean and amplitude of the load with respect to the axes. These were measured from the input load diagram as was explained in Section 3.1. Different values for the phase angle ϕ in Equations (3.1), (3.2) were tried, to fit the load diagram as close as possible to the experimental one. Table 5.1 lists the load amplitude, mean load and phase angles used in reconstructing the 28 cases.

The second group of data was based on data recorded by Blundell. It included:

Shaft diameter = 2.4567".

Bearing inside diameter varied between 2.4598" to 2.4603" on a nominal inside diameter of 2.46". Since these were not given for each individual test, an average value of 2.46" was adopted.

Diametral clearance = .0033". This was calculated as the difference between the average value of the bearing's inside diameter and the shaft diameter.

The bearing's land length was 1.16" for the one land bearing and 0.5" for the two land bearing (bearings with a circumferential oil groove in the middle).

Viscosity = 20 centipose. This was based on an average outlet oil temperature of 48.6^{O}C and the atmospheric pressure.

Finite difference meshes were 112 nodes at graded spacing in the circumferential direction given in Section 3.1 and 16 nodes at uniform spacing in the axial direction.

Shaft speed = 1050 RPM.

Load frequency = 1050 cycles/min.

The third group of data comprised the information required by the FEM program to calculate the stresses. It included :

Centreline pressures at different instants of time which were computed by the bearing performance program.

White metal thickness = .02".

Steel backing thickness = .0623".

Housing thickness = 3.4375".

Material properties of the white metal and steel backing are listed in Table 5.2. The white metal layer had the following composition:

Test No.	Load Amplitude (A–AXIS) Lb–F	Load Amplitude (B–AXIS) Lb–F	Mean Load (A–AXIS) Lb–F	Mean Load (B–AXIS) Lb–F	Phase Angle Deg.
501	1500	8900	0	–1250	70
502	2200	11560	940	–3750	15
503	1875	11250	–450	–3590	75
504	3000	10310	0	–4060	–20
505	1000	13280	–500	–2200	0.
506	5500	12500	0	–2340	10.
507	7200	12200	800	–2200	–8.
508	850	8900	–300	–400	80
509	2150	11560	940	–3750	20
510	2340	11720	–625	–3900	70
511	1100	13600	–500	–2030	0.
512	1100	9375	+1000	–940	20
513	5500	11090	0.	–2340	0.
514	7200	12200	800	–2200	–8.
515	320	8750	620	–300	0.
516	2200	11560	940	–3750	15.
517	1875	11250	–450	–3590	75.
518	3000	10310	0	–3120	20.
519	1300	13440	0	–2970	0.
520	5500	12500	0	–2343	0.
521	7500	11700	780	–2790	–8.
522	500	9060	1170	–400	0.
523	2200	11560	940	–3750	15.
524	470	9218	230	–300	75.
525	2300	10310	0	–2960	10.
526	1300	13750	–500	–2400	0.
527	5500	11090	0	–2340	0.
528	7200	12200	450	–2300	–8.

Table 5.1

89.33% tin, 7.2% antimony, 3% copper, 0.29% lead, 0.08% iron, 0.1% nickel.

Metal	Modulus of Elasticity LbF/in^2	Poisson ratio (μ)
White Metal	7.59 x 10^6	0.4
Steel backing	30 x 10^6	0.3

Table 5.2

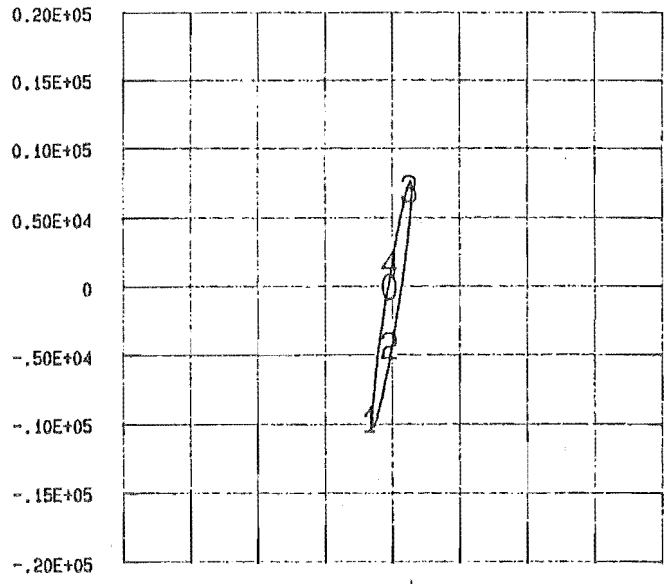

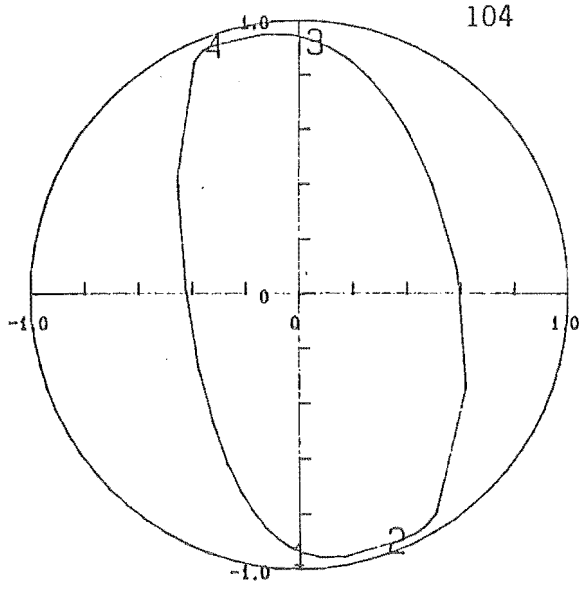

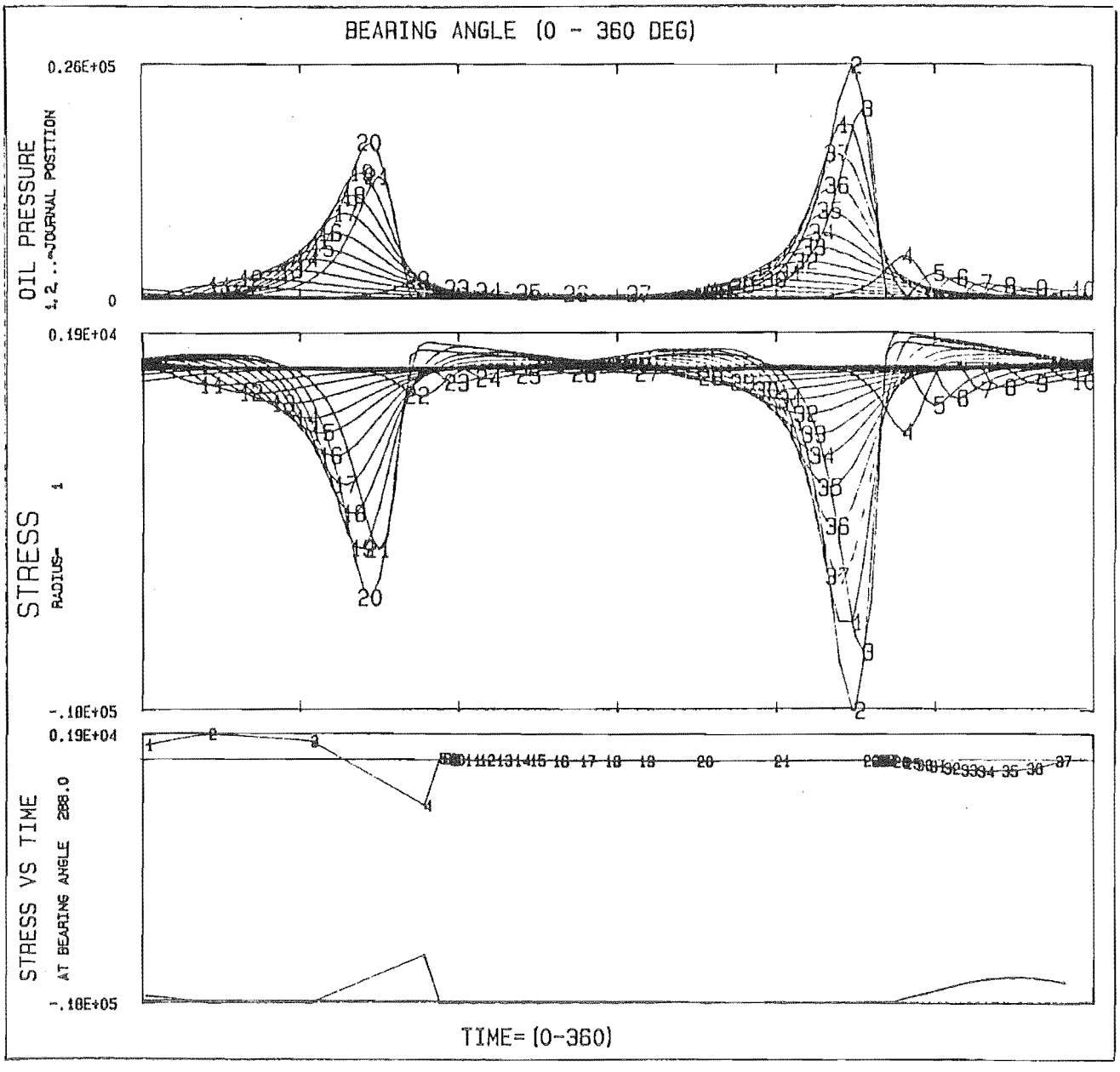

TEST NO 501 CO ROTATIONAL LOAD, 1 LAND BEARING

MAX STRESS = 0.189E+04 , AT ANGLE= 288.0

MIN STRESS = -0.183E+05 , AT ANGLE= 268.8 STRESS TYPE= TANGENTIAL

Fig.56

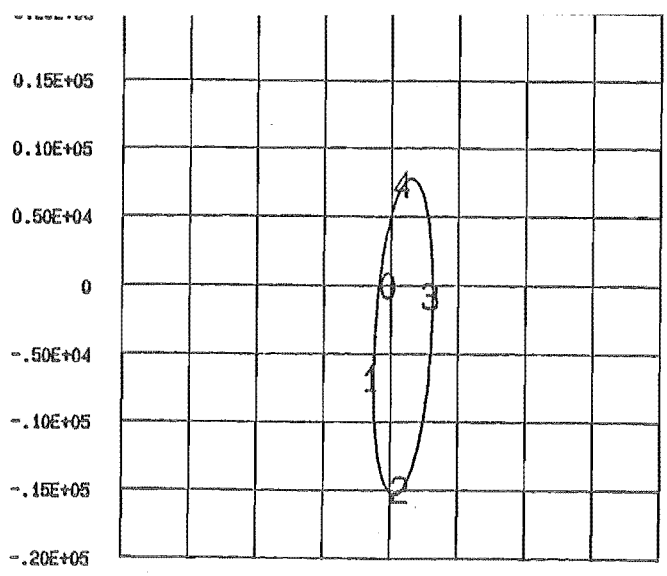

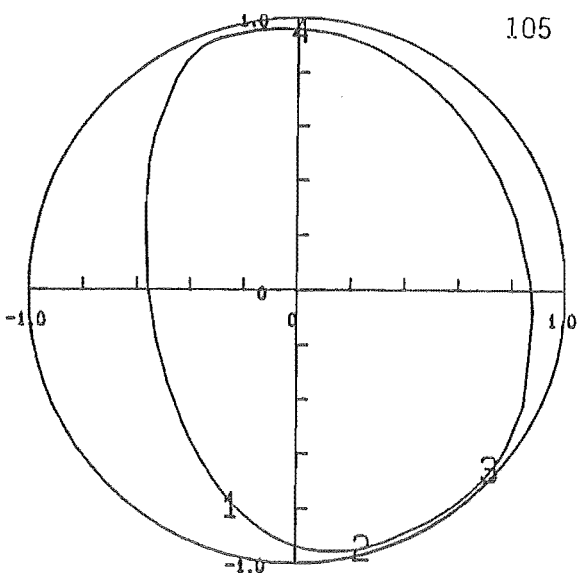

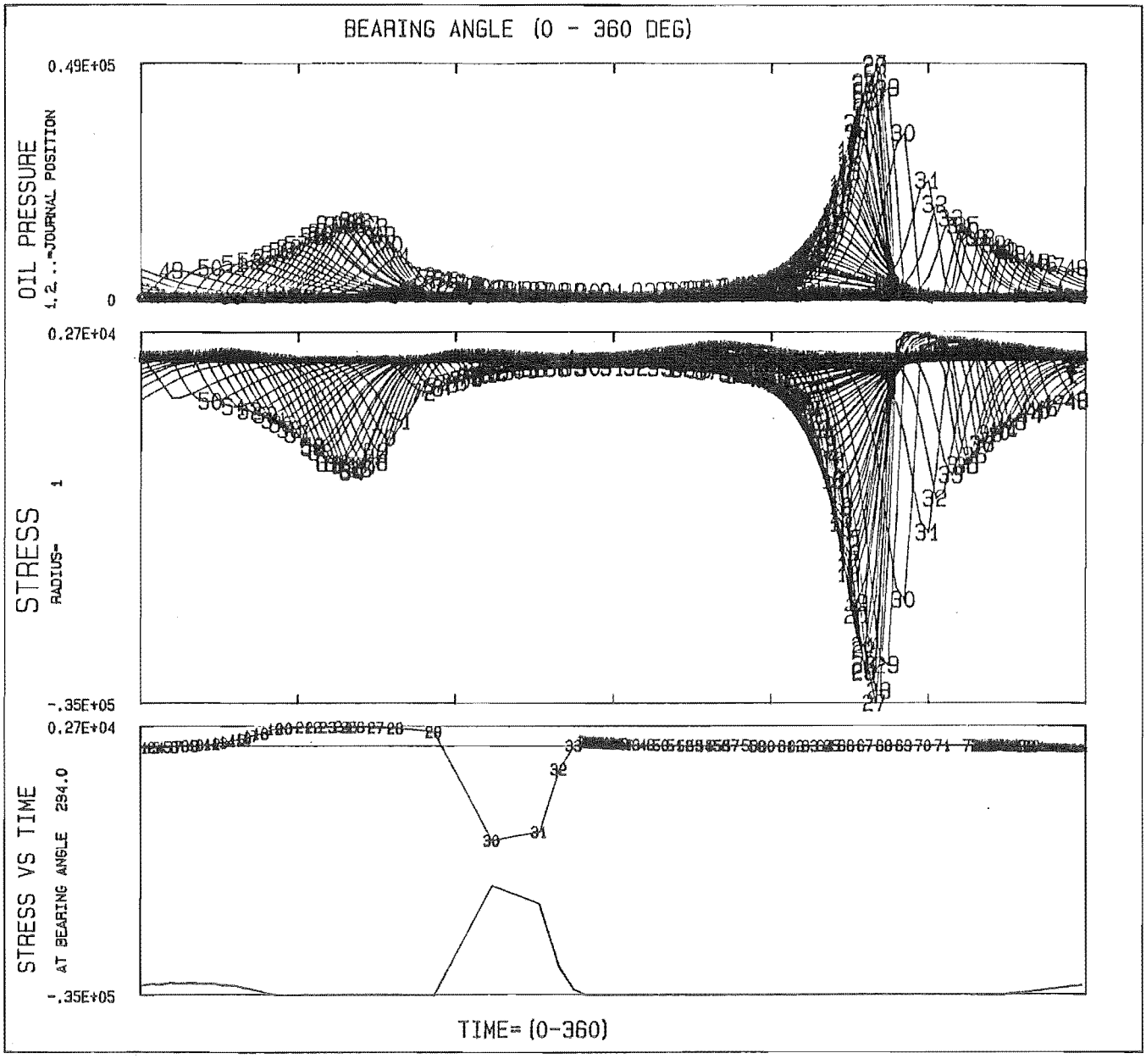

TEST NO 502 CO ROTATIONAL LOAD , 1 LAND BEARING

MAX STRESS = 0.275E+04 , AT ANGLE= 294.0

MIN STRESS = -0.352E+05 , AT ANGLE= 280.2 STRESS TYPE= TANGENTIAL

Fig.57

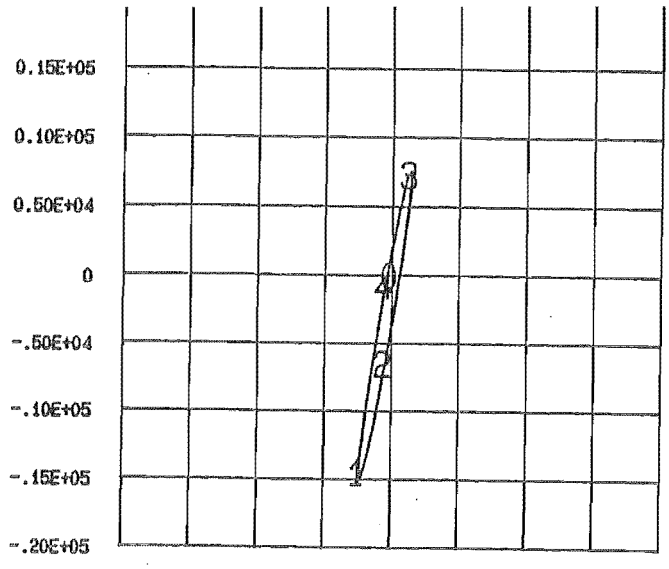

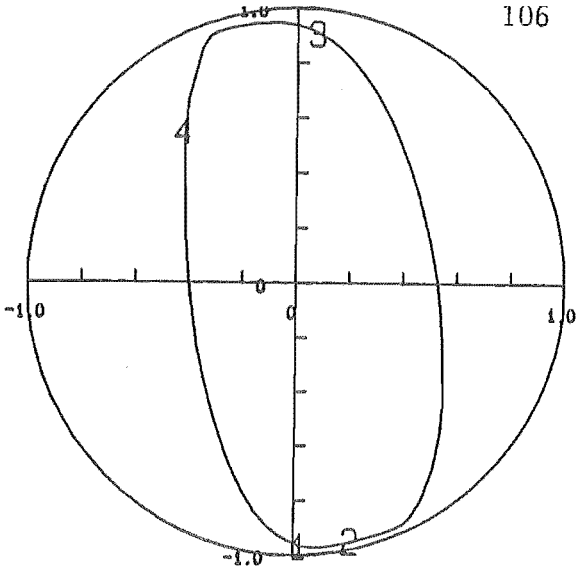

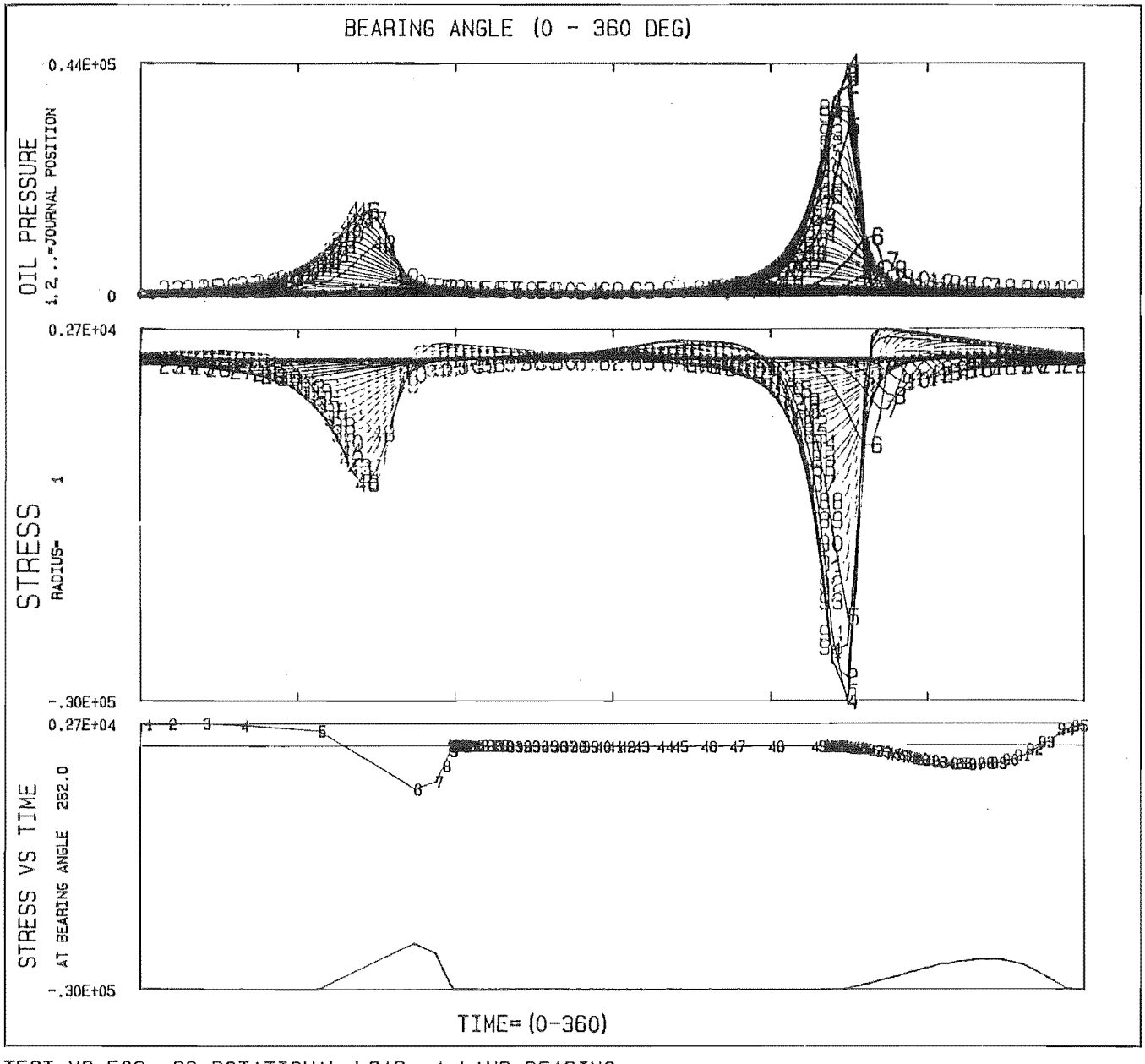

TEST NO 503 CO ROTATIONAL LOAD , 1 LAND BEARING

MAX STRESS = 0.265E+04 , AT ANGLE= 282.0

MIN STRESS = -0.301E+05 , AT ANGLE= 269.5 STRESS TYPE= TANGENTIAL

Fig.5.8

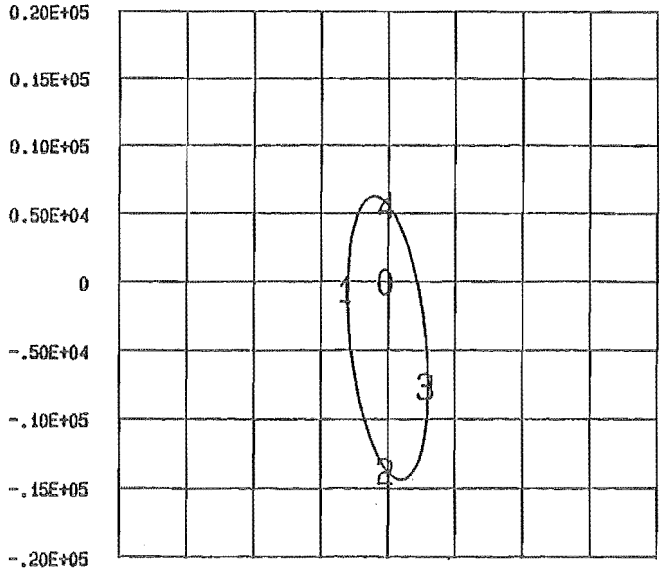

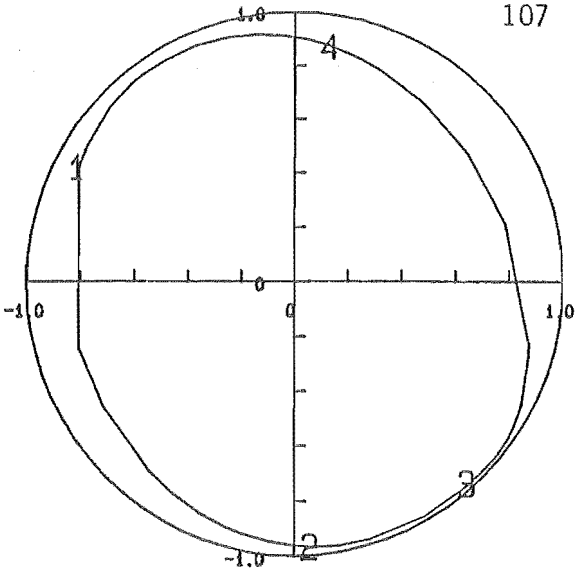

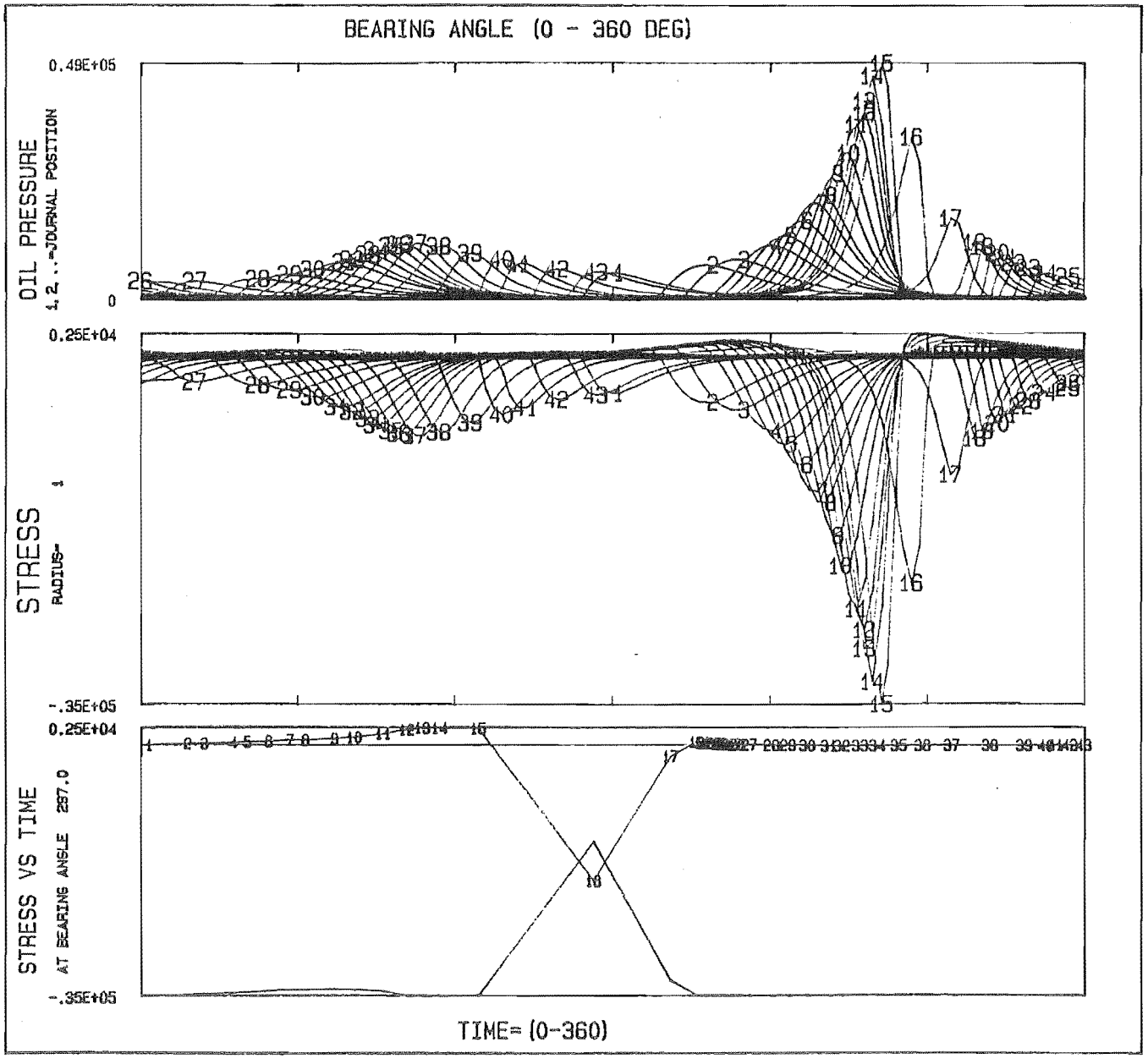

TEST NO 504 CO ROTATIONAL LOAD, 1 LAND BEARING

MAX STRESS = 0.249E+04 , AT ANGLE= 297.0

MIN STRESS = -0.354E+05 , AT ANGLE= 282.0 STRESS TYPE= TANGENTIAL

Fig. 5.9

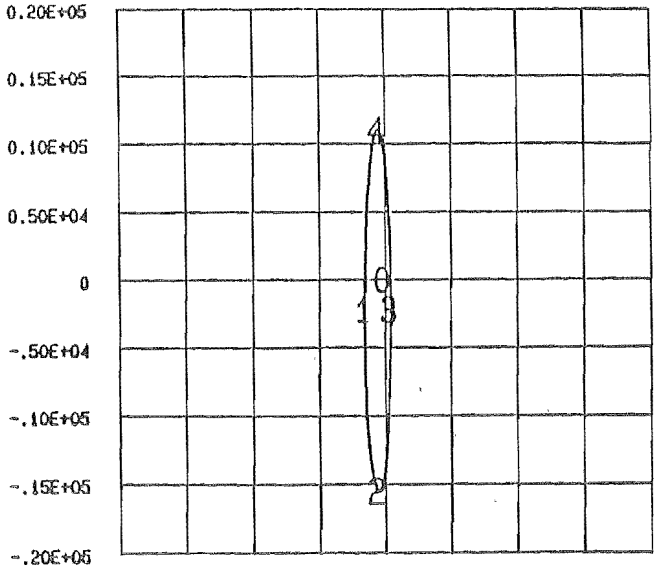

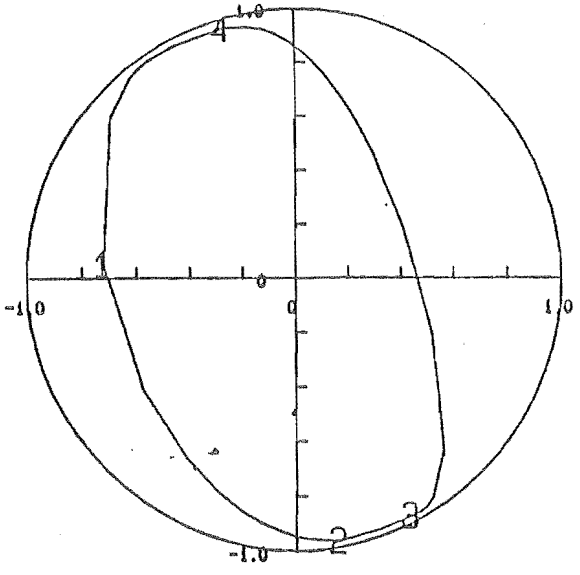

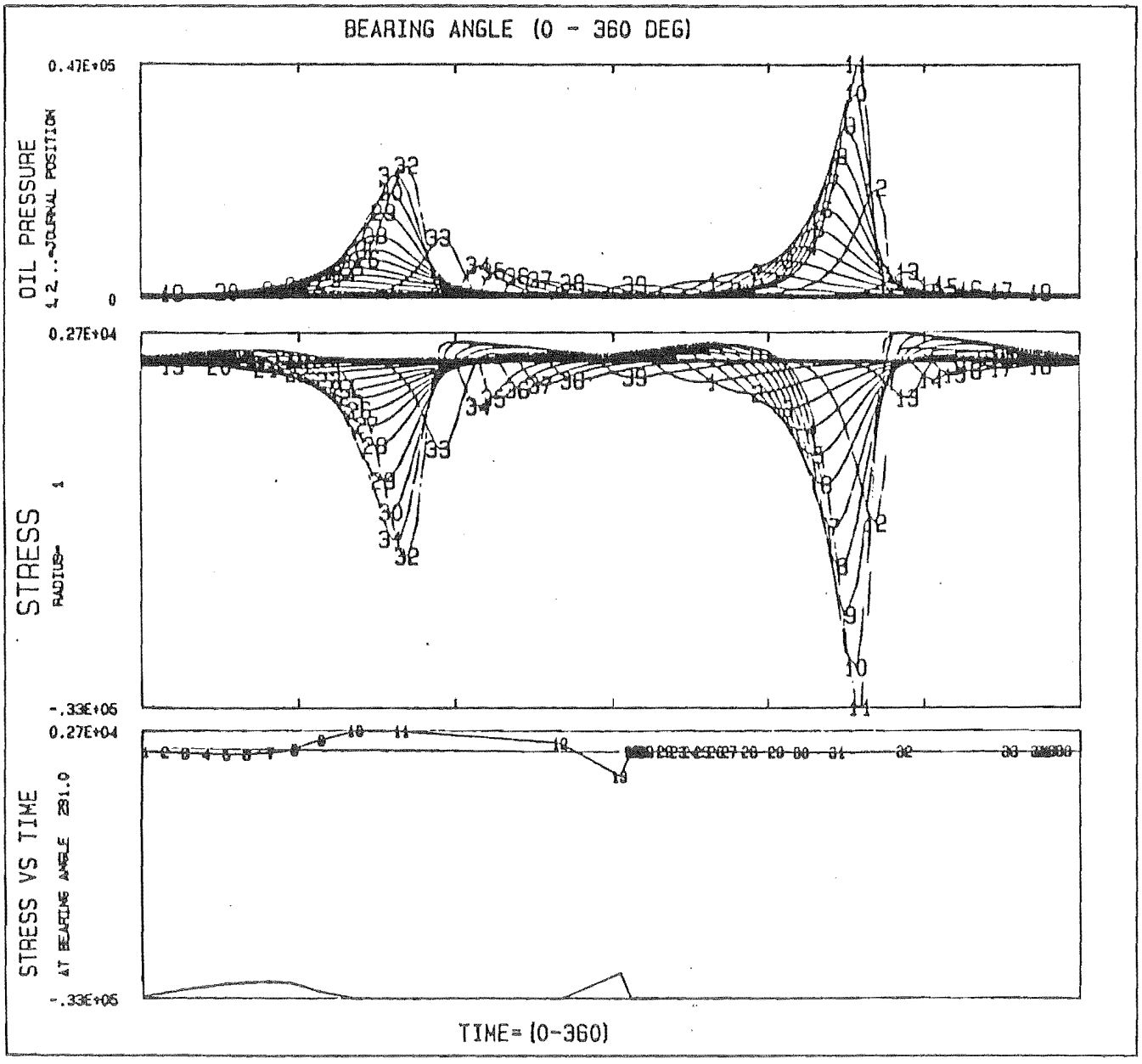

TEST NO 505 CO ROTATIONAL LOAD, 1 LAND BEARING

MAX STRESS = 0.270E+04 , AT ANGLE= 291.0

MIN STRESS = -0.331E+05 , AT ANGLE= 274.2 STRESS TYPE= TANGENTIAL

Fig.5.10

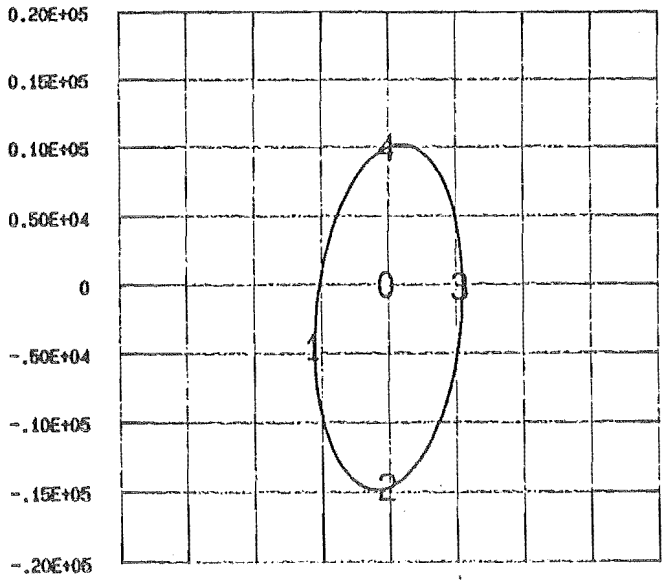

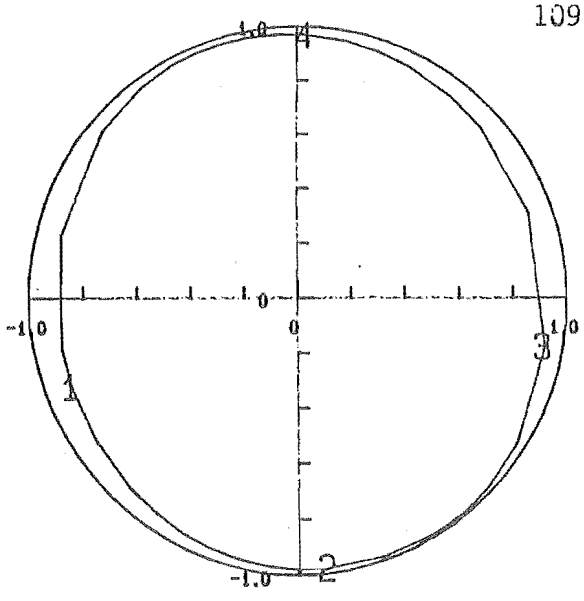

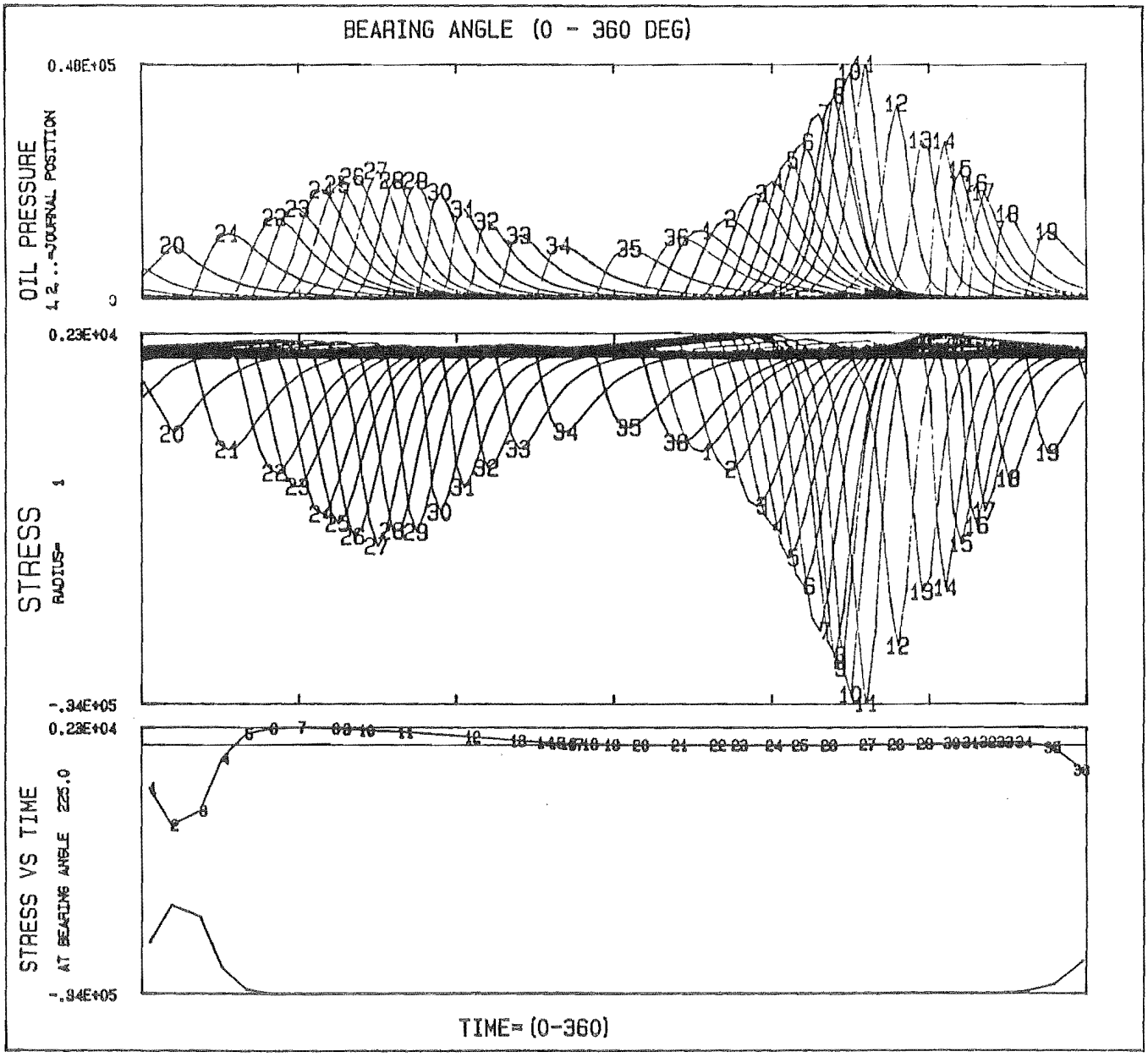

TEST NO 506 CO ROTATIONAL LOAD, 1 LAND BEARING

MAX STRESS = 0.223E+04 , AT ANGLE= 297.0

MIN STRESS = -0.342E+05 , AT ANGLE= 275.5 STRESS TYPE= TANGENTIAL

Fig. 5.11

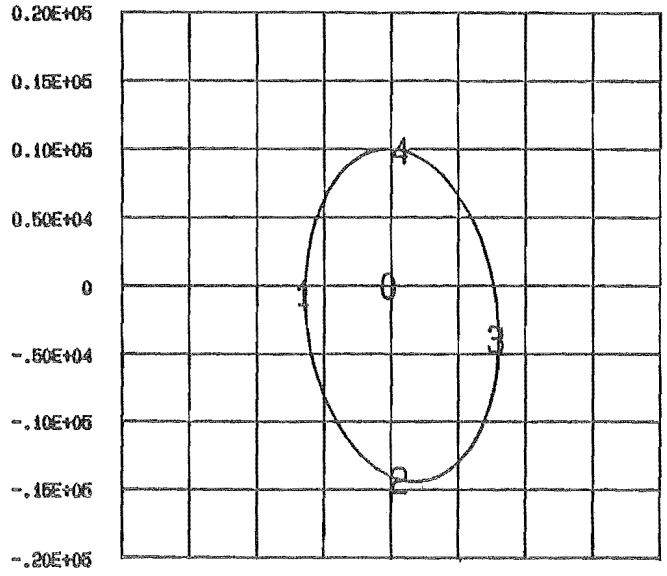

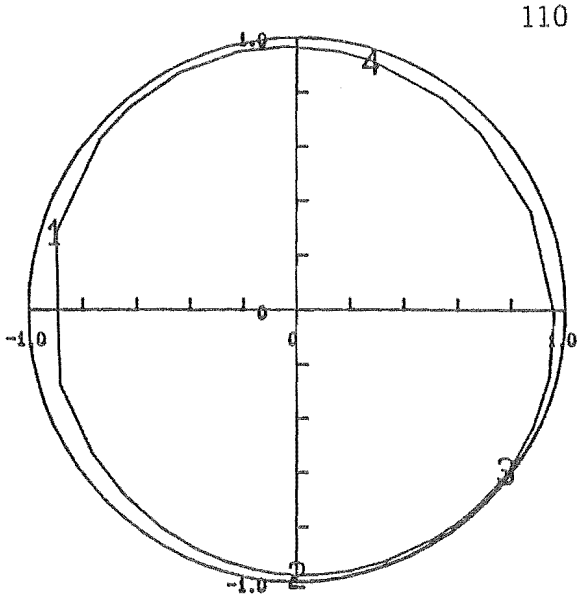

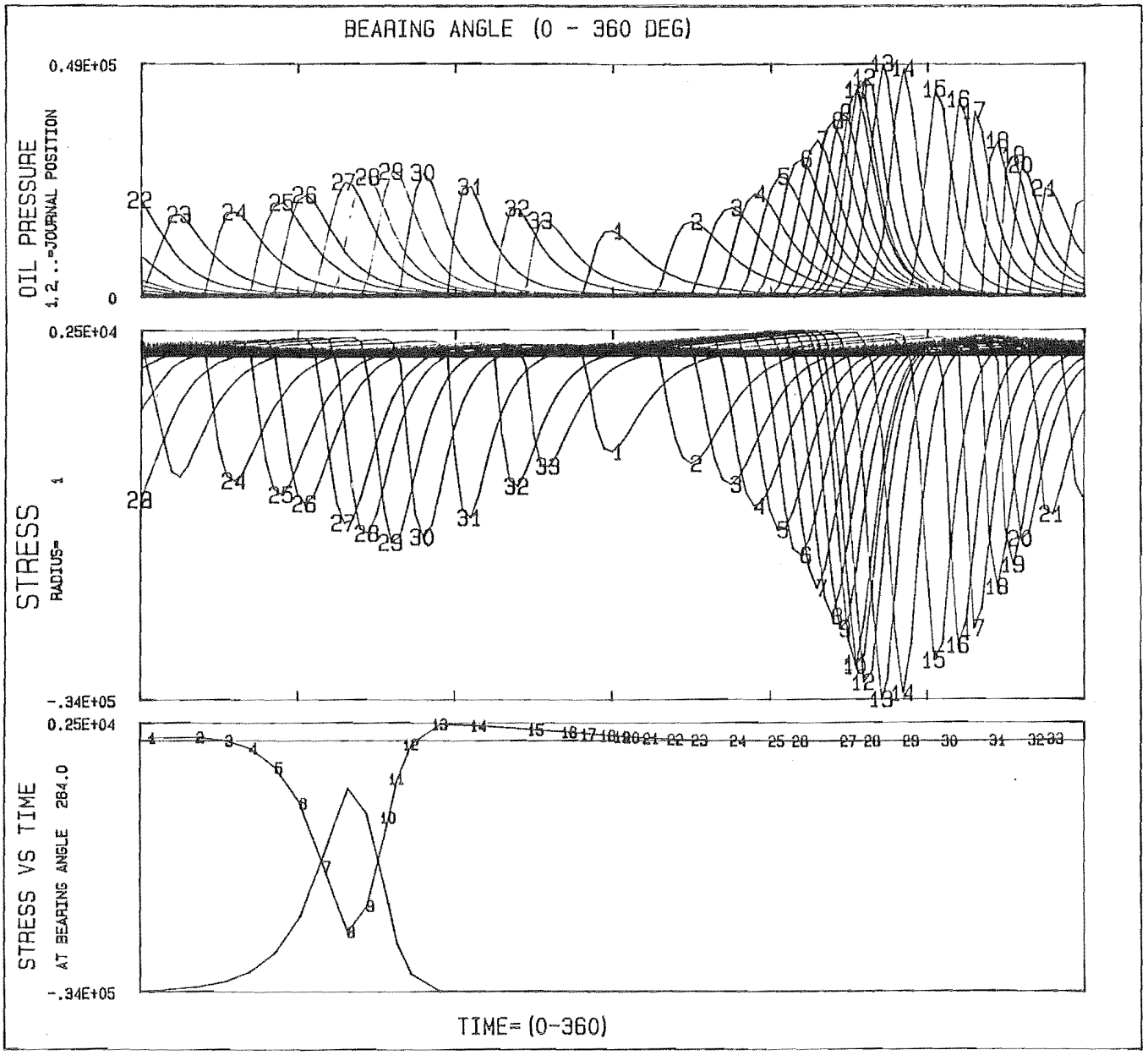

TEST NO 507 CO ROTATIONAL LOAD, 1 LAND BEARING

MAX STRESS = 0.249E+04 , AT ANGLE= 264.0

MIN STRESS = -0.344E+05 , AT ANGLE= 282.9 STRESS TYPE= TANGENTIAL

Fig. 5.12

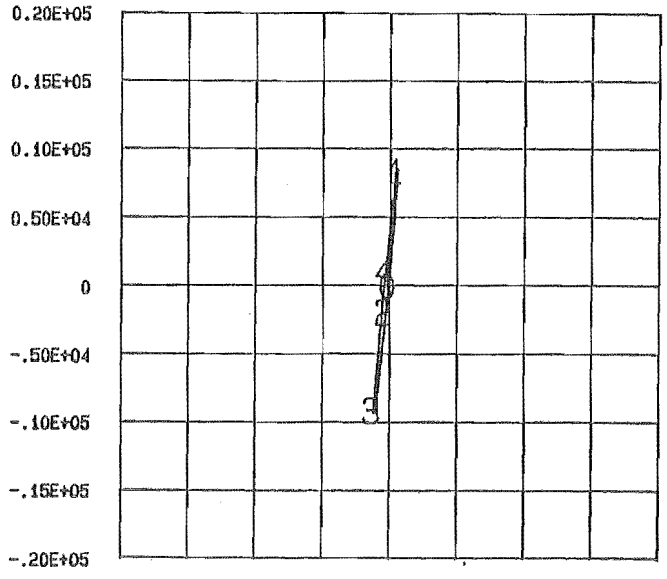

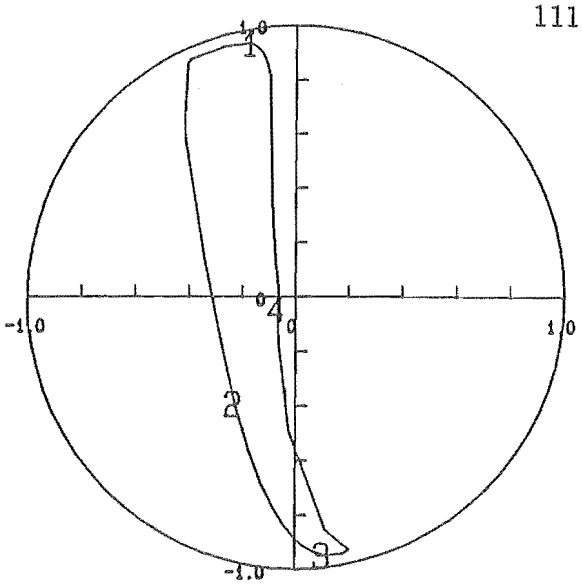

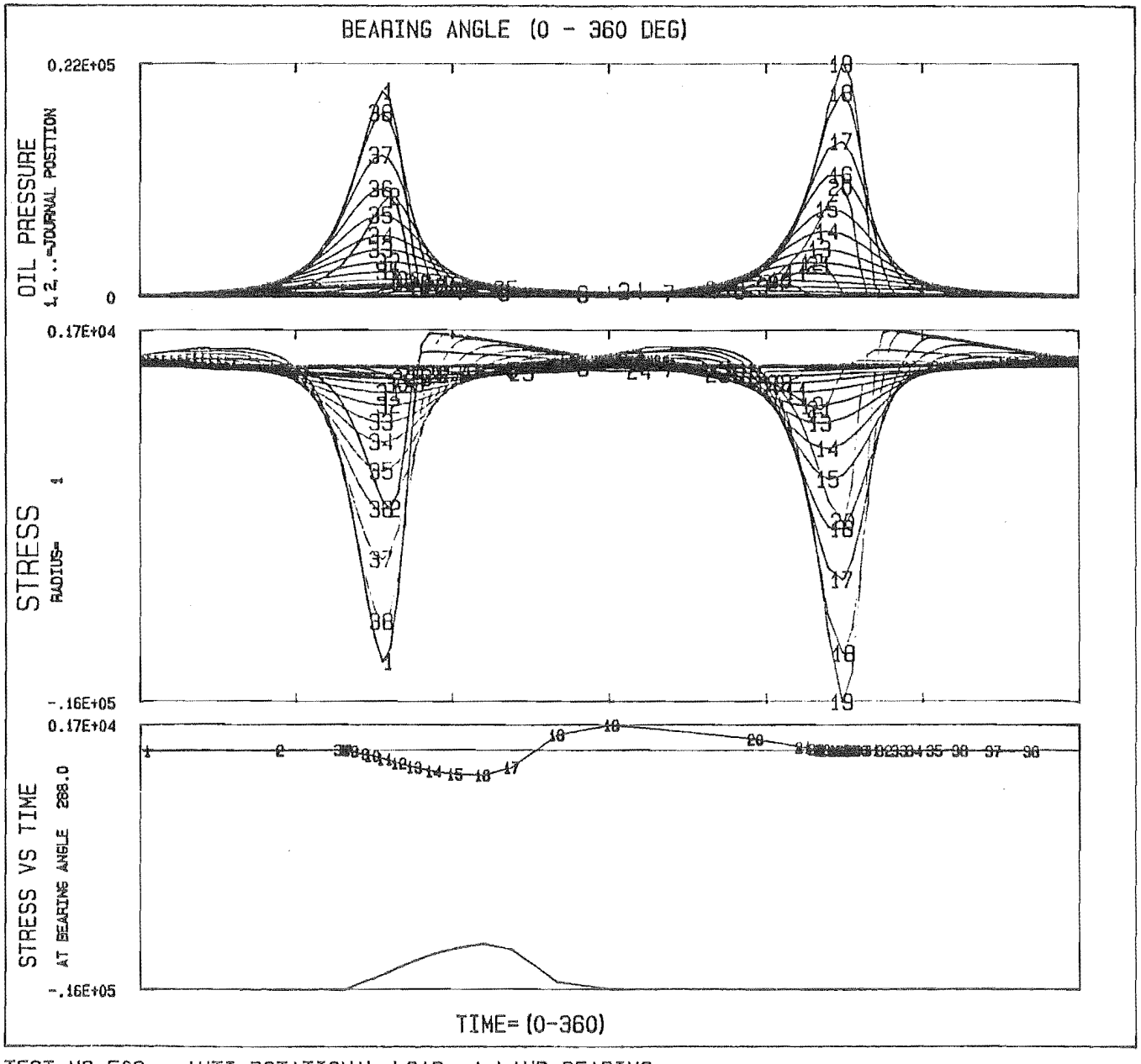

TEST NO 508 ANTI ROTATIONAL LOAD, 1 LAND BEARING

MAX STRESS = 0.166E+04 , AT ANGLE= 288.0

MIN STRESS = -0.156E+05 , AT ANGLE= 269.3 STRESS TYPE= TANGENTIAL

Fig.5.13

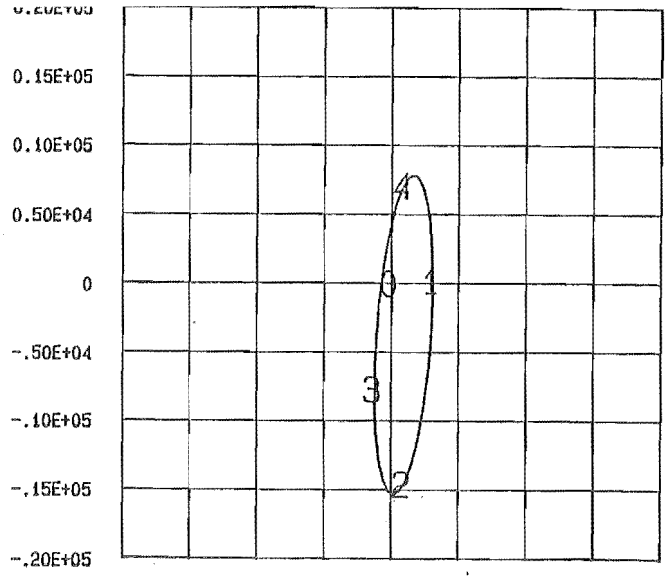

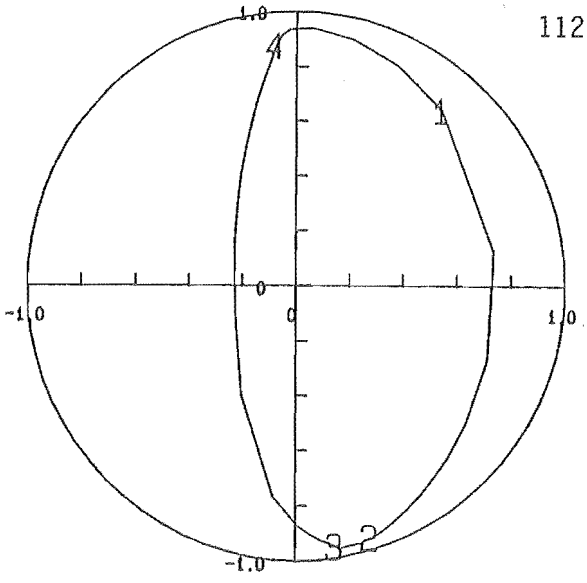

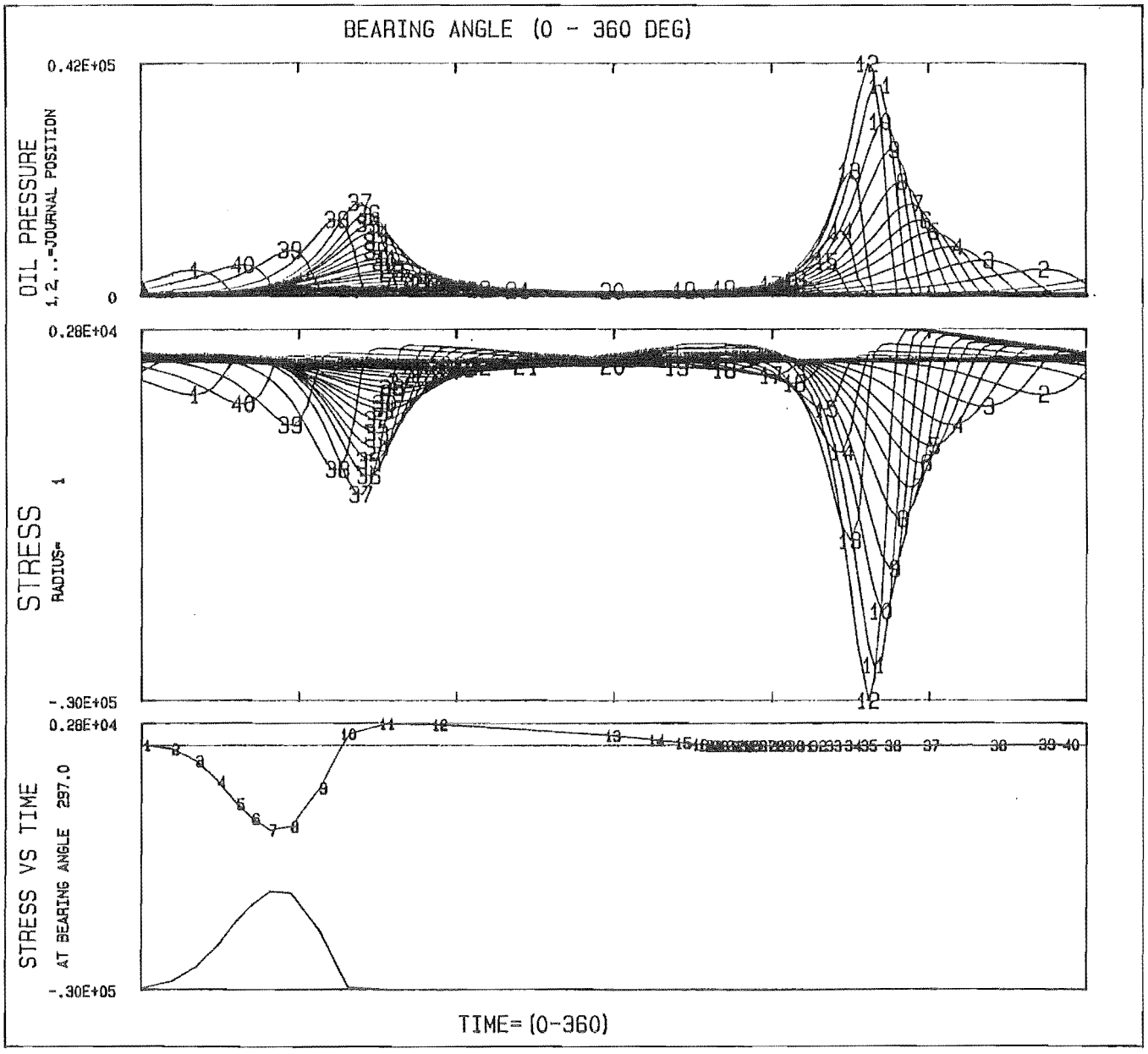

TEST NO 509 ANTI ROTATIONAL LOAD, 1 LAND BEARING

MAX STRESS = 0.277E+04 , AT ANGLE= 297.0

MIN STRESS = -0.298E+05 , AT ANGLE= 277.2 STRESS TYPE= TANGENTIAL

Fig.5.14

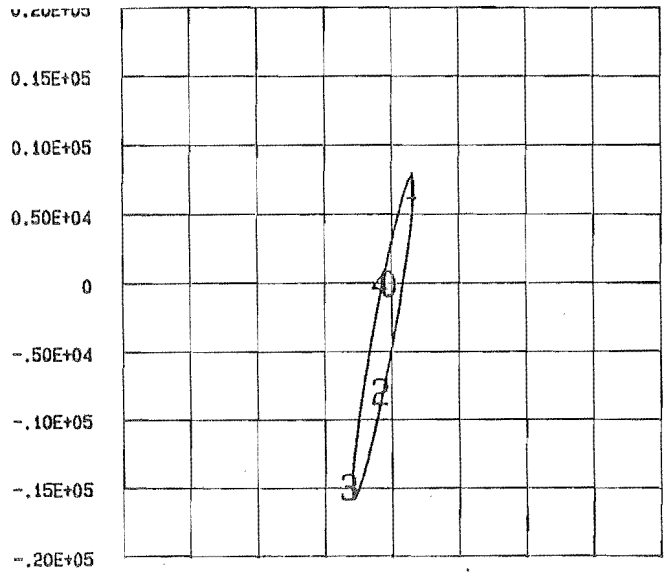

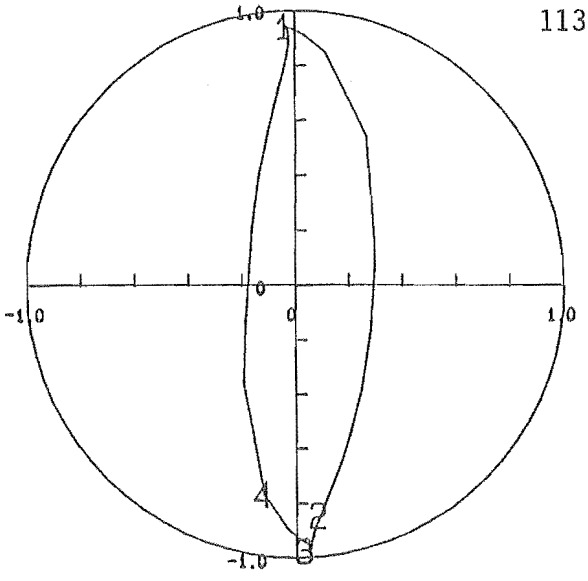

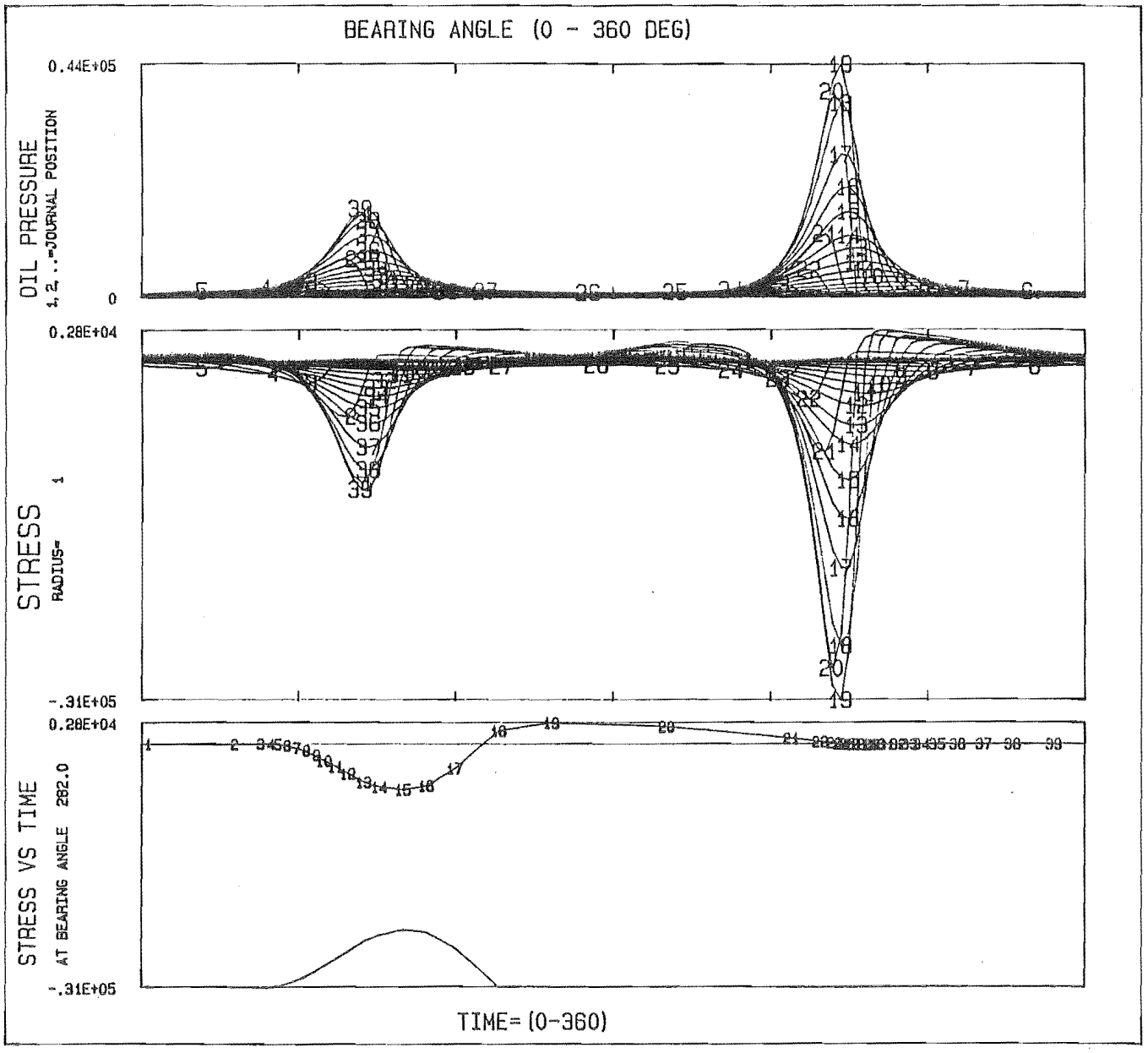

TEST NO 510 ANTI ROTATIONAL LOAD, 1 LAND BEARING

MAX STRESS = 0.280E+04 , AT ANGLE= 282.0

MIN STRESS = -0.307E+05 , AT ANGLE= 267.1 STRESS TYPE= TANGENTIAL

Fig 5.15

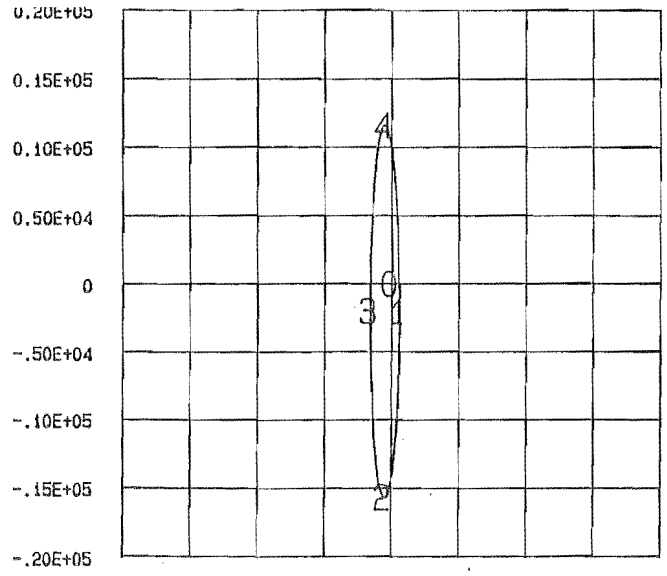

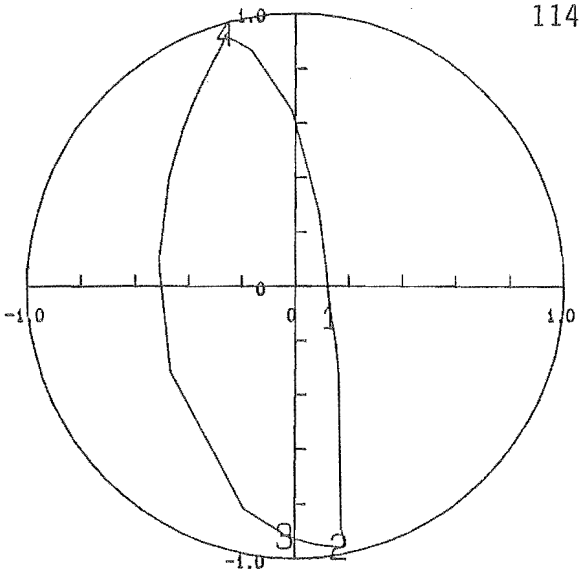

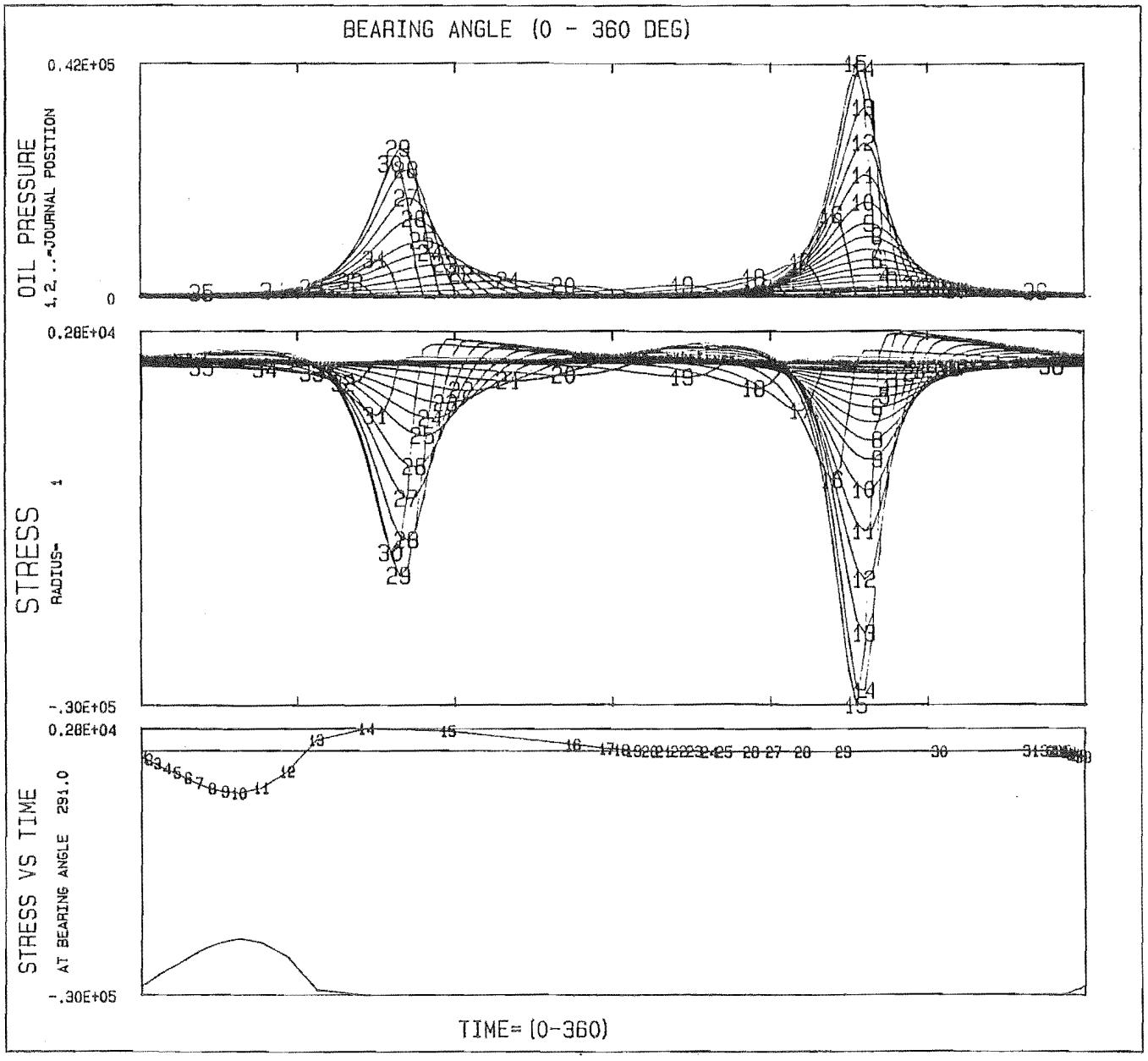

TEST NO 511 ANTI ROTATIONAL LOAD, 1 LAND BEARING

MAX STRESS = 0.278E+04 , AT ANGLE= 291.0

MIN STRESS = -0.301E+05 , AT ANGLE= 273.1 STRESS TYPE= TANGENTIAL

Fig. 5.16

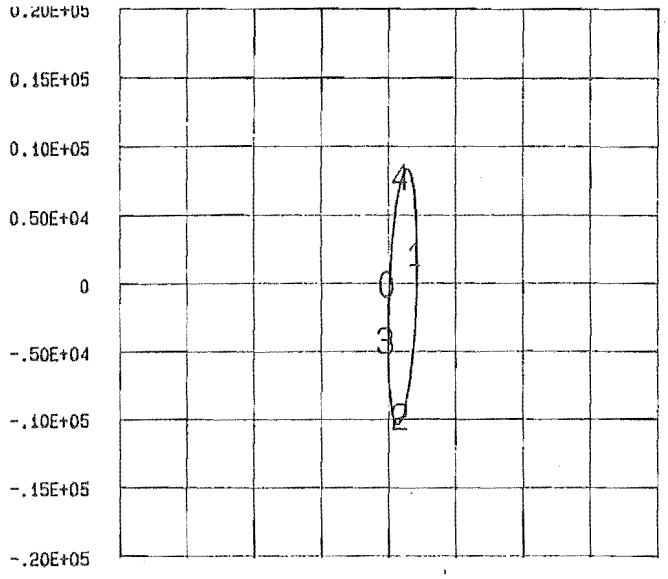

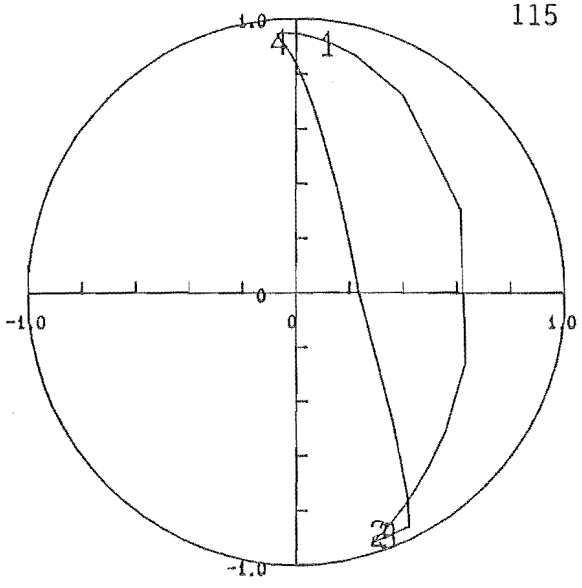

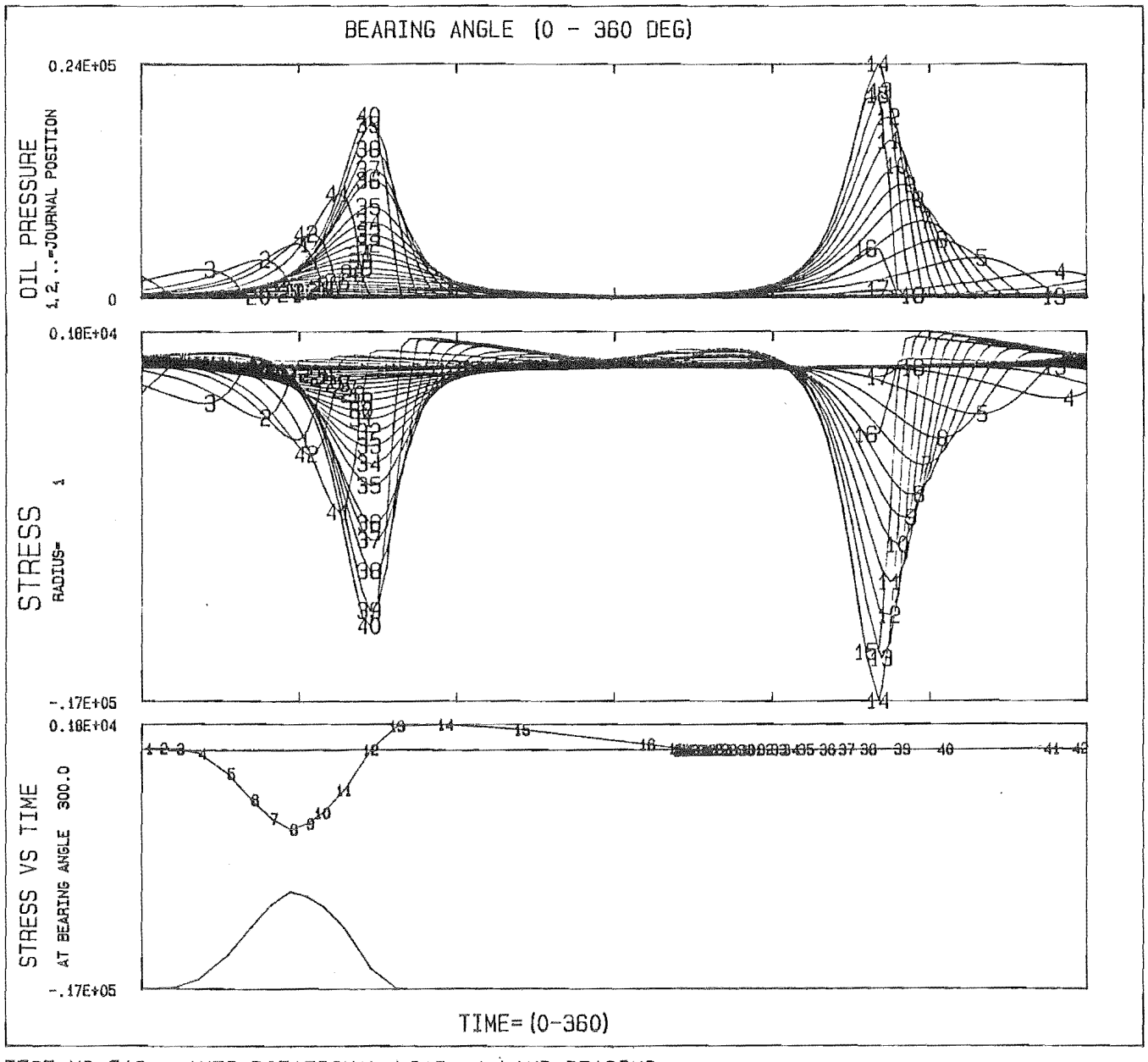

TEST NO 512 ANTI ROTATIONAL LOAD, 1 LAND BEARING

MAX STRESS = 0.181E+04 , AT ANGLE= 300.0

MIN STRESS = -0.173E+05 , AT ANGLE= 280.8 STRESS TYPE= TANGENTIAL

Fig. 5.17

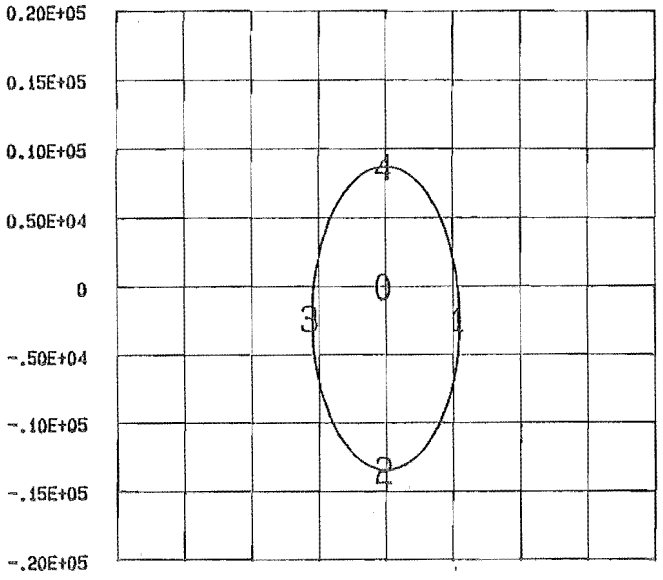

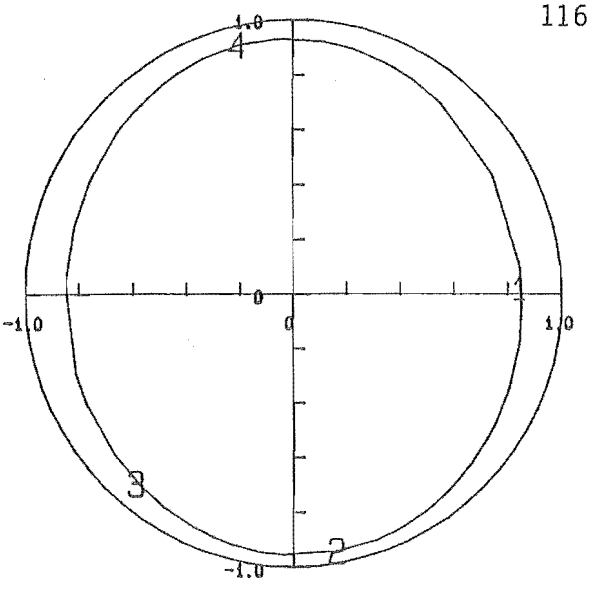

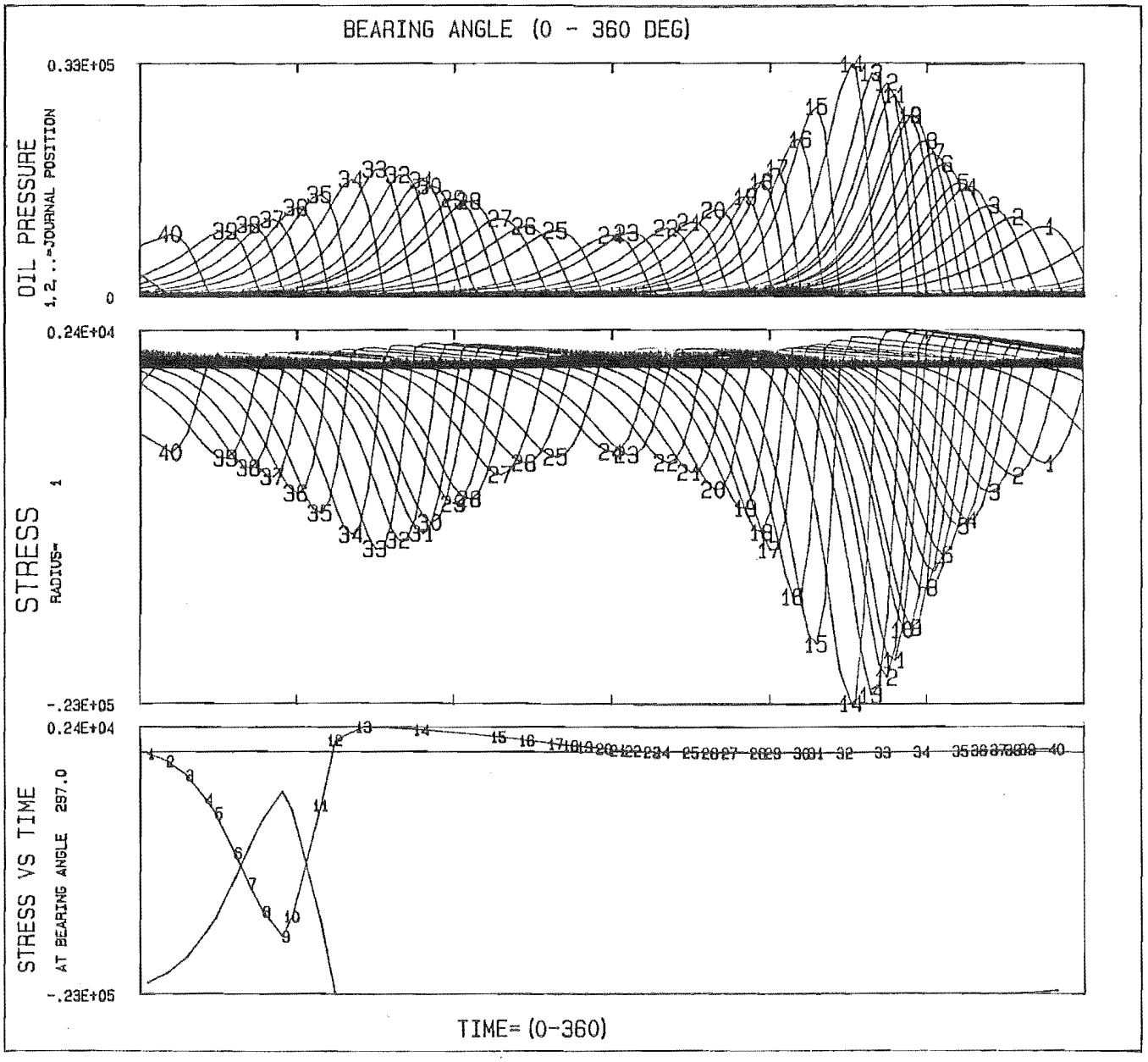

TEST NO 513 ANTI ROTATIONAL LOAD, 1 LAND BEARING

MAX STRESS = 0.240E+04 , AT ANGLE= 297.0

MIN STRESS = -0.229E+05 , AT ANGLE= 271.4 STRESS TYPE= TANGENTIAL

Fig.5.18

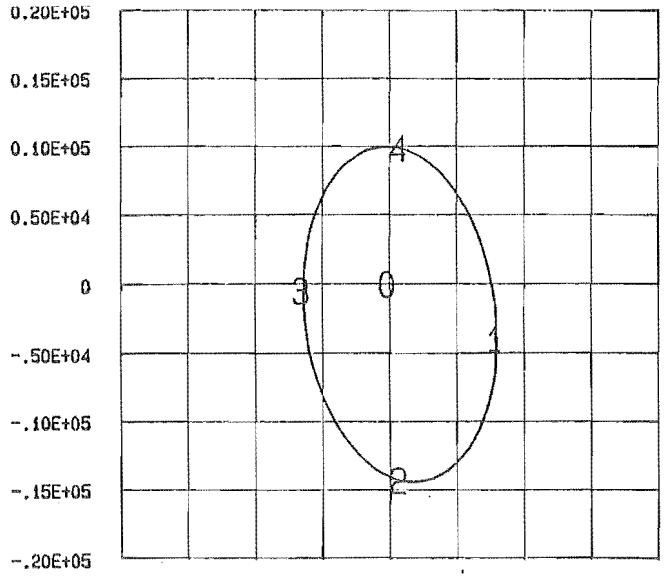

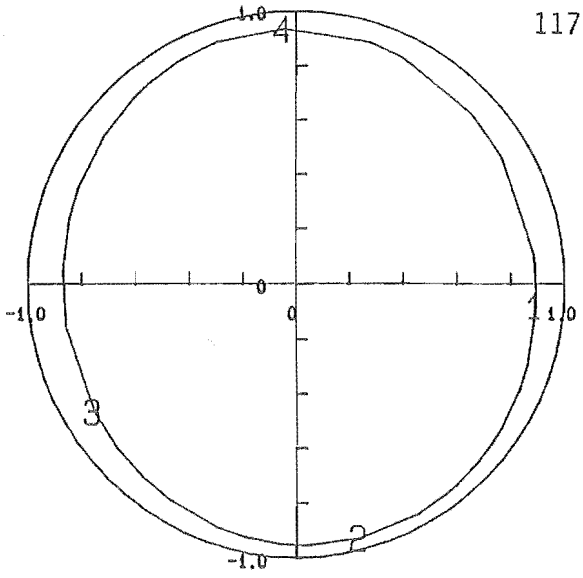

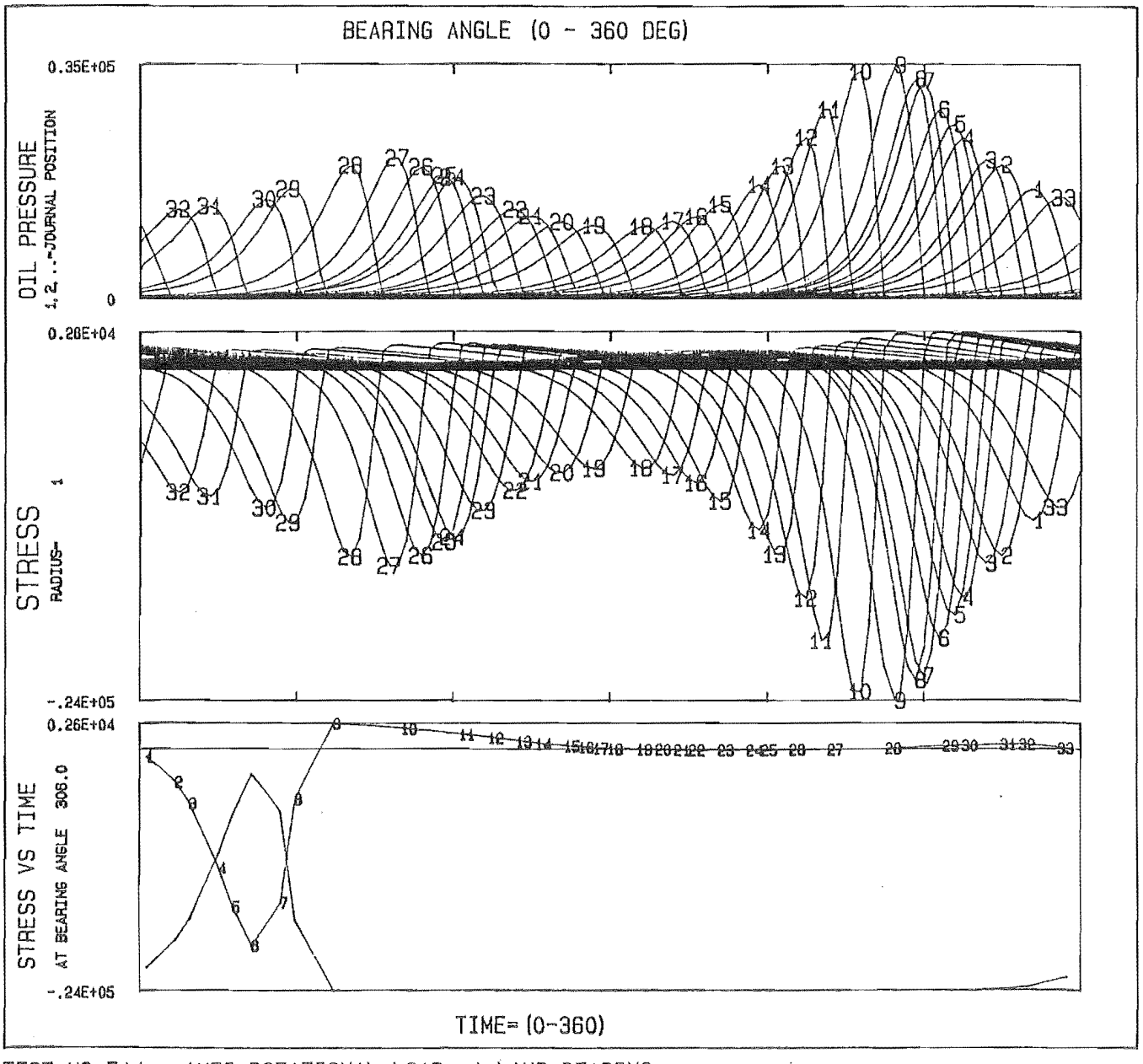

TEST NO 514 ANTI ROTATIONAL LOAD, 1 LAND BEARING

MAX STRESS = 0.262E+04 , AT ANGLE= 306.0

MIN STRESS = -0.245E+05 , AT ANGLE= 289.3 STRESS TYPE= TANGENTIAL

Fig. 5.19

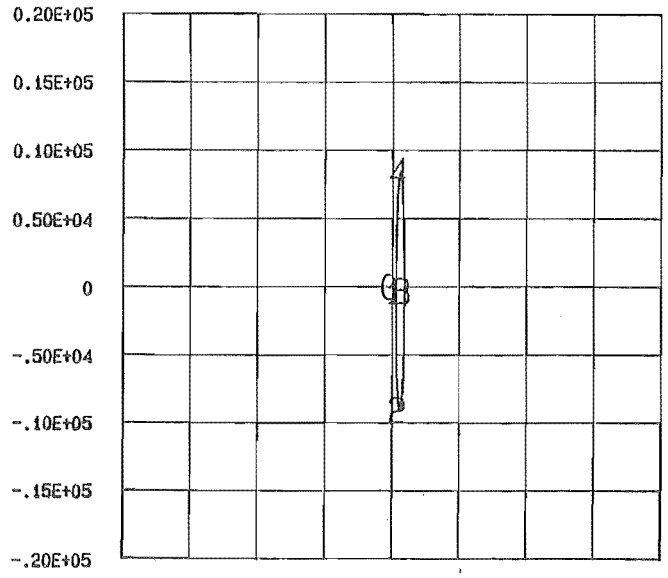

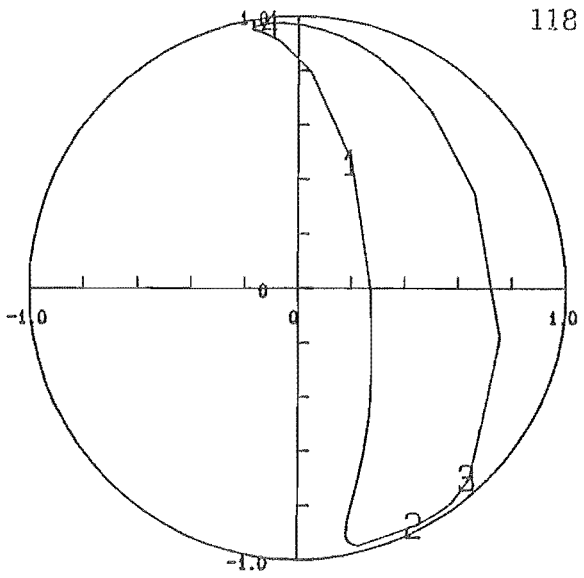

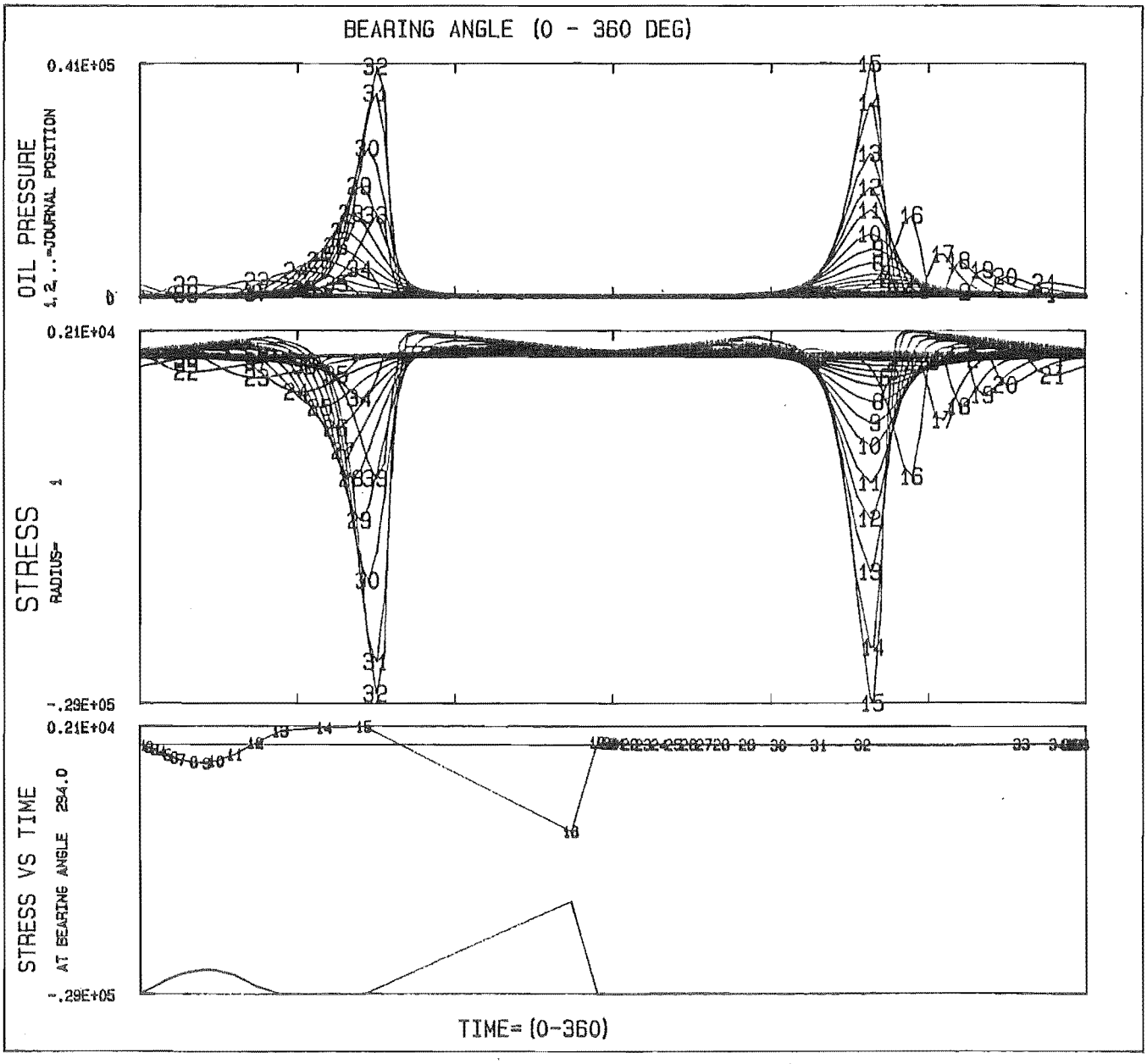

TEST NO 515 CO ROTATIONAL LOAD, 2 LAND BEARING

MAX STRESS = 0.207E+04 , AT ANGLE= 294.0

MIN STRESS = -0.289E+05 , AT ANGLE= 279.0 STRESS TYPE= TANGENTIAL

Fig. 5.20

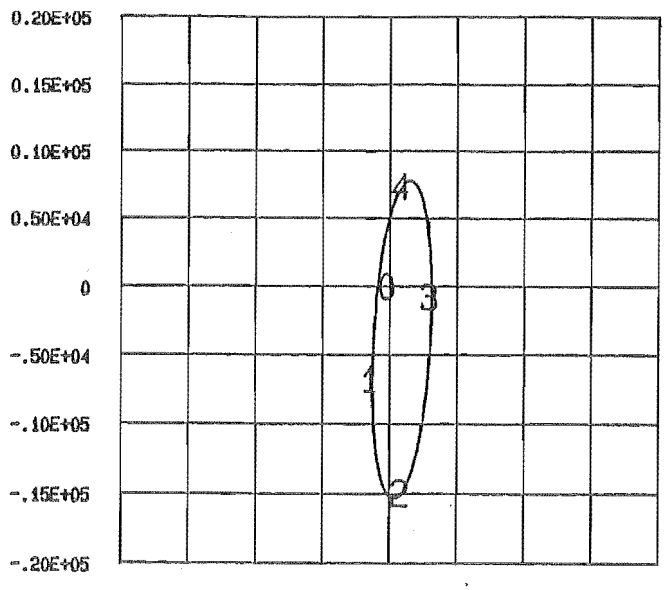

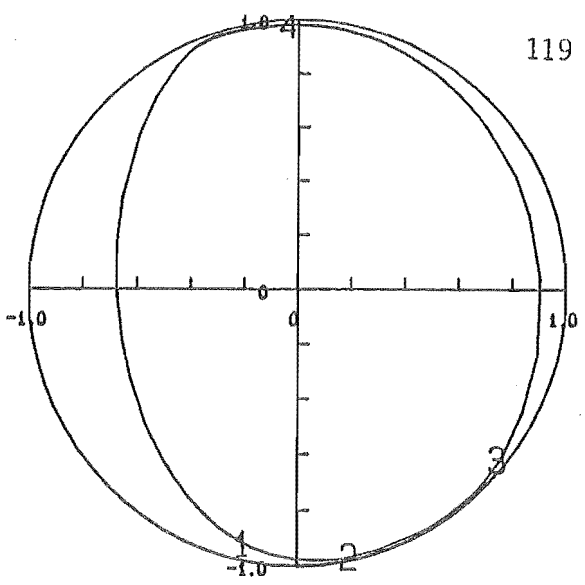

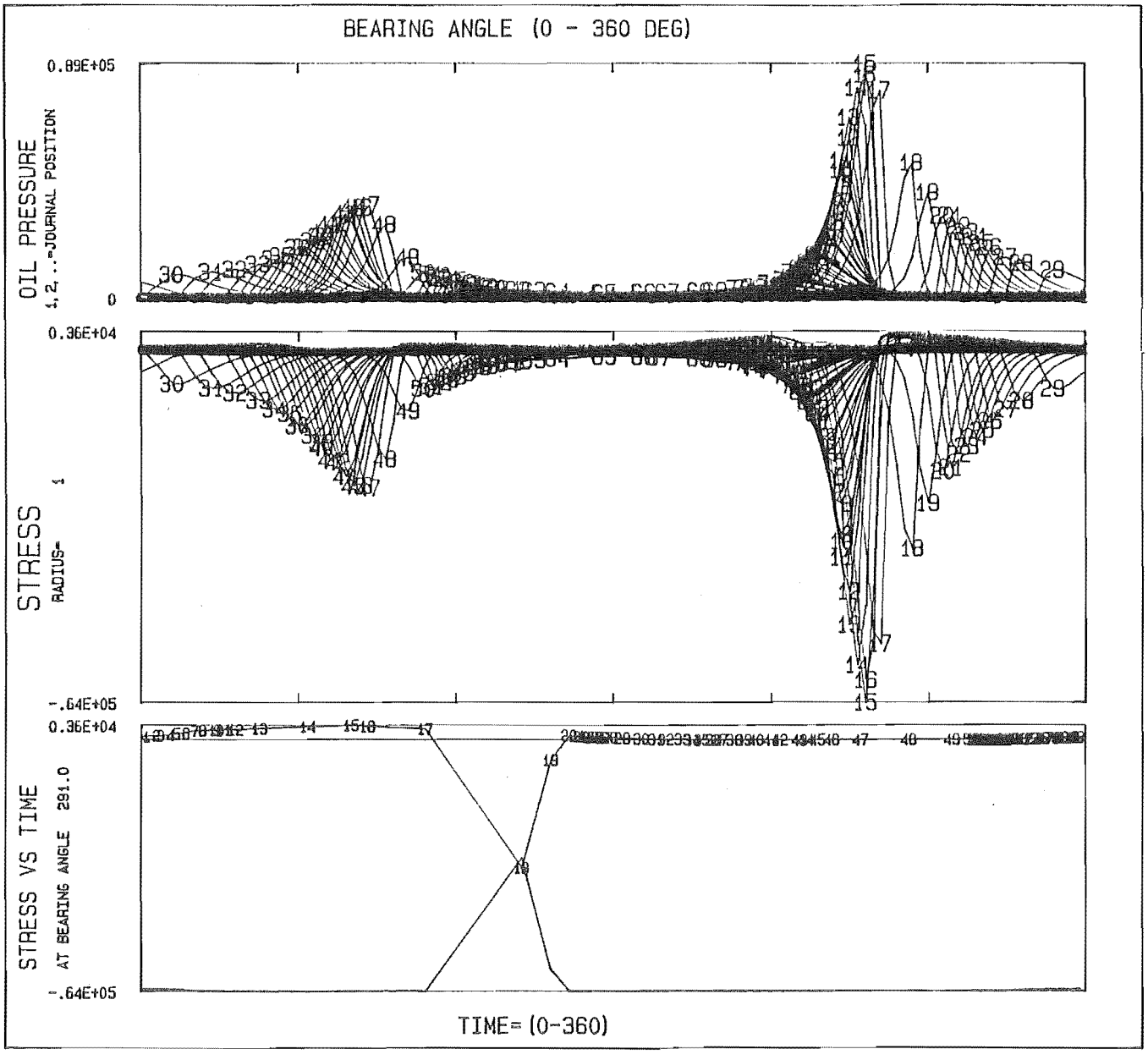

TEST NO 516 CO ROTATIONAL LOAD , 2 LAND BEARING

MAX STRESS = 0.361E+04 , AT ANGLE= 291.0

MIN STRESS = -0.637E+05 , AT ANGLE= 276.2 STRESS TYPE= TANGENTIAL

Fig 5.21

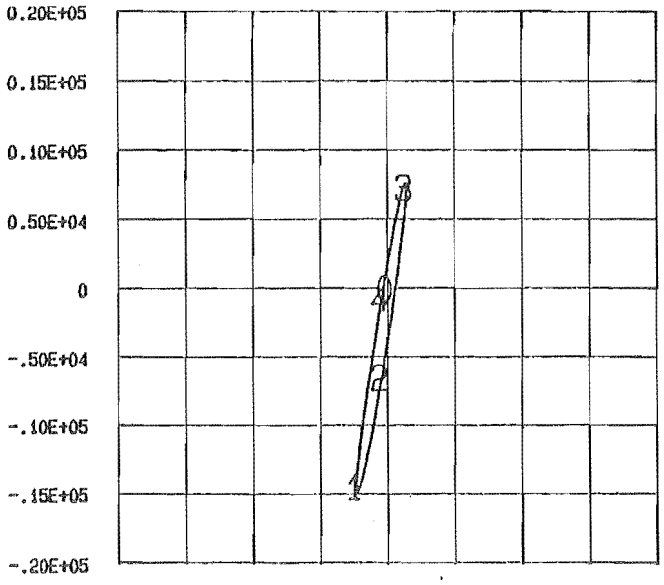

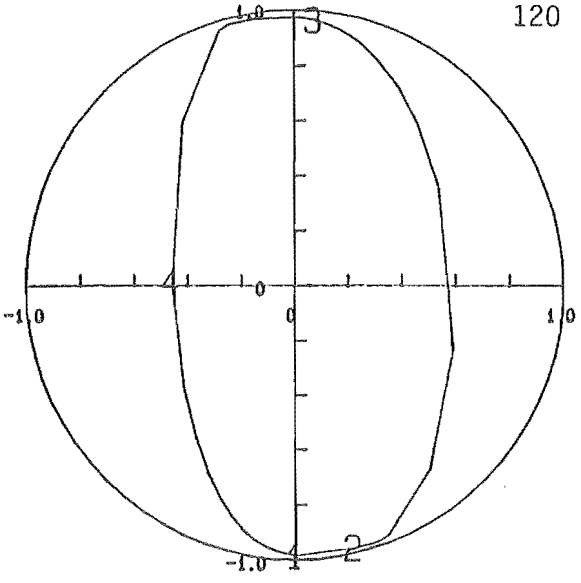

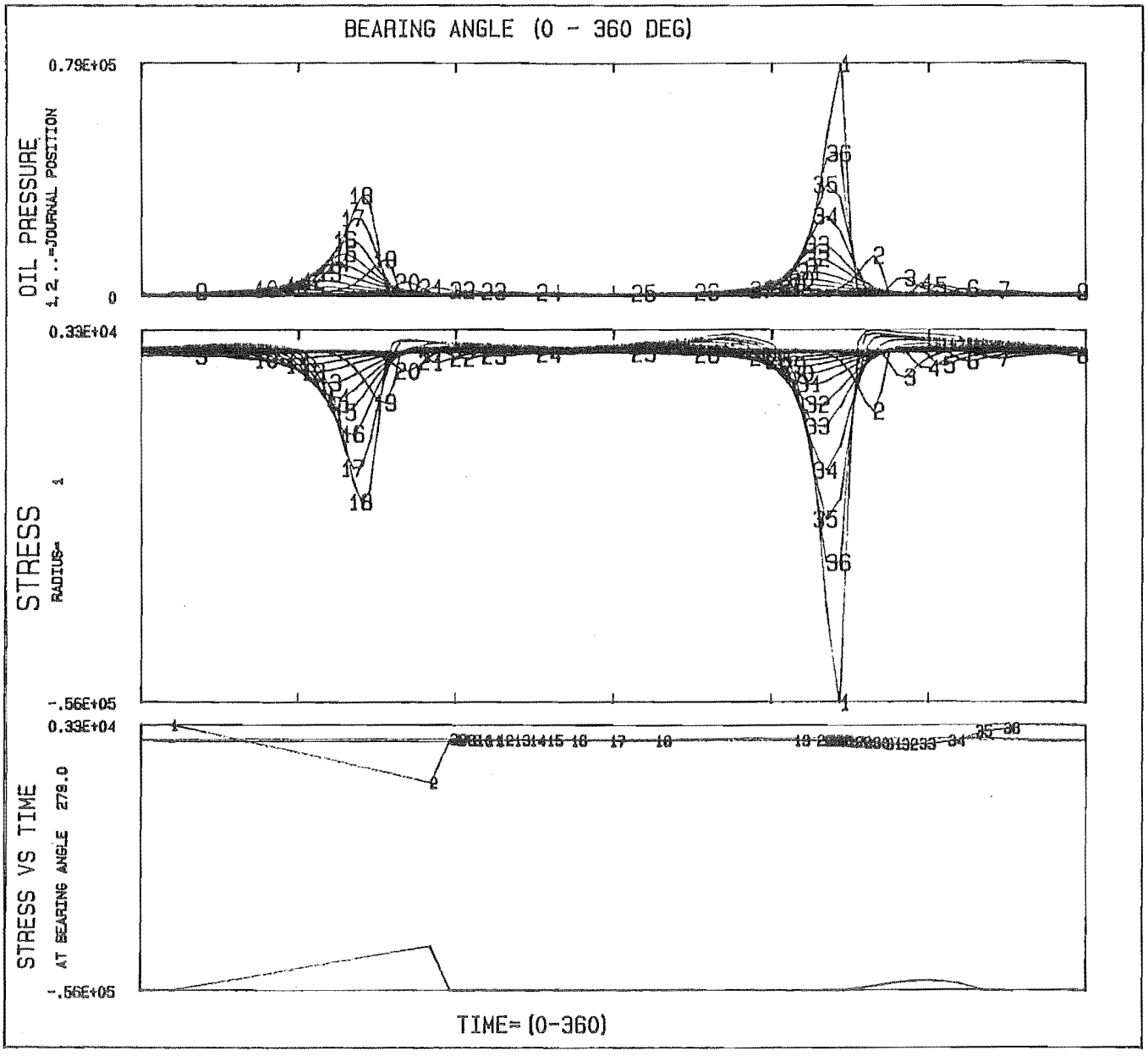

TEST NO 517 CO ROTATIONAL LOAD, 2 LAND BEARING

MAX STRESS = 0.335E+04 , AT ANGLE= 279.0

MIN STRESS =-0.562E+05 , AT ANGLE= 266.2 STRESS TYPE= TANGENTIAL

Fig 5.22

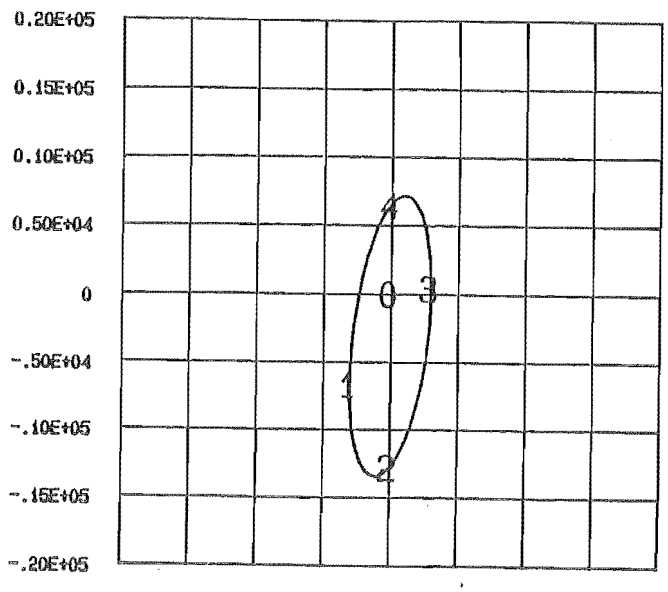

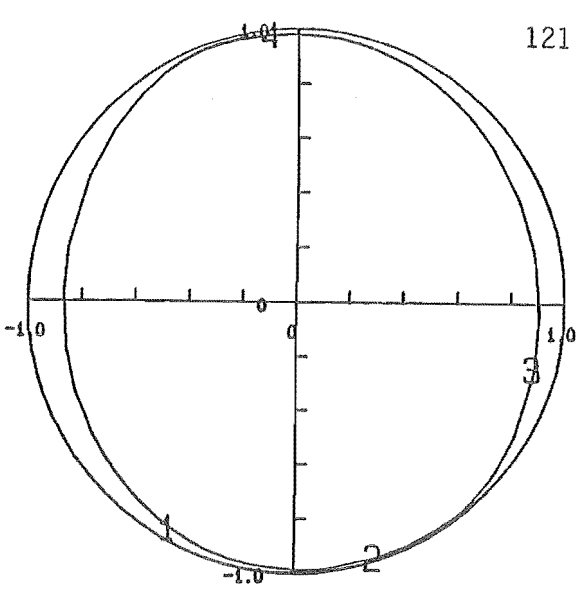

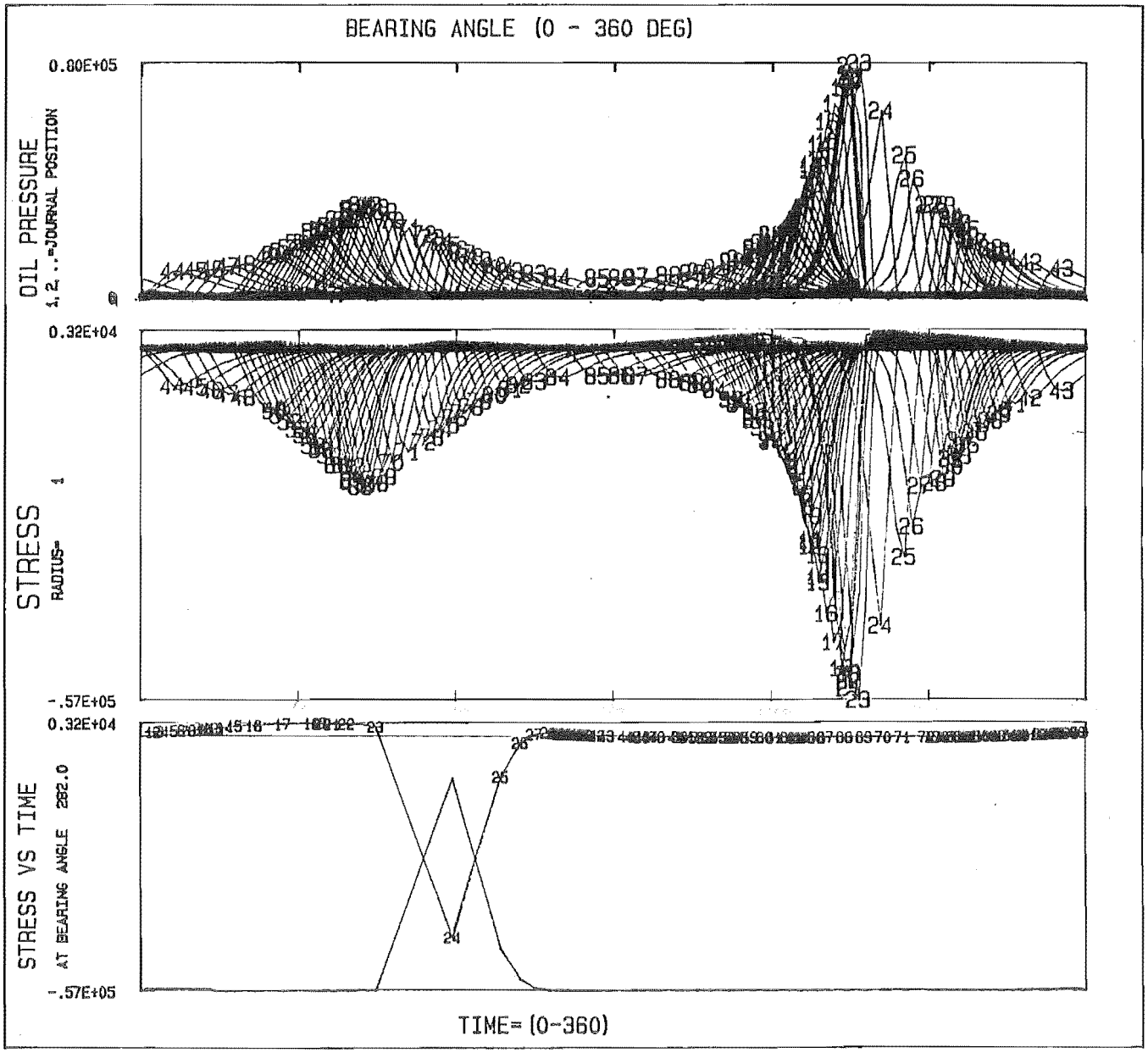

TEST NO 518 CO ROTATIONAL LOAD , 2 LAND BEARING

MAX STRESS = 0.316E+04 , AT ANGLE= 282.0

MIN STRESS = -0.569E+05 , AT ANGLE= 273.6 STRESS TYPE= TANGENTIAL

Fig.5.23

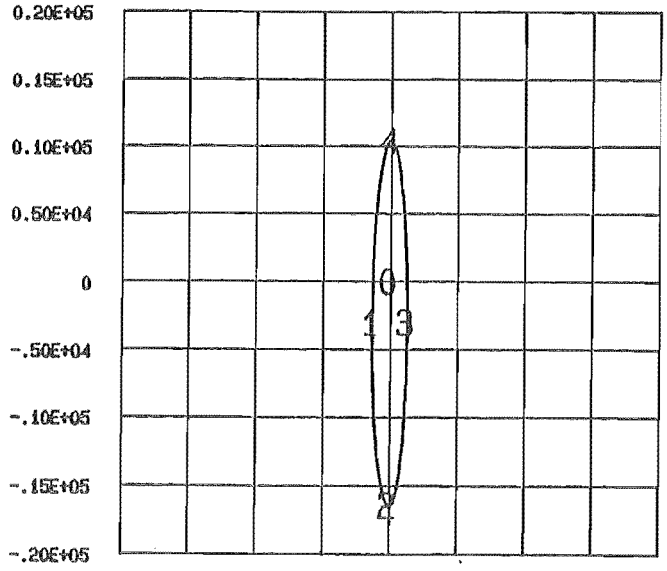

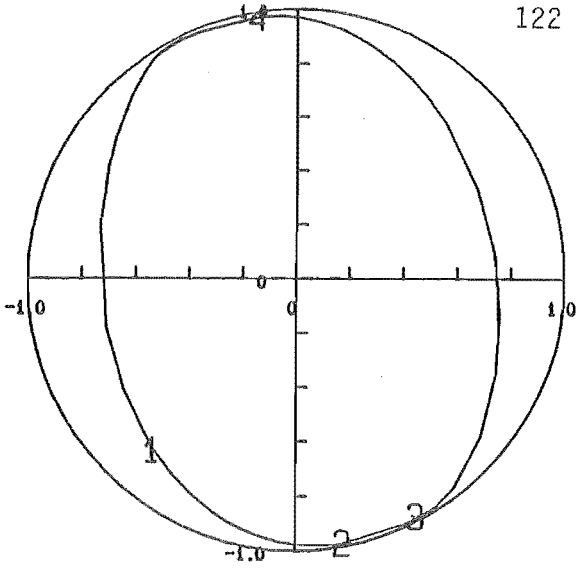

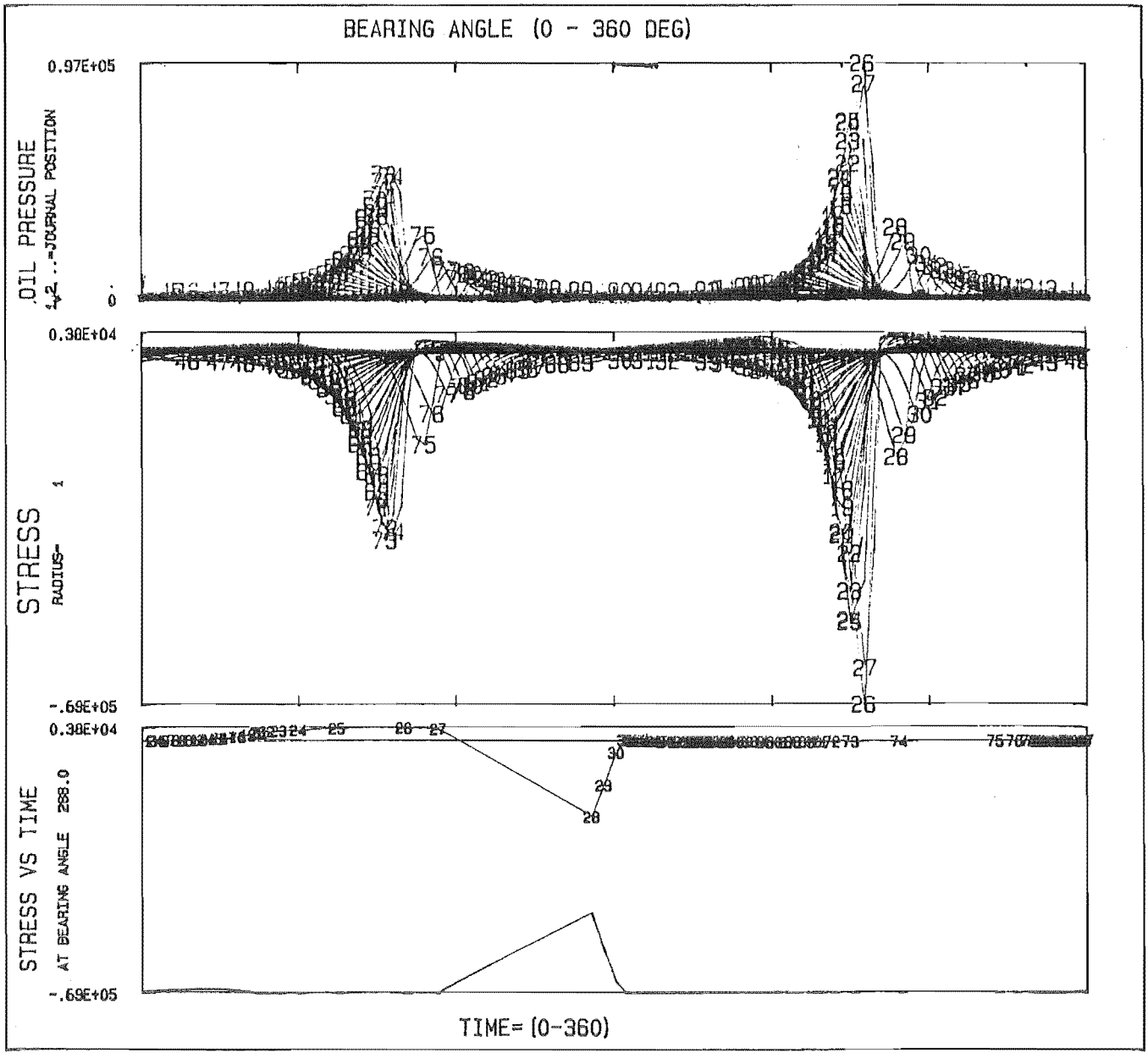

TEST NO 519 CO ROTATIONAL LOAD , 2 LAND BEARING

MAX STRESS = 0.379E+04 , AT ANGLE= 288.0

MIN STRESS = -0.692E+05 , AT ANGLE= 275.4 STRESS TYPE= TANGENTIAL

Fig 5.24

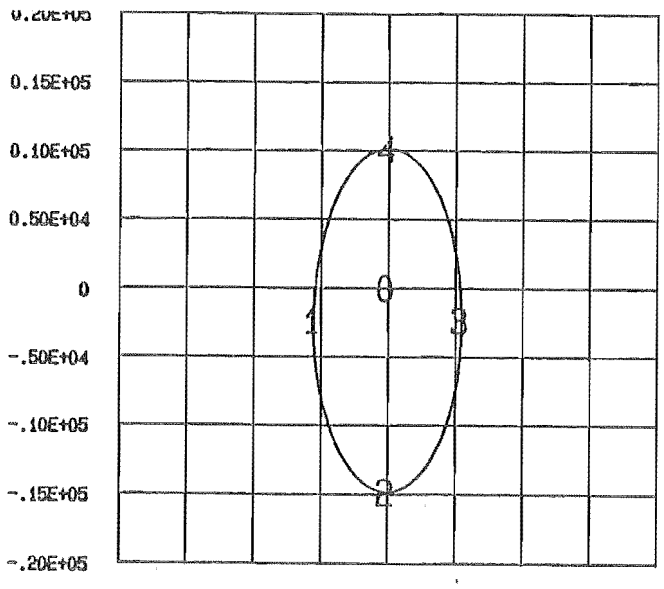

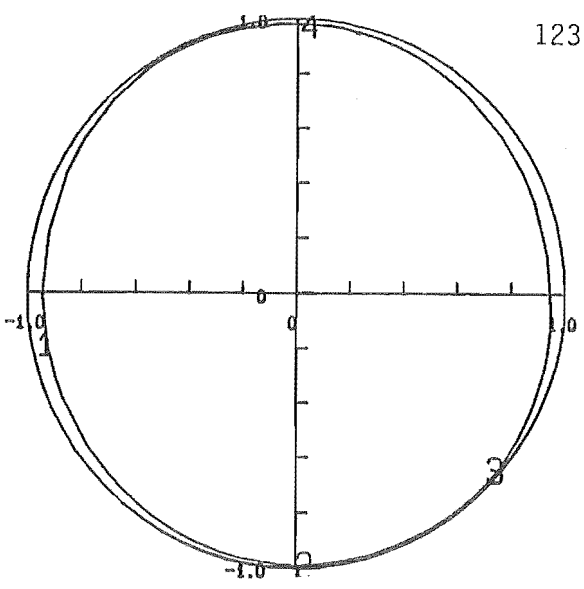

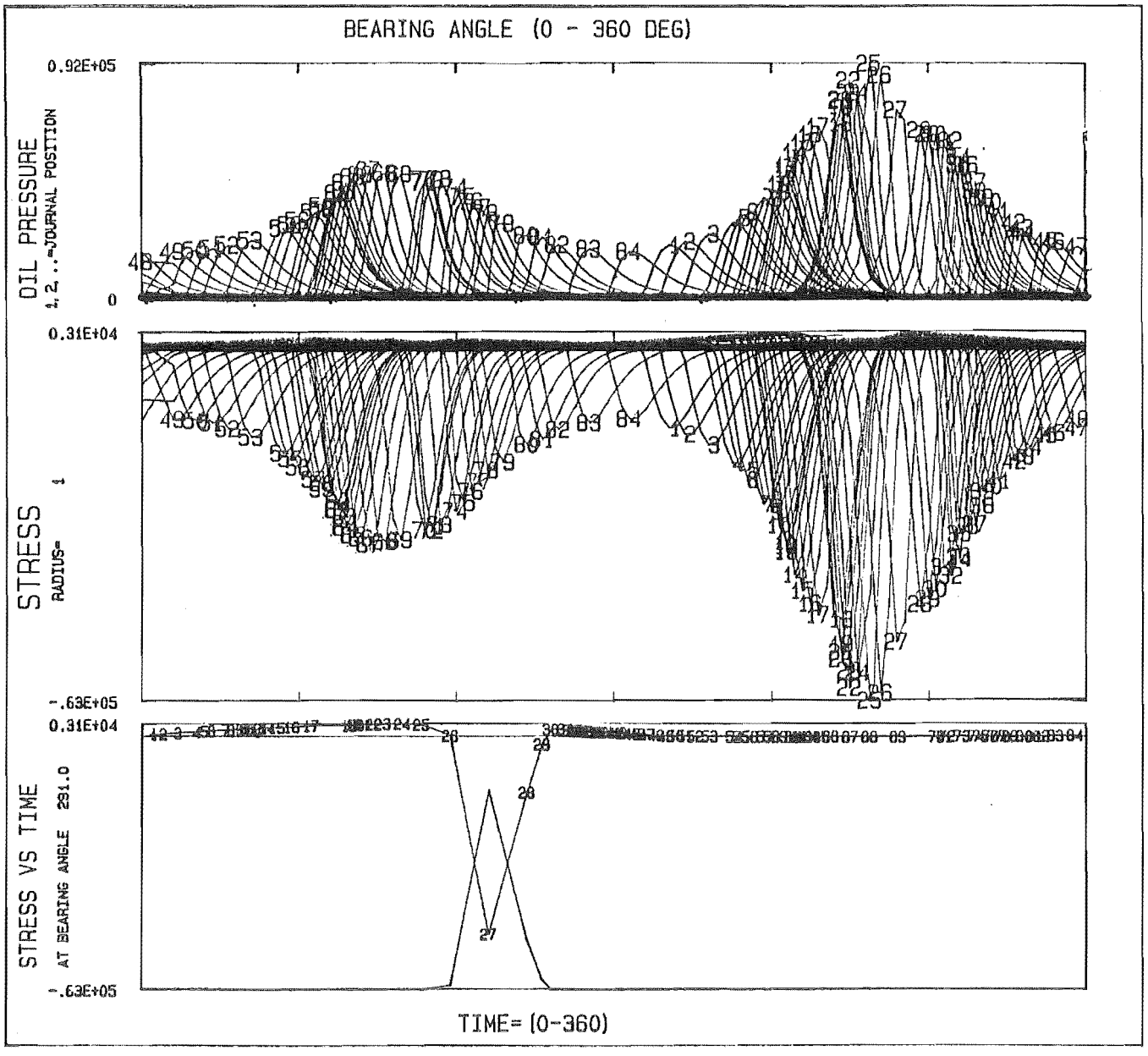

TEST NO 520 CO ROTATIONAL LOAD , 2 LAND BEARING

MAX STRESS = 0.312E+04 , AT ANGLE= 291.0

MIN STRESS = -0.631E+05 , AT ANGLE= 277.7 STRESS TYPE= TANGENTIAL

Fig525

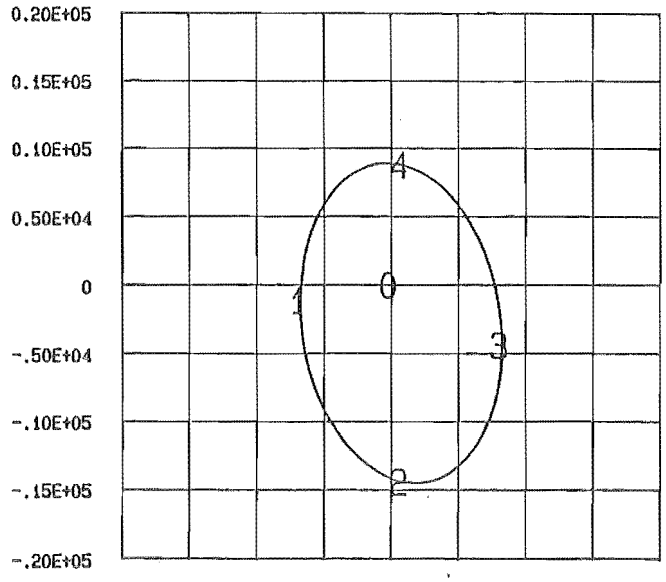

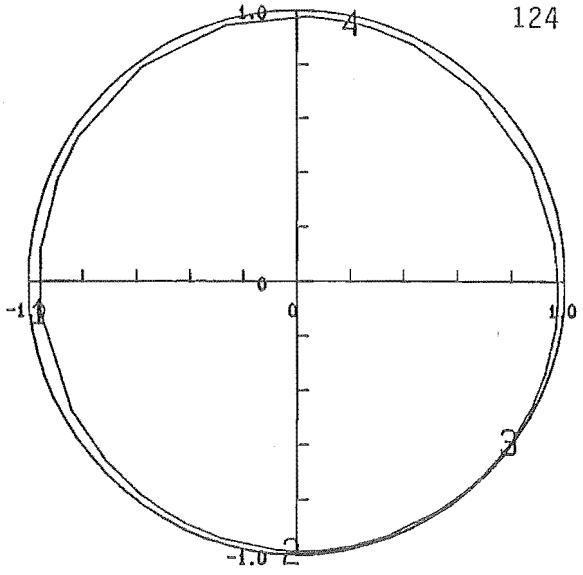

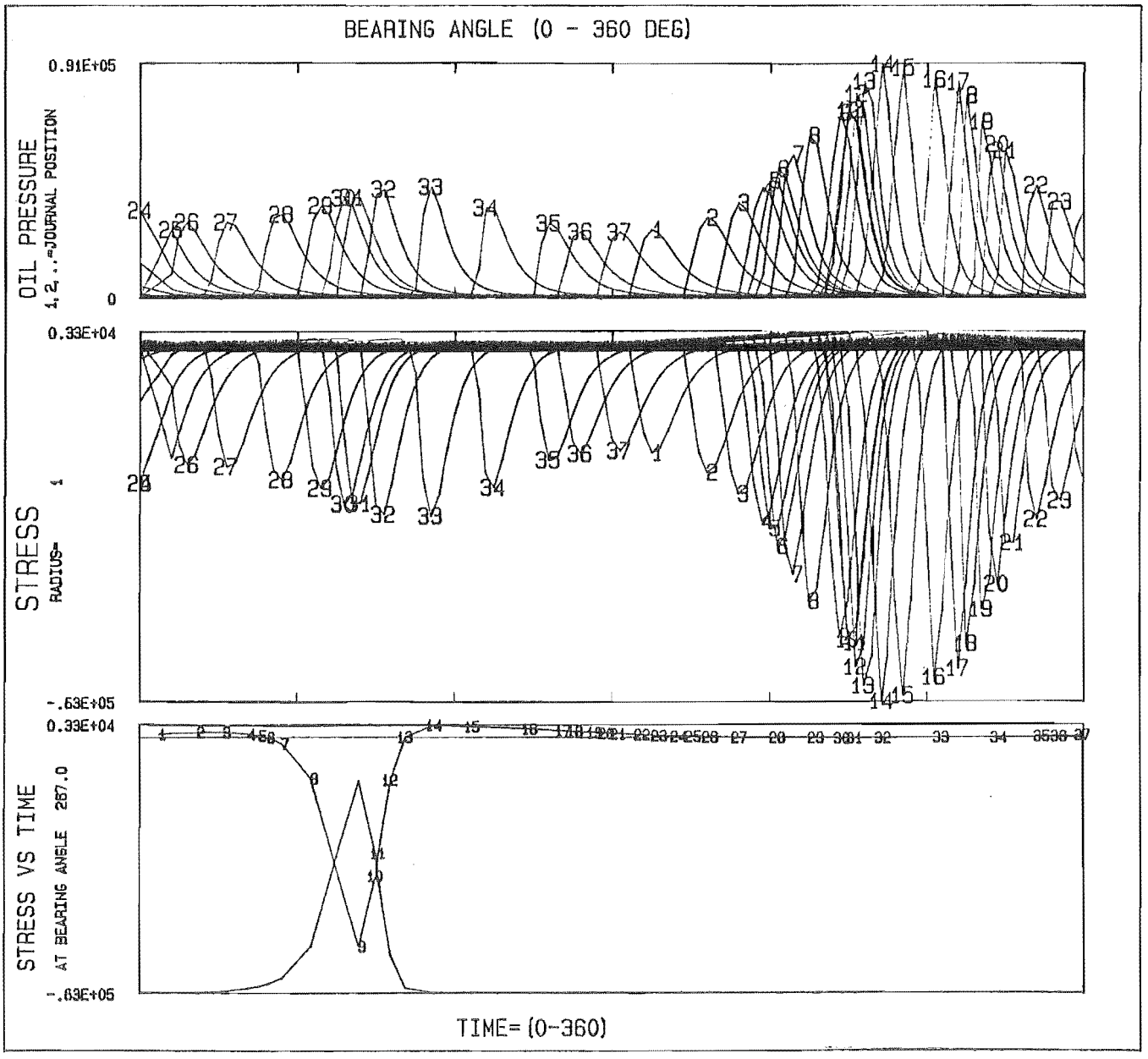

TEST NO 521 CO ROTATIONAL LOAD, 2 LAND BEARING

MAX STRESS = 0.327E+04 , AT ANGLE= 267.0

MIN STRESS = -0.629E+05 , AT ANGLE= 283.0 STRESS TYPE= TANGENTIAL

Fig. 526

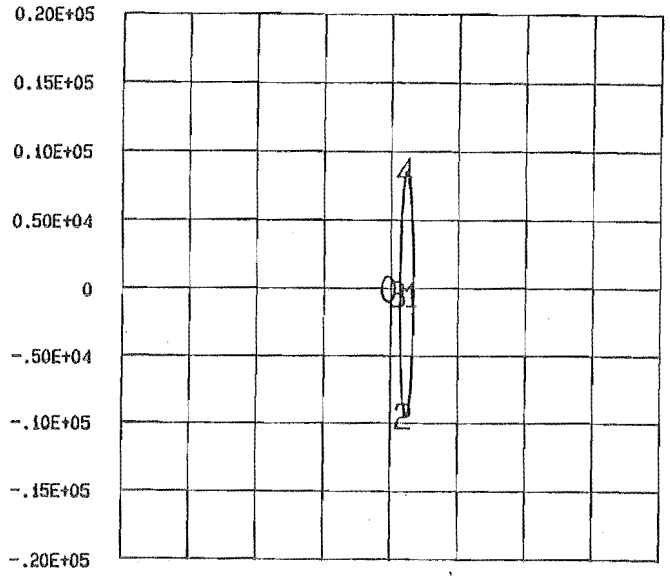

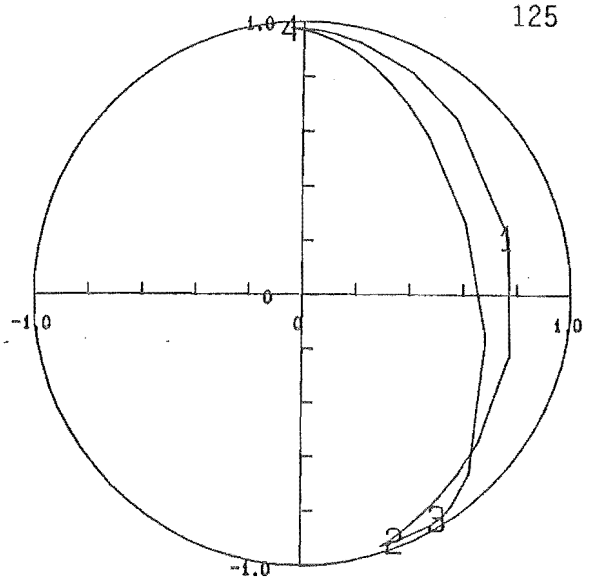

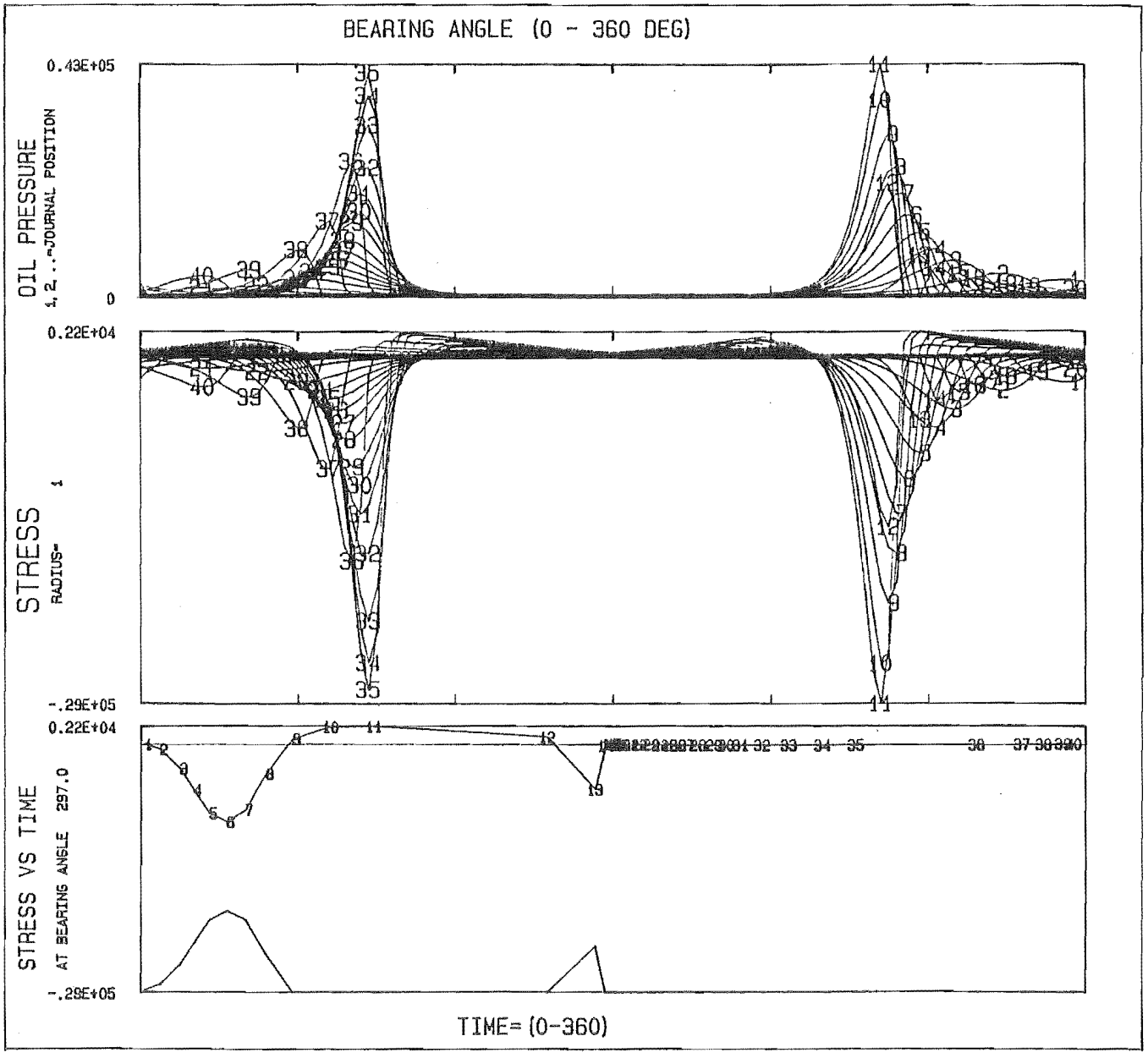

TEST NO 522 ANTI ROTATIONAL LOAD, 2 LAND BEARING

MAX STRESS = 0.216E+04 , AT ANGLE= 297.0

MIN STRESS = -0.295E+05 , AT ANGLE= 282.1 STRESS TYPE= TANGENTIAL

Fig.527

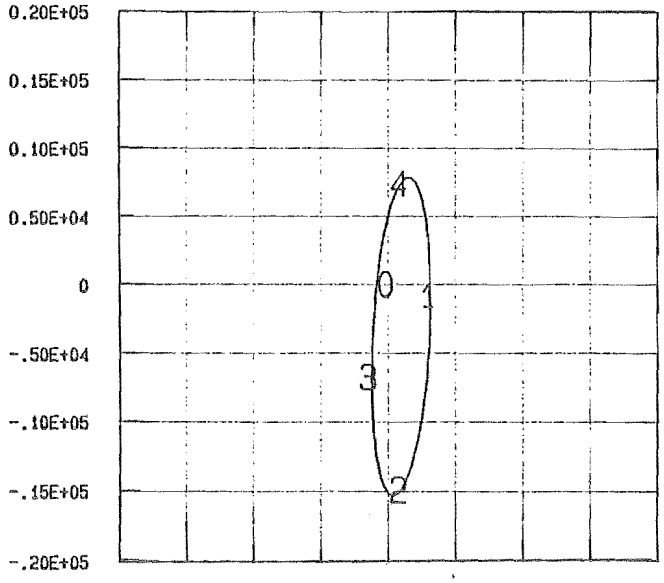

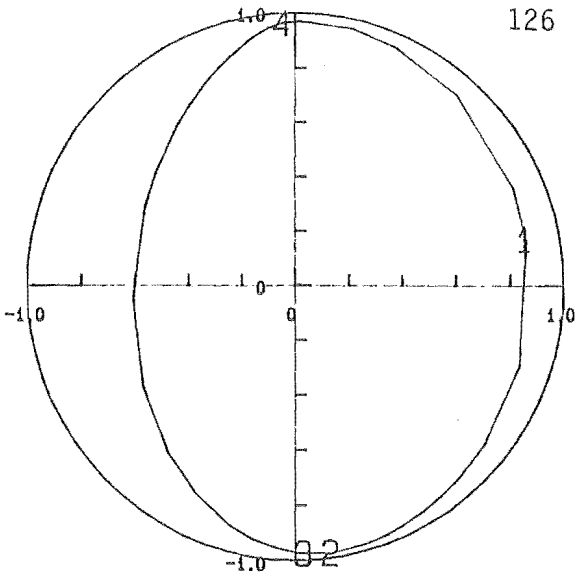

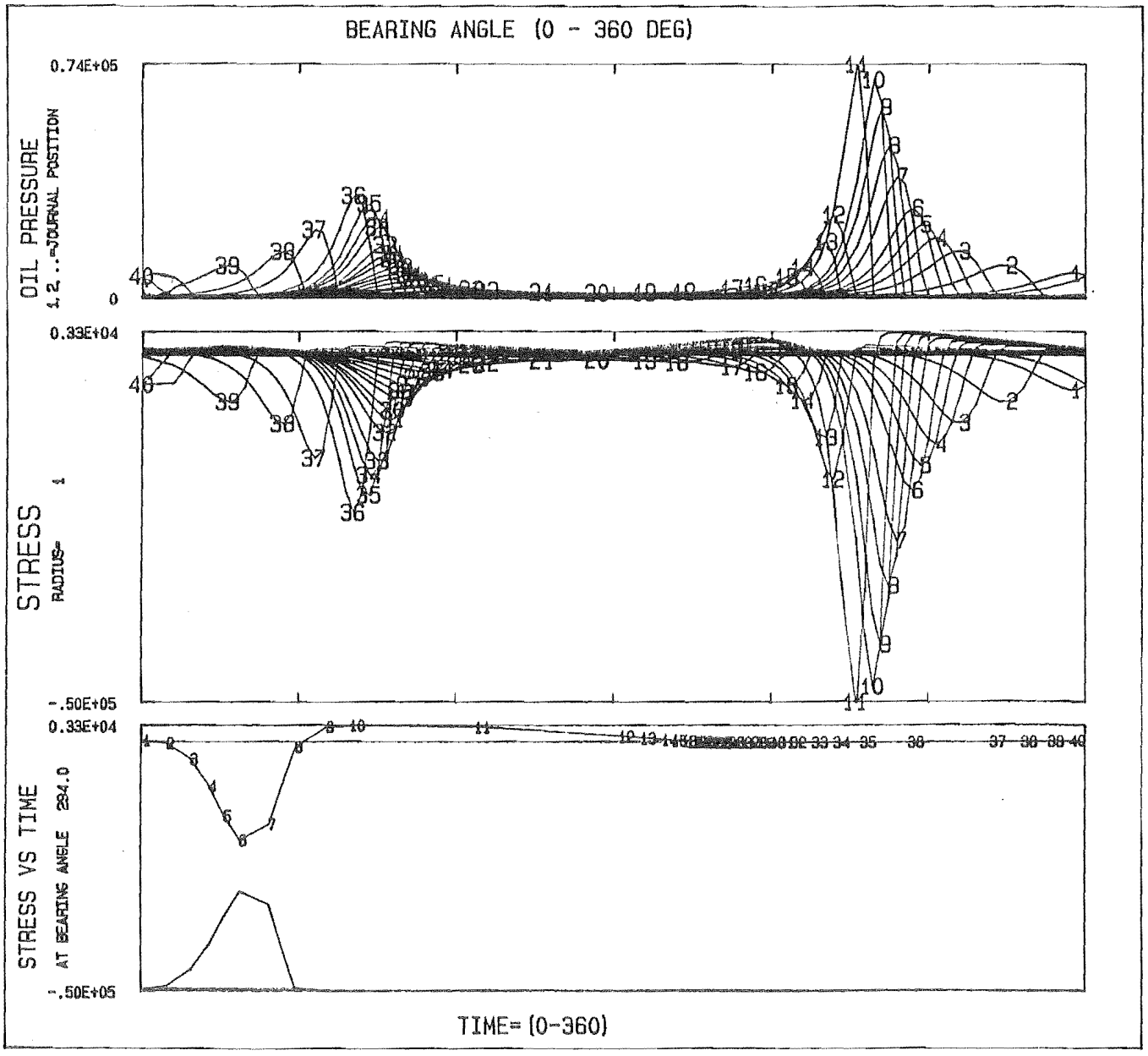

TEST NO 523 ANTI ROTATIONAL LOAD, 2 LAND BEARING

MAX STRESS = 0.327E+04 , AT ANGLE= 294.0

MIN STRESS = -0.500E+05 , AT ANGLE= 272.5 STRESS TYPE= TANGENTIAL

Fig. 5.28

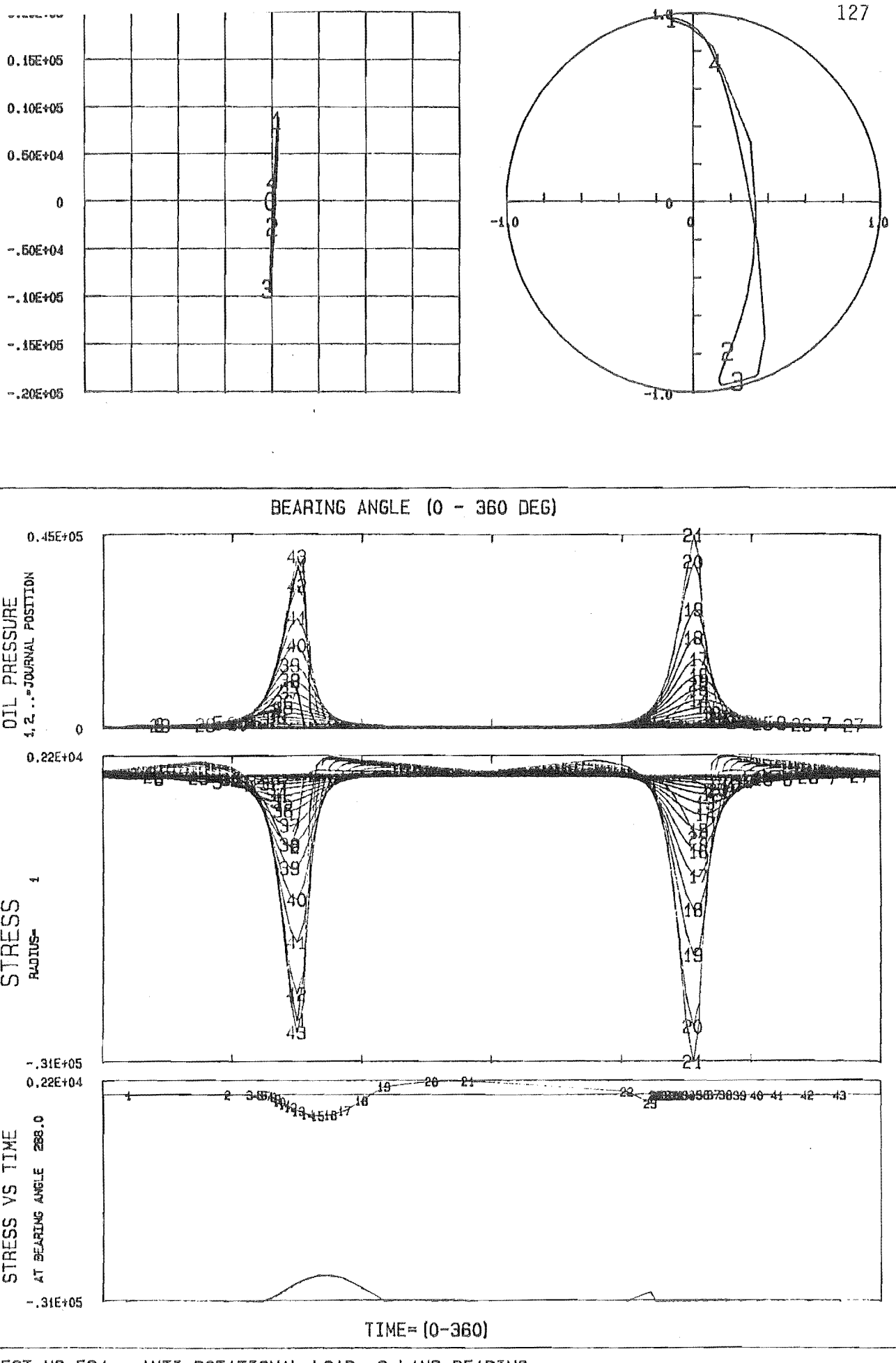

TEST NO 524 ANTI ROTATIONAL LOAD, 2 LAND BEARING

MAX STRESS = 0.215E+04 , AT ANGLE= 288.0

MIN STRESS = -0.312E+05 , AT ANGLE= 273.4 STRESS TYPE= TANGENTIAL

Fig. 5.29

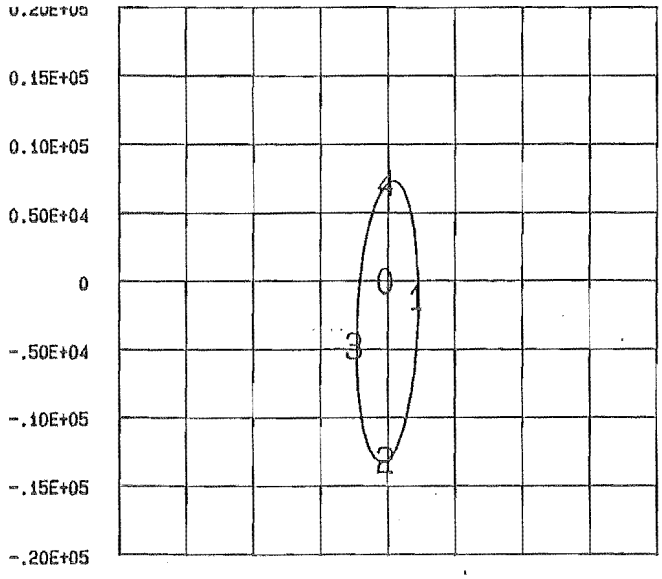

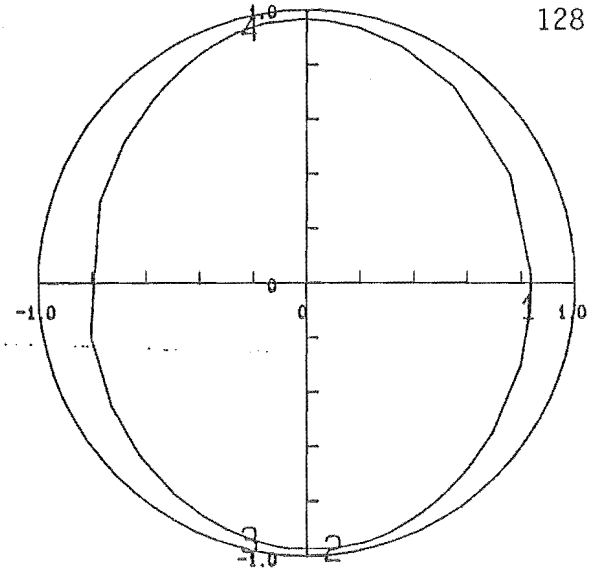

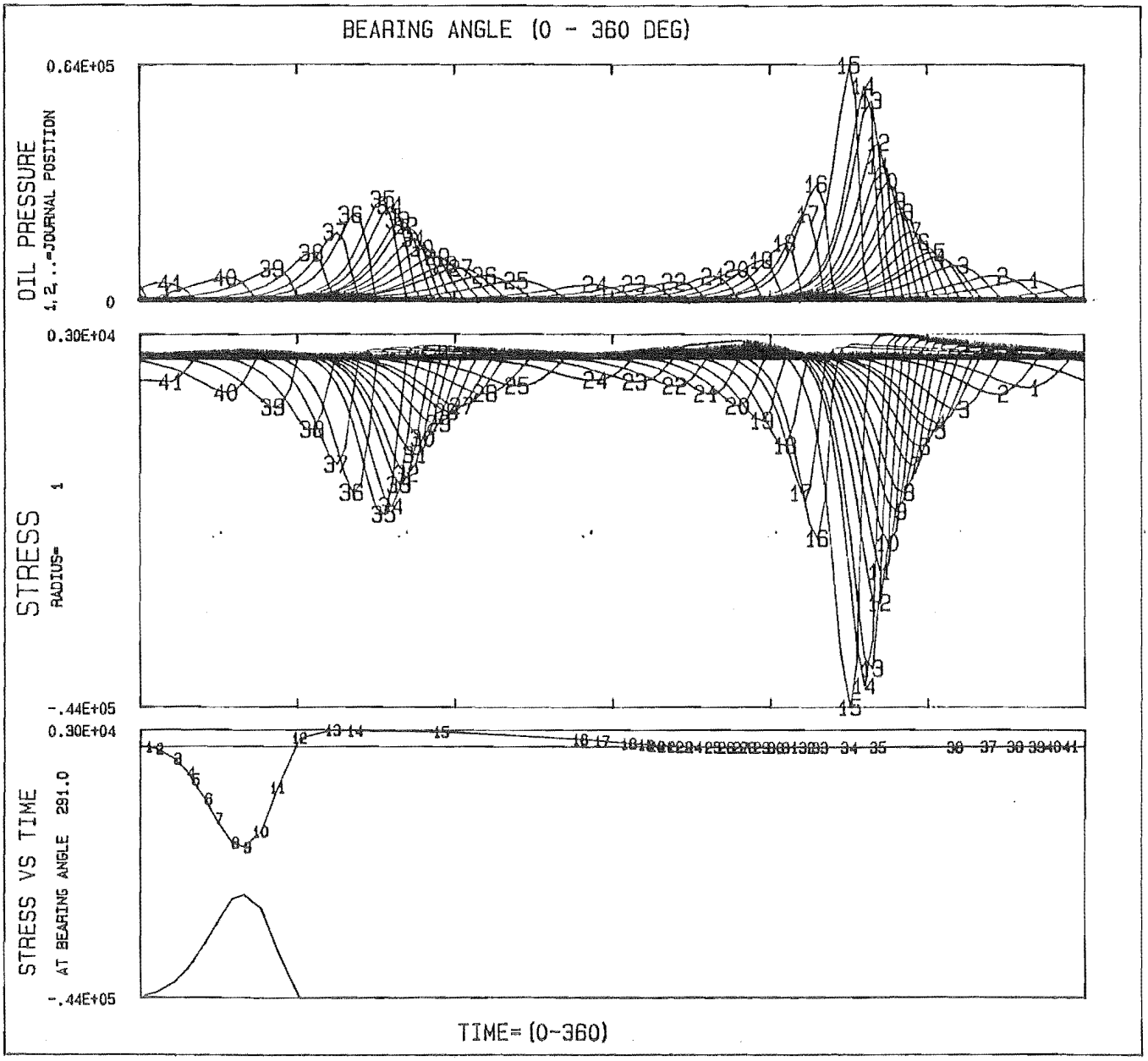

TEST NO 525 ANTI ROTATIONAL LOAD, 2 LAND BEARING

MAX STRESS = 0.296E+04 , AT ANGLE= 291.0

MIN STRESS = -0.437E+05 , AT ANGLE= 270.7 STRESS TYPE= TANGENTIAL

Fig 530

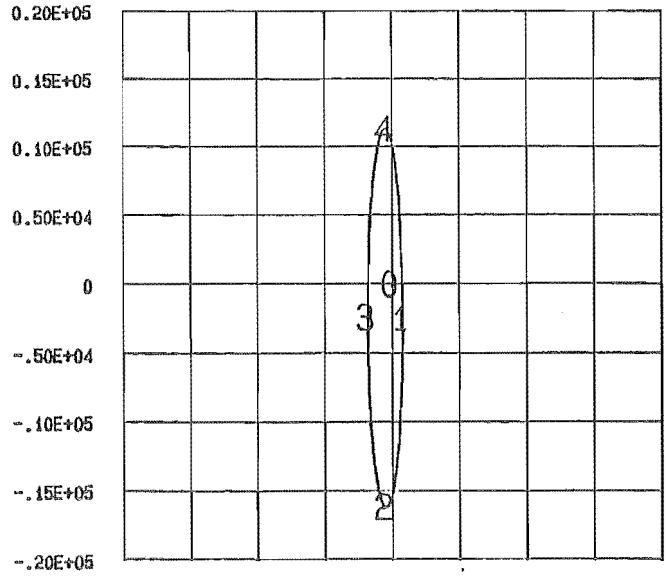

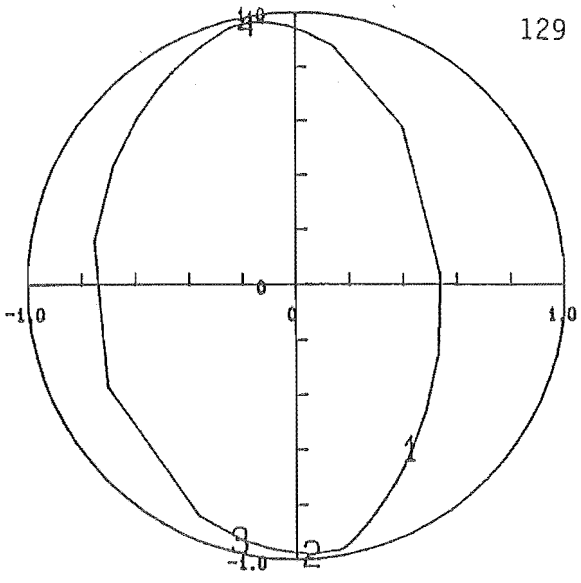

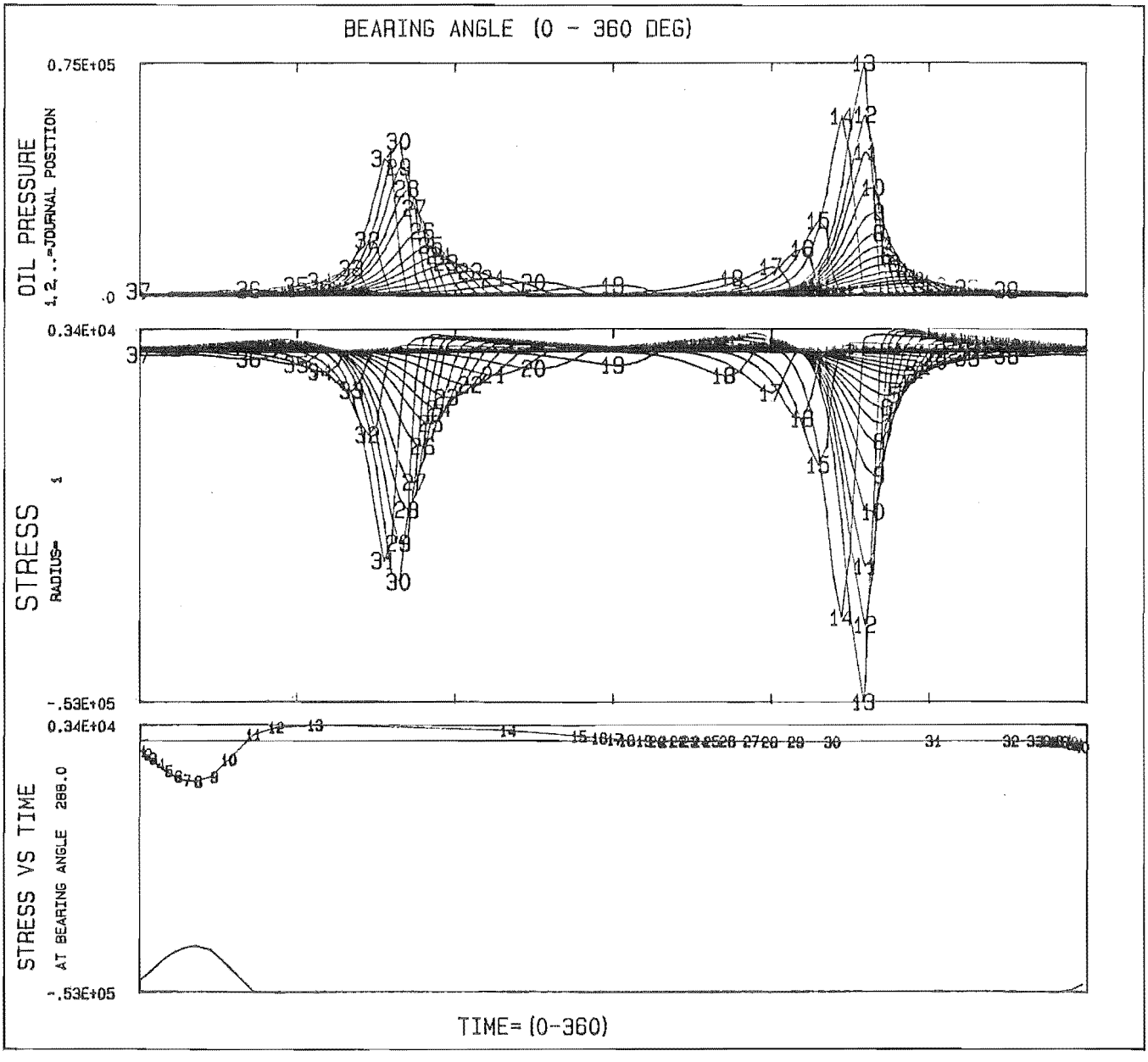

TEST NO 526 ANTI ROTATIONAL LOAD, 2 LAND BEARING

MAX STRESS = 0.339E+04 , AT ANGLE= 288.0

MIN STRESS = -0.533E+05 , AT ANGLE= 275.3 STRESS TYPE= TANGENTIAL

Fig 5.31

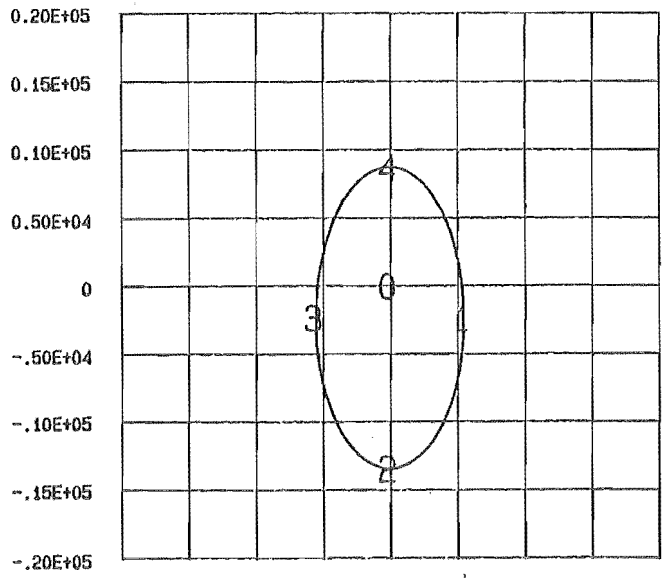

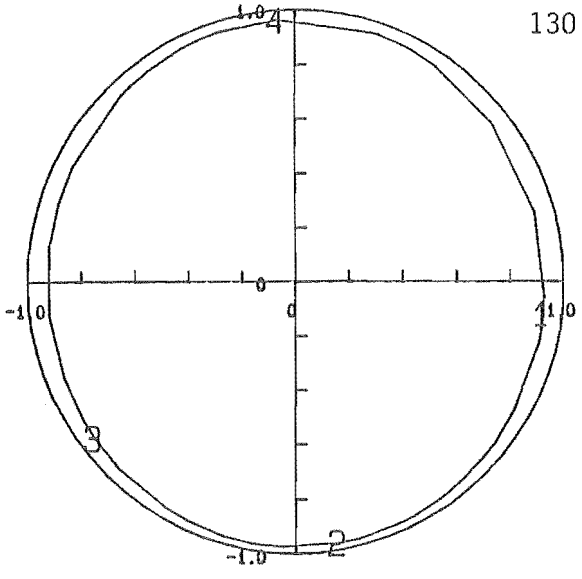

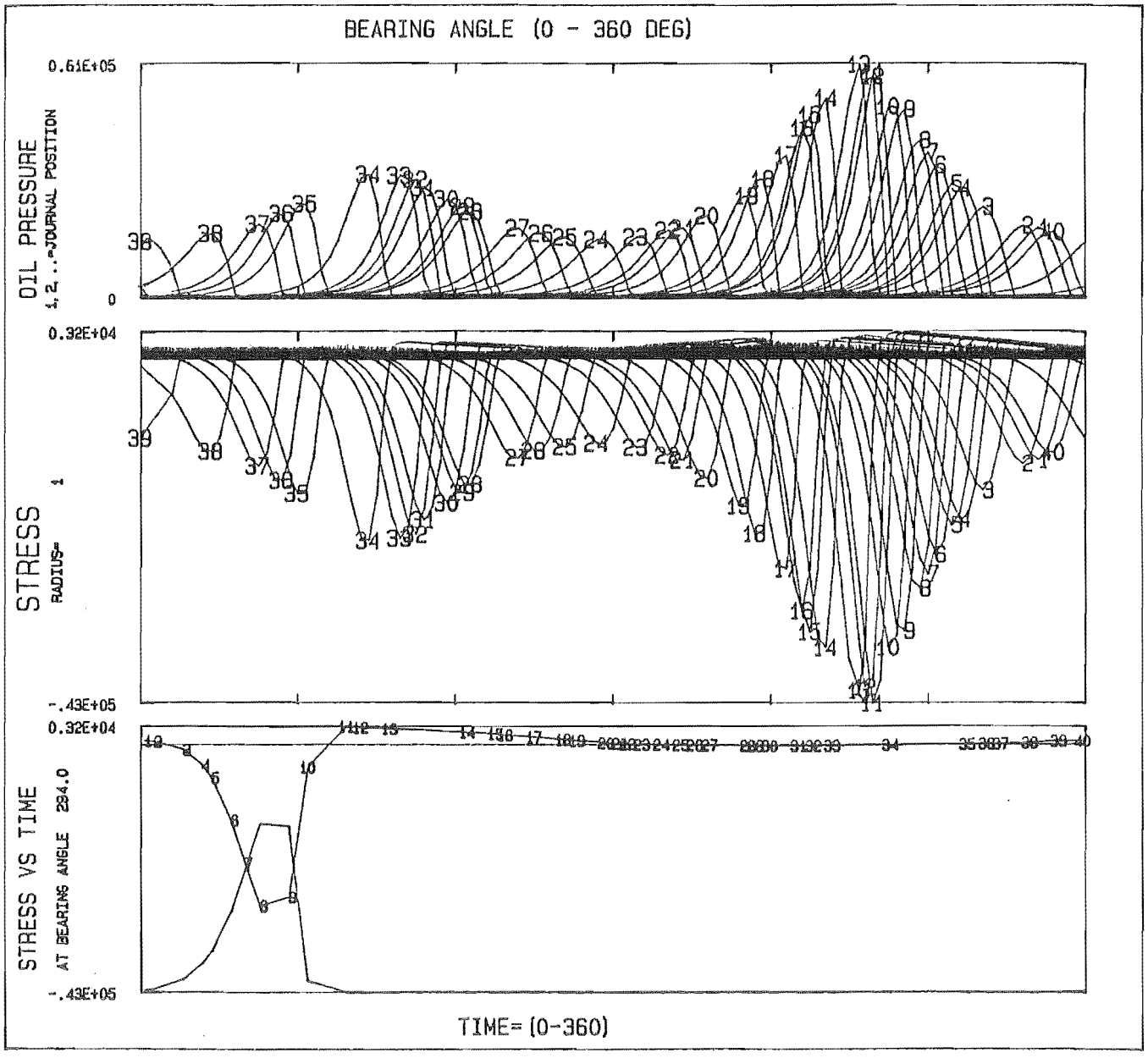

TEST NO 527 ANTI ROTATIONAL LOAD, 2 LAND BEARING

MAX STRESS = 0.318E+04 , AT ANGLE= 294.0

MIN STRESS = -0.430E+05 , AT ANGLE= 279.0 STRESS TYPE= TANGENTIAL

Fig 5.32

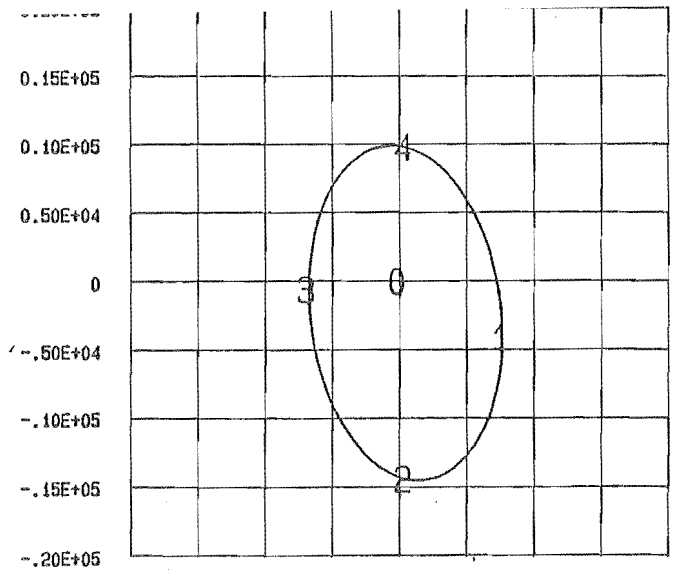

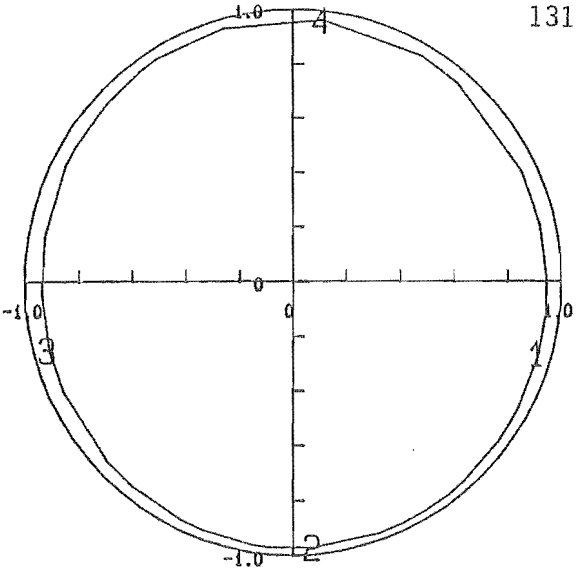

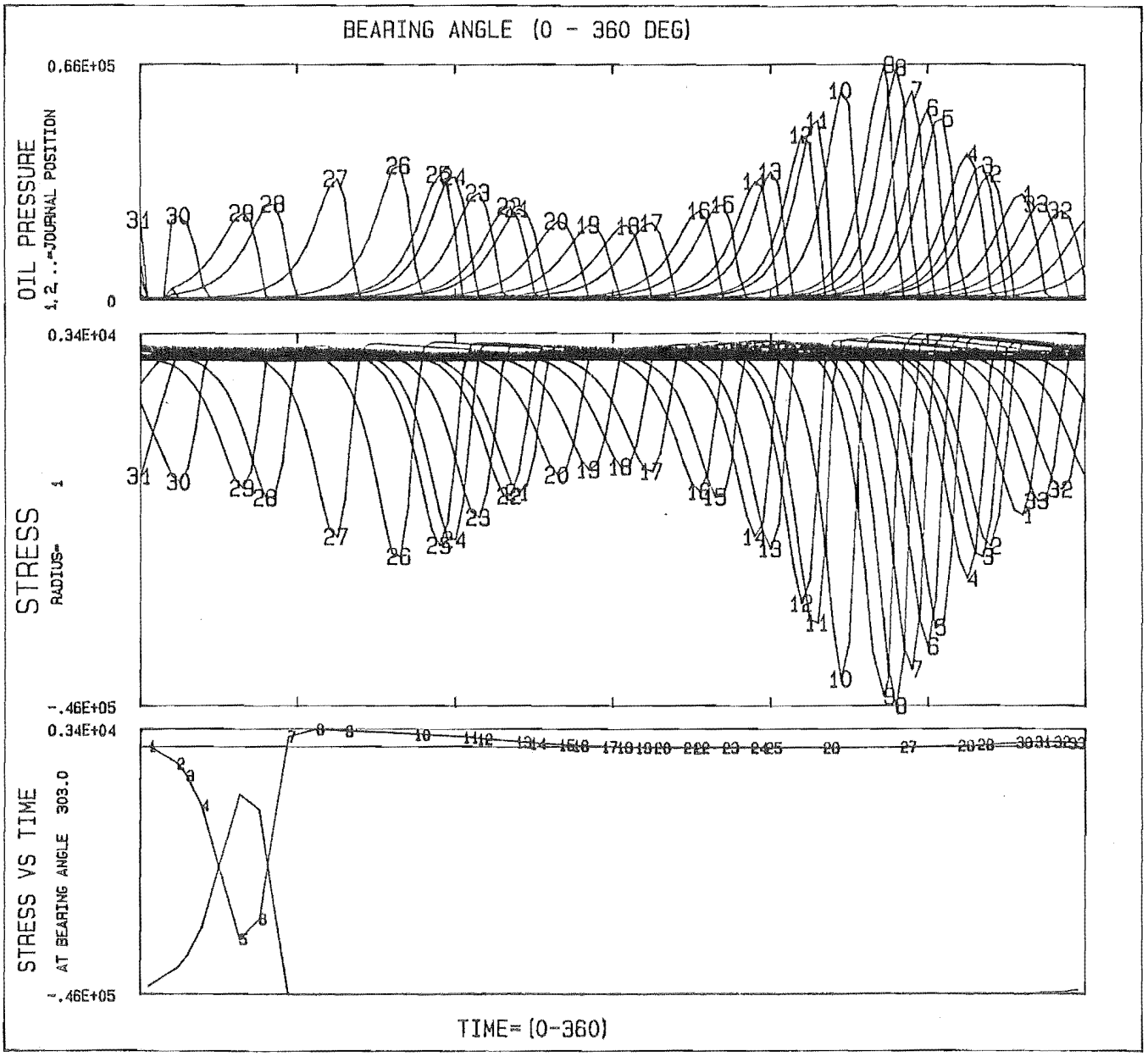

TEST NO 528 ANTI ROTATIONAL LOAD, 2 LAND BEARING

MAX STRESS = 0.338E+04 , AT ANGLE= 303.0

MIN STRESS = -0.464E+05 , AT ANGLE= 288.0 STRESS TYPE= TANGENTIAL

Fig.533

5.2 GYDE'S EXPERIMENTS, INPUT DATA

5.2.1 Gyde's Experiments

Gyde [2] used a different type of equipment for testing his bearings. The machine which he used was designed by himself and its working principle, shown in Fig. 5.34, was simpler than the one used by Blundell, but it was restricted to exerting the dynamic load on one axis only. The machine consisted of two 2.7527" diameter steel shafts (3), (4) each supported on two bearings (6) held in rigid housings. The two test bearings (1) which were also held in rigid housings and connected by the rod (2) were located half–way between the supporting bearings. The two adjustable and unbalanced masses (5) rotated with the shaft, creating different magnitude of centrifugal forces. The horizontal components of these forces were taken up by the prestressed steel strips (7) and their vertical components transmit a sinusoidal load on the test bearings. The constant spring force (F) is transmitted to the test bearings, applying a mean load on them. Figs. 4.18, 4.19 show how the above static and dynamic loads may be combined to produce four different load patterns. The bearings had a circumferential oil groove in their "top" half. The "bottom" half, which carried most of the load, was plain. Gyde selected different combinations of mean and alternating loads in testing his bearings. Each test was performed for 10^7 cycles, after which the bearing was inspected for possible failure. He then made the plot, Fig. 5.36, of failed and unfailed bearings (marked with crosses and circles respectively) with respect to the applied mean, maximum and minimum loads divided by the projected area of the bearing as shown in Fig. 5.35. Gyde's experiment was aimed at determining a boundary on that plot between failed and good bearings.

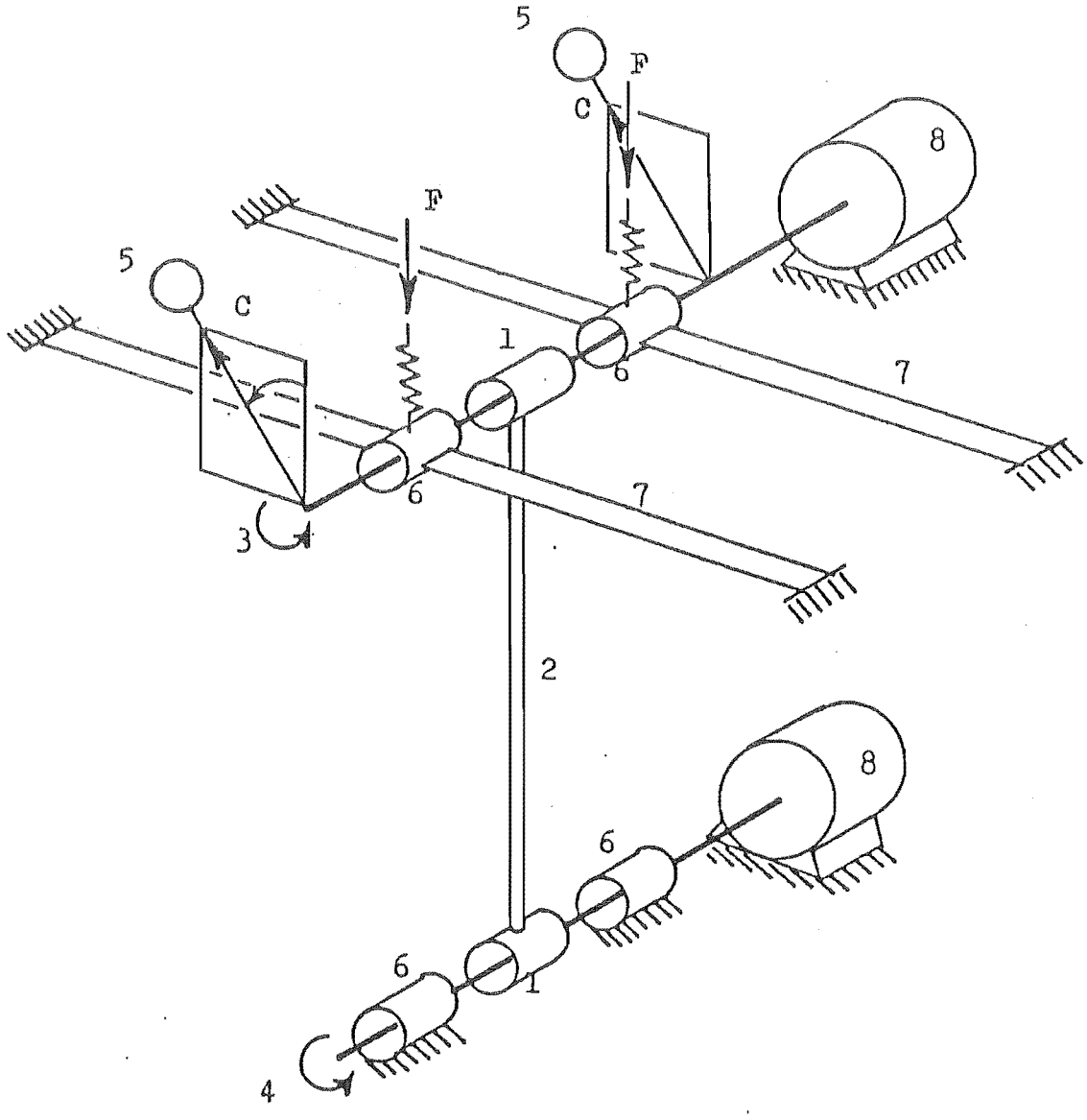

Sketch showing working principle of the Bearing Test Machine (after Gyde [2])

Legend: F Static load, C Dynamic load amplitude. 1) Test bearing, 2) Con rod, 3) Upper shaft, 4) Lower shaft, 5) Unbalanced mass creating centrifugal force C. The vertical component of C puts load on the test bearing. 6) Supporting bearing, 7) Prestressed steel strip perpendicular to the con rod. The strip takes up the horizontal component of C). 8) Electric motor (5 to 8 BHP).

Fig.5.34

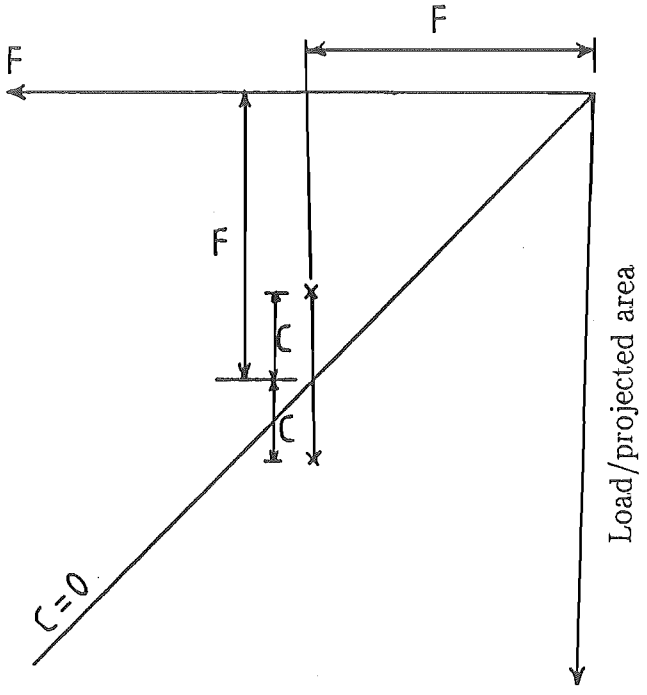

C = load amplitude/projected area

F = mean load/projected area

Fig.5.35

Allowable dynamic component and max. bearing load as a function of the mean bearing load. (after Gyde [2])

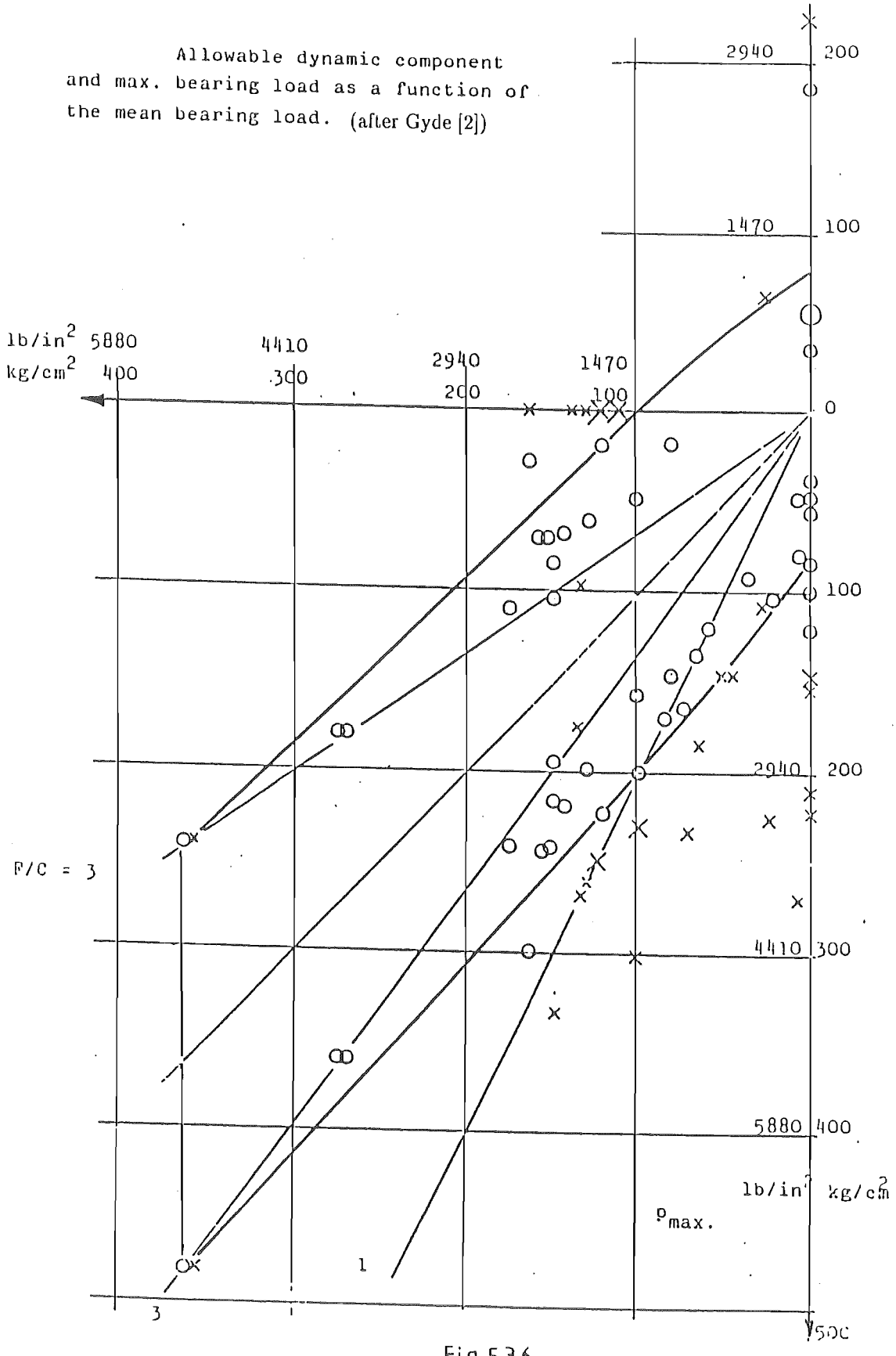

Fig. 5.36

5.2.2 Input Data

For the numerical reconstruction of Gyde's experiment, different points on his plot (Fig. 5.36) were numbered according to Fig. 5.37. The first group of input data comprised those required to generate the input load diagrams. They were obtained by measuring the load amplitude and mean load from Fig. 5.37, and are listed in Table 5.3.

The second group of data, required by the bearing performance program, was:

Shaft diameter = 2.7527".

Bearing inside diameter = 2.756".

Diametral clearance = .0033".

Bearings land length = 1.26".

Operating temperature = 90^{O}–110^{O}C.

Operating viscosity = 10 centipose.

Shaft speed = 1800 RPM.

Finite difference meshes, given in Section 3.1, were 112 nodes at graded spacings in the circumferential direction and 16 nodes at uniform spacings in the axial direction.

The third group of data comprised the information required by the FEM program. It included :

Centreline pressure data which were computed by bearing performance program.

White metal thicknes = .01".

Steel backing thickness = 0.118".

Allowable dynamic component and max. bearing load as a function of the mean bearing load.

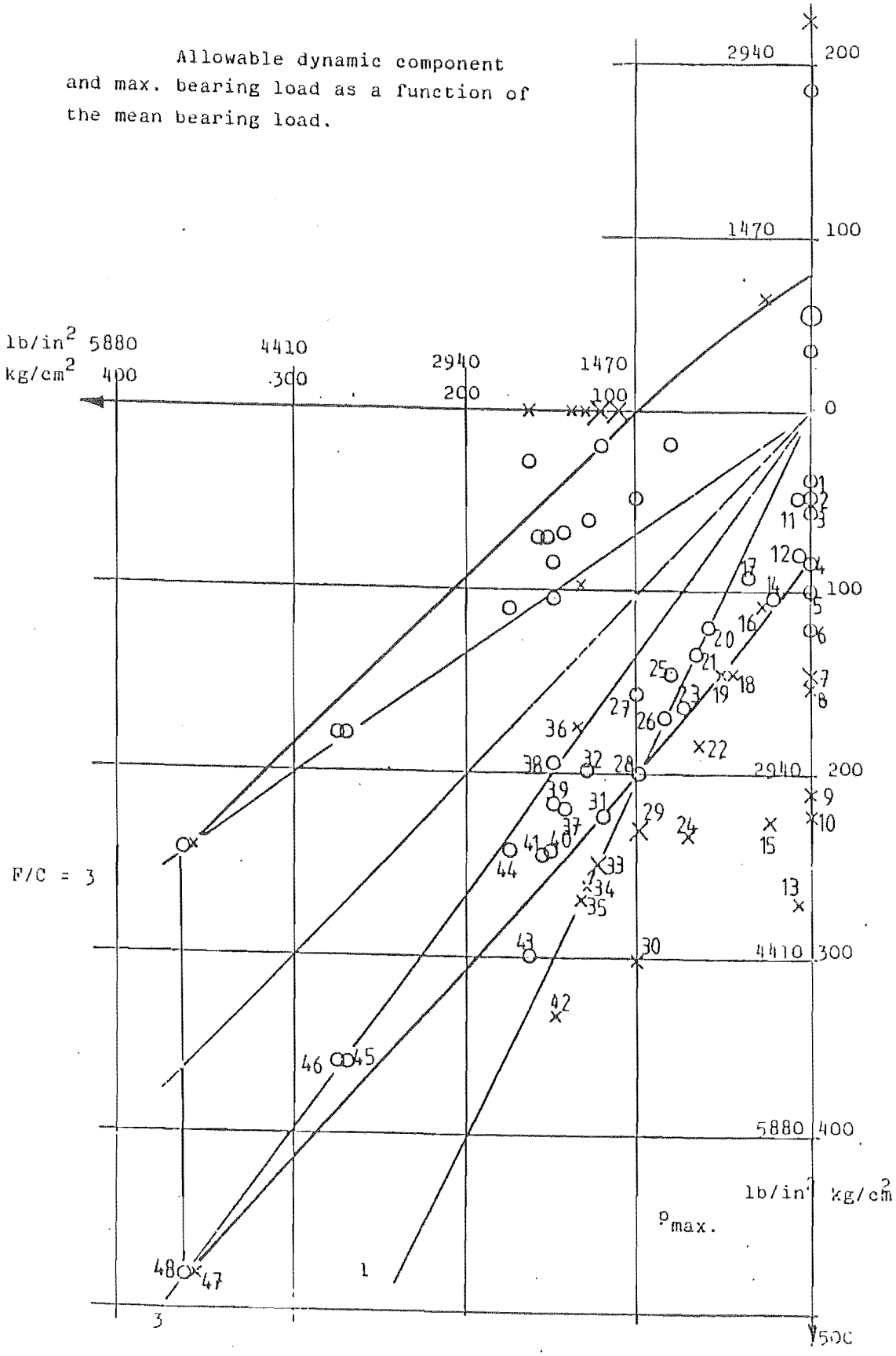

Fig. 5.37 - (Test Nos. 701–748)

Test No.	Load Amplitude (B–AXIS) Lb–F	Mean Load (B–AXIS) Lb–F	Test No.	Load amplitudes (B–AXIS) Lb–F	Mean Load (B–AXIS) Lb–F
701	1985	0	726	4253	–4253
702	2481	0	727	2764	–5104
703	2835	0	728	4395	–5104
704	4324	0	729	6592	–5104
705	5104	0	730	10209	–5104
706	6167	0	731	5316	–6096
707	7514	0	732	3544	–6521
708	7868	0	733	6167	–6238
709	10917	0	734	6663	–6521
710	11484	0	735	6593	–6734
711	2134	–425	736	1985	–6805
712	3686	–425	737	3828	–7230
713	13398	–425	738	2268	–7514
714	4253	–1134	739	3403	–7514
715	10490	–1276	740	4395	–7655
716	4111	–1417	741	4395	–7655
717	2835	–1843	742	9215	–7372
718	5104	–2268	743	7088	–8293
719	4678	–2623	744	3331	–8790
720	3119	–2977	745	4536	–13540
721	4607	–3260	746	4536	–13540
722	6096	–3260	747	6096	–18000
723	4678	–3686	748	6096	–18000
724	8293	–3544			
725	3260	–4111			

Table 5.3

Housing thickness = 1.8".

material properties of the white metal and steel backing are listed in Table 5.4. The white metal layer had the following composition : 90% tin, 6.5% antimony, and 3.5% copper.

Metal	Modulus of Elasticity LbF/in^2	Poisson ratio (μ)
White Metal	7.7 x 10^6	.33
Steel backing	30. x 10^6	.3

Table 5.4

The plots of results from some of the numerical reconstructions of Gyde's experiments are shown in Figs. 5.38–5.49. They include the input load and eccentricity ratio loci and pressure curves obtained from the bearing performance program, and the tangential stress curves on the surface and its variation at its maximum point with respect to time. Variation of surface pressure at this point was also plotted on the same frame but to a different scale (same as that on pressure curves plot).

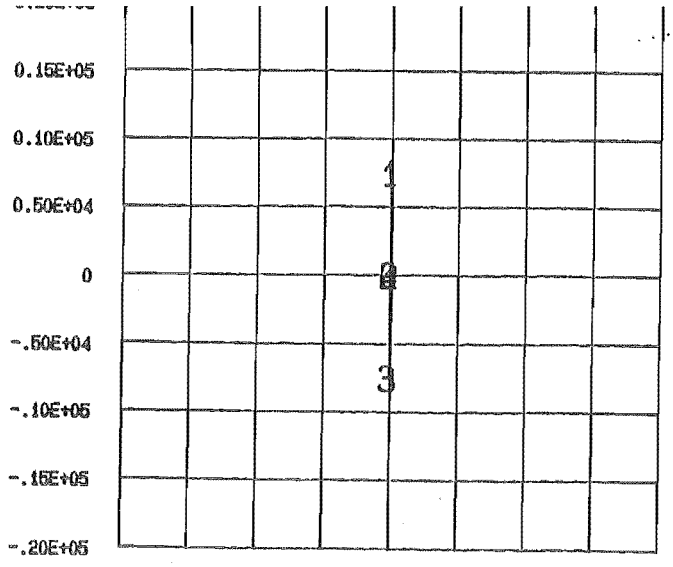

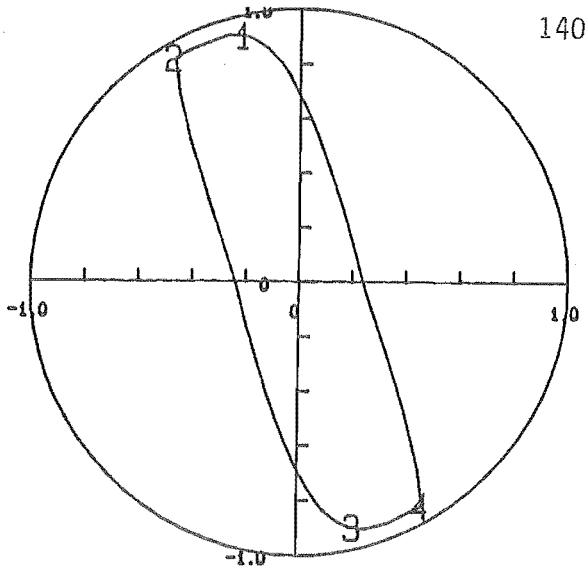

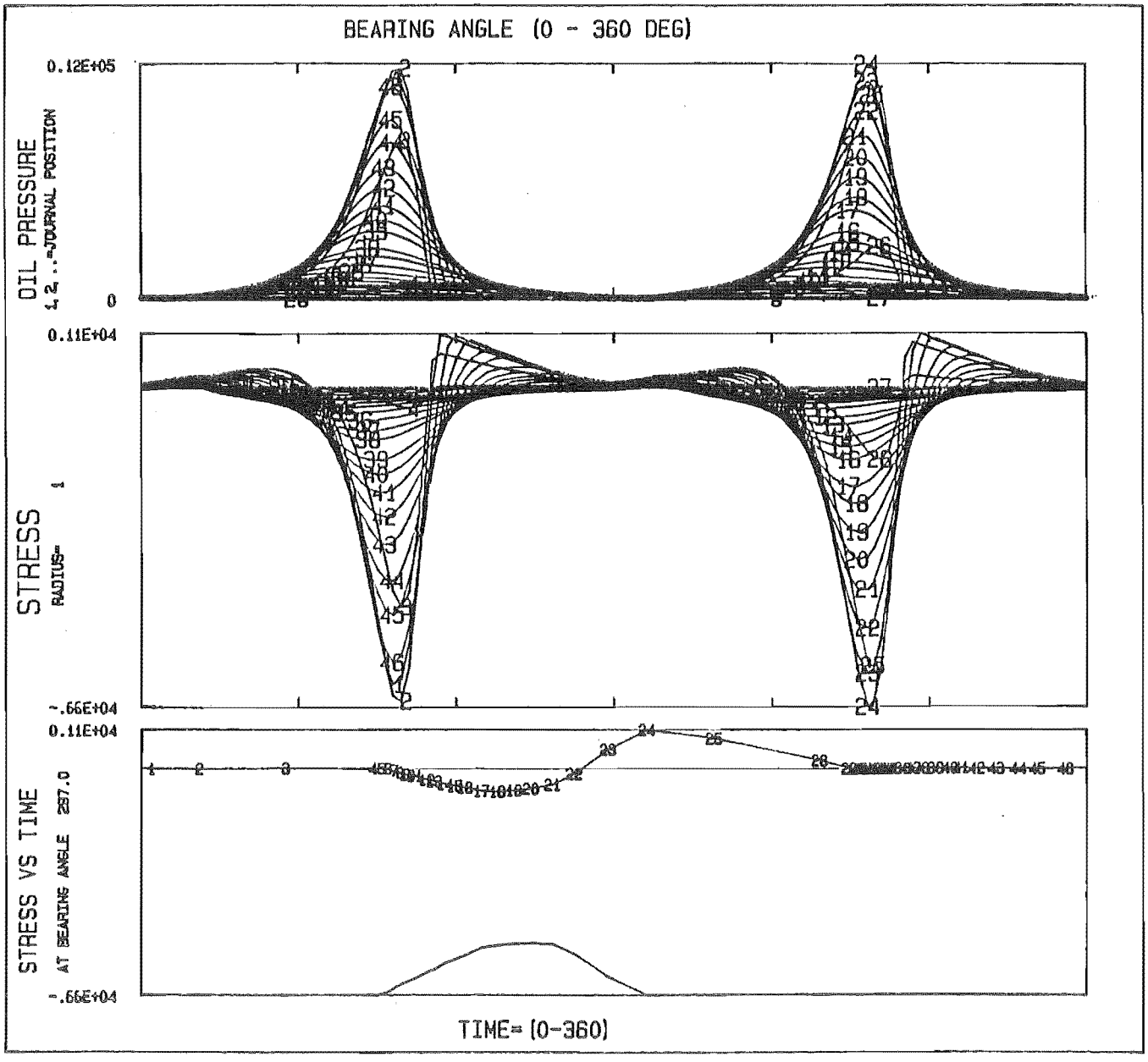

TEST NO 707 CO ROTATIONAL LOAD , 1 LAND BEARING

MAX STRESS = 0.112E+04 , AT ANGLE= 297.0

MIN STRESS = -0.662E+04 , AT ANGLE= 277.1 STRESS TYPE= TANGENTIAL

Fig.5.38

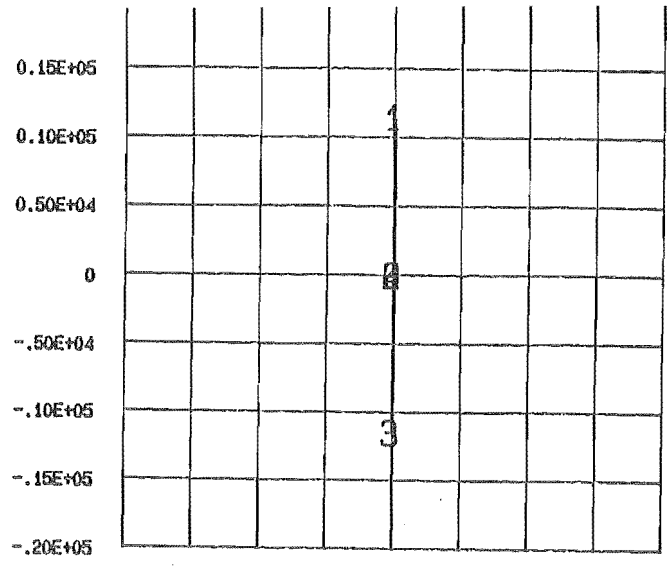

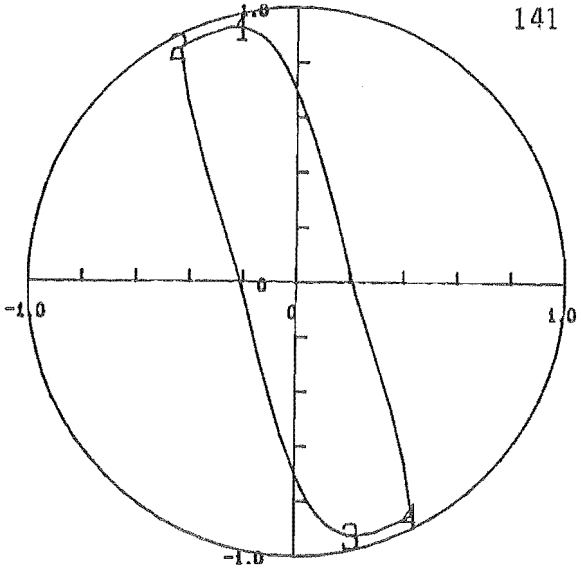

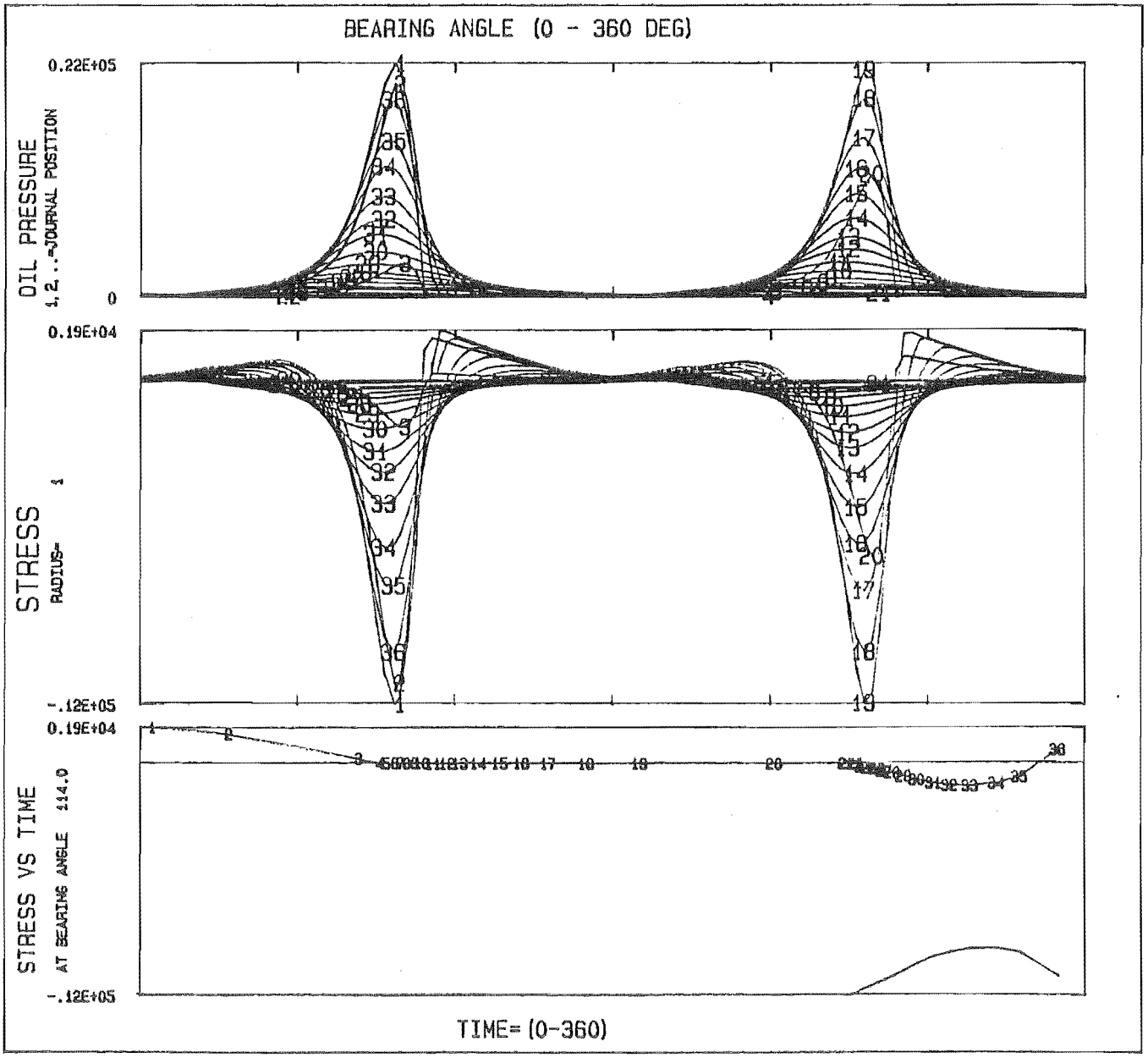

TEST NO 710 CO ROTATIONAL LOAD , 1 LAND BEARING

MAX STRESS = 0.187E+04 , AT ANGLE= 114.0

MIN STRESS = -0.120E+05 , AT ANGLE= 97.0 STRESS TYPE= TANGENTIAL

Fig.539

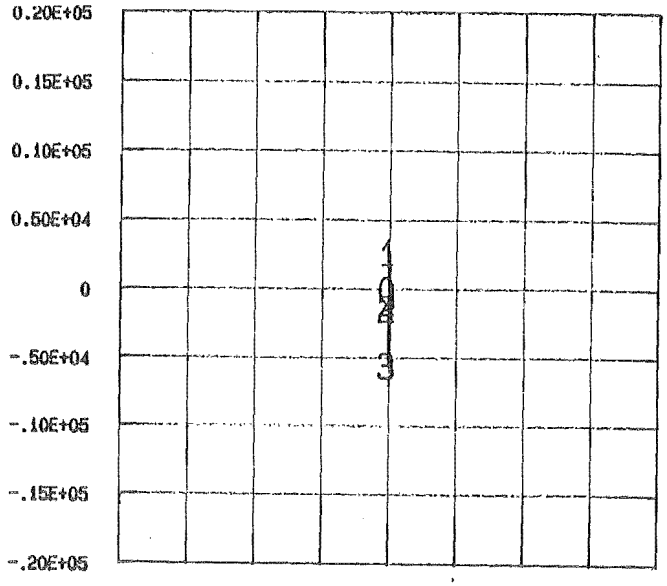

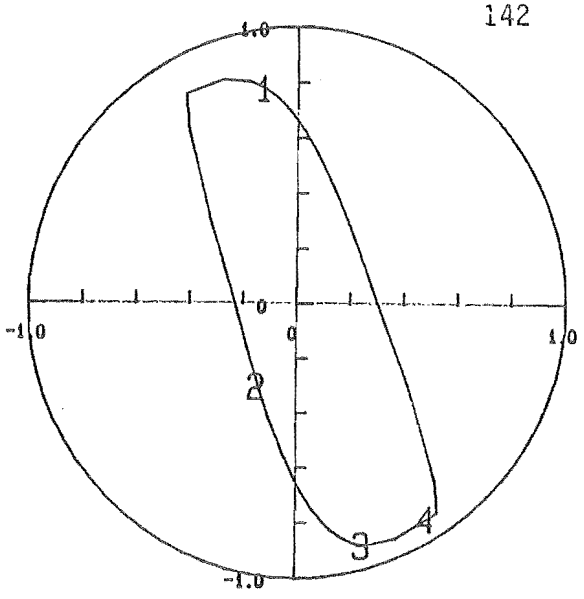

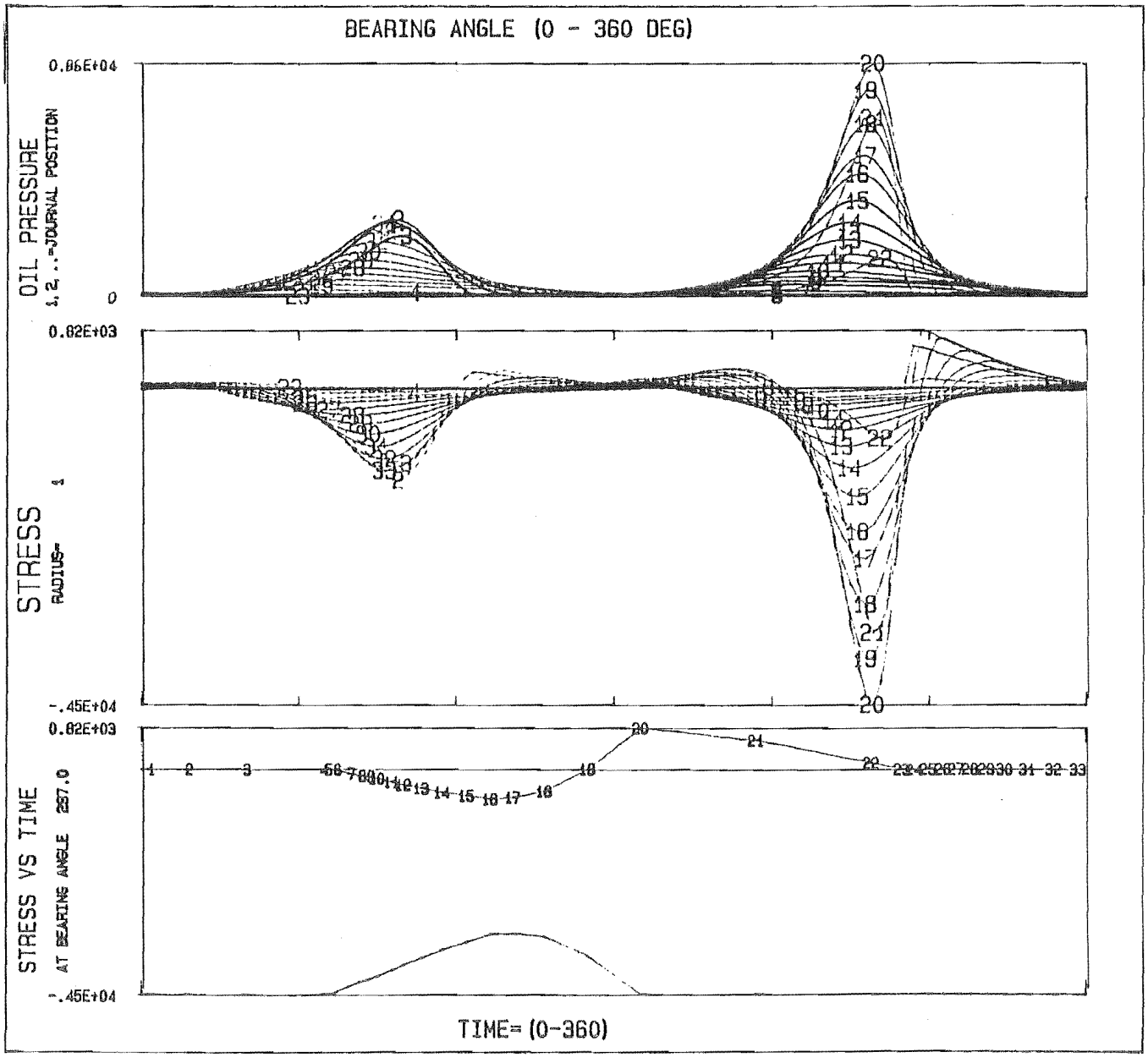

TEST NO 716 CO ROTATIONAL LOAD , 1 LAND BEARING

MAX STRESS = 0.817E+03 , AT ANGLE= 297.0

MIN STRESS = -0.452E+04 , AT ANGLE= 279.0 STRESS TYPE= TANGENTIAL

Fig.540

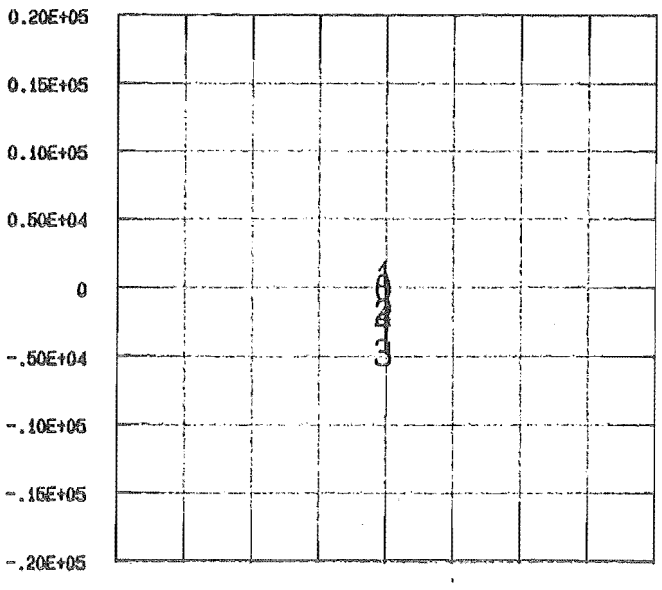

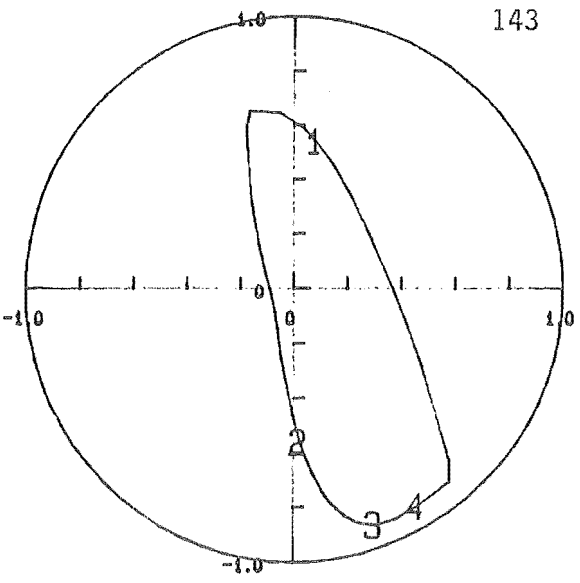

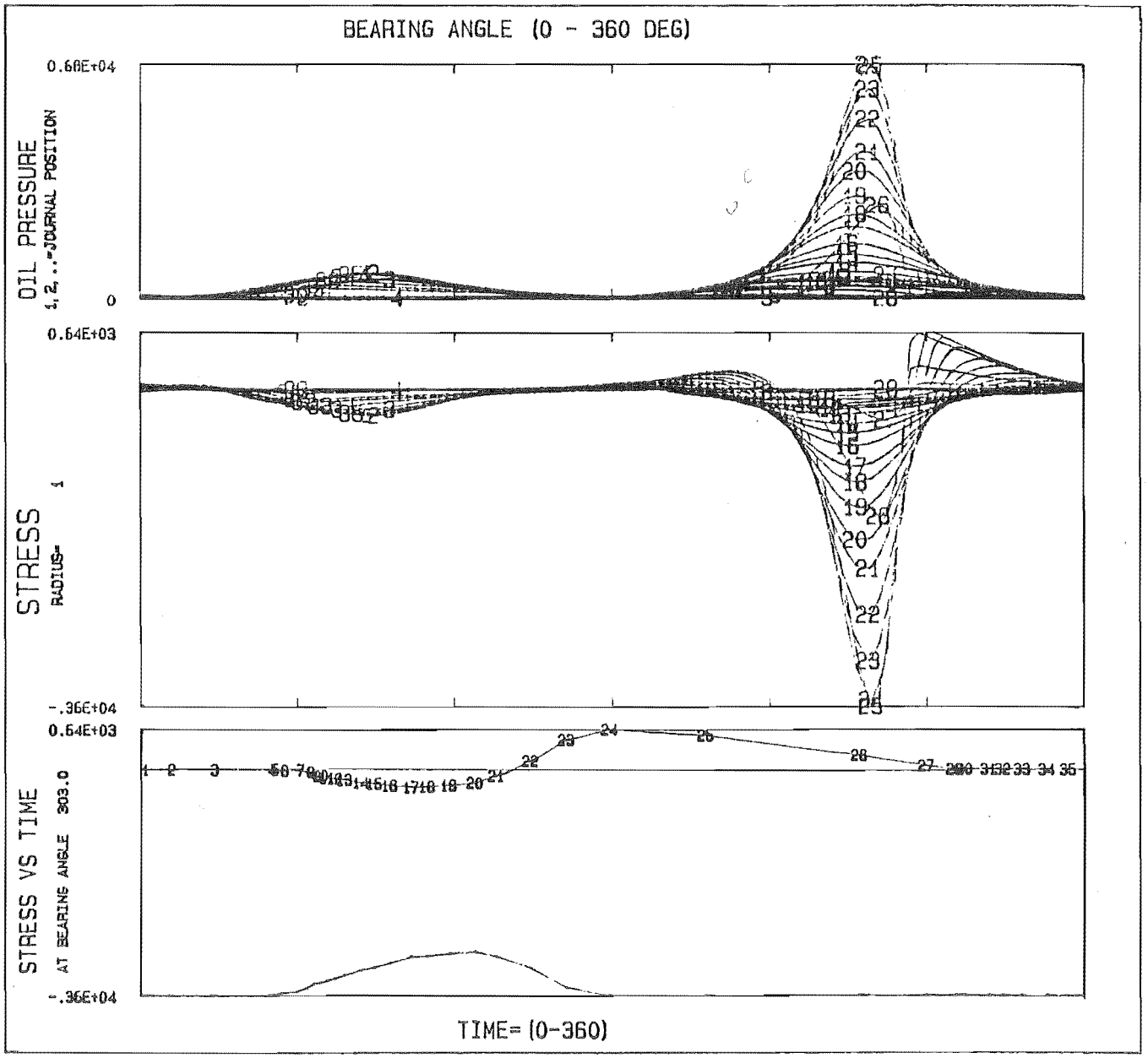

TEST NO 717 CO ROTATIONAL LOAD , 1 LAND BEARING

MAX STRESS = 0.641E+03 , AT ANGLE= 303.0

MIN STRESS = -0.358E+04 , AT ANGLE= 279.0 STRESS TYPE= TANGENTIAL

Fig.5.41

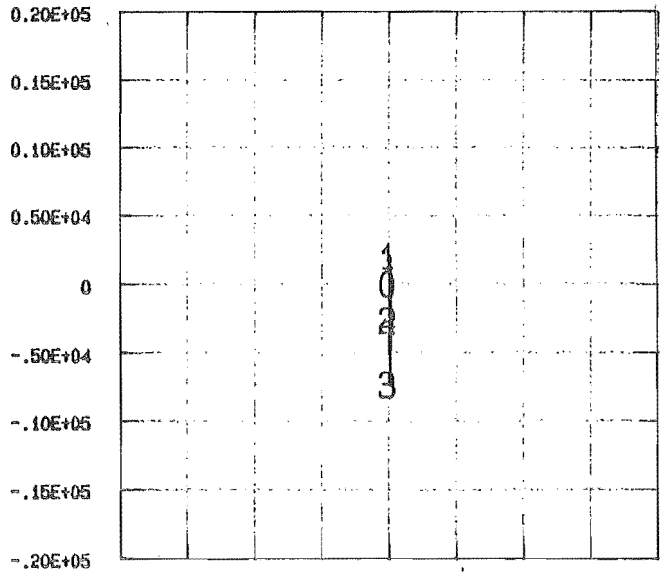

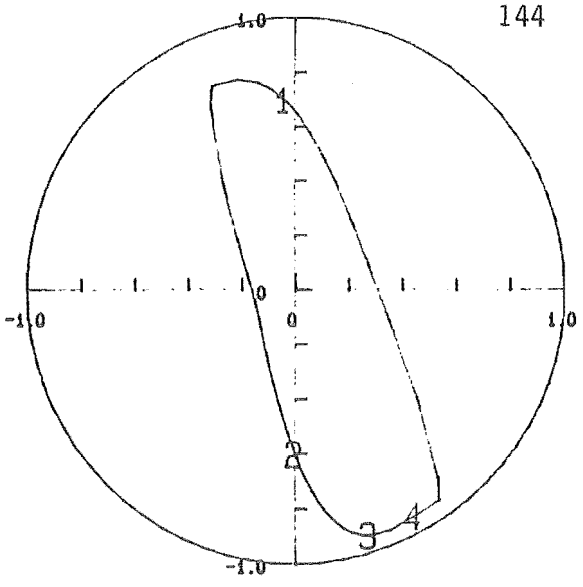

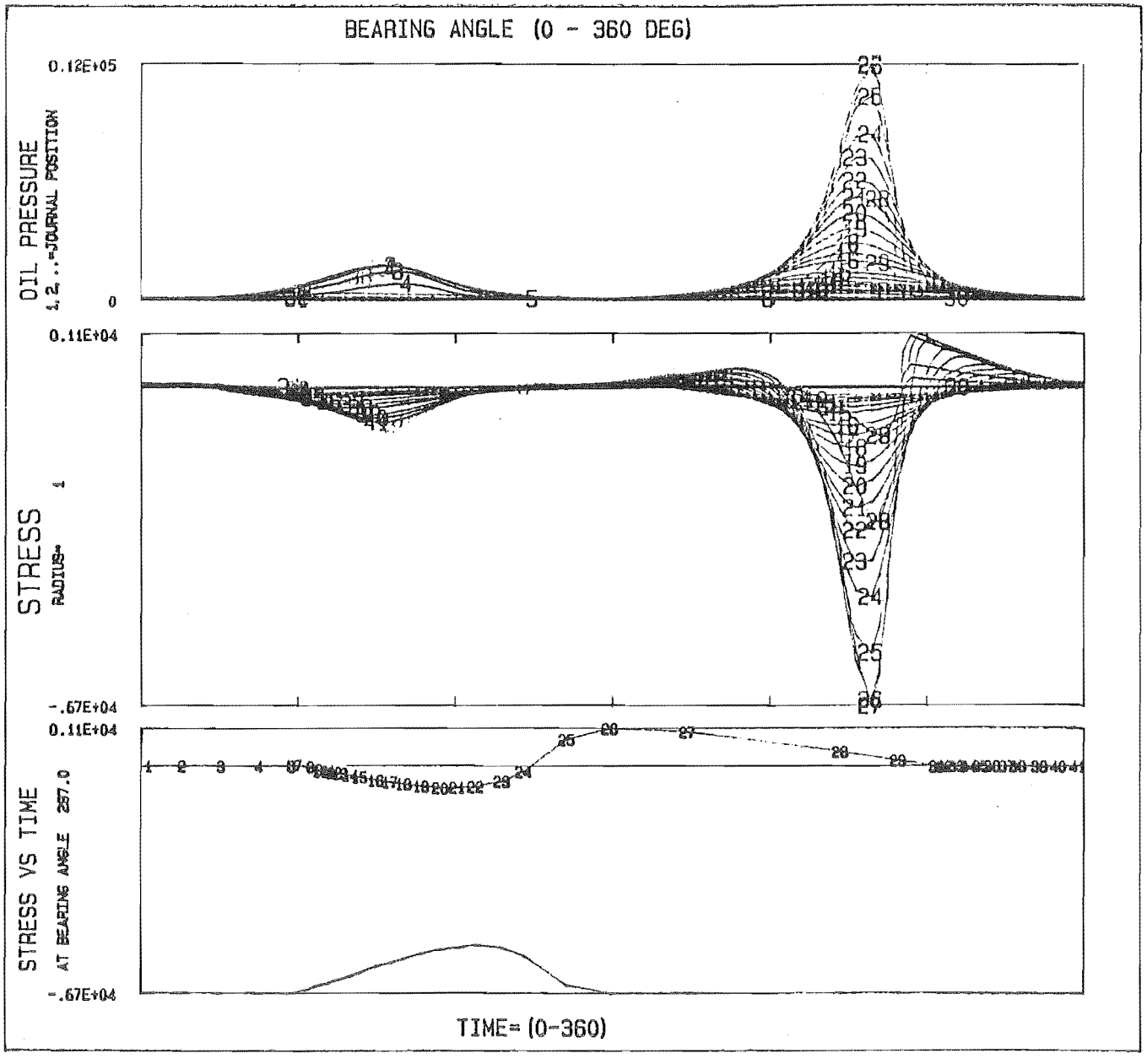

TEST NO 719 CO ROTATIONAL LOAD , 1 LAND BEARING

MAX STRESS = 0.111E+04 , AT ANGLE= 297.0

MIN STRESS = -0.668E+04 , AT ANGLE= 278.9 STRESS TYPE= TANGENTIAL

Fig.5.42

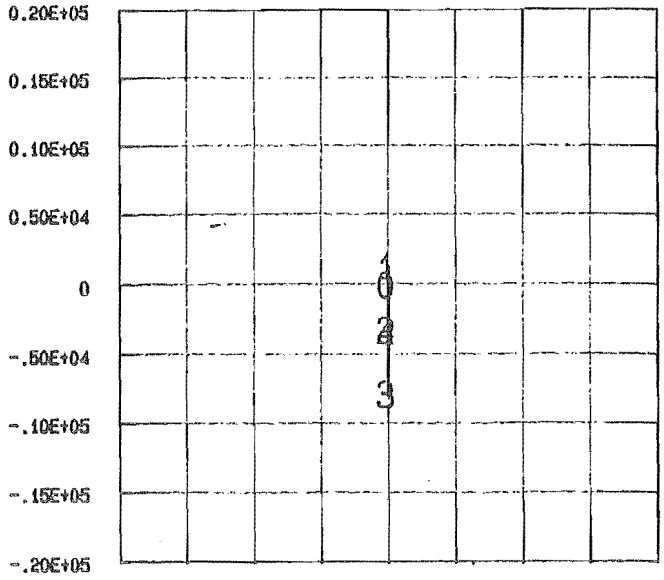

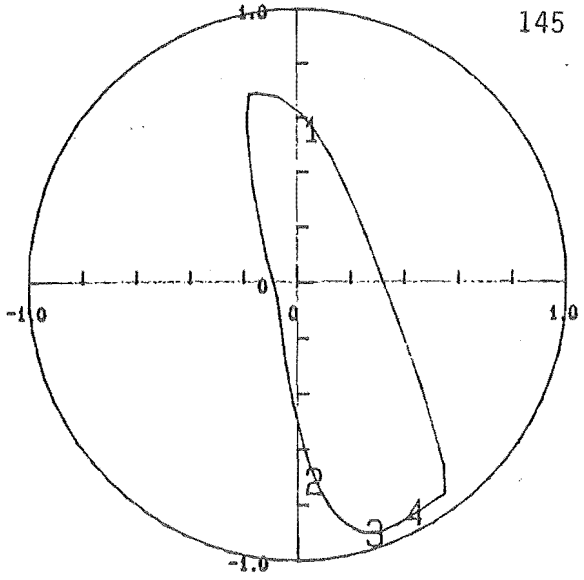

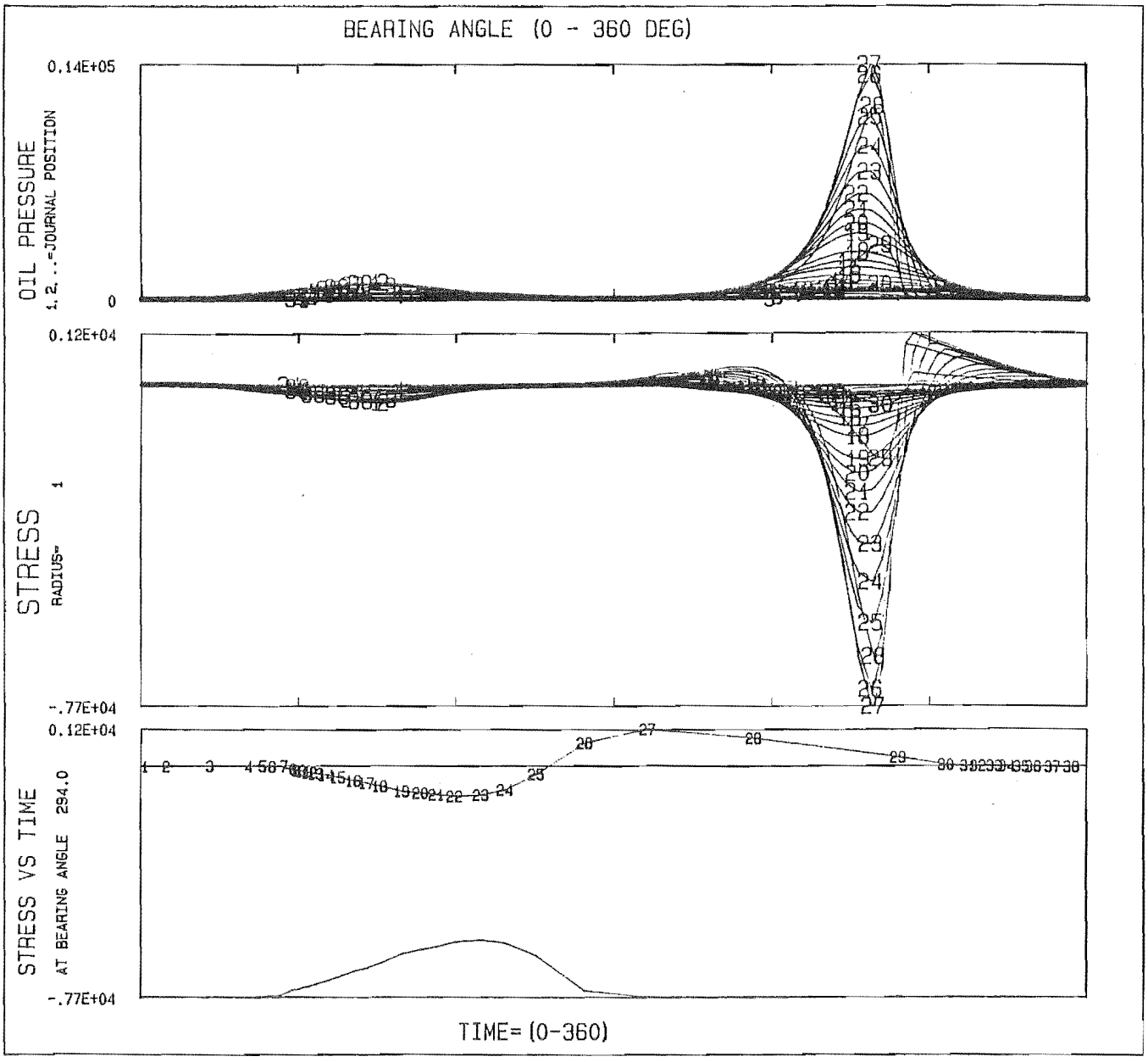

TEST NO 721 CO ROTATIONAL LOAD , 1 LAND BEARING

MAX STRESS = 0.124E+04 , AT ANGLE= 294.0

MIN STRESS = -0.767E+04 , AT ANGLE= 279.0 STRESS TYPE= TANGENTIAL

Fig.543

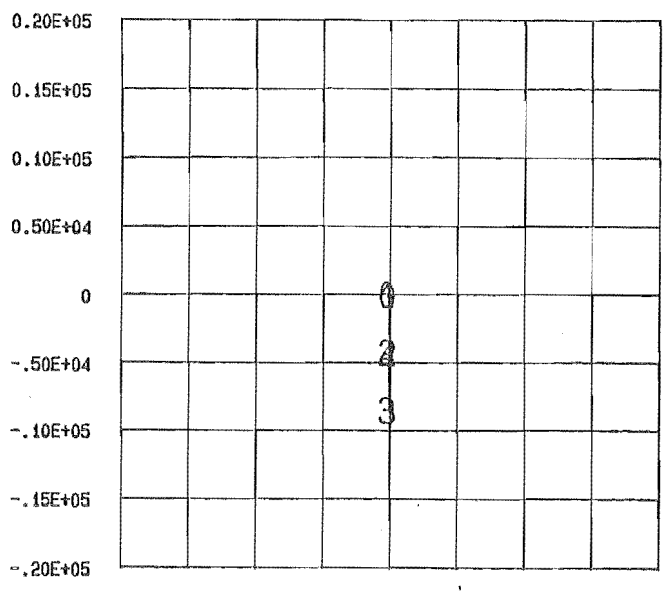

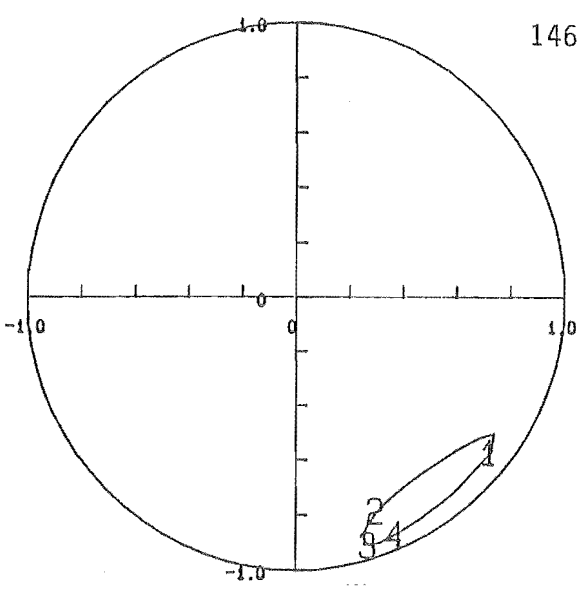

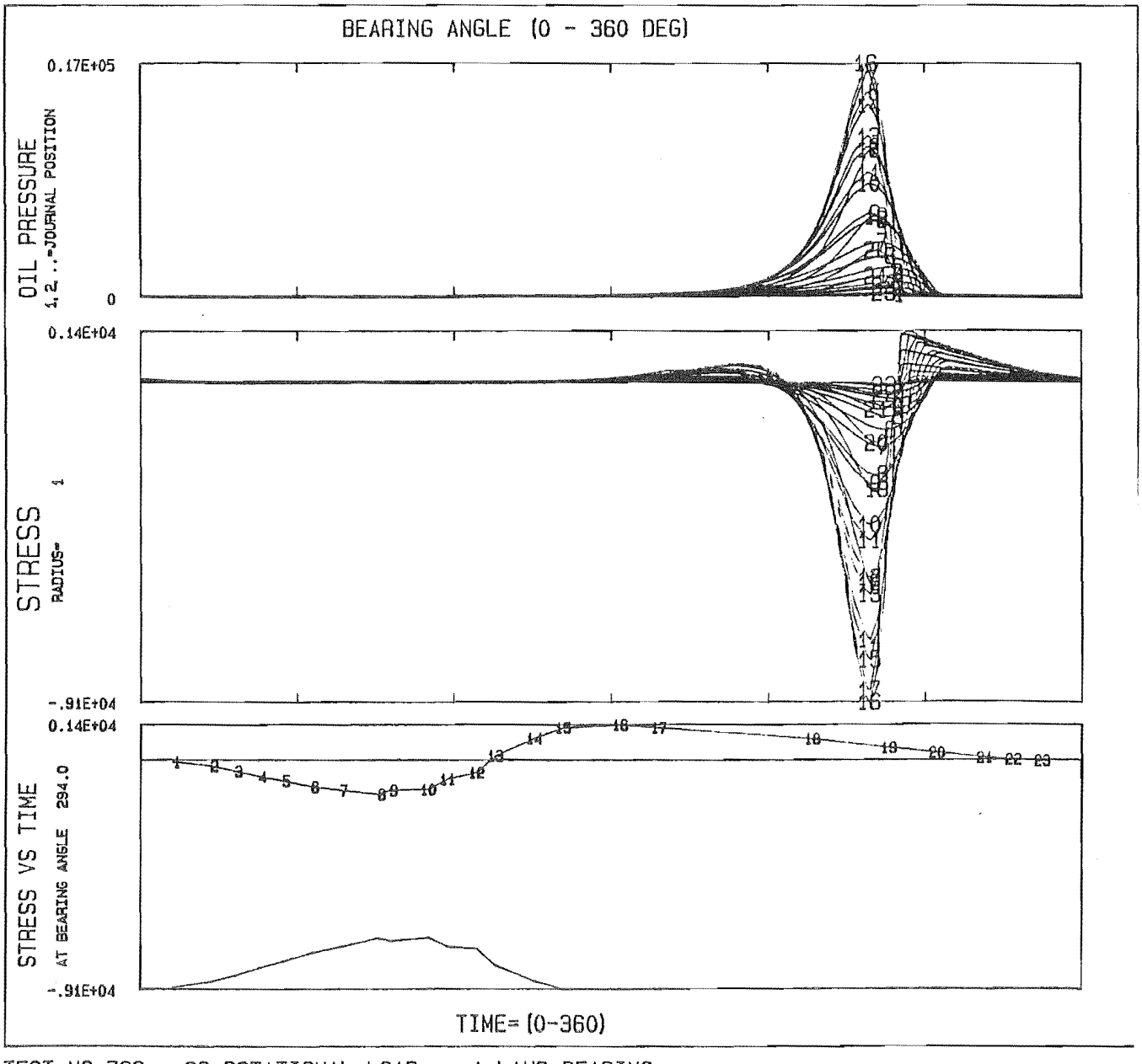

TEST NO 726 CO ROTATIONAL LOAD , 1 LAND BEARING

MAX STRESS = 0.143E+04 , AT ANGLE= 294.0

MIN STRESS = -0.912E+04 , AT ANGLE= 279.0 STRESS TYPE= TANGENTIAL

Fig.5.44

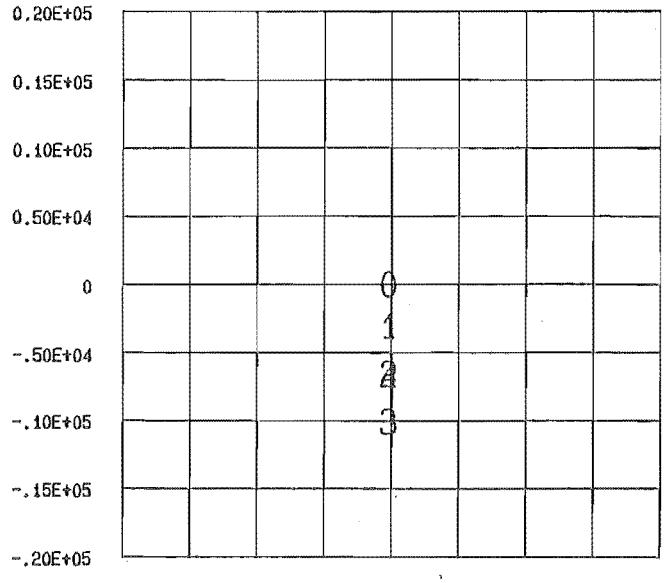

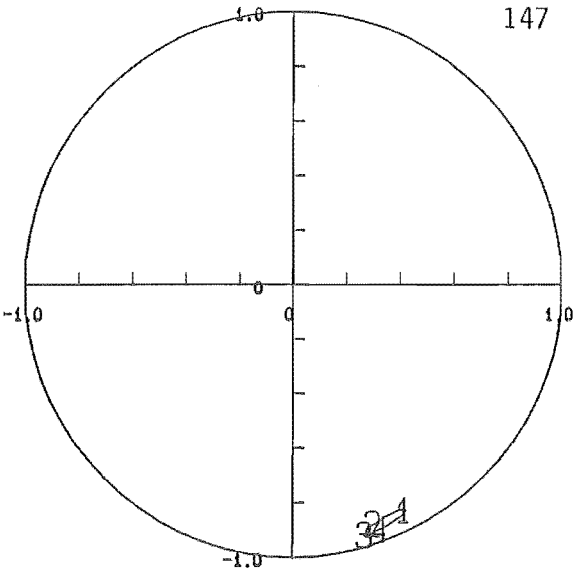

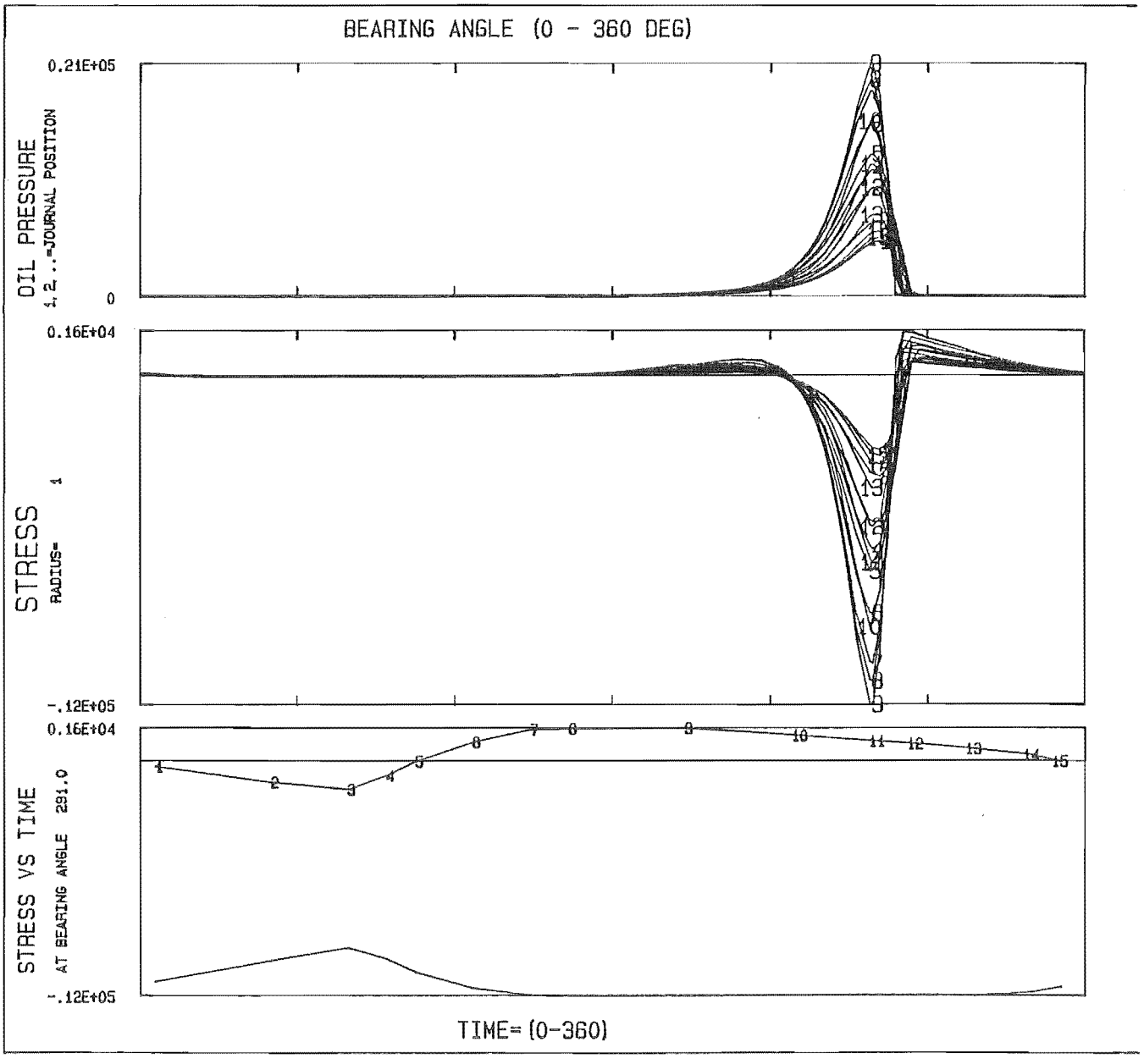

TEST NO 732 CO ROTATIONAL LOAD , 1 LAND BEARING

MAX STRESS = 0.162E+04 , AT ANGLE= 291.0

MIN STRESS = -0.116E+05 , AT ANGLE= 279.0 STRESS TYPE= TANGENTIAL

Fig.5.45

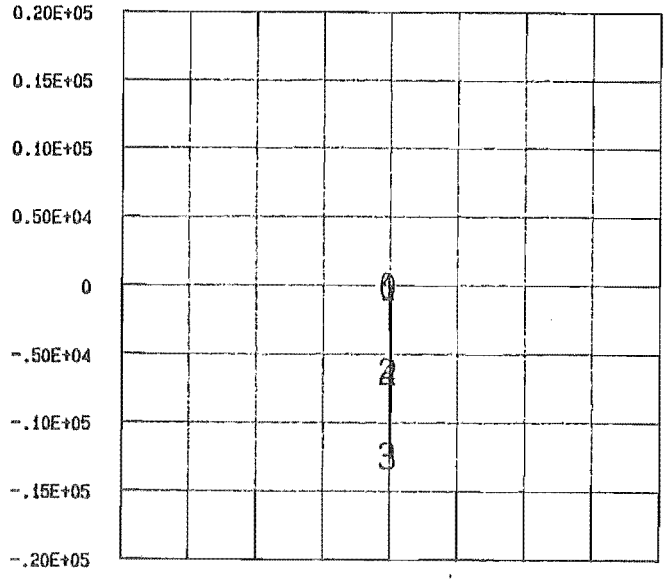

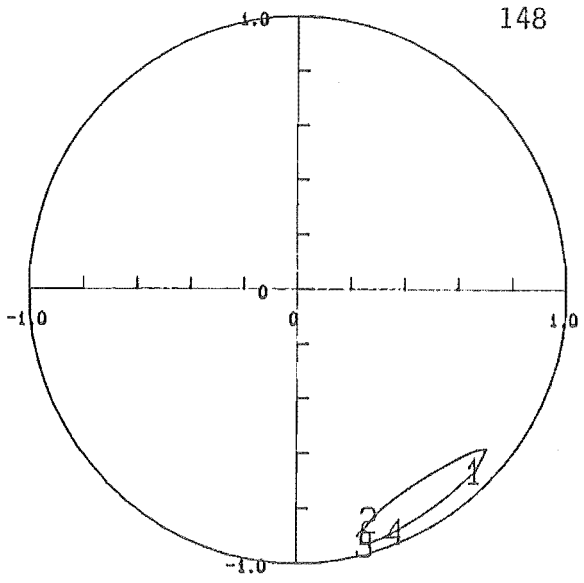

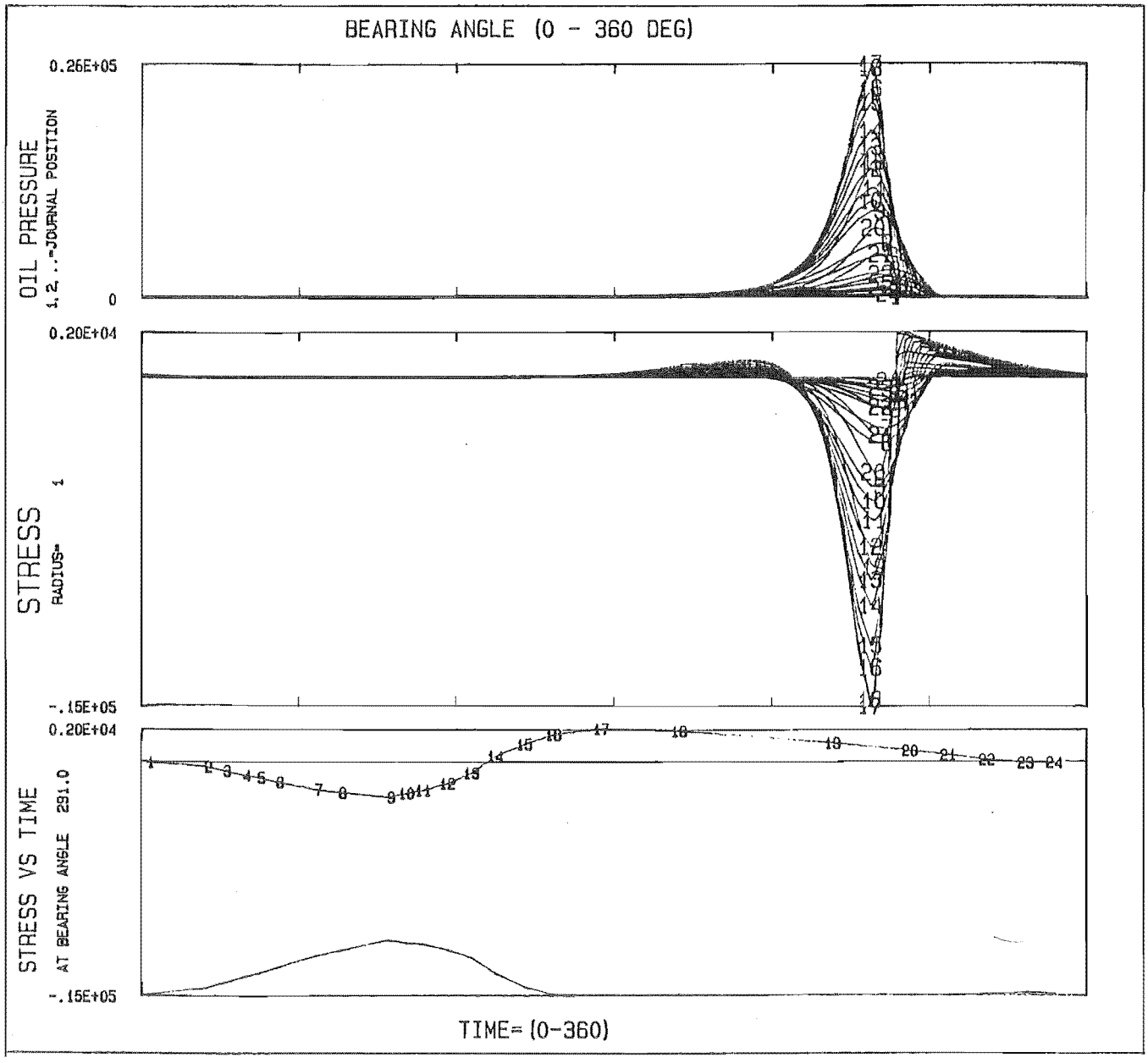

TEST NO 733 CO ROTATIONAL LOAD , 1 LAND BEARING

MAX STRESS = 0.203E+04 , AT ANGLE= 291.0

MIN STRESS = -0.147E+05 , AT ANGLE= 277.8 STRESS TYPE= TANGENTIAL

Fig.5.46

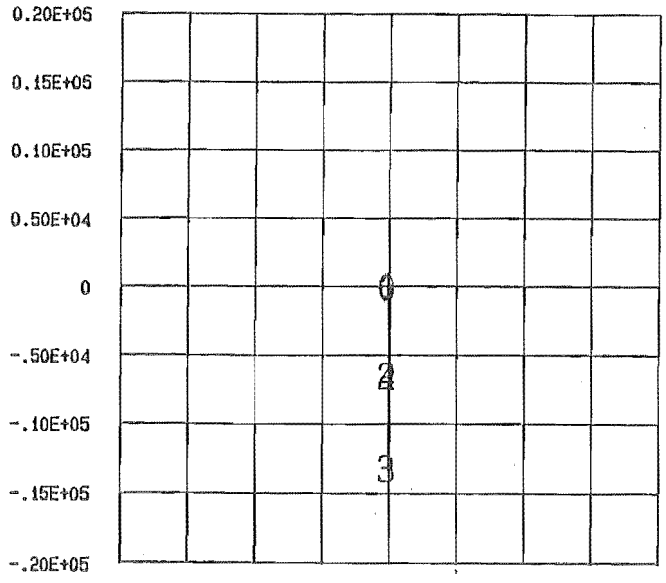

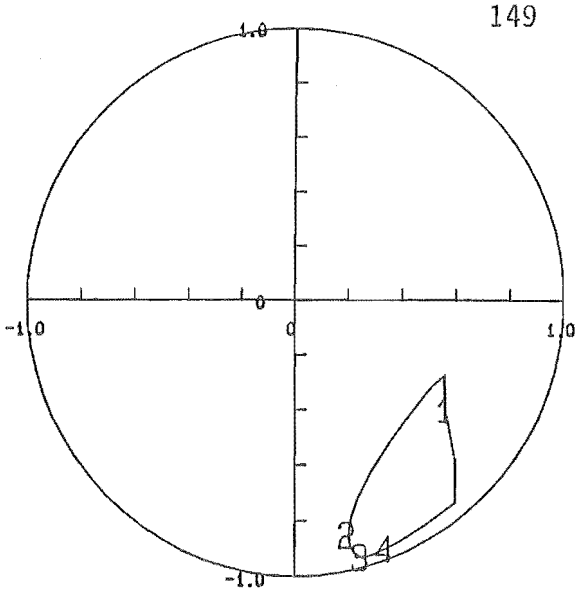

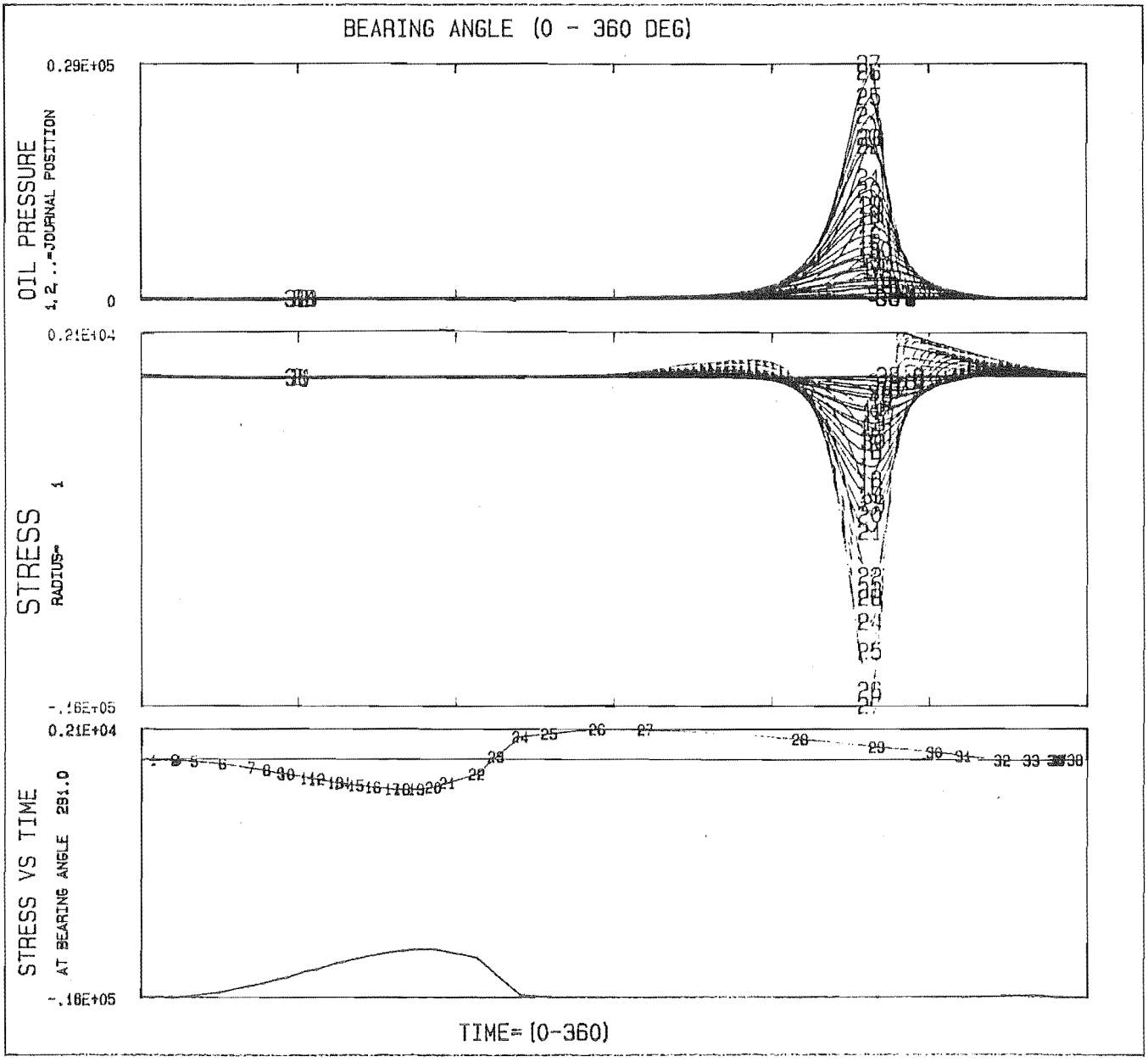

TEST NO 734 CO ROTATIONAL LOAD, 1 LAND BEARING

MAX STRESS = 0.215E+04 , AT ANGLE= 291.0

MIN STRESS = -0.163E+05 , AT ANGLE= 277.8 STRESS TYPE= TANGENTIAL

Fig 5.47

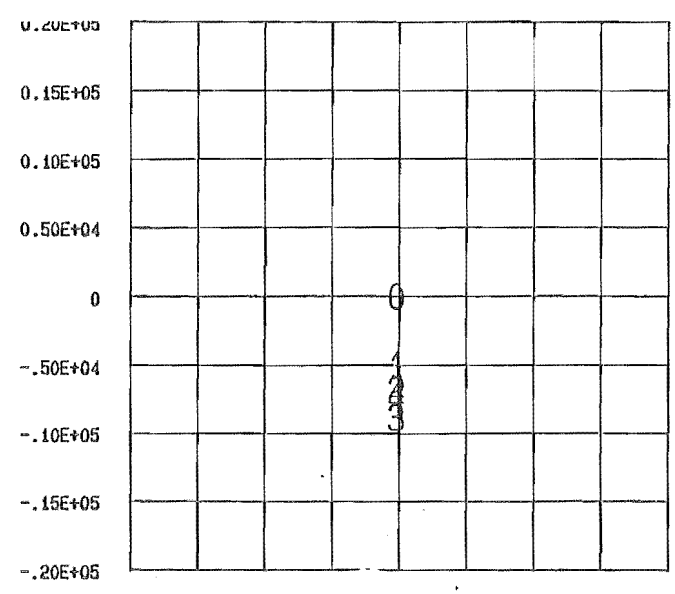

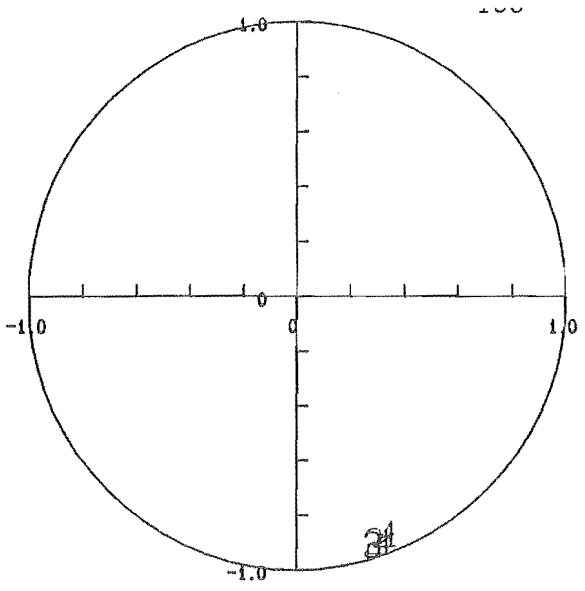

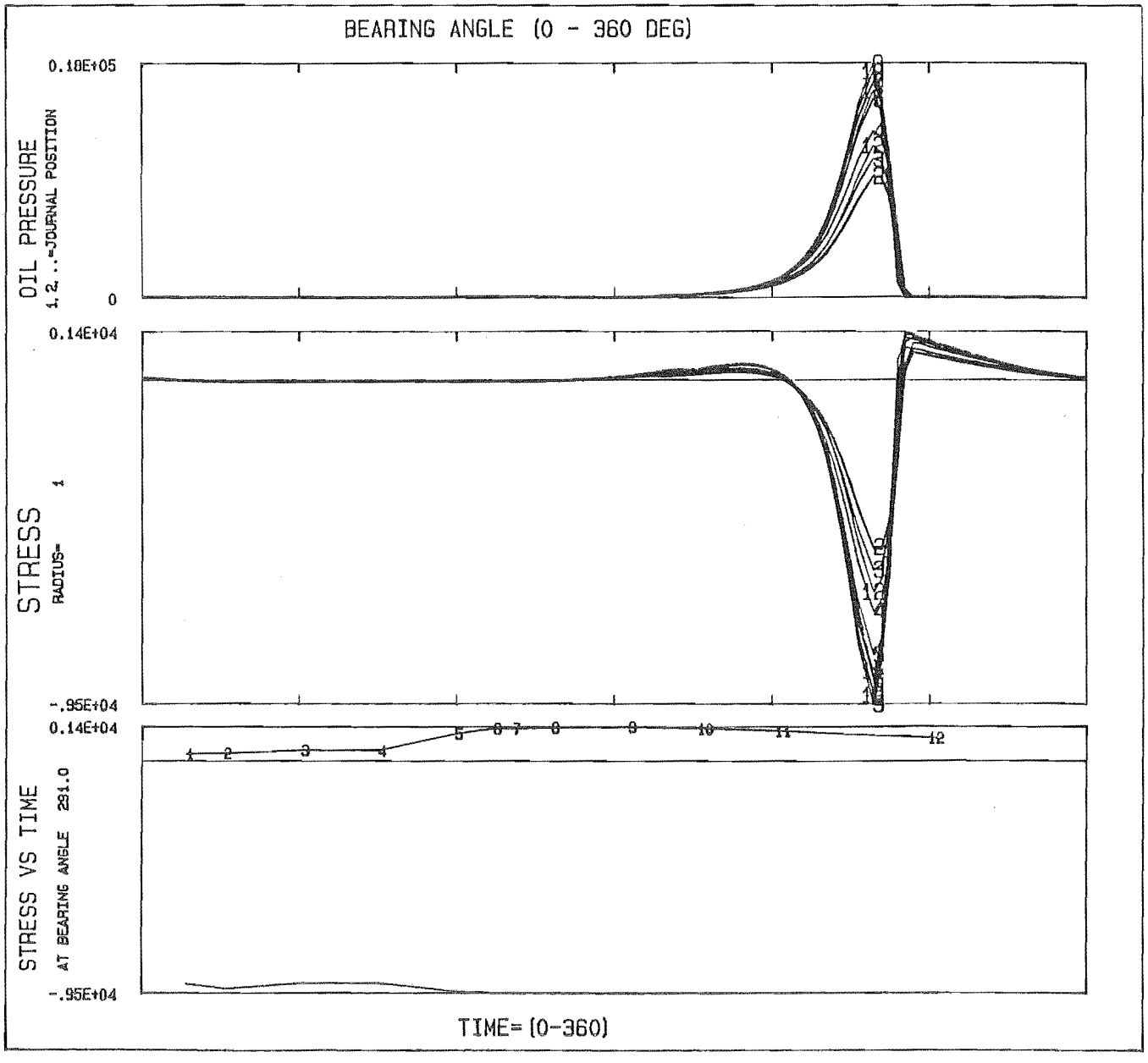

TEST NO 736 CO ROTATIONAL LOAD , 1 LAND BEARING

MAX STRESS = 0.143E+04 , AT ANGLE= 291.0

MIN STRESS = -0.953E+04 , AT ANGLE= 278.9 STRESS TYPE= TANGENTIAL

Fig 5.48

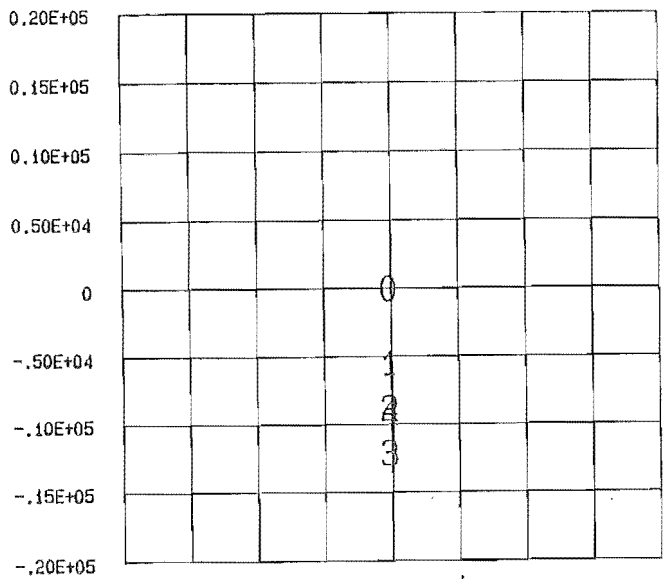

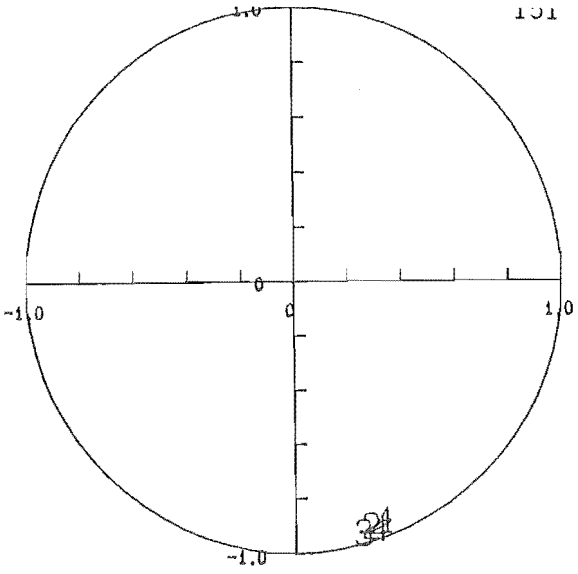

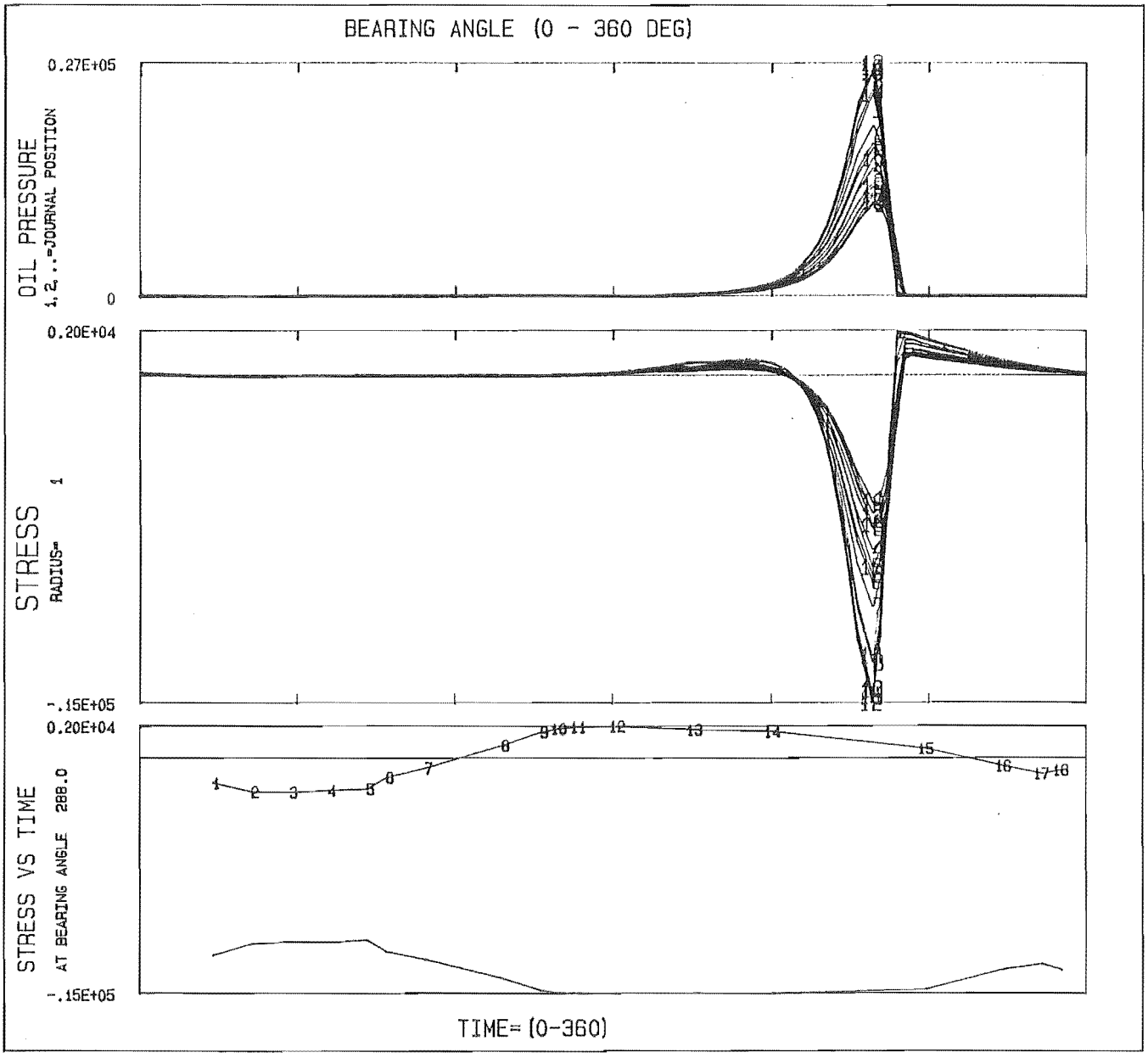

TEST NO 744 CO ROTATIONAL LOAD, 1 LAND BEARING

MAX STRESS = 0.203E+04 , AT ANGLE= 288.0

MIN STRESS = -0.149E+05 , AT ANGLE= 278.7 STRESS TYPE= TANGENTIAL

Fig 549

5.3 STRESS ANALYSIS

Angular positions of failures for the 28 tests of Blundell (numbered 501–528 in here) are listed in Table 5.5. In the Gyde's experiment, the angular position of failure for his tests (numbered 701–748 in here) were approximately 20 degrees downstream from the position of maximum load (i.e. 290^{O}). Upon comparing these with the position of maximum peak pressure in Tables 5.5 and 5.6, it was noticed that the failure occurred at points away from the peak pressure and closer to the position of maximum tangential stress. The angular positions of maximum shear stress and maximum distortion energy stress were the same as those of maximum peak pressure and away from the point of failure. These are shown in Figs. 5.50–5.55. Blundell believed the failure to be due to the shear stress at the interface of the white metal and steel backing. However this was not correct, because if the failure had been induced by shear stress, it would have appeared at the maximum shear stress which occurred under the peak pressure and it did not. Also Hassan showed that the metallic bond at the interface was so strong that the cracks which originated at the surface did not stop at the interface: they continued to propagate into the steel backing. The tangential stress at the surface of the white metal which repeatedly cycled through tension and compression and which had its maximum value closer to the position of failure was more likely to have induced the failure.

In order to be able to plot the S–N diagram (stress versus the number of cycles to failure), maximum tangential stress for different cases were calculated and listed in Tables 5.5 and 5.6. The time periods to failure for different cases are listed in Table 5.7. Fig. 5.56 shows the resulting S–N diagram which indicates considerable scatter in the results.

Upon studying the points on the diagram more closely, it was noticed that the difference in the time period to failure between the co and antirotational

loading cases had an important role in scattering the results. This becomes more evident when the extreme points on the S–N diagrams (i.e. points 18 and 28) are taken into consideration. Thus, it was decided to investigate the co and antirotational loading cases in more detail This required all these cases to be simulated again and their stress history at their maximum points to be saved on files. To get a more accurate record of stress variation at the point of investigation, it was necessary to simulate six of the Blundell cases (Figures 5.7, 5.8, 5.21, 5.23, 5.24, 5.25) with finer time steps than others. As shown on the stress–time plots of Figs. 5.23 and 5.33, the time period between the maximum tension to maximum compression of Case 518 (points 23 to 24), was a lot shorter than the similar time period for Case 528 (points 8 to 5). This meant that if a crack existed on the surface, the closing time period from maximum tension to maximum compression would be shorter and the oil in the crack would have less time to escape. Consequently, this trapped oil would increase the stresses at the tip of the crack during the closing period. The reason for this difference in closing time period between the co and antirotational loading cases becomes more evident when we consider the movements of the tangential stress distributions for these two cases in time (see Fig. 5.50 and Figs. 5.23 and 5.33).

In the corotational case, as the wave approaches the failure point, the tangential stress increases to maximum tension. As the wave passes over this point the stress suddenly changes to compression; while in the antirotational loading case, as the wave passes over the failure point the stress changes from compression to maximum tension. The above interesting difference in the stress histories at the point of failure convinced us to study them in a more detail way, which will be discussed in the next chapter.

Test No.	Max. peak pressure (PSI)	Angular position of max. peak pressure (Deg)	Max. princ. stress (PSI)	Angular position of max.princ.stress (Deg)	* Experimental Angles of Failures 1	2	3
501	26000	268.8	1900	288	281.3	284.1	276.5
502	49000	280.2	2750	294	279.8	286.2	–
503	44000	269.5	2650	282	284.8	288.	–
504	49000	282.8	2490	297	286.7	291.6	–
505	47000	274.2	2700	291	288.6	288.	287.2
506	48000	275.5	2330	297	292	295.	–
507	49000	282.9	2490	264	306.5	295.8	302
508	22000	269.3	1660	288	285.4	287.2	283.2
509	42000	277.2	2770	297	290.4	287.5	–
510	44000	267.1	2800	282	295.8	290.7	–
511	42000	273.1	2780	291	289.6	294.5	292.5
512	24000	280.8	1810	300	295.4	296.	–
513	33000	271.4	2400	297	298.4	300.2	296.6
514	35000	289.3	2620	306	299.6	290.7	295.8
515	41000	279	2070	294	283	281.6	283
516	89000	276.2	3610	291	289.4	286.3	282.2
517	79000	266.2	3350	279	273.9	276	–
518	80000	273.6	3160	282	276.7	277.6	–
519	97000	275.4	3790	288	282.4	281.2	–
520	92000	277.7	3120	291	282.5	286.4	–
521	91000	283.	3270	267	287.4	289.9	–
522	43000	282.1	2160	297	283.2	280.7	–
523	74000	272.5	3270	294	285.5	276.	–
524	45000	273.4	2150	288	290.3	288.1	–
525	64000	270.7	2960	291	284.4	291.8	–
526	75000	275.3	3390	288	290.	284.9	–
527	61000	279.	3180	294	294.	287.5	–
528	66000	288.	3380	303	290.	293.5	–

* Each case was tested by Blundell up to three times.

Table 5.5

Test No.	Max. Peak pressure (PSI)	Angular position of Max.peak pressure (Deg)	Max. princ. stress (PSI)	Angular position of Max. princ.stress (Deg)	Failed Unfailed	X O
701	2061	277.9	193	315	O	
702	2738	278.0	274	306	O	
703	3407	277.9	328	312	O	
704	5938	277.0	570	306	O	
705	7340	278.6	709	300	O	
706	9416	278.1	848	297	O	
707	12410	277.1	1120	297	X	
708	13500	276.7	1170	297	X	
709	20400	277.6	1720	294	X	
710	22420	277.0	1870	294	X	
711	3078	277.8	300	312	O	
712	5522	277.8	529	306	O	
713	28510	277.7	2200	291	X	
714	8400	278.2	800	300	O	
715	23900	277.4	1910	294	X	
716	8587	279.0	817	297	X	
717	6819	279.0	641	303	O	
718	12600	278.2	1110	297	X	
719	12460	278.9	1110	297	X	
720	10730	279.4	943	297	O	
721	14230	279.0	1240	294	O	
722	17700	278.7	1450	291	X	
723	16100	279.2	1380	294	O	
724	11800	276.7	1850	294	X	
725	13800	279.5	1170	294	O	

Table 5.6 (Continued)

Table 5.6. continued

Test No.	Max. Peak pressure (PSI)	Angular position of Max.peak pressure (Deg)	Max. princ. stress (PSI)	Angular position of Max. princ.stress (Deg)	Failed Unfailed	X O
726	16760	279.0	1430	294	O	
727	15700	279.4	1300	291	O	
728	18600	279.1	1570	294	O	
729	24600	278.0	1890	291	X	
730	33000	277.5	2480	291	X	
731	25200	278.6	1920	291	O	
732	21230	279.0	1620	291	O	
733	26300	277.8	2030	291	X	
734	28900	277.8	2150	291	X	
735	28570	277.5	2160	291	X	
736	17570	278.9	1430	291	X	
737	23940	277.4	1830	291	O	
738	20500	278.3	1600	291	O	
739	23650	277.5	1810	291	O	
740	26000	278.6	1980	291	O	
741	26000	278.6	1980	291	O	
742	39100	276.6	2700	291	X	
743	37500	277.2	2610	288	O	
744	27000	278.7	2030	288	O	
745	47300	276.9	3050	288	O	
746	47300	276.9	3050	288	O	
747	66200	276.9	3970	288	X	
748	66200	276.9	3970	288	O	

Table 5.6

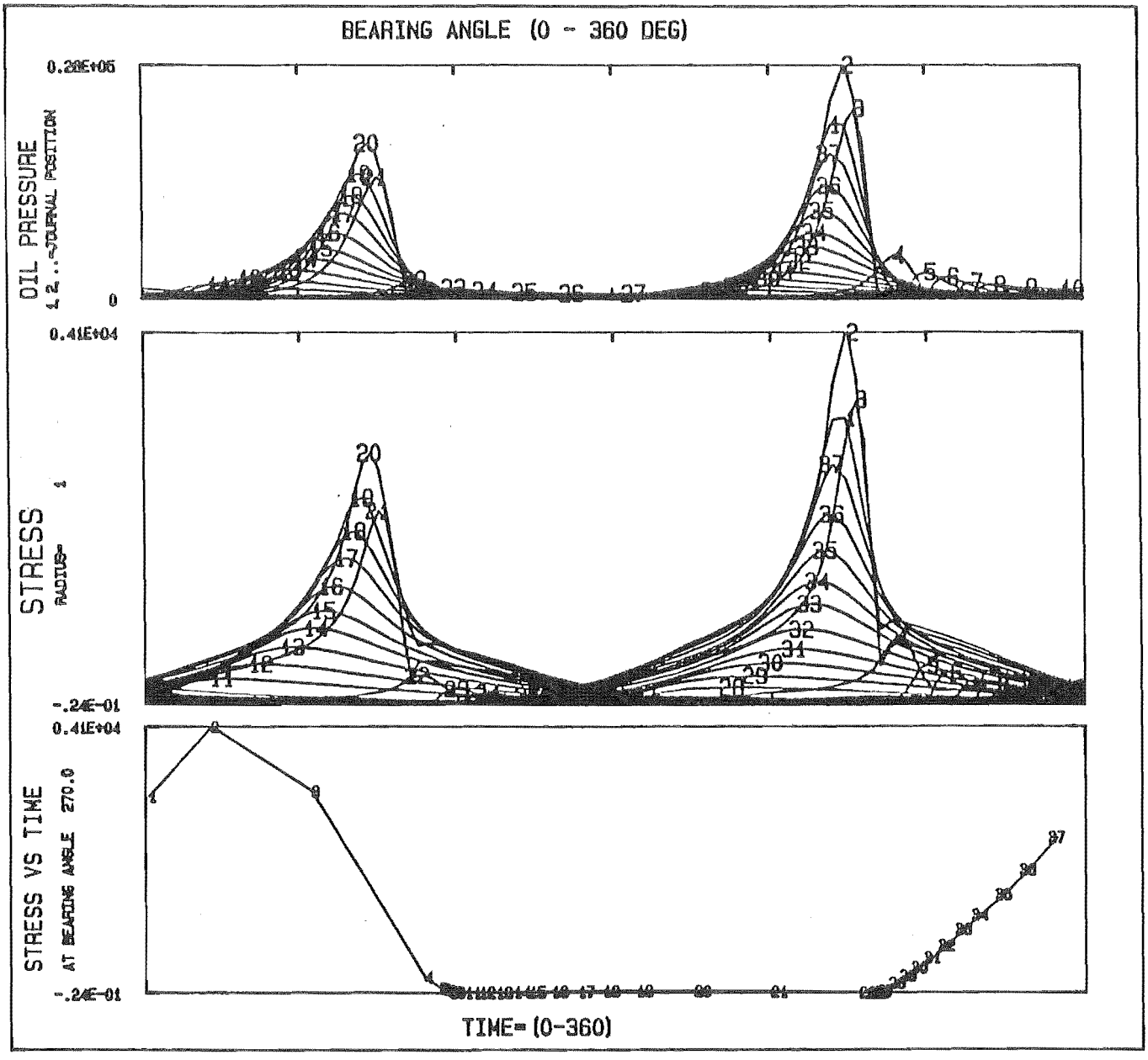

TEST NO 501 CO ROTATIONAL LOAD, 1 LAND BEARING

MAX STRESS = 0.409E+04 , AT ANGLE= 270.0

MIN STRESS = -0.242E-01 , AT ANGLE= 57.0 STRESS TYPE= MAX SHEAR

Fig.5.50

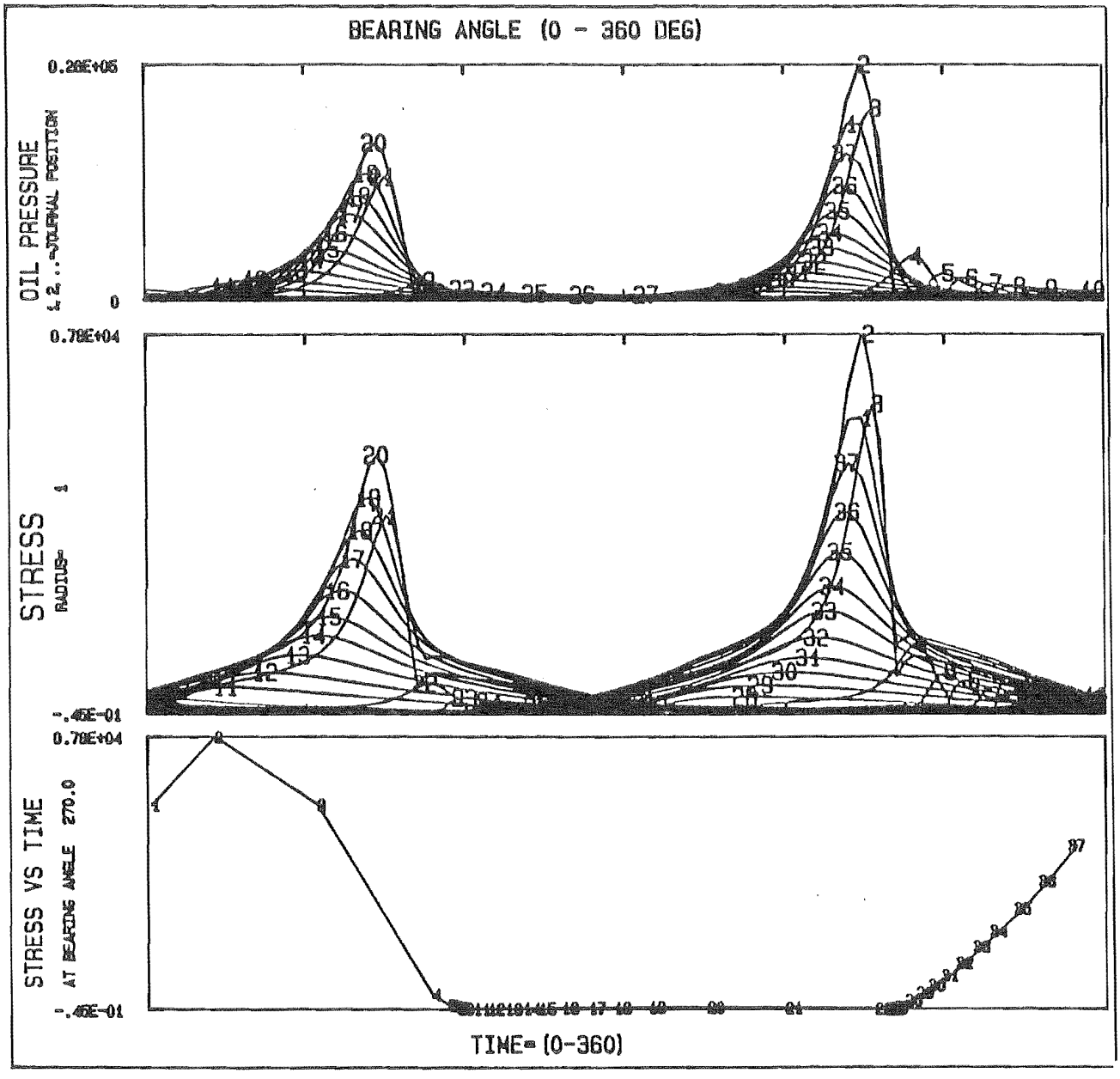

TEST NO 501 CO ROTATIONAL LOAD, 1 LAND BEARING

MAX STRESS = 0.709E+04 , AT ANGLE= 270.0

MIN STRESS = -0.454E-01 , AT ANGLE= 57.0 STRESS TYPE= MAX DISTORTION

Fig.5.51

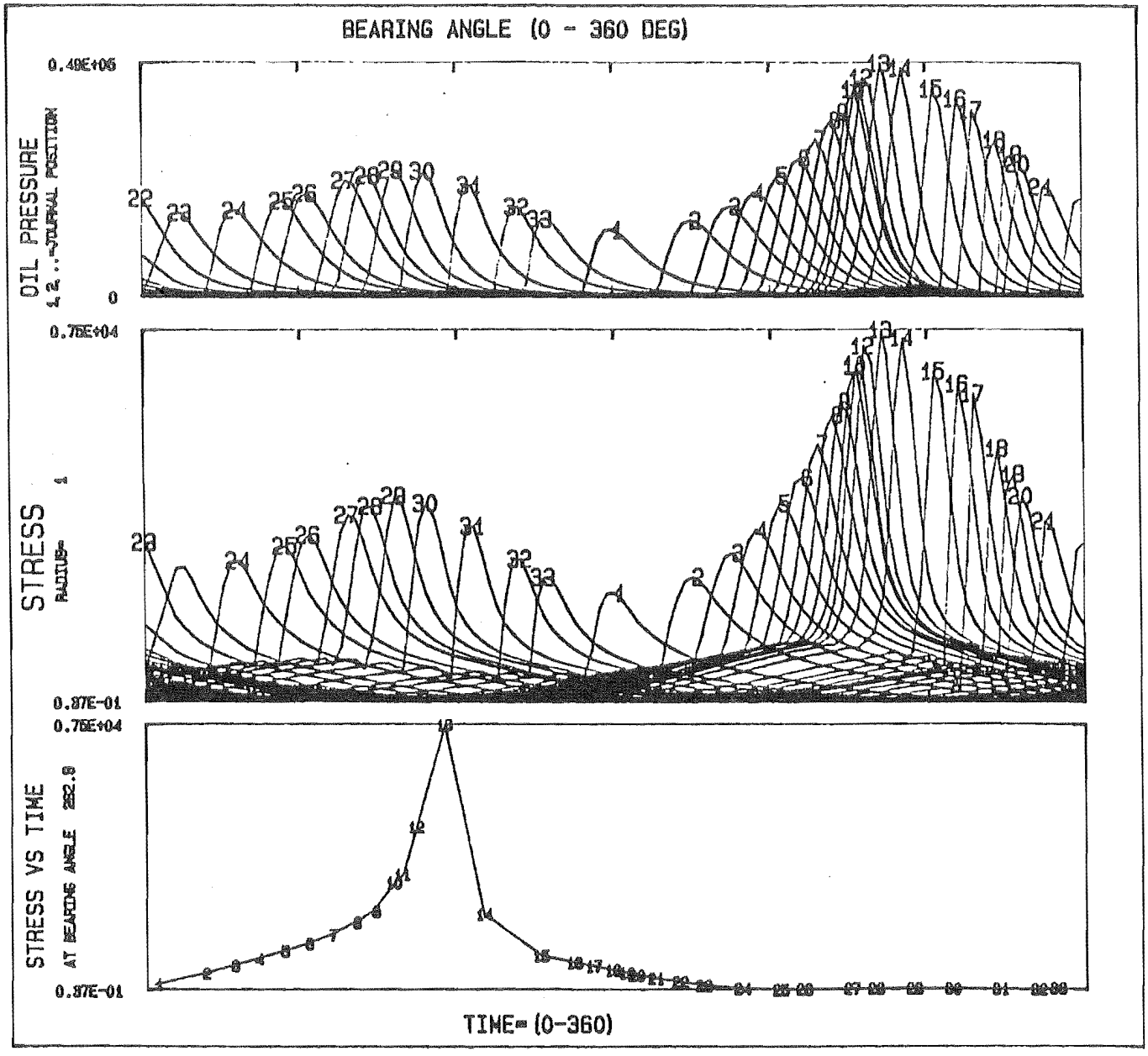

TEST NO 507 CD ROTATIONAL LOAD, 1 LAND BEARING

MAX STRESS = 0.747E+04 , AT ANGLE= 282.9

MIN STRESS = 0.375E-01 , AT ANGLE= 150.0 STRESS TYPE= MAX SHEAR

Fig.5.52

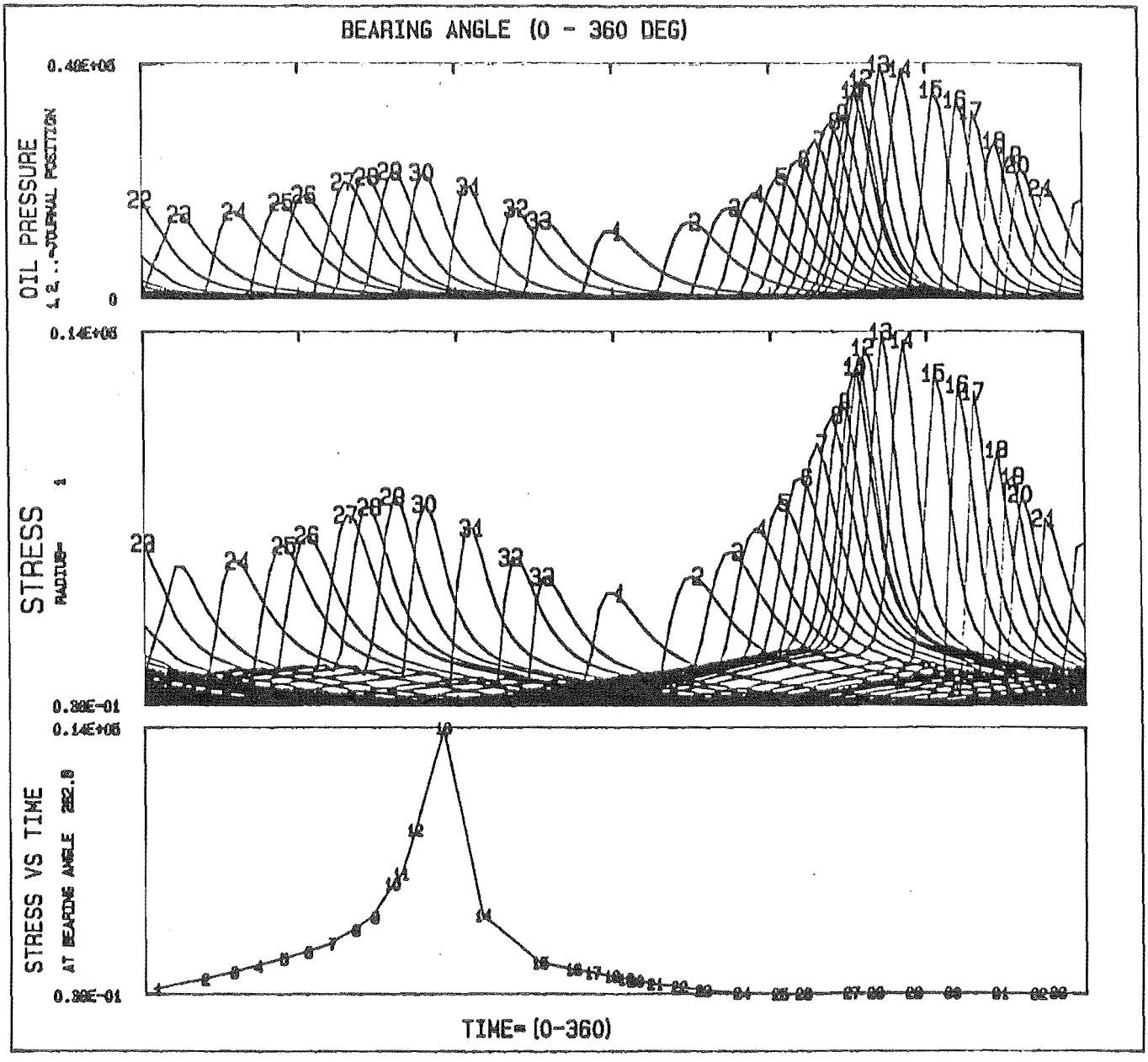

TEST NO 507 CO ROTATIONAL LOAD, 1 LAND BEARING

MAX STRESS = 0.142E+05 , AT ANGLE= 282.9

MIN STRESS = 0.391E-01 , AT ANGLE= 150.0 STRESS TYPE= MAX DISTORTION

Fig.5.53

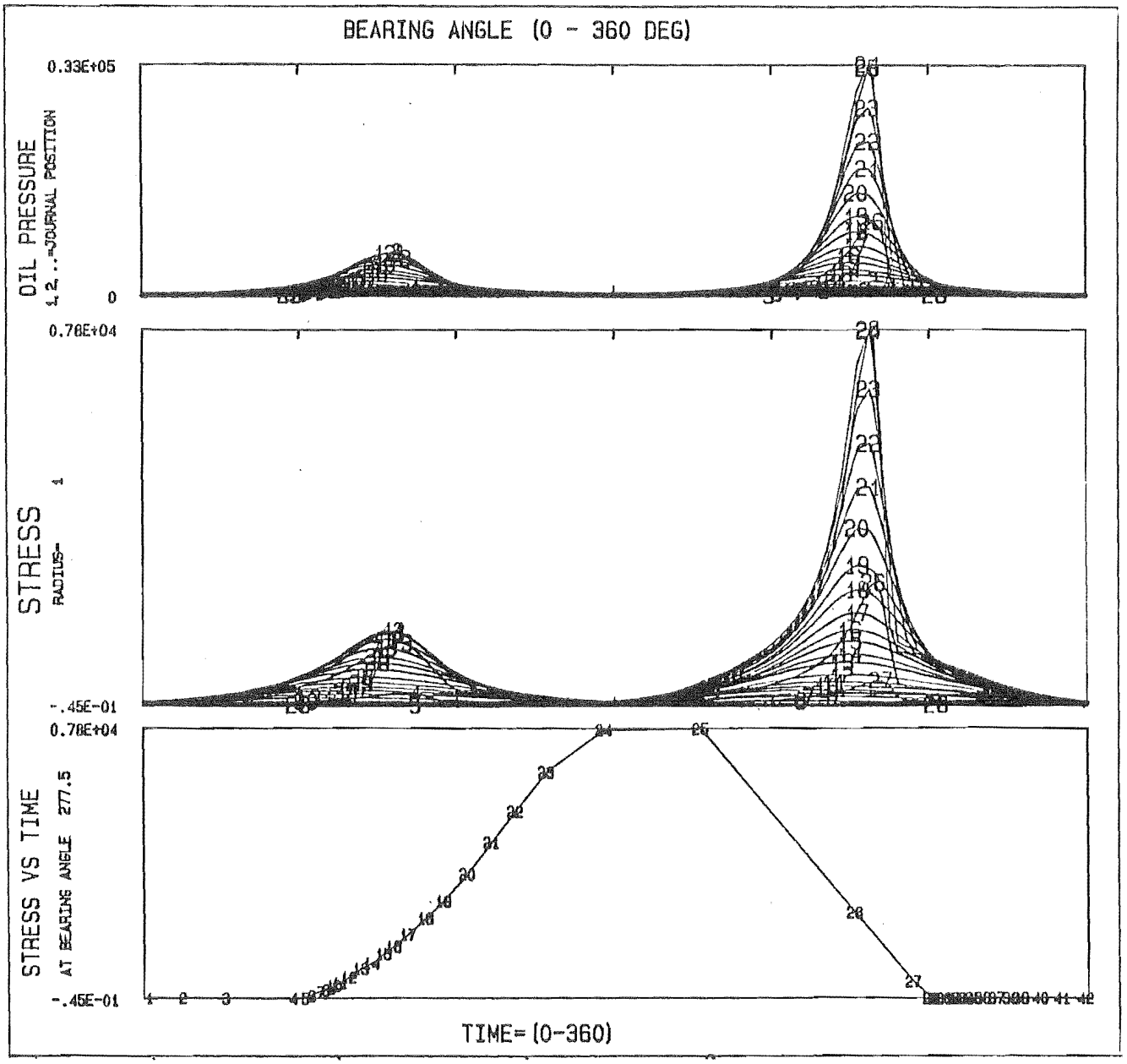

TEST NO 730 CO ROTATIONAL LOAD, 1 LAND BEARING

MAX STRESS = 0.784E+04 , AT ANGLE= 277.5

MIN STRESS = -0.454E-01 , AT ANGLE= 333.0 STRESS TYPE= MAX SHEAR

Fig.5.54

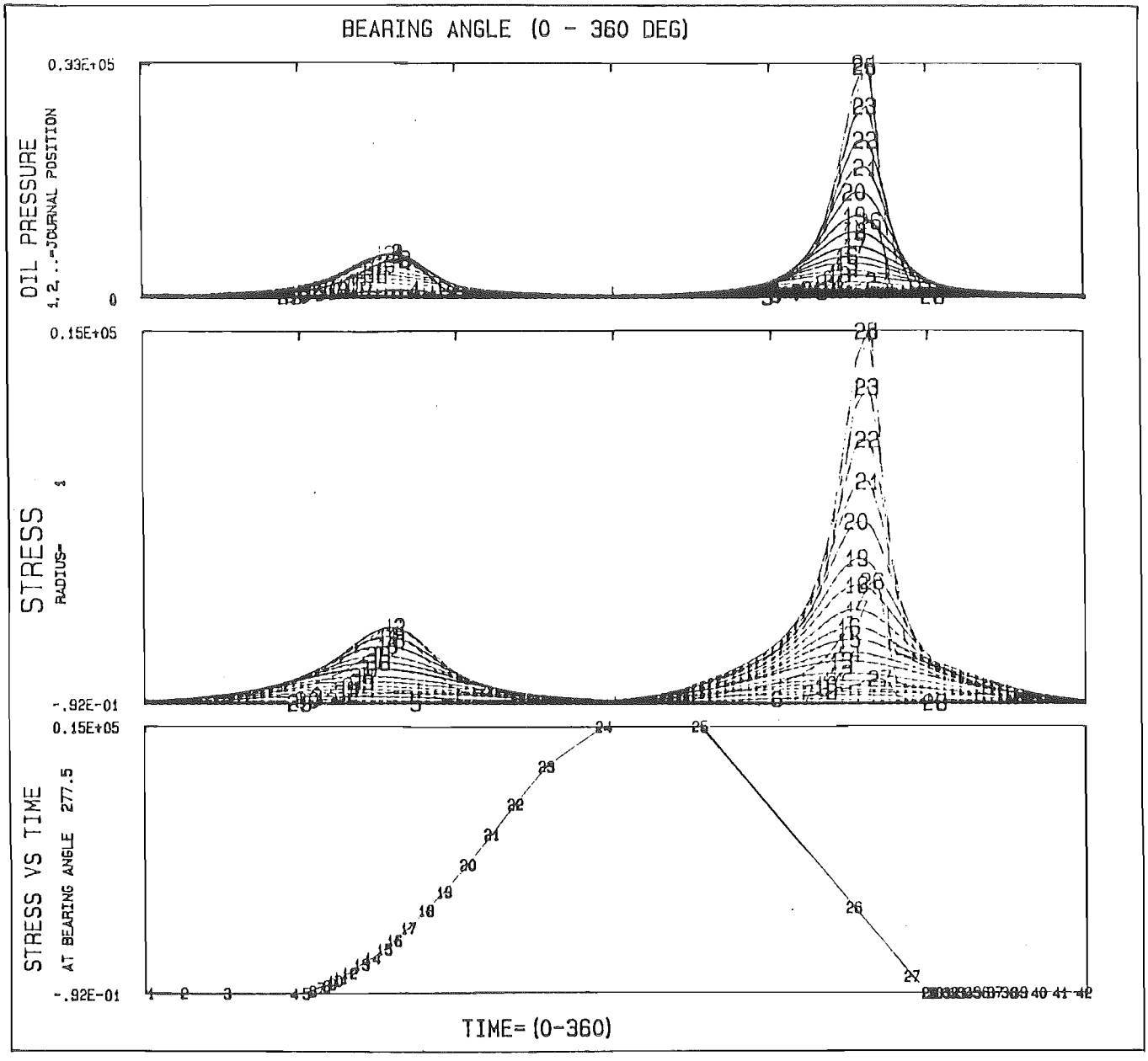

TEST NO 730 CO ROTATIONAL LOAD, 1 LAND BEARING

MAX STRESS = 0.149E+05 , AT ANGLE= 277.5

MIN STRESS = -0.917E-01 , AT ANGLE= 333.0 STRESS TYPE= MAX DISTORTION

Fig. 5.55

Test No.	Hours to *		Failures	Test No.	Hours to *		Failures
	1	2	3		1	2	3
501	37.	39.5	40.	515	26.	27.	24.
502	29.5	36.	—	516	21.	14.	26.
503	16.75	22.	—	517	12.	17.	—
504	20.	17.	—	518	6.6	6.	—
505	14.	17.5	16.	519	6.	5.8	—
506	26.	37.	—	520	24.	13.	—
507	28.	41.	39.	521	30.	32.	—
508	31.	57.	72.	522	28.	33	—
509	41.	36.	—	523	14.	16.5	—
510	30.	39.	—	524	10	13.	—
511	27.	31.	40.	525	9.	14.	—
512	27.	25.	—	526	12.	17.	—
513	29.	14.5	32.	527	35.	27.	—
514	42.	26.	44.	528	38.	35.	—

* Each case was tested up to three times

Table 5.7

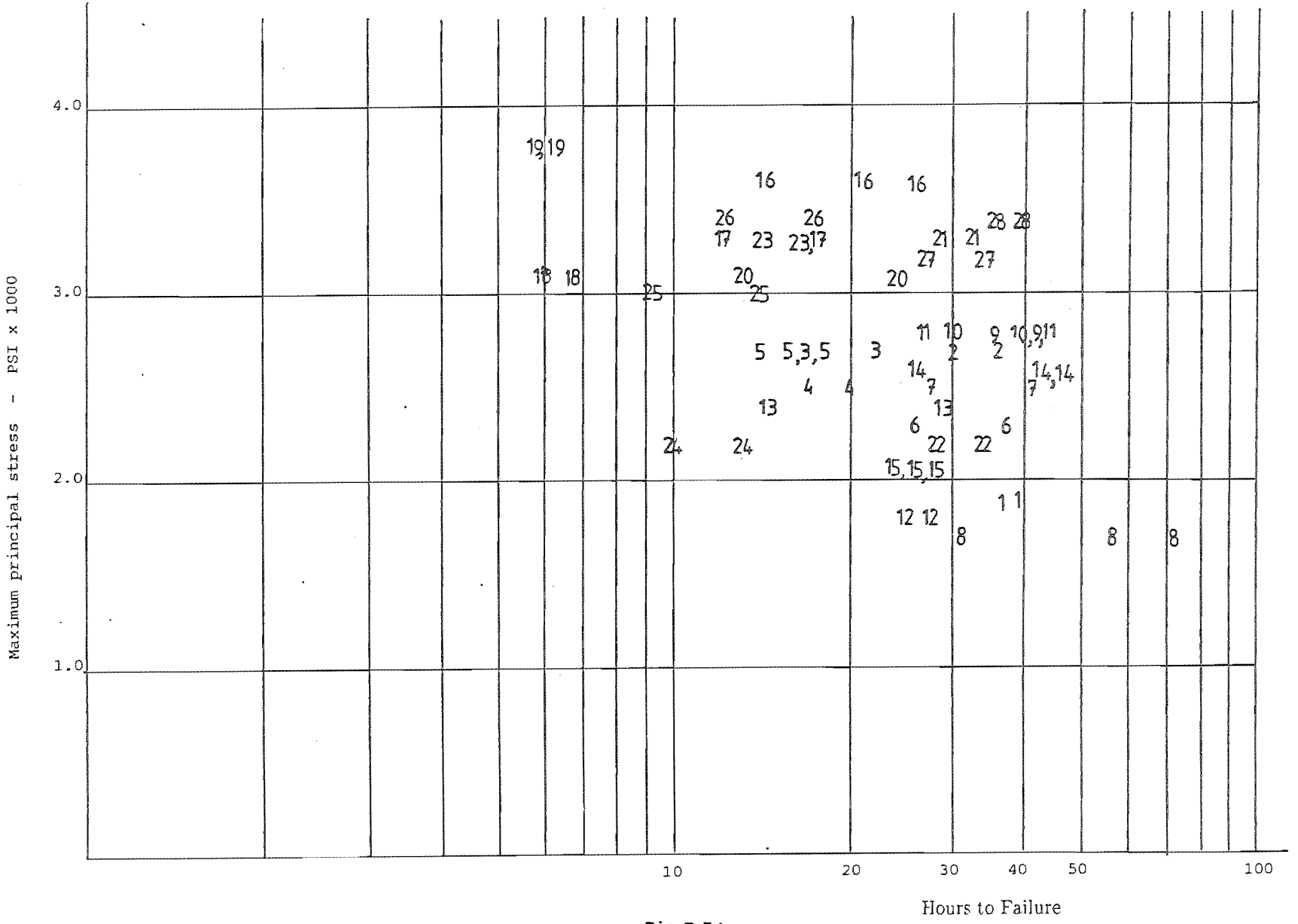
Maximum principal stress - PSI x 1000
4.0
3.0
2.0
1.0
10
20
30
40
50
100
Hours to Failure

Fig.5.56

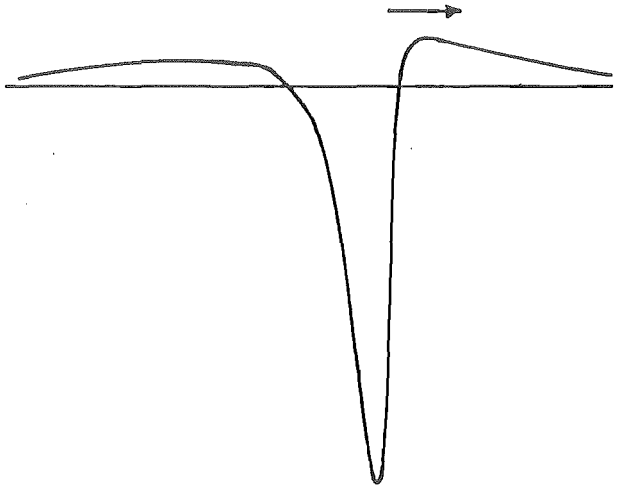

co-rotational

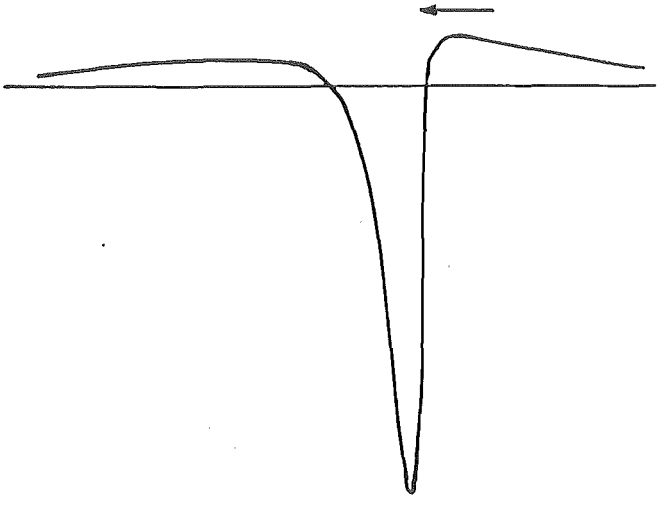

anti rotational

Fig. 557

5.4 PLOTTING THE RESULTS

One of the usual ways of investigating failure is by plotting the stresses on the modified Goodman diagram, where the maximum and minimum values of the stresses for each case at its maximum point are plotted with respect to the mean stress at that point. The aim of the diagram is to find a boundary line, which would separate the failed bearings from the unfailed ones with respect to the stresses generated in that particular material. The above data for Blundell's and Gyde's experiments are listed in Tables 5.8 and 5.9. Since Blundell's experiments were aimed at plotting an S–N diagram, as stated earlier, and since all of his bearings failed, it was not possible to draw such a boundary line on the modified Goodman diagram shown in Fig. 5.58. The stresses had a negative mean value and varied between tension and high compression, hence plotted mainly in the third quadrant of the diagram.

Gyde tested all of his bearings for 10^7 cycles, after which they were inspected for failure. The stresses, as shown in Fig. 5.59, mainly had positive mean values. The endurance limit S_e on the plot seems to be near the point 6 (i.e. S_e = 850 PSI). The boundary lines from ultimate stress of material ($S_u \approx$ 10600 PSI) to endurance limits were drawn. Some of the points marked with a circle (O), which represent the unfailed bearing tests, were outside the safe boundary limit (i.e. points 21, 28, 37, 39, 40, 41 43, 45). This indicates that the modified Goodman diagram cannot be used as a criterion of failure in dynamically loaded journal bearings which requires a more complicated stress analysis. However, the diagram shows that the bearings were mainly under positive mean stresses and all the failed bearing cases (marked with cross (X)) were under repetitive tension to compression changes.

Test No.	Max.tangential stress (PSI)	Angular position of Max. tan stress *	Min.tangential stress (PSI) at *	Mean tangential stress (PSI) at *	Max. oil pressure (PSI) at *
501	1900	288	–3410	–760	4780
502	2750	294	–13500	–5370	20000
503	2650	282	–5290	–1320	7810
504	2490	297	–19200	–8350	28200
505	2700	291	–3330	–288	4690
506	2230	297	–11082	–4376	16124
507	2490	264	–26100	–11900	36700
508	1660	288	–1650	2.8	3800
509	2770	297	–10300	–3770	15400
510	2800	282	–5800	–1500	9620
511	2780	291	–5170	–1190	8920
512	1810	300	–5760	–1970	8970
513	2400	297	–17300	–7450	25000
514	2620	306	–19900	–8630	28500
515	2070	294	–10000	–3980	14300
516	3610	291	–32600	14500	44600
517	3350	279	–9590	–3120	13400
518	3160	282	–44900	–20900	63400
519	3790	288	–20800	–8500	29200
520	3120	291	–49100	–23000	692000
521	3270	267	–45000	–20900	63000
522	2160	297	–9140	–3490	13200
523	3270	294	–19700	–8190	27800
524	2170	288	–3210	–530	5230
525	2960	291	–17500	–7250	24900
526	3390	288	–8690	–2650	13100
527	3180	294	–27900	–12300	39000
528	3380	303	–35900	–16300	50100

Table 5.8

Test No.	Max. tangential stress (PSI)	Angular position of Max. tan. stress *	Min.tangential stress (PSI) at *	Mean tangential stress (PSI) at *	Max Oil pressure (PSI) at *	Failed X Unfailed O
701	193	315	–66	63	361	O
702	274	306	–145	64	704	O
703	328	312	–97	116	524	O
704	570	306	–205	183	953	O
705	709	300	–386	161	1580	O
706	848	297	–635	106	2190	O
707	1120	297	–673	222	2450	X
708	1170	297	–708	233	2520	X
709	1720	294	–1170	273	3900	X
710	1870	294	–1210	329	3970	X
711	300	312	–91	104	473	O
712	529	306	–196	166	896	O
713	2200	291	–2000	98	5910	X
714	800	300	–391	205	1640	O
715	1910	294	–1200	357	4240	X
716	817	297	–592	113	1980	X
717	641	303	–275	183	1120	O
718	1110	297	–662	223	2260	X
719	1110	297	–628	240	2240	X
720	943	297	–723	110	2050	O
721	1240	294	–997	123	3030	O
722	1450	291	–1690	–123	4580	X
723	1380	294	–1080	151	3140	O
724	1850	294	–1130	361	3870	X

Table 5.9 (Continued)

Test No.	Max. tangential stress (PSI)	Angular position of Max. tan. stress *	Min.tangential stress (PSI) at *	Mean tangential stress (PSI) at *	Max Oil pressure (PSI) at *	Failed X Unfailed O
725	1170	294	−1170	− 2	2690	O
726	1430	294	−1360	38	3310	O
727	1300	291	−1490	− 96	3480	O
728	1570	294	−1170	201	3090	O
729	1890	291	−1790	50	4880	X
730	2480	291	−2010	235	5880	X
731	1920	291	−1970	− 25	4950	O
732	1620	291	−1420	103	3810	O
733	2030	291	−2300	−135	5410	X
734	2150	291	−2030	59	5250	X
735	2160	291	−2340	− 92	5370	X
736	1430	291	280	853	716	X
737	1830	291	−918	454	2940	O
738	1600	291	506	1050	313	O
739	1810	291	−208	802	1920	O
740	1980	291	−1330	325	3730	O
741	1980	291	−1330	325	3730	O
742	2700	291	−2000	328	5870	X
743	2610	288	−3810	−599	8270	O
744	2030	288	−2140	− 56	5370	O
745	3050	288	1130	2090	302	O
746	3050	288	1130	2090	302	O
747	3970	288	−2530	722	7700	X
748	3970	288	−2530	722	7700	O

Table 5.9

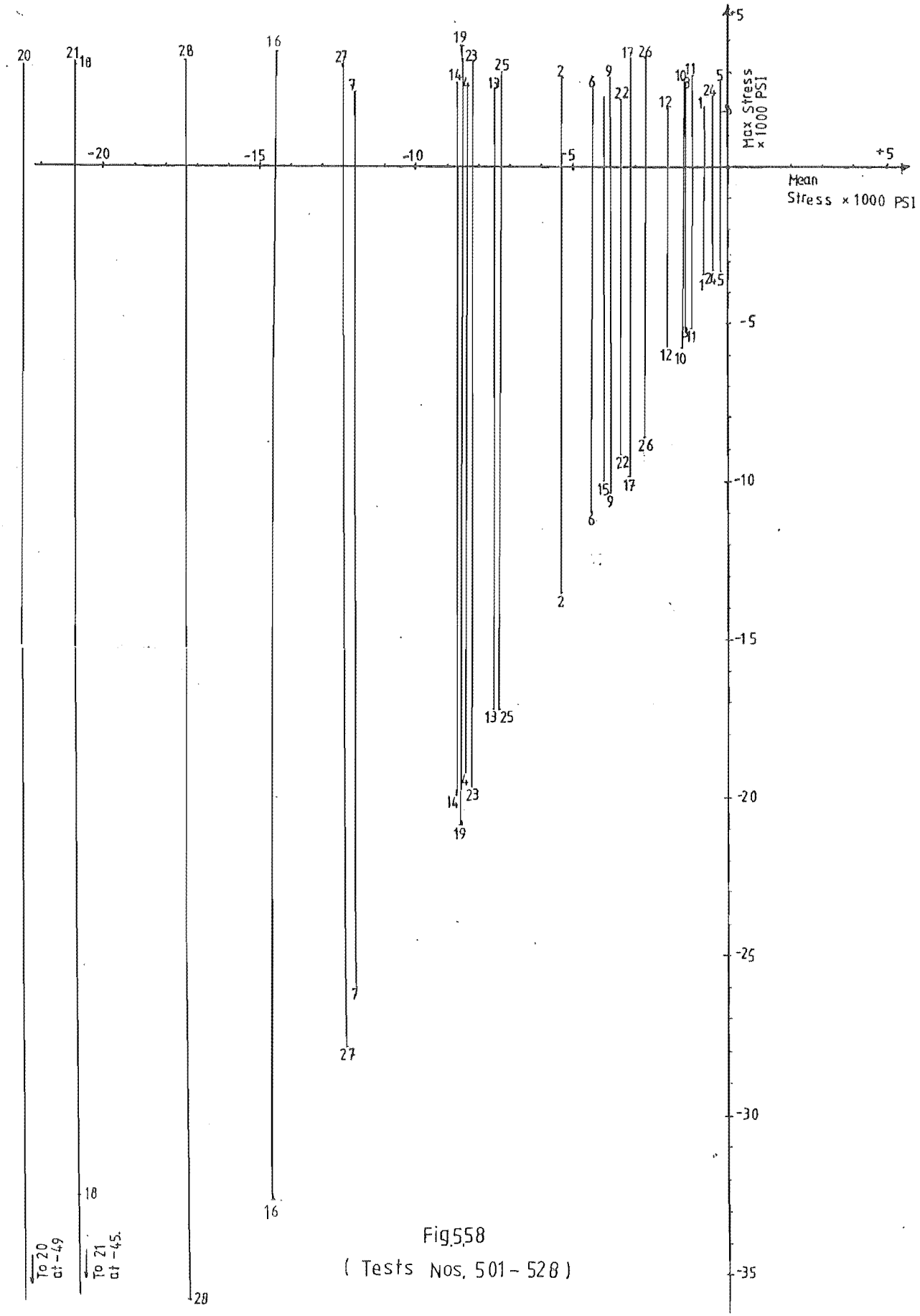

Fig.558

(Tests Nos. 501 - 528)

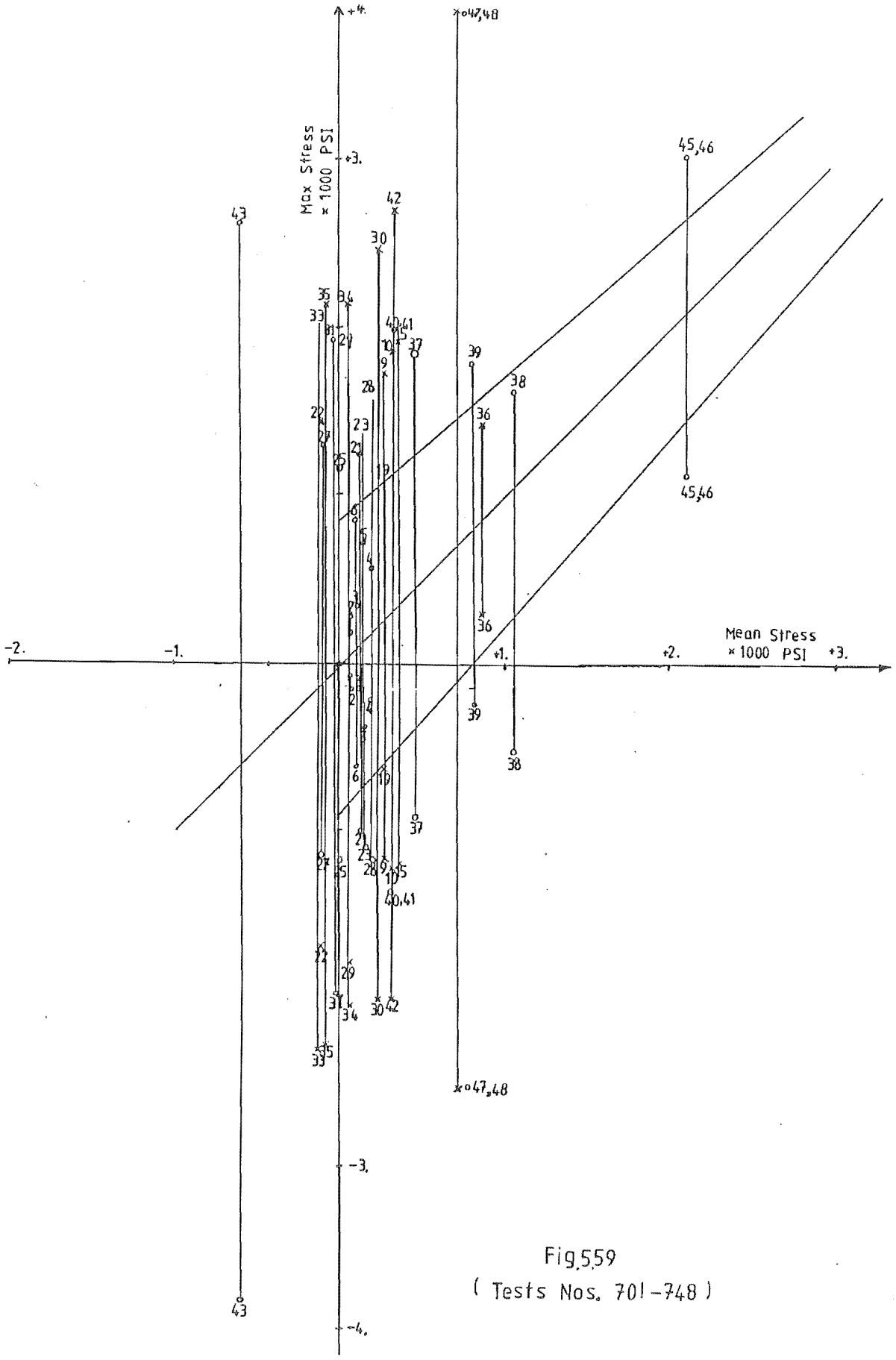

Fig.559
(Tests Nos. 701-748)

CHAPTER SIX

STRESS ANALYSIS OF A SURFACE CRACK

As it was shown in Chapter Five, there existed an interesting difference in the behaviour of the stresses at the point of maximum tangential stress between the co– and anti–rotational loading cases which was thought to be related to the scattering of the results on the S–N diagrams. At this point the stresses were under repetitive tension–compression changes and the time period between the maximum tensile stress to minimum compressive stress of a co–rotational loading case (i.e. points 23 to 24 of stress–time plot of Fig. 5.23) was found to be considerably shorter than the similar time of an anti–rotational loading case (i.e. Points 8 to 5 of Fig. 5.33). This meant that if a micro crack filled with oil existed at this point, then in a co–rotational loading case the oil has less time to escape than in an anti–rotational loading case. Consequently the squeeze action due to the crack closing increases the stresses at the tip of crack. This mechanism was thought to be partly responsible for the quicker failure of the co–rotational loading case (i.e. Case No. 518 compared to Case No. 528).

Crossland [24] investigated the effect of hydrostatic pressure on the torsional fatigue strength of cylindrical rods made of an alloy steel. He reported longer lives for the specimens, which had their surfaces protected from contact with oil by a rubber type coating similar to that used in the tyre industry. This coating was found to be resistant to the hydrostatic pressure even after a long period of testing. The machine which he used was designed to subject a cylindrical rod specimen to torsional fatigue with superimposed static fluid pressure. Later on Parry [25] investigated fatigue in a hollow cylinder which was subjected to the repeated internal pressure. The cyclic pressure was produced by reciprocating a ram inside the cylinder which was filled with oil, the

pressure being produced by compression of the oil. He also protected the surface of the specimens with the rubber film similar to that used by Crossland. The results from his tests are shown in Fig. 6.1.

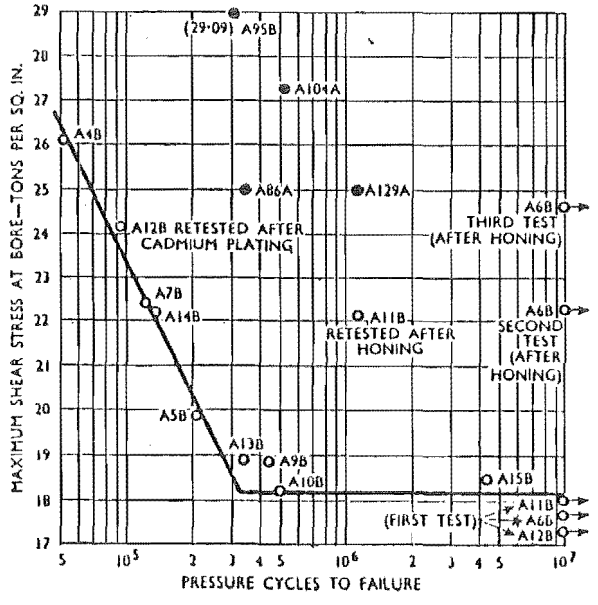

○ Unprotected cylinders.
● Bore protected by rubber film (castor oil as high-pressure fluid).

Fig.6.1

(after Parry [25])

White, Crossland and Morrison [26] did some testing to discover the effect of hydrostatic pressure on the cylindrical rods subjected to fluctuating direct stress. They designed a machine which was capable of applying repetitive tension–compression forces in a hydrostatic pressure environment. Again they covered the surface of some of the specimens with the rubber film. Fig. 6.2

shows how this protected the specimens from the early failure.

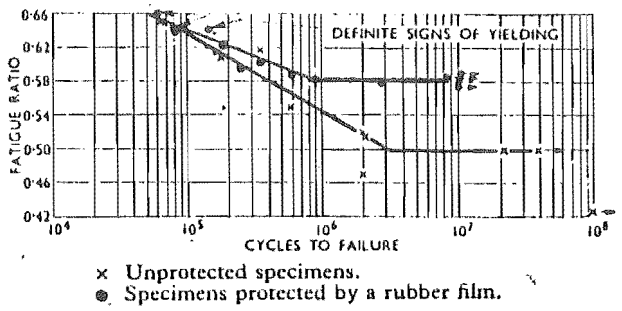

Fig.6.2

(after White, Crossland, Morrison [26])

In a separate set of tests Crossland, Morrison and Parry [27] investigated the strength of hollow cylinders subjected to repeated internal pressure similar to the experiment performed by Parry [25]. Again, they noticed that protecting the surface of specimens by rubber film lengthened their lives.

The surface of a plain journal bearing has different kinds of unevenness with magnitudes depending on the surface finish. These may be developed to micro cracks, which the oil could penetrate and generate extra stresses at their tips during crack closure. Thus, it was decided to make a more detailed investigation of this matter, by the following steps :

- Analysing the fluid in a parallel and V–shaped crack.
- Finite element representation of the crack.
- Numerical analysis of the crack closure.
- Application of the crack closure model.

6.1 ANALYSING THE FLUID IN A PARALLEL AND V–SHAPED CRACK

Fig. 6.3 shows a parallel shaped crack at the surface of a journal bearing. The crack is filled with oil and it is under direct force F due to tangential stress, which varies repeatedly from tension to compression.

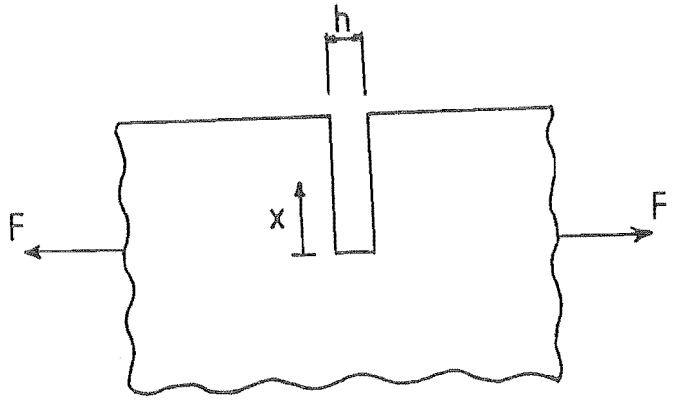

Fig. 6.3

Reynolds' equation for a one dimensional fluid flow (squeeze action) may be written as

$$\frac{\partial}{\partial x}\left(\frac{h^3}{\eta}\frac{\partial P}{\partial x}\right) = -12V \tag{6.1}$$

where h, P, V and x are crack opening, pressure inside the crack, its closing velocity, and the distance along the length of crack respectively. Since it was assumed that the longitudinal surfaces of the crack remains parallel, the crack opening and its closing velocity did not vary with x, thus

$$\frac{h^3}{\eta}\frac{d^2P}{dx^2} = -12V \tag{6.2}$$

after integrating twice with respect to x and applying the boundary conditions (6.5)

$$\frac{dP}{dx} = -\frac{12\eta}{h^3} Vx + A \tag{6.3}$$

$$P = -\frac{12\eta V}{h^3}\frac{x^2}{2} + Ax + B \tag{6.4}$$

$$@ \quad x = L \qquad P = P_o \tag{6.5a}$$

$$@ \quad x = 0 \qquad \frac{dP}{dx} = 0 \tag{6.5b}$$

A and B were found to be

$$A = 0 \tag{6.6a}$$

$$B = P_o + \frac{12\eta V}{h^3}\frac{L^2}{2} \tag{6.6b}$$

Pressure distribution P inside the parallel shape crack was then determined as

$$P = \frac{6\eta V L^2}{h^3}\left(1 - \frac{x^2}{L^2}\right) + P_o \tag{6.7}$$

(6.7) is the superposition of a parabolic and a uniform pressure distribution as shown in Fig. 6.5a.

The Reynolds' equation for a one dimensional fluid flow was also solved for a crack in which the surfaces were assumed to remain V–shape as shown in Fig. 6.4.

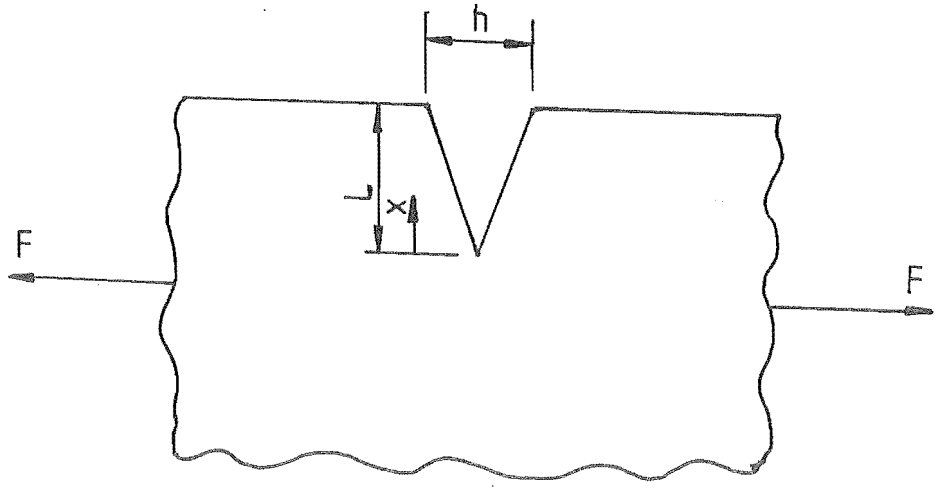

Fig. 6.4

The distance between the two surfaces h and their closing velocity v varies with x as

$$h = \frac{H}{L} x \tag{6.8a}$$

$$v = \frac{V}{L} x \tag{6.8b}$$

where H and V are the crack opening and its closing velocity at the surface of bearing. Equation (6.1) may now be written as

$$\frac{d}{dx}\left(\frac{H^3}{L^3}\frac{x^3}{\eta}\frac{dP}{dx}\right) = -12\frac{V}{L}x \tag{6.9}$$

After integrating twice with respect to x and applying the boundary conditions (6.12)

$$\frac{dP}{dx} = -\frac{6VL^2\eta}{H^3x} + \frac{AL^3\eta}{H^3x^3} \tag{6.10}$$

$$P = -\frac{6VL^2\eta}{H^3}\ell nx - \frac{AL^3\eta}{2H^3x^2} + B \tag{6.11}$$

$$@ \quad x = L \qquad P = P_o \tag{6.12a}$$

$$@ \quad x = 0 \qquad \frac{dP}{dx} = \infty \tag{6.12b}$$

A and B were found to be

$$A = 0 \tag{6.13a}$$

$$B = P_o + \frac{6vL^2\eta}{H^3}\ell nL \tag{6.13b}$$

pressure distribution P inside the V–shape crack was then determined as (6.14) and it is shown in Fig. 6.5b.

$$P = -\frac{6\eta v L^2}{H^3} \ell n\left(\frac{x}{L}\right) + P_o \tag{6.14}$$

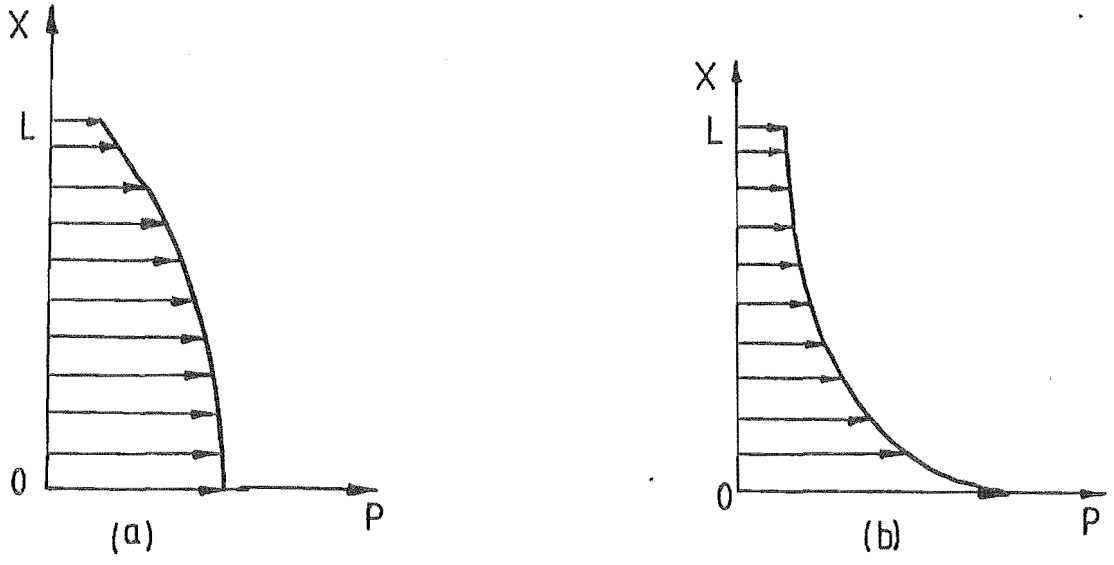

Fig. 6.5

6.2 FINITE ELEMENT REPRESENTATION OF THE CRACK

Fig. 6.6 shows an existing crack at the surface of the white metal layer. Finite element method were used to compute the force displacement parameters a_1, a_2, a_0, (defined by equation 6.22 and Fig. 6.7) and the stress at the tip of the crack due to different types of loadings. These were needed in the numerical analysis of a crack filled with oil (Section 6.3), and in calculating the stresses at its tip. Because of the symmetry, only half of the geometry was considered, which was very economical in terms of computational time. Figs. 6.7 a,c show an existing crack subjected to a parabolic and uniform pressure distribution applied to its inner surface similar to the oil pressure inside a parallel shape crack given in Section 6.1, while Figs. 6.7 b,c show the pressure distribution in a V–shape crack. Figs. 6.7 d,e show the uniform pressure and the tangential stress on the surface of bearing next to the crack respectively.

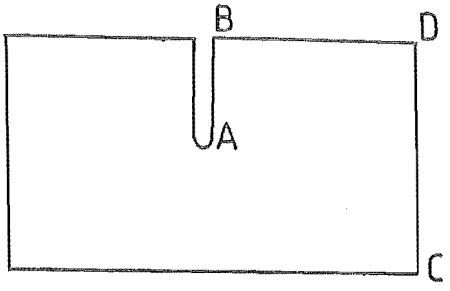

Fig. 6.6

Fig. 6.8 shows how the (25 x 10) eight noded isoparametric elements were finely graded for the .001" crack length. Tables 6.1, 6.2 give the 25 and 10 elements grading in the directions of crack length and bearing surface respectively.

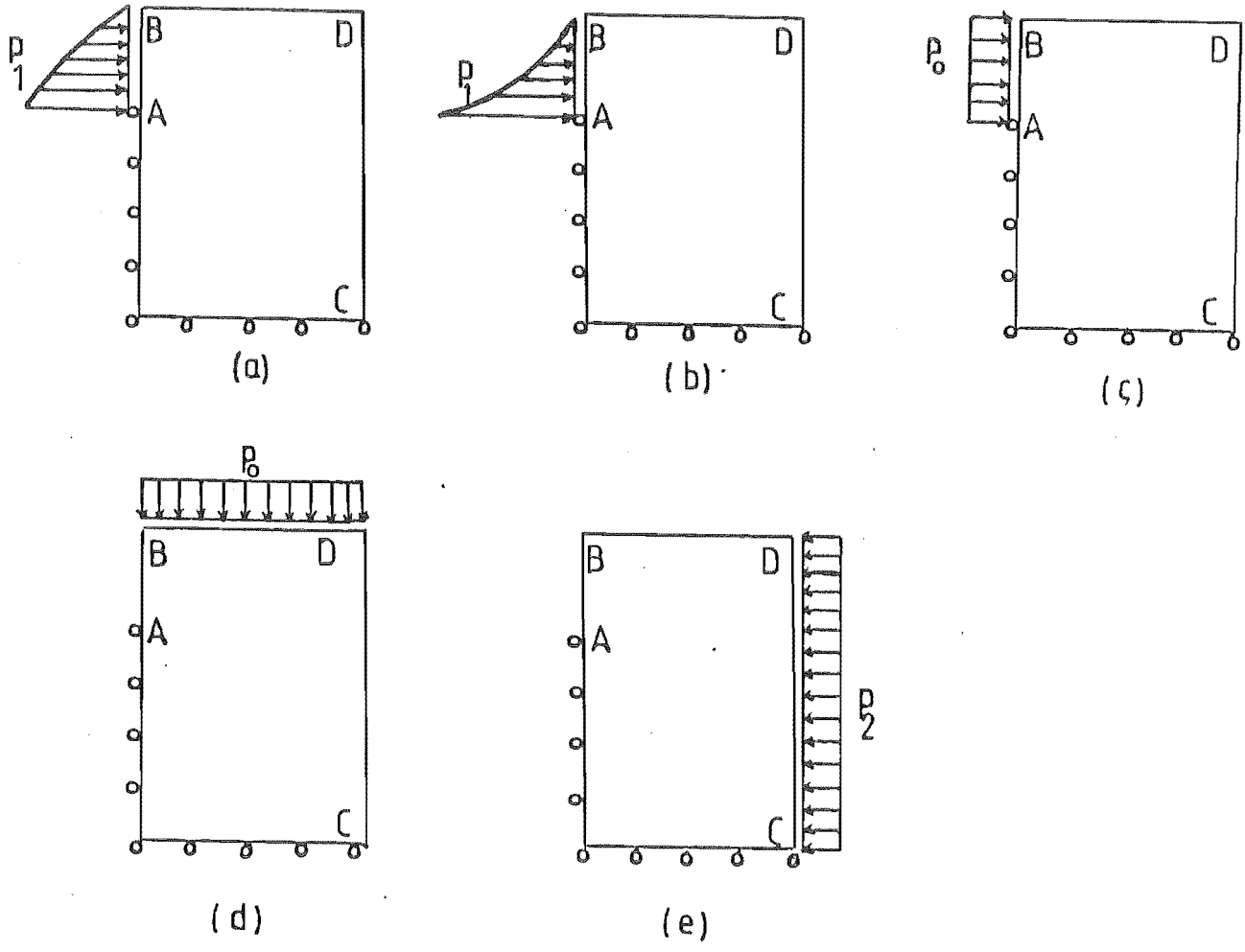

Fig. 6.7

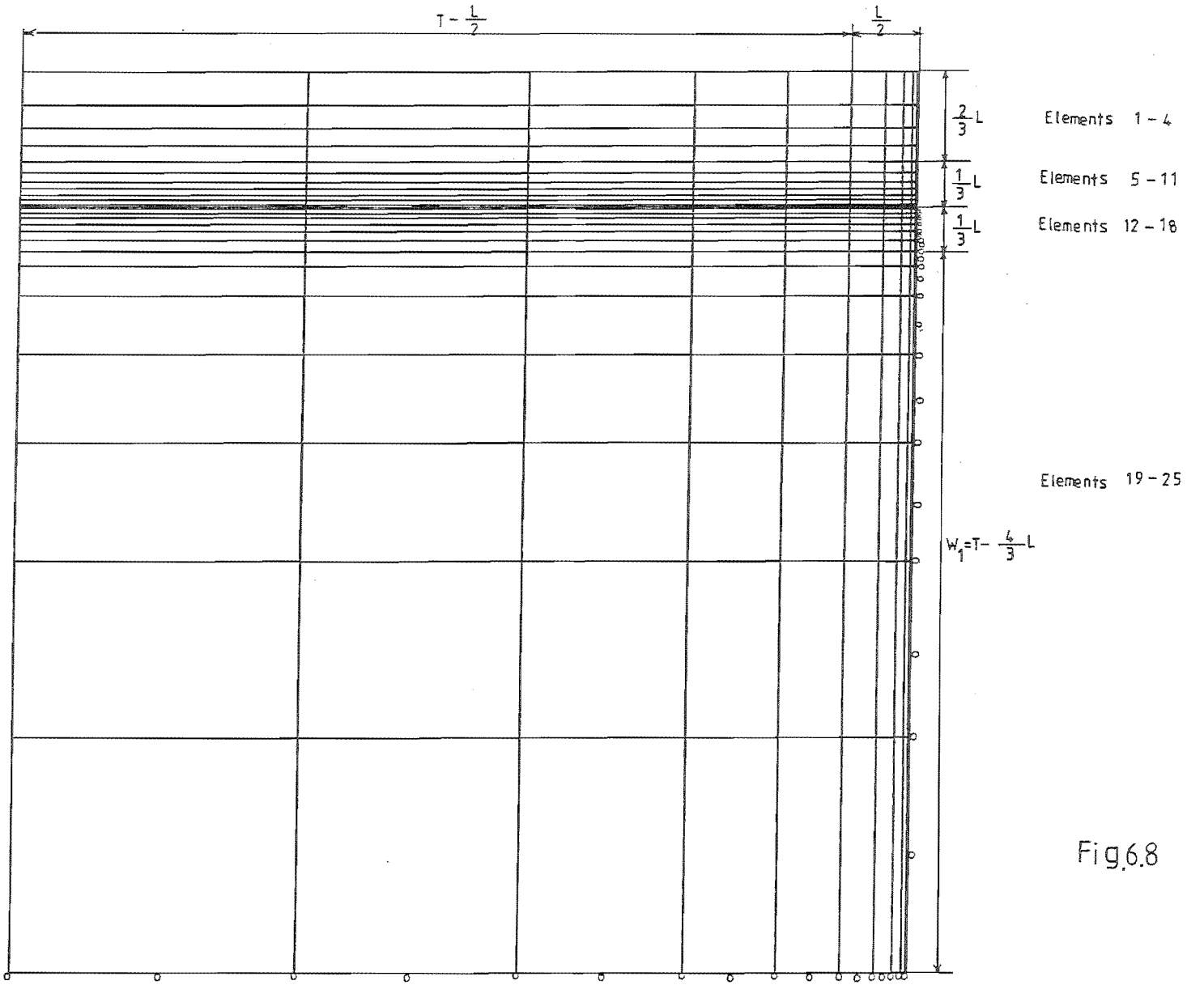
T - L/2
L/2
2/3 L
1/3 L
1/3 L
Elements 1 - 4
Elements 5 - 11
Elements 12 - 18
Elements 19 - 25
W1=T- 4/3 L

Fig.6.8

Element No.	Element Size	Total
1– 4	$\frac{15L}{60}$, $\frac{10L}{60}$, $\frac{8L}{60}$, $\frac{7L}{60}$	$\frac{2}{3}$ L
5–11	$\frac{5L}{60}$, $\frac{4L}{60}$, $\frac{3L}{60}$, $\frac{2L}{60}$, $\frac{2L}{60}$, $\frac{L}{60}$	$\frac{1}{3}$ L
12–18	$\frac{L}{60}$, $\frac{2L}{60}$, $\frac{2L}{60}$, $\frac{3L}{60}$, $\frac{3L}{60}$, $\frac{4L}{60}$, $\frac{5L}{60}$	$\frac{1}{3}$ L
19–25	$\frac{1w_1}{49}$, $\frac{2w_1}{49}$, $\frac{4w_1}{49}$, $\frac{6w_1}{49}$, $\frac{8w_1}{49}$, $\frac{12w_1}{49}$, $\frac{16w_1}{49}$	w_1

L = crack length

T = white metal thickness

$w_1 = T - \frac{4}{3} L$

Table 6.1

Element No.	Element Size	Total
1– 5	$\frac{L}{60}$, $\frac{2L}{60}$, $\frac{4L}{60}$, $\frac{8L}{60}$, $\frac{15L}{60}$	$\frac{L}{2}$
6–10	$\frac{28w_2}{360}$, $\frac{40w_2}{360}$, $\frac{72w_2}{360}$, $\frac{96w_2}{360}$, $\frac{124w_2}{360}$	w_2

$w_2 = T - \frac{L}{2}$

Table 6.2

Since the finite element program calculates the stresses at (3 x 3) gauss points within each element, the stresses were extrapolated to the nodal points and were averaged with respect to the surrounding elements. To check the fineness of the graded meshes, it was decided to compare the stresses in the vicinity of

crack tip of Fig. 6.7b subjected to uniformly distributed load of 1 psi with an analytical method [29]. Equation (6.15) gives the stresses on line AC of Fig. 6.9 at a distance r from the crack tip.

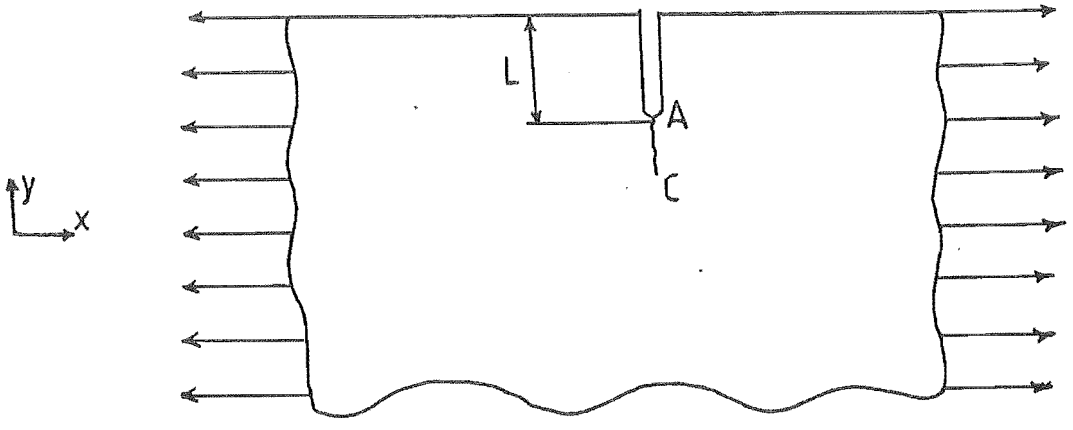

Fig. 6.9

$$\sigma_x = K_1(2r)^{-\frac{1}{2}} \tag{6.15}$$

$$K_1 = 1.1214\, L^{\frac{1}{2}} \tag{6.16}$$

For a semi infinite geometry, [28] gives Equation (6.16) to evaluate K_1. Fig. 6.10 is a plot of stresses on line AC obtained through the FEM and the analytical methods.

As it is shown, the FEM result was reasonably close to that obtained by analytical method, which indicates that an adequate number of elements were chosen around the crack tip.

As it is shown in Fig. 6.5a, the pressure inside a parallel shape crack may be treated as superposition of a parabolic and uniform pressure distribution. A

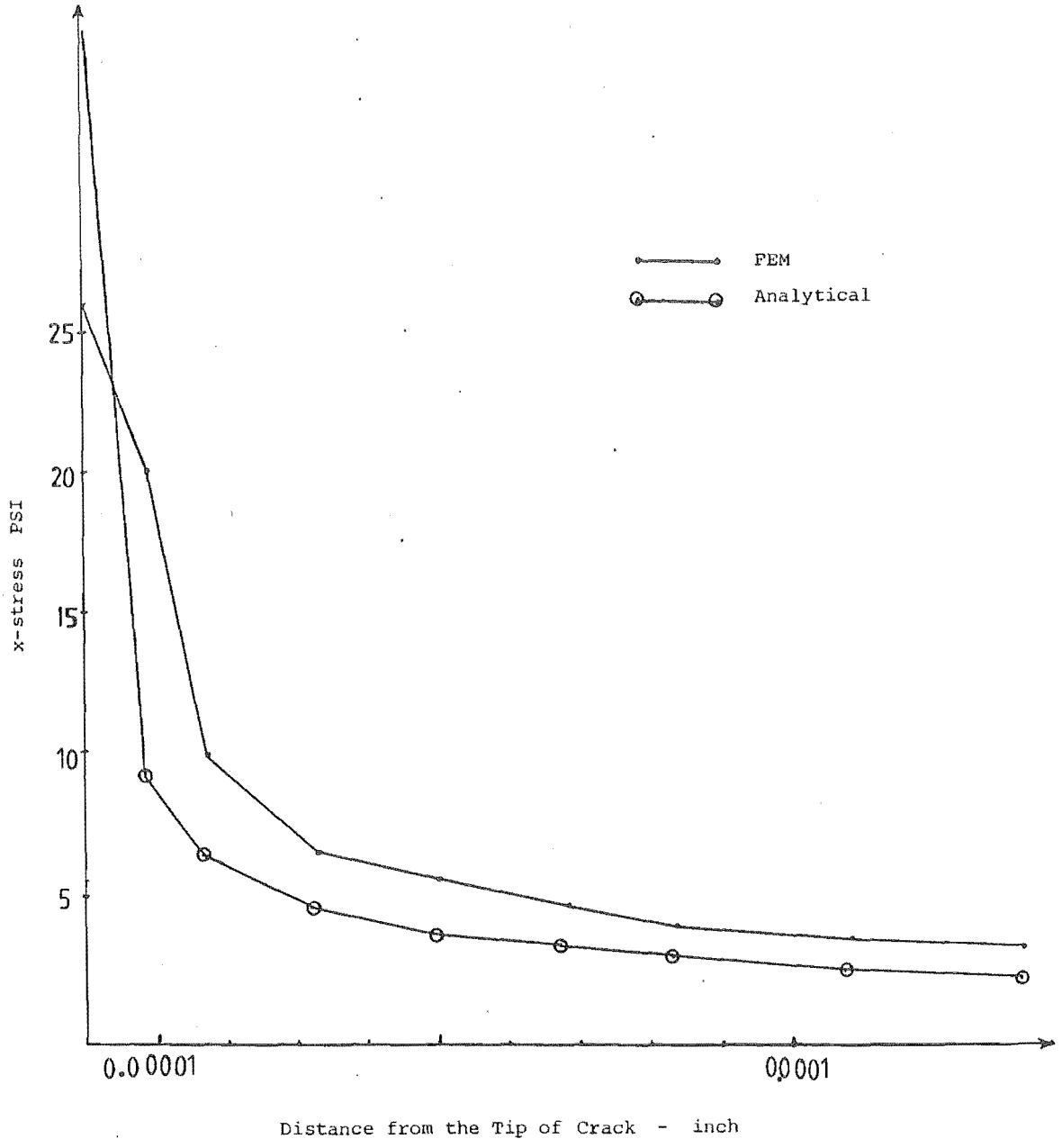

Crack length = .001"

Fig. 6.10

parabolic pressure distribution of peak 1 PSI was exerted on the crack nodes as shown in Fig. 6.7a. Displacement at the top of crack (Fig. 6.6, point B) and stresses at a point close to the tip of crack (point A) were computed. Similar procedures were followed for the other type of loading shown in Fig. 6.7 and the result for a .001" crack length are listed in Table 6.3.

Fig No.	Type of Loading	Displacement (Point B) inch	Principal stress (Point A) PSI
6.7a	Parabolic pressure on crack	0.146×10^{-9}	5.21
6.7b	Pressure in a V–shaped crack	0.153×10^{-9}	9.18
6.7c	Uniform pressure on crack	0.321×10^{-9}	7.39
6.7d	Uniform pressure on top of crack	-0.127×10^{-9}	–2.32
6.7e	Tangential stress	0.491×10^{-9}	11.3

Table 6.3

Tangential stress at the surface of bearing (Fig. 6.7e) produced the highest stress at the tip of the crack and highest displacement on the surface (Point B). The pressure in a parallel shape crack caused a surface displacement close to that of the V–shape crack but the principal stress at the tip of the latter type of crack was higher. Stresses and displacement due to a uniform load on the surface of the crack (Fig. 6.7c) were approximately three times higher in magnitude than those due to the pressure on the surface perpendicular to the crack (Fig. 6.7d), which was in compression.

6.3 NUMERICAL ANALYSIS OF CRACK CLOSURE

Equation (6.7) gives the pressure distribution P inside a parallel shaped crack. Rearranging it and substituting for velocity V results

$$V = -\dot{H} \tag{6.17}$$

$$P_1 = P - P_0 = \frac{-6\eta \dot{H}\ L^2}{H^3}\left(1 - \frac{x^2}{L^2}\right) \tag{6.18}$$

At the tip of the crack (x = 0), the parabolic pressure distribution P_1 is at its maximum value $\overline{P}_1$

$$\overline{P}_1 = \frac{-6\eta \dot{H}\ L^2}{H^3} \tag{6.19}$$

or

$$\dot{H} = -\frac{1}{6\eta L^2} H^3 \overline{P}_1 \tag{6.20}$$

(6.20) is a first order differential equation to be solved.

The crack opening H at any instant of time may be represented by (6.21)

$$H = H_1 + H_2 + H_0 \tag{6.21}$$

where H_1, H_2, H_0 are the crack opening contributions due to the pressure distribution P_1, uniform stress P_2 and uniform pressure P_0 acting on the crack as shown in Fig. 6.7.

$$H_1 = a_1\overline{P}_1 \tag{6.22a}$$

$$H_2 = a_2P_2 \tag{6.22b}$$

$$H_0 = a_0P_0 \tag{6.22c}$$

a_1, a_2, a_0 are the force displacement parameters, which were determined by the FEM method explained in Section 6.2. The expressions of (6.22) were substituted in (6.21) and the equation was rearranged for $\overline{P}_1$.

$$H = a_1\overline{P}_1 + a_2P_2 + a_0P_0 \tag{6.23}$$

$$\overline{P}_1 = \frac{1}{a_1}(H - a_2P_2 - a_0P_0) \tag{6.24}$$

$\overline{P}_1$ was then substituted in (6.20)

$$\dot{H} = -\frac{H^3}{6\eta L^2 a_1}(H - a_2P_2 - a_0P_0) \tag{6.25}$$

Equation (6.25) may be written as

$$\dot{H} = c_1H^3(H - c_2) \tag{6.26}$$

where

$$c_1 = -\frac{1}{6\eta L^2 a_1} \tag{6.27a}$$

$$c_2 = a_2P_2 + a_0P_0 \tag{6.27b}$$

(6.26) is a first order differential equation. As an initial condition, the crack was taken fully open. A first order Runge Kutta method (6.28) was used for solving it. The process was continued until a steady state condition was achieved.

$$H_{n+1} = H_n + \frac{1}{6}(K_1 + 2K_2 + 2K_3 + K_4) \tag{6.28}$$

The four factors K_1 ,.... , K_4 were defined as

$$K_1 = \Delta t\, f(t_n , H_n) \tag{6.29a}$$

$$K_2 = \Delta t\, f(t_n + \frac{\Delta t}{2}, H_n + \frac{1}{2} K1) \tag{6.29b}$$

$$K_3 = \Delta t\, f(t_n + \frac{\Delta t}{2}, H_n + \frac{1}{2} K_2) \tag{6.29c}$$

$$K_4 = \Delta t\, f(t_n + \Delta t , H_n + K_3) \tag{6.29d}$$

Using the linear interpolation, the values of c_2 at finite time steps Δt were obtained. At each instant of time, the pressure inside the crack was calculated by substituting for H in (6.24). Any negative pressure was set to zero. Having obtained the pressure inside the crack, the total maximum principal stress was then calculated as

$$\sigma = \sigma_p + \sigma_s \tag{6.30}$$

where σ_p and σ_s are the maximum principal stress contributions at the tip of the crack due to the pressure inside the crack and to the tangential stress acting on the surface of the bearing.

At this point, it was decided to check the program before applying it to the

Blundell's and Gyde's cases. This was done by considering a crack which was initially opened ($H_0 = .6 \times 10^{-5}$ inch) and then was left to close. The tangential stress and surface pressure were neglected ($c_2 = 0$ in 6.26) so that it would be possible to solve the equation analytically.

$$\frac{dH}{dt} = c_1 H^4 \tag{6.31}$$

$$\int \frac{dH}{H^4} = \int c_1 dt \tag{6.32}$$

$$H = \frac{H_0}{(1-3c_1 H_0^3 t)^{1/3}} \tag{6.33}$$

The crack opening H plotted in Fig. 6.11 was then compared at different time intervals with those obtained by the numerical method. The results were identical. The slow rate of closure was due to term c_1 in Equations (6.33), (6.27a), which was dependent on viscosity μ. Lowering the viscosity to 10 or 1 centipose increases the closing rate considerably.

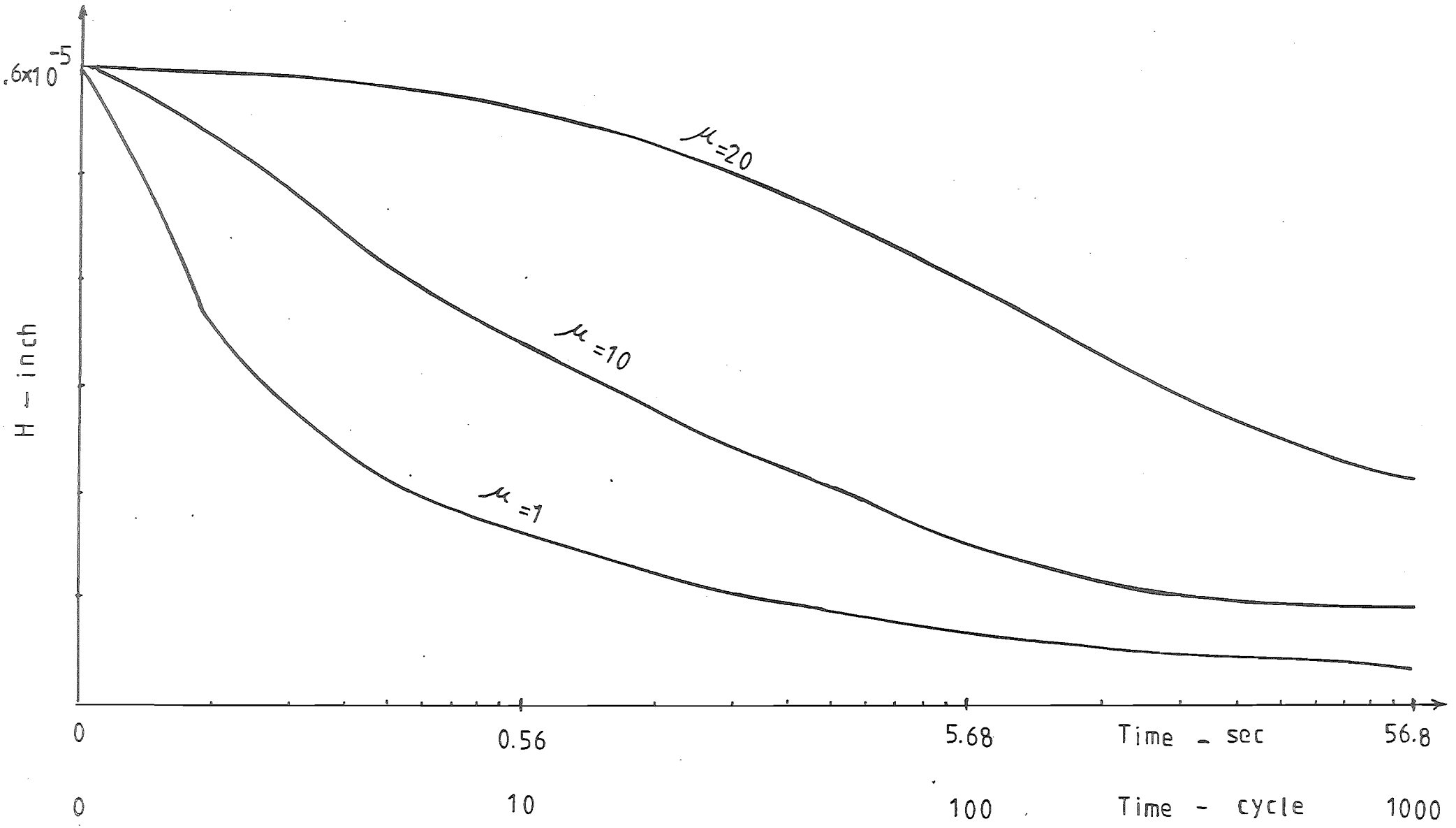
.6x10⁻⁵
H - inch
μ=20
μ=10
μ=1
0
0.56
5.68
Time - sec
56.8
0
10
100
Time - cycle
1000

Fig. 6.11

6.4 APPLICATION OF THE CRACK CLOSURE MODEL

Upon satisfactory testing of the crack closure model, it was decided to apply the model to simulation of Blundell's and Gyde's tests cases. In this way, the surface stresses which were found responsible for the failure of material were related to the stresses at the tip of a surface crack, which has oil inside it. Crack closure causes oil pressure build up inside the crack, which affects the shape of S–N diagram by increasing the stresses at the tip of the crack.

6.4.1 Application of the Crack Model to Blundell's Test Cases

Case No. 518 of Blundell, which had a sudden change of surface stresses from maximum tensile to maximum compressive, was chosen to apply the model on. To represent the results better, the time variation of stresses, pressure, and crack opening were plotted. Different instants of time (journal positions) were labelled on each plot (i.e. 1, 2, 3....). The top plot on Fig. 6.19 shows the time variation of surface stress (p_2 in Equation 6.25) at a position on the bearing surface where its maximum occurs, as a solid line. This plot also shows the time variation of surface pressure (p_0 in Equation 6.25) at the same position on bearing as a dashed line, but to a different scale (zero to maximum pressure at that position). The peak of the pressure curve is labelled with its magnitude. The next plot shows the time variation of the crack opening displacement H, which indicates very low decay (0.15235×10^{-5} inch to 0.1551×10^{-5} inch, shown only to two decimal point on the computer plot). The third plot gives the time variation of peak pressure $\overline{p_1}$ inside the crack, which shows a rapid increase in the time interval 23 to 24, that is as the maximum tangential

stress drops to its minimum value (3200 PSI to –45000 PSI). The fourth plot, with a peak at time instant 24, shows the time variation of maximum principal stress at the tip of the crack. This is the superposition of principal stress due to oil pressure generated inside the crack and to the stresses on the surface of bearing. Fig. 6.23 shows the time variation of stresses, pressure and crack opening H for Case No. 528, which was compared earlier with Case No. 518, in Chapter Five. The crack opening H is maximum at time instant 8, before the surface stress goes through a gradual decline from maximum tension to maximum compression (point 8 to point 5). The peak pressure $\overline{p_i}$ inside the crack and the stresses at its tip become maximum at this point (5).

The crack closure model was applied to the remainder of the Blundell's test cases. Figs. 6.12 – 6.23 show the stress and pressure plots for some of those cases. Maximum principal stress at the tip of the crack for each case and the corresponding times of failure listed in Table 6.4 were used in plotting the new S–N diagram shown in Fig. 6.24. A comparison of Fig. 5.56 and Fig. 6.24 indicates some shifting of points due to pressure build up inside the crack, which spreads the points in a wider stress range, but the new diagram still shows the points to have considerable scatter. Point 18, which was at a lower stress level than point 19 in Fig. 5.56 has moved to a higher stress level in Fig. 6.24. This was because of higher oil pressure and higher rate of stress drop at the maximum stress point for Case No. 518 with respect to Case No. 519 (Fig. 5.23 and Fig. 5.24). In the first case, as shown in Fig. 6.19, the stresses at bearing angle 282 vary between 3200 PSI to –45000 PSI and the pressure reaches 63400 PSI, while for Case No. 519 shown in Fig. 6.20, the tangential stress at the position of its maximum tensile value varies between 38000 PSI to –21000 PSI and the pressure reaches 29200 PSI, giving lower rate of stress drop. This causes slower crack closure and hence lower pressure build up in the crack, resulting in a lower stress at the tip of the crack for Case No. 519 compared to Case No. 518. Similar

argument may be used to explain why point 28 representing Test Case No. 528 (see Fig. 6.23), which was at a higher stress level than point 18 in Fig. 5.56, has moved to a lower stress level in Fig. 6.24, or to compare any other points between the two diagrams.

The other important parameter in spreading the points in Fig. 6.24 was thought to be the sensitivity of bearing performance to the uncontrollable fluctuation of input load reported by Blundell. This may also have produced the variation in failure positions (Table 5.5 page 154) and in times to failure (Table 5.7 page 163) reported by Blundell for his nominally identical tests. Hence, it was decided to investigate how a 600 LbF change in input amplitude, that is the uncertainty reported by Blundell, may affect two of the points on the S–N diagram (points 19 and 20 in Fig. 6.24). A 600 LbF increase of load amplitude in the directions of A and B axes in Test No. 519 (Fig. 6.2.5) increases the pressure and stresses on the surface of the bearing and the stresses at the tip of the crack (point 19 shifts to 1.9 x 10^5 PSI stress level on Fig. 6.24). A 600 LbF reduction of load amplitude in the directions of A and B axes in Test No. 520 (Fig. 6.26) reduces the stresses at the tip of the crack to 1.9 x 10^5 PSI. These show the sensitivity to small variations of input loads on the stresses inducing in a bearing shell. Experimentalists in this field should be aware of this. Another parameter which may produce scattering of results on the S–N diagram is the deviation of the theoretically generated input load diagram, from the actual experimental load diagram (Fig. 3.3 a, b). However, sensitivity tests have not been conducted for this parameter.

Shape of the crack may also become an important parameter, influencing the stresses at the tip of the crack. Similar steps as explained for a parallel shape crack were taken for a V–shape crack. Force displacement factor a_1 required in Equation 6.25 and stresses at the tip of the crack given in Table 6.3 were used for this purpose. Fig. 6.27 shows the pressure and stress plots for Case No. 518; the

lay out was explained earlier. Again, the maximum principal stress at the tip of the crack for all the cases listed in Table 6.5 were used in plotting the S–N diagram shown in Fig. 6.28. A comparison of Figs. 6.24, 6.28 show that the V–shaped crack assumption gave higher stress levels than the parallel shaped crack, due to the higher stress factor given in Table 6.3.

In the finite element computation of stresses at the tip of the crack, for simplicity plane strain was assumed (i.e. the crack was assumed infinitely long in the axial direction). However, a crack may have other shapes in an axial direction, such as part circular or semi eliptical. Rooke and Cartwright [29] have shown that the stresses at the tip of the first type crack may be as low as 47% of stresses due to plane strain assumption, while this figure may vary between 55% to 95% for the latter type crack depending on the side ratio of ellipse. Hence the shape of the crack in the axial plane could have a significant effect on fatigue life and be another source of scatter.

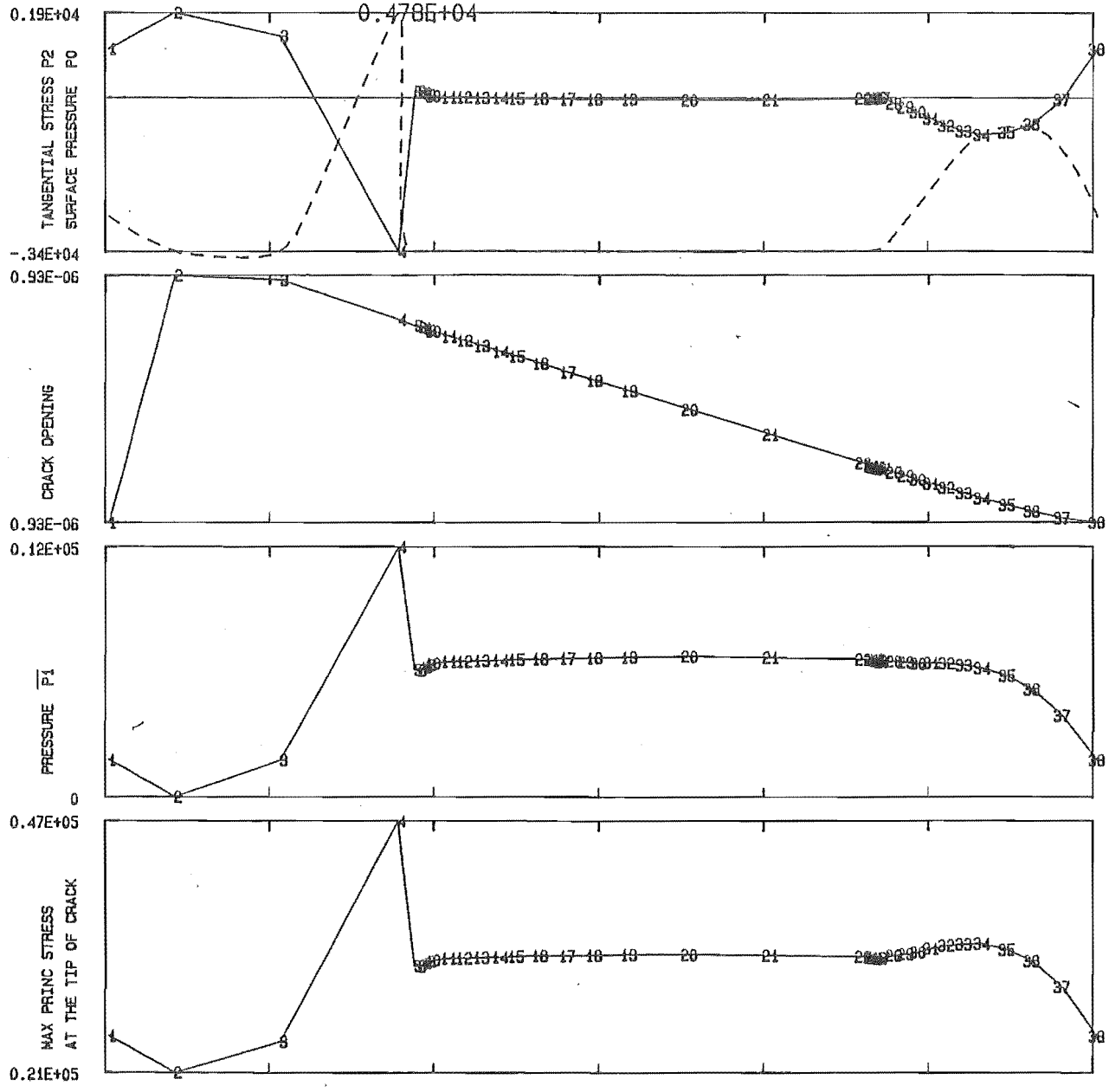

TEST NO 501 CO ROTATIONAL LOAD, 1 LAND BEARING

Fig. 6.12

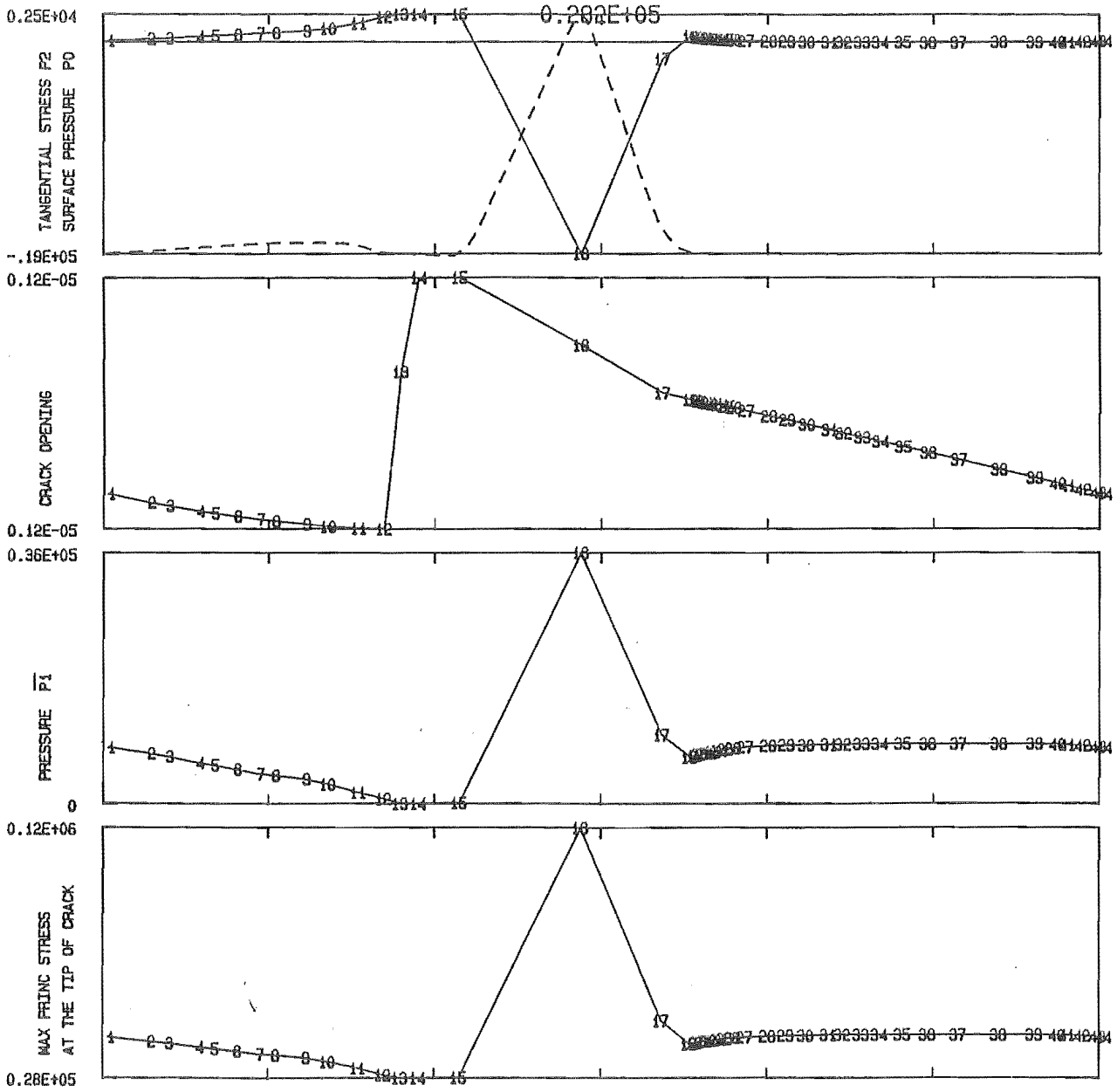

TEST NO 504 CO ROTATIONAL LOAD, 1 LAND BEARING

Fig.6.13

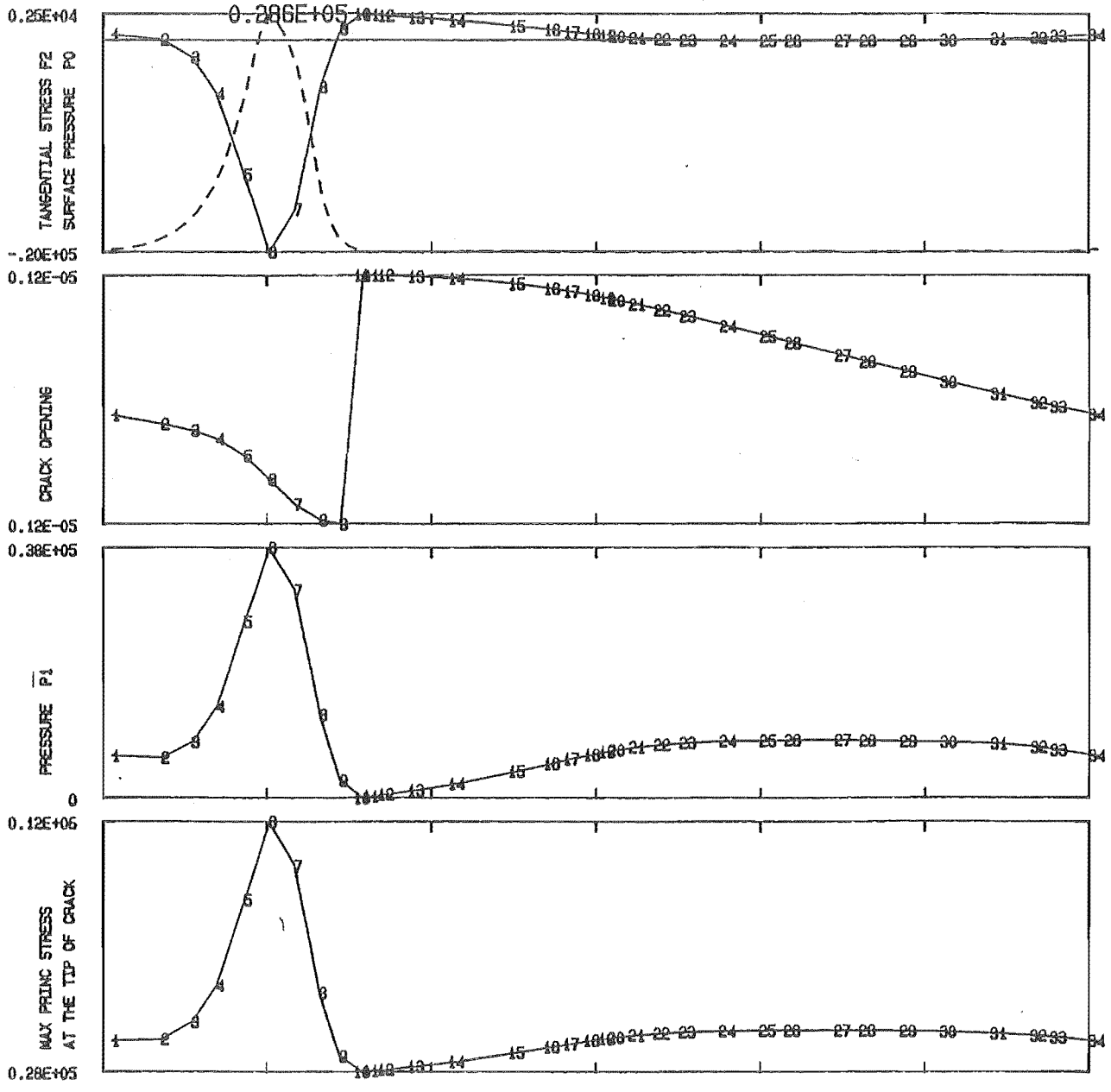

TEST NO 507 CO ROTATIONAL LOAD, 1 LAND BEARING

Fig.6.14

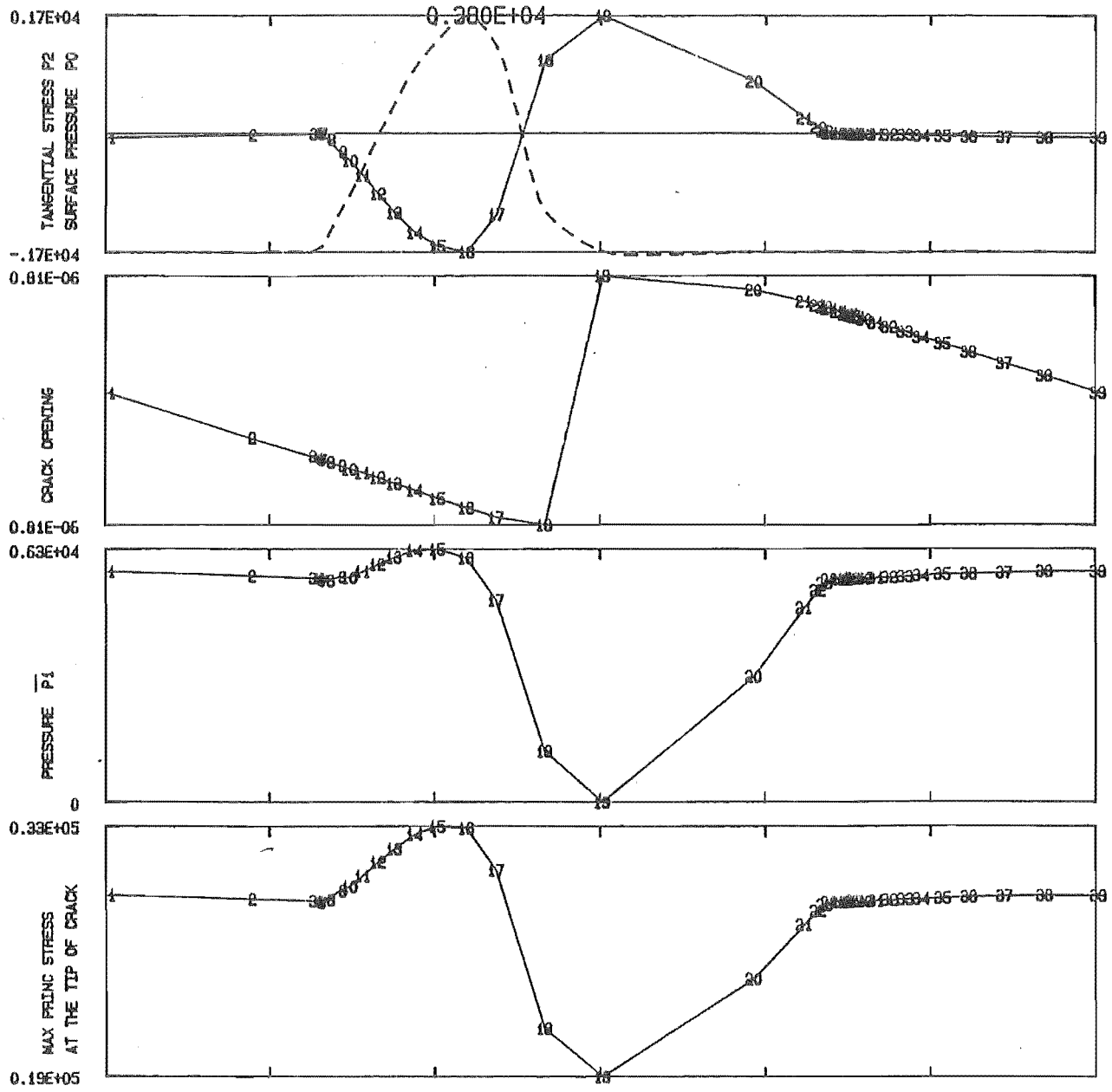

TEST NO 508 ANTI ROTATIONAL LOAD, 1 LAND BEARING

Fig.6.15

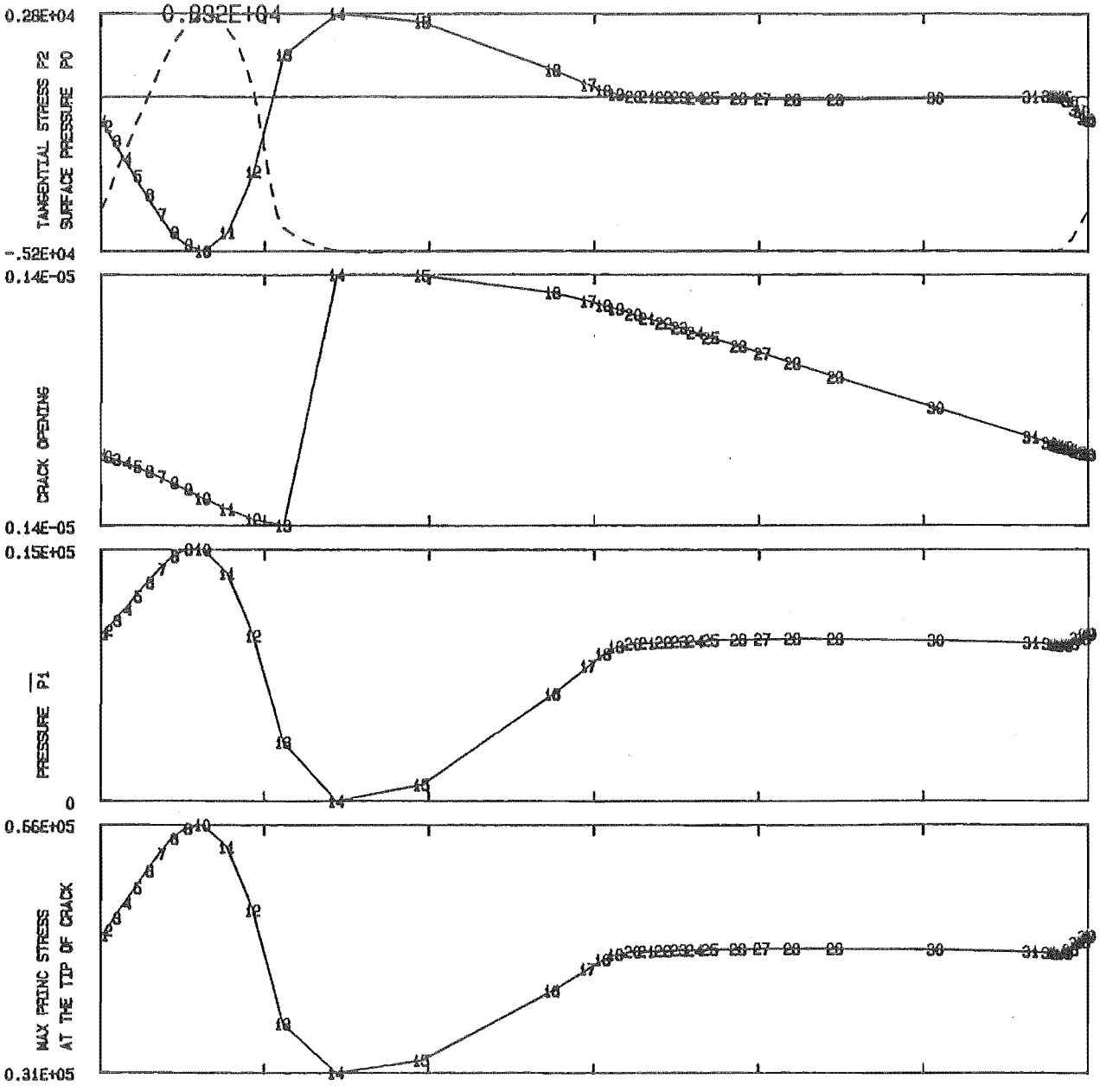

TEST NO 511 ANTI ROTATIONAL LOAD, 1 LAND BEARING

Fig.6.16

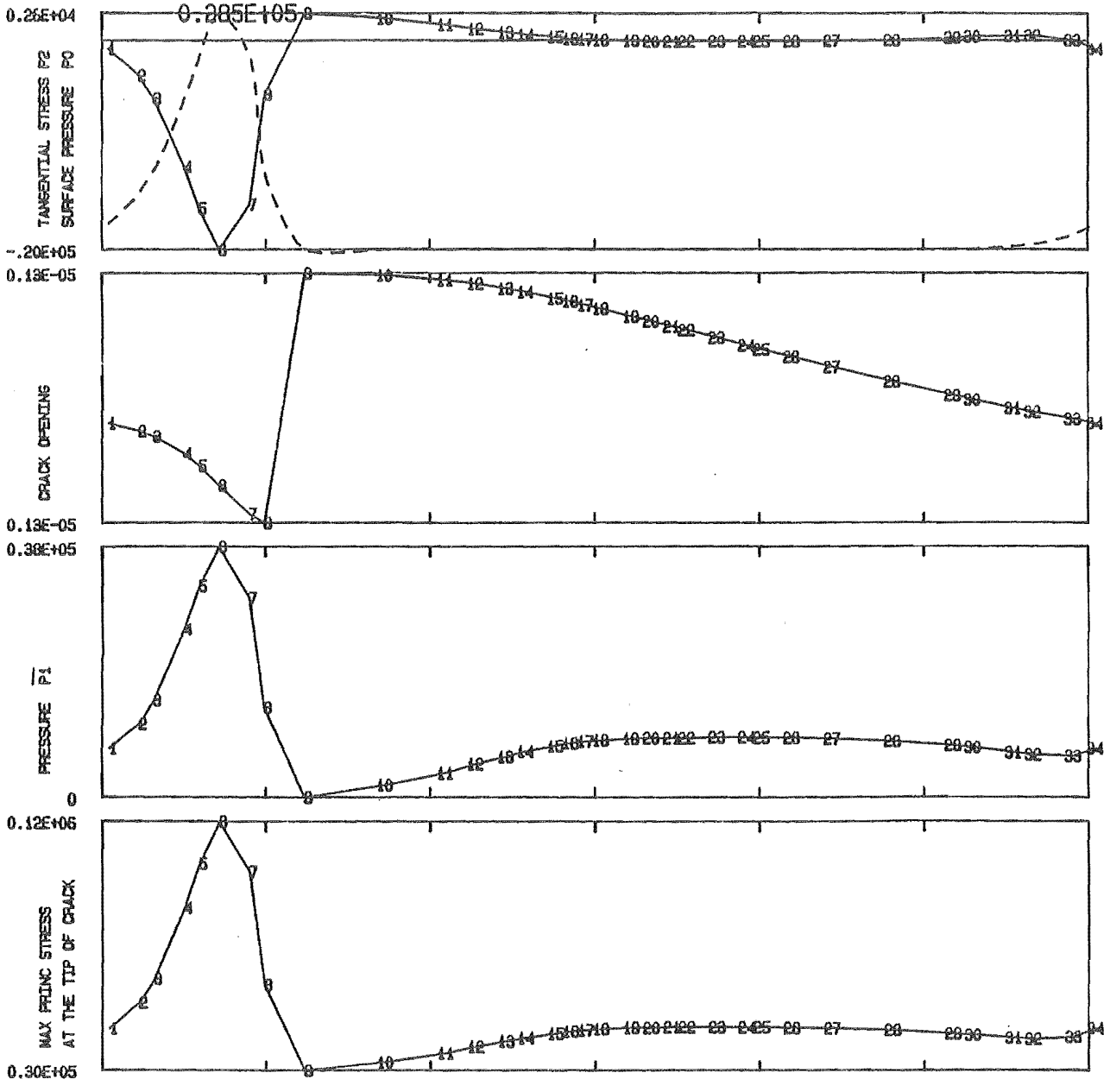

TEST NO 514 ANTI ROTATIONAL LOAD, 1 LAND BEARING

Fig.6.17

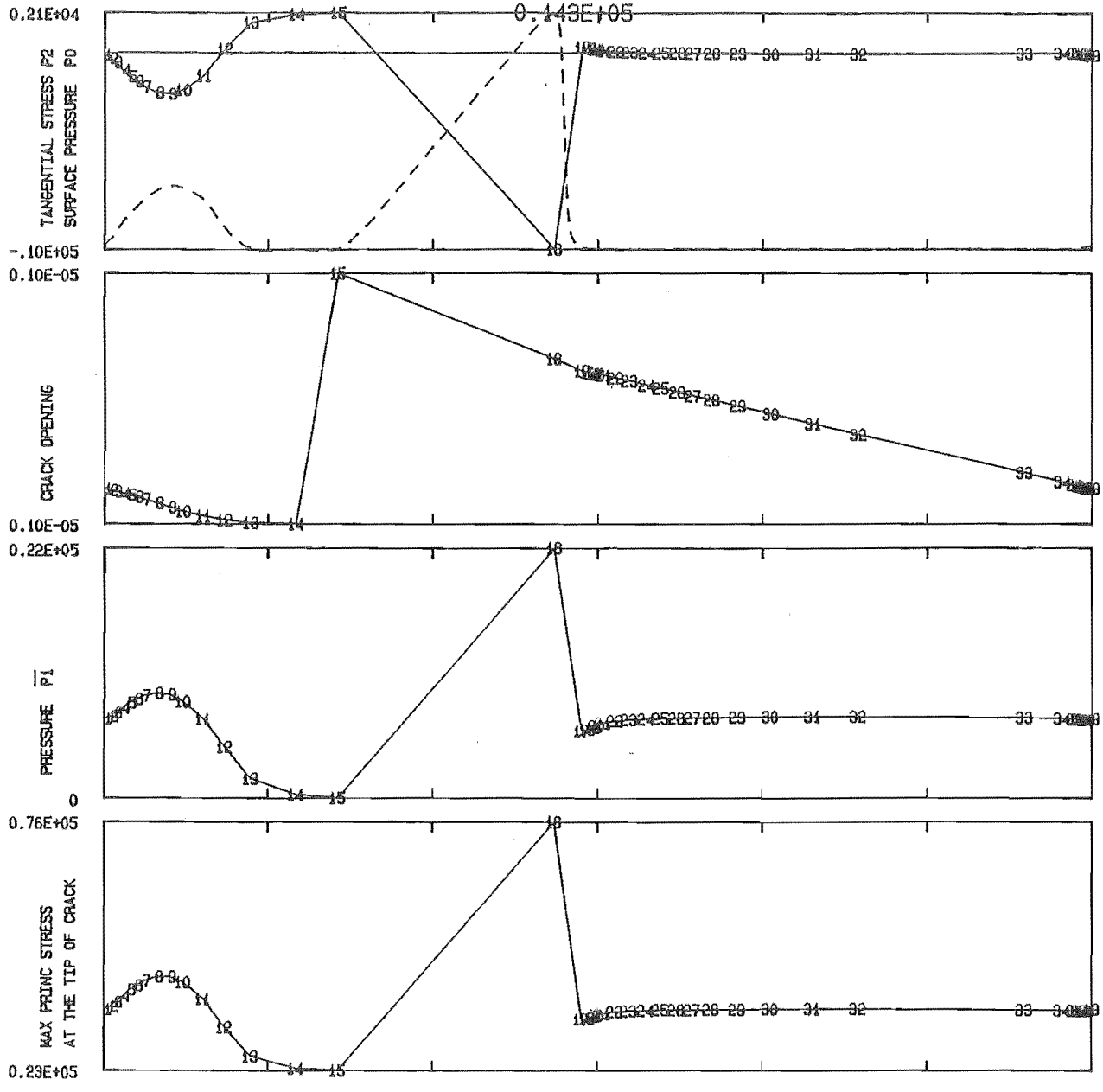

TEST NO 515 CO ROTATIONAL LOAD, 2 LAND BEARING

Fig.6.18

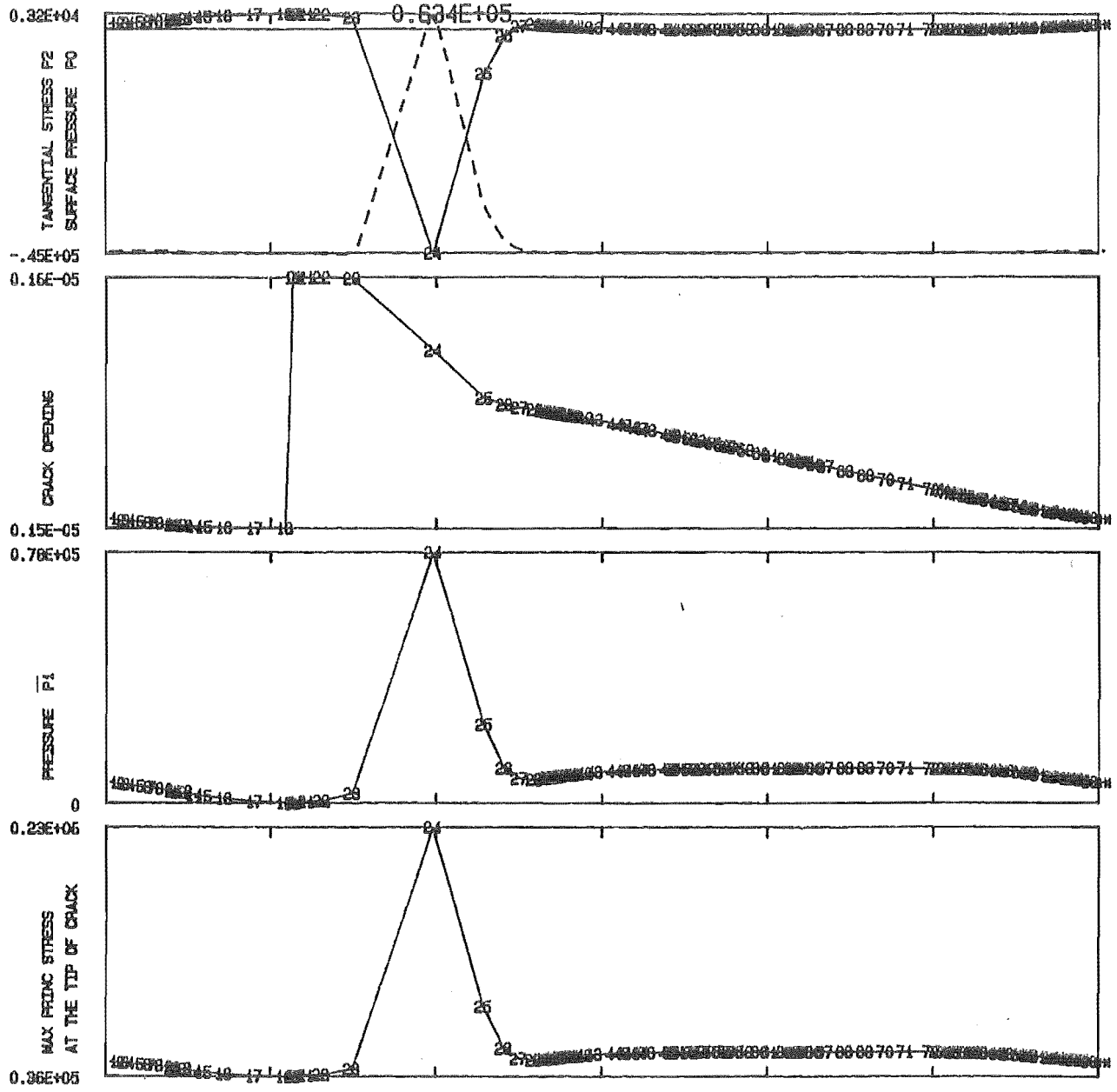

TEST NO 518 CO ROTATIONAL LOAD , 2 LAND BEARING

Fig 6.19

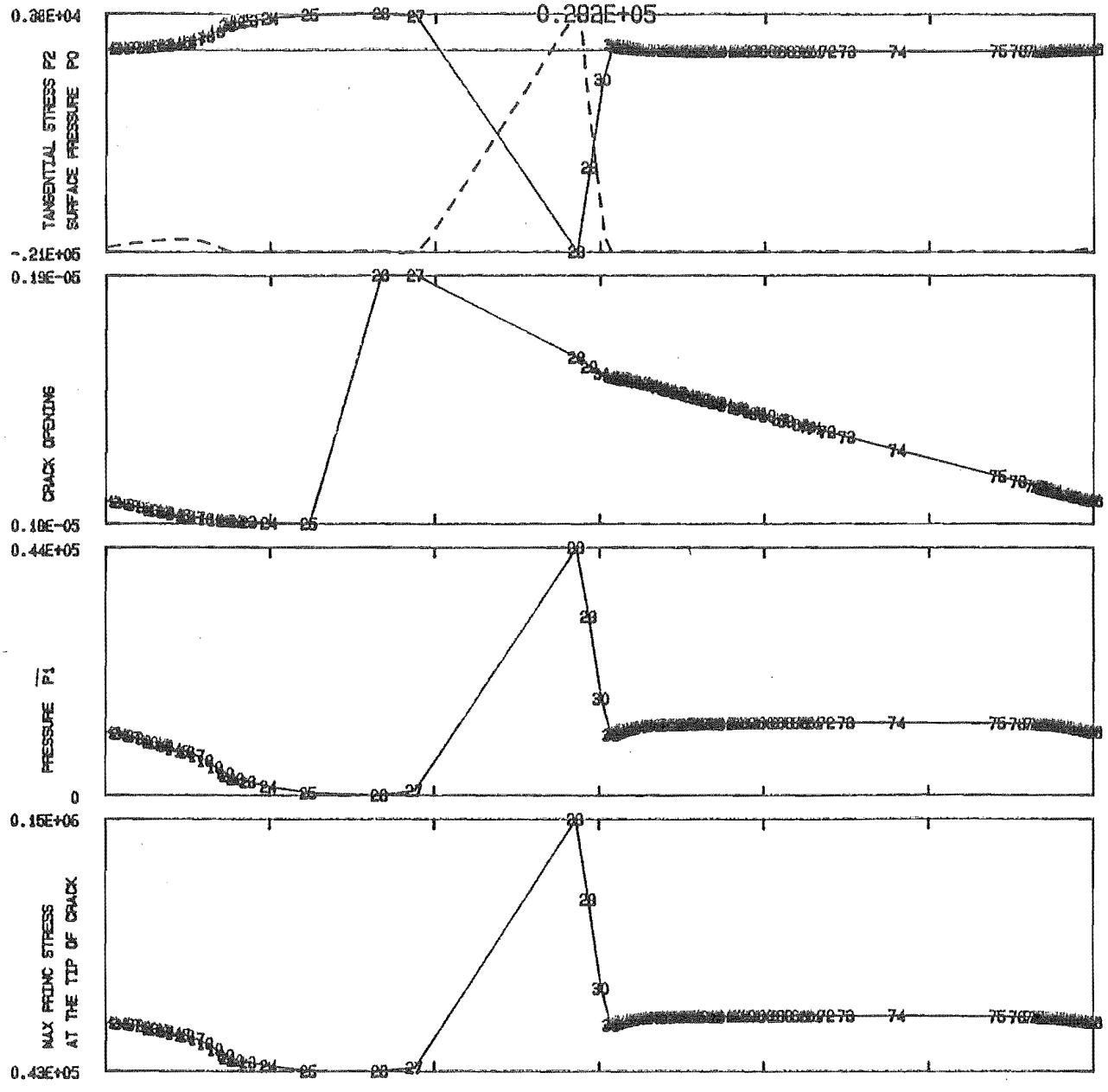

TEST NO 519 CO ROTATIONAL LOAD , 2 LAND BEARING

Fig.620

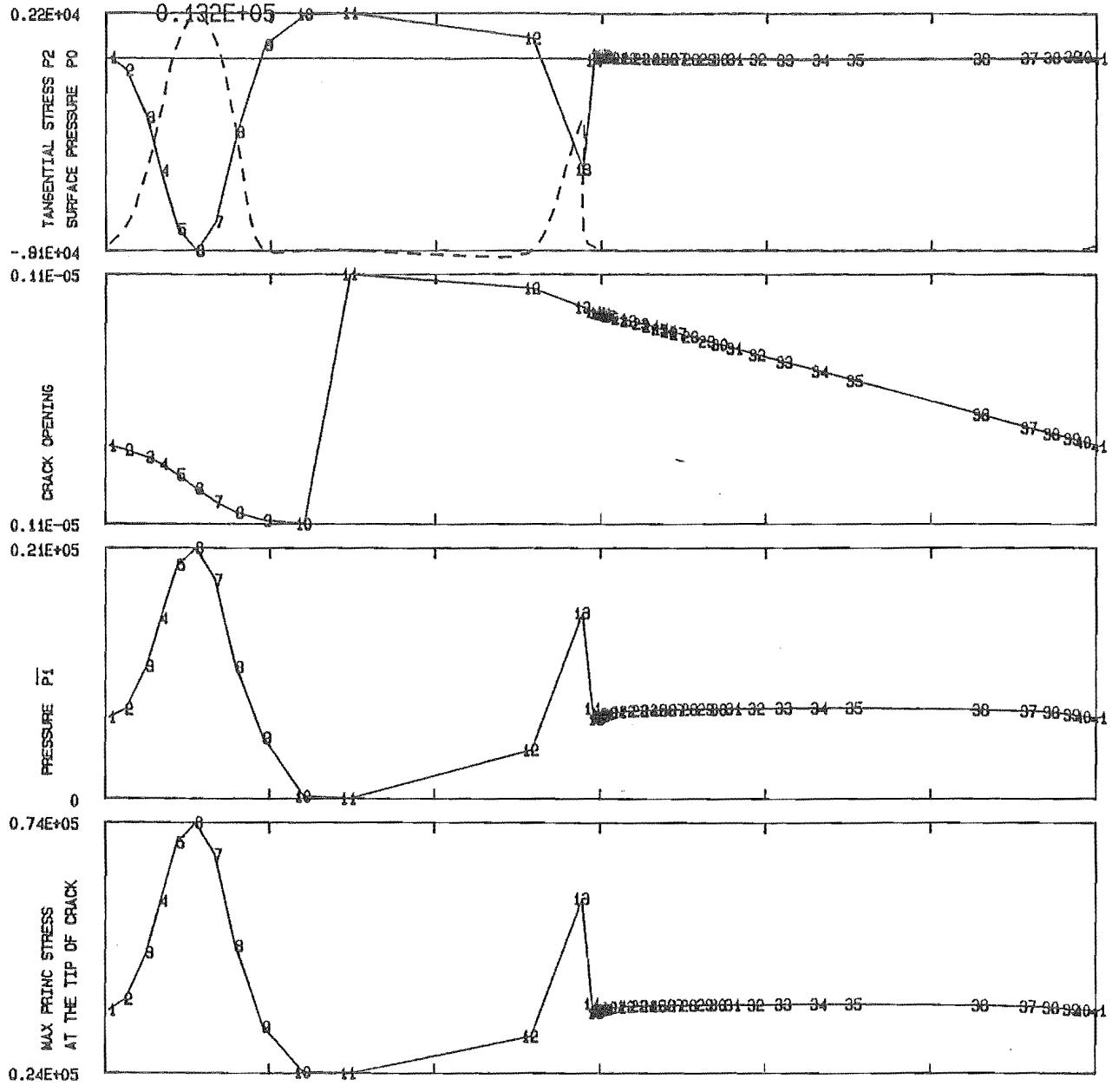

TEST NO 522 ANTI ROTATIONAL LOAD, 2 LAND BEARING

Fig.6.21

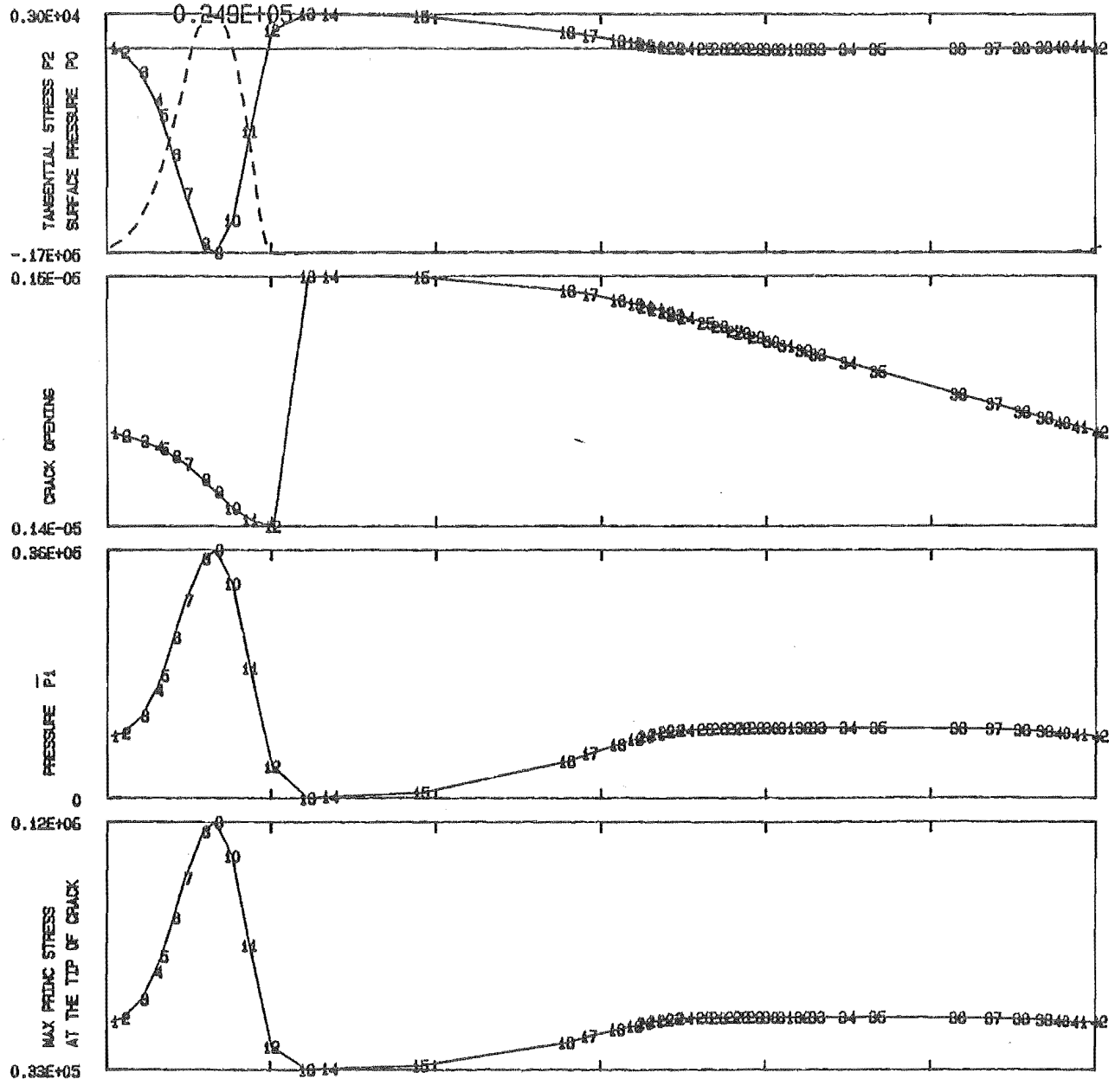

TEST NO 525 ANTI ROTATIONAL LOAD, 2 LAND BEARING

Fig.6.22

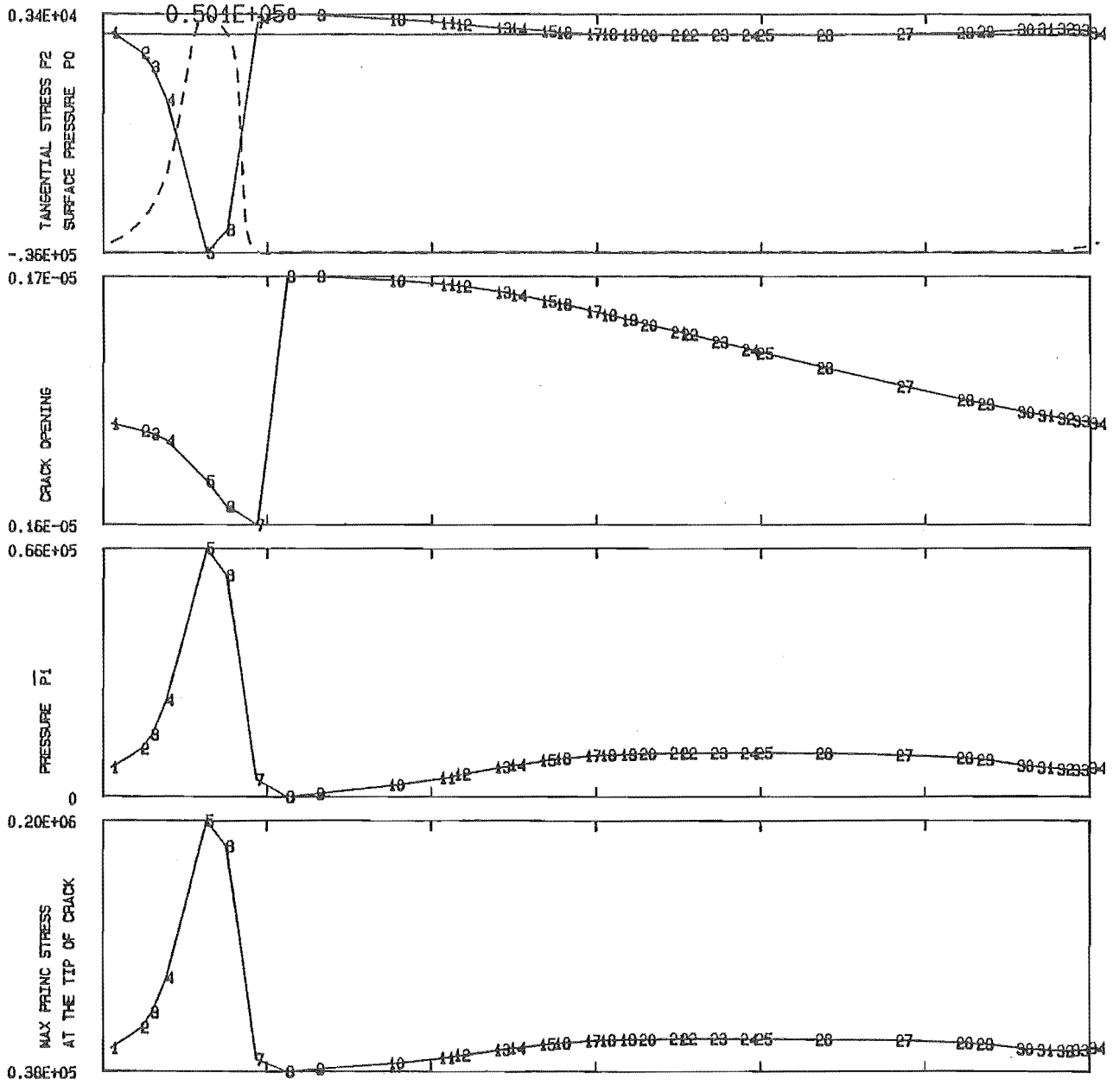

TEST NO 528 ANTI ROTATIONAL LOAD, 2 LAND BEARING

Fig.6.23

Test No.	Maximum Principle Stress at the tip of crack x 10^5 PSI	Hours to Failure		
		1	2	3
501	0.47	37	39.5	40
502	1.0	29.5	36	–
503	0.67	16.75	22	–
504	1.20	20	17	–
505	0.61	14	17.5	16
506	0.84	26	37	–
507	1.2	28	41	39
508	0.33	31	57	72
509	0.88	41	36	–
510	0.70	30	39	–
511	0.66	27	31	40
512	0.53	27	25	–
513	1.10	29	14.5	32
514	1.20	42	26	44
515	0.76	26	27	24
516	1.95	21	14	26
517	0.97	12	17	–
518	2.30	6.6	6.	–
519	1.50	6.	5.8	–
520	2.50	24	13	–
521	2.60	30	32	–
522	0.74	28	33	–
523	1.40	14	16.5	–
524	0.49	10	13.	–
525	1.2	9	14.	–
526	0.92	12	17.	–
527	1.7	35	27.	–
528	2.10	38	35.	–

Crack shape = parallel

Table 6.4

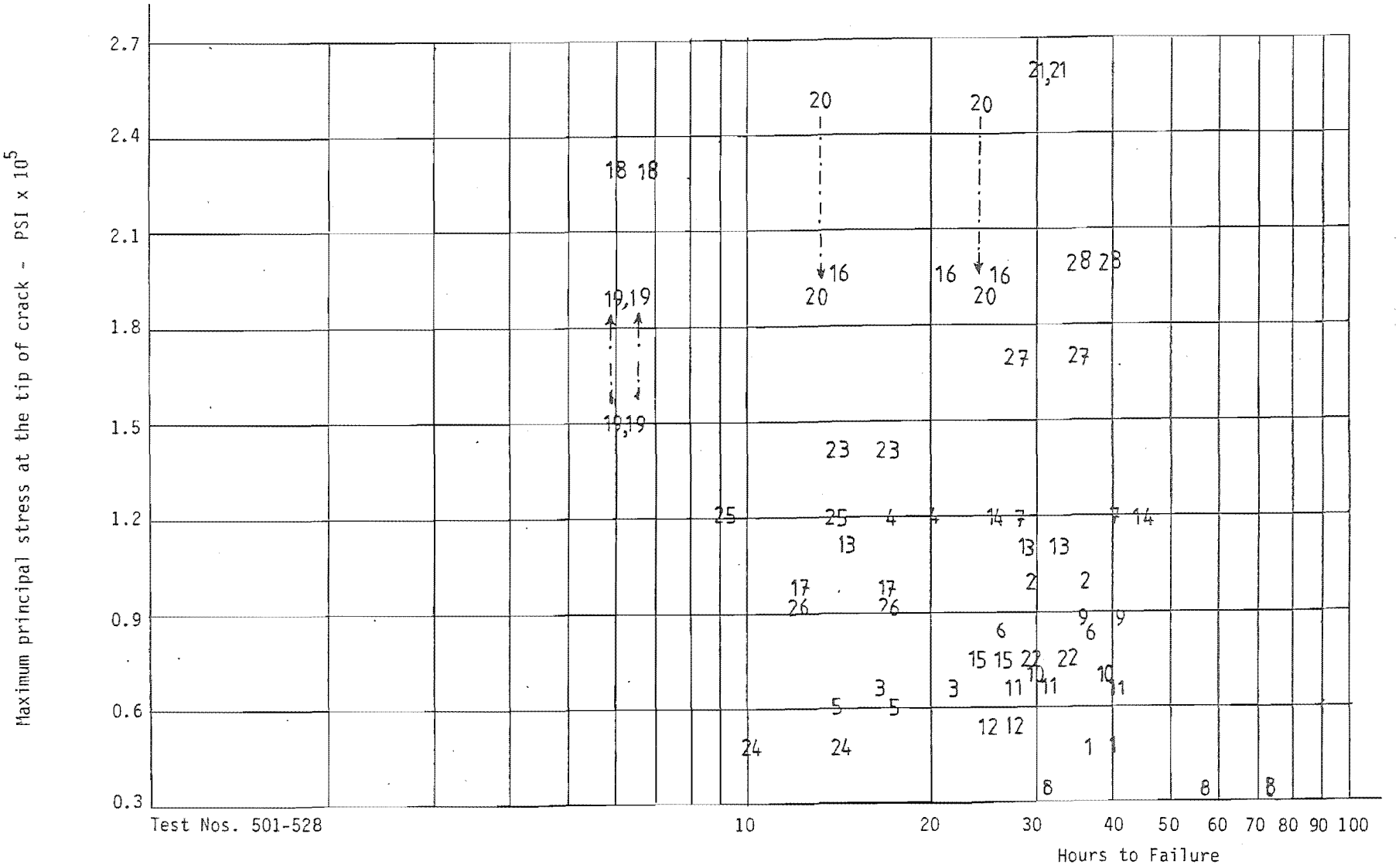

Fig.6.24

(Parallel Crack Assumption)

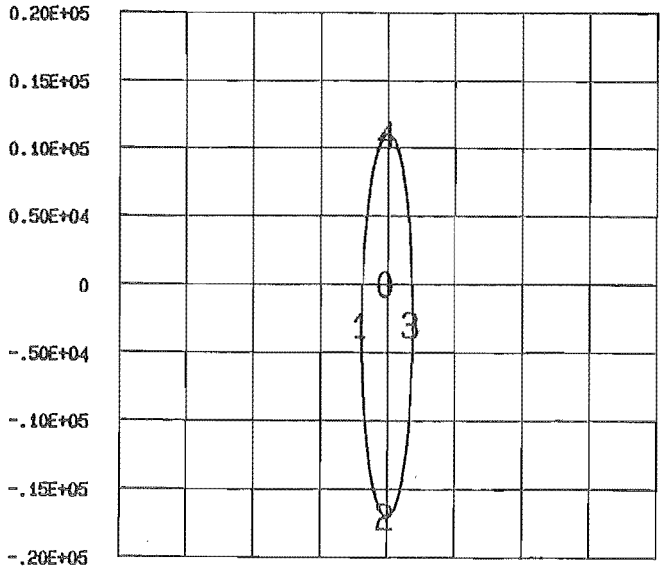

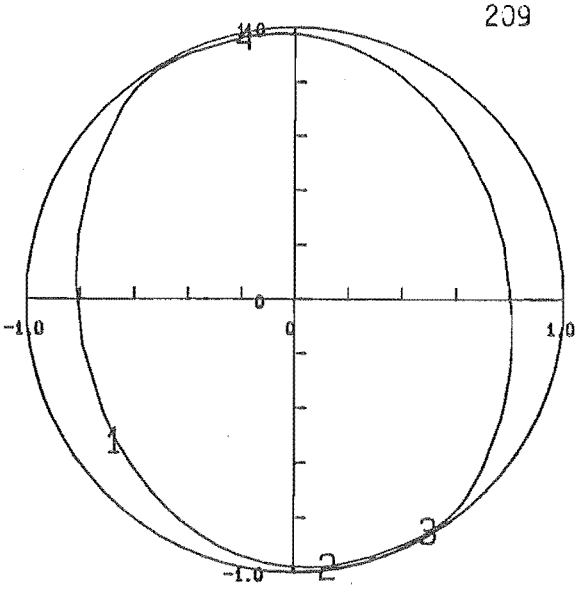

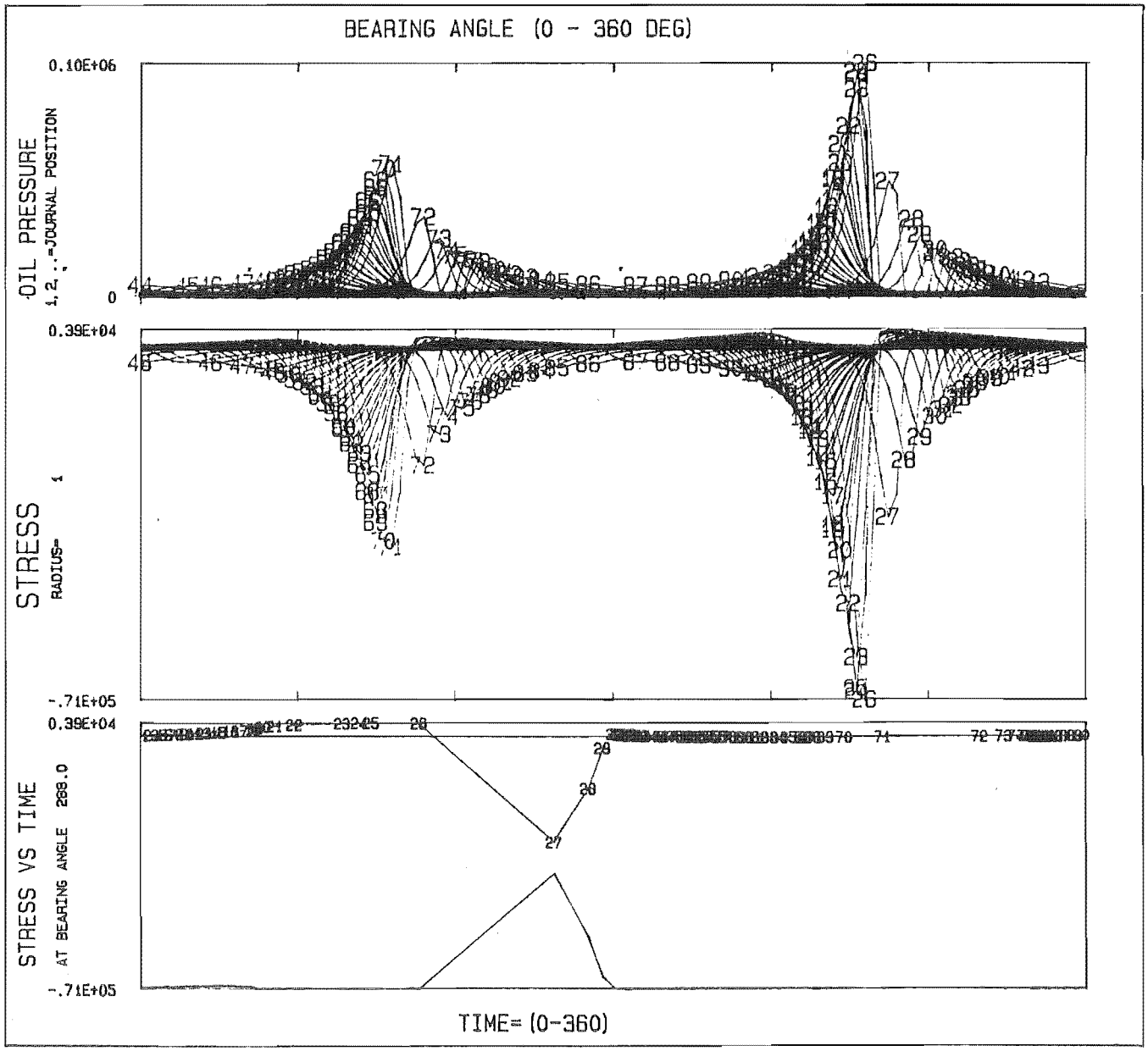

TEST NO 519 CO ROTATIONAL LOAD, 2 LAND BEARING (SENST. TEST)

MAX STRESS = 0.392E+04 , AT ANGLE= 288.0

MIN STRESS = -0.713E+05 , AT ANGLE= 276.2 STRESS TYPE= TANGENTIAL

Fig.6.25

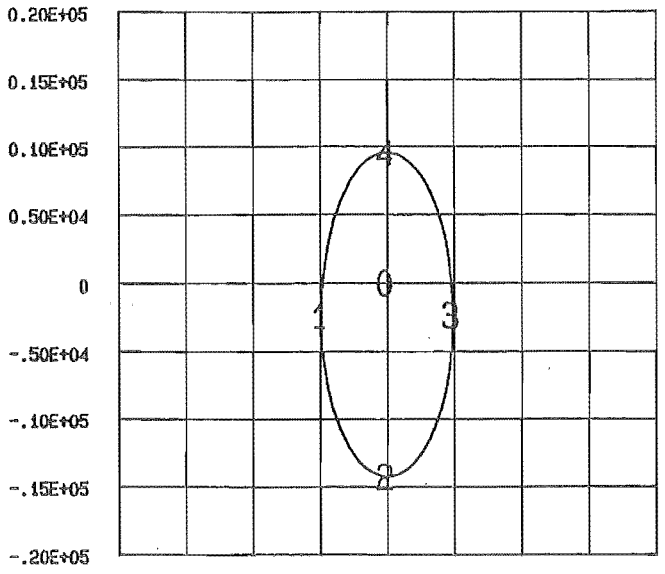

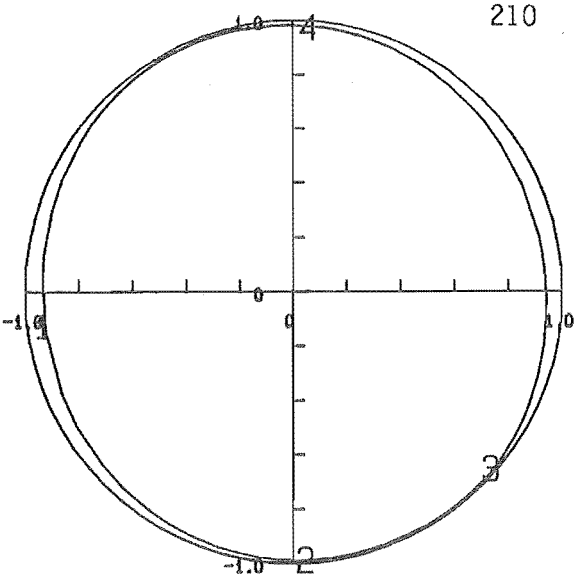

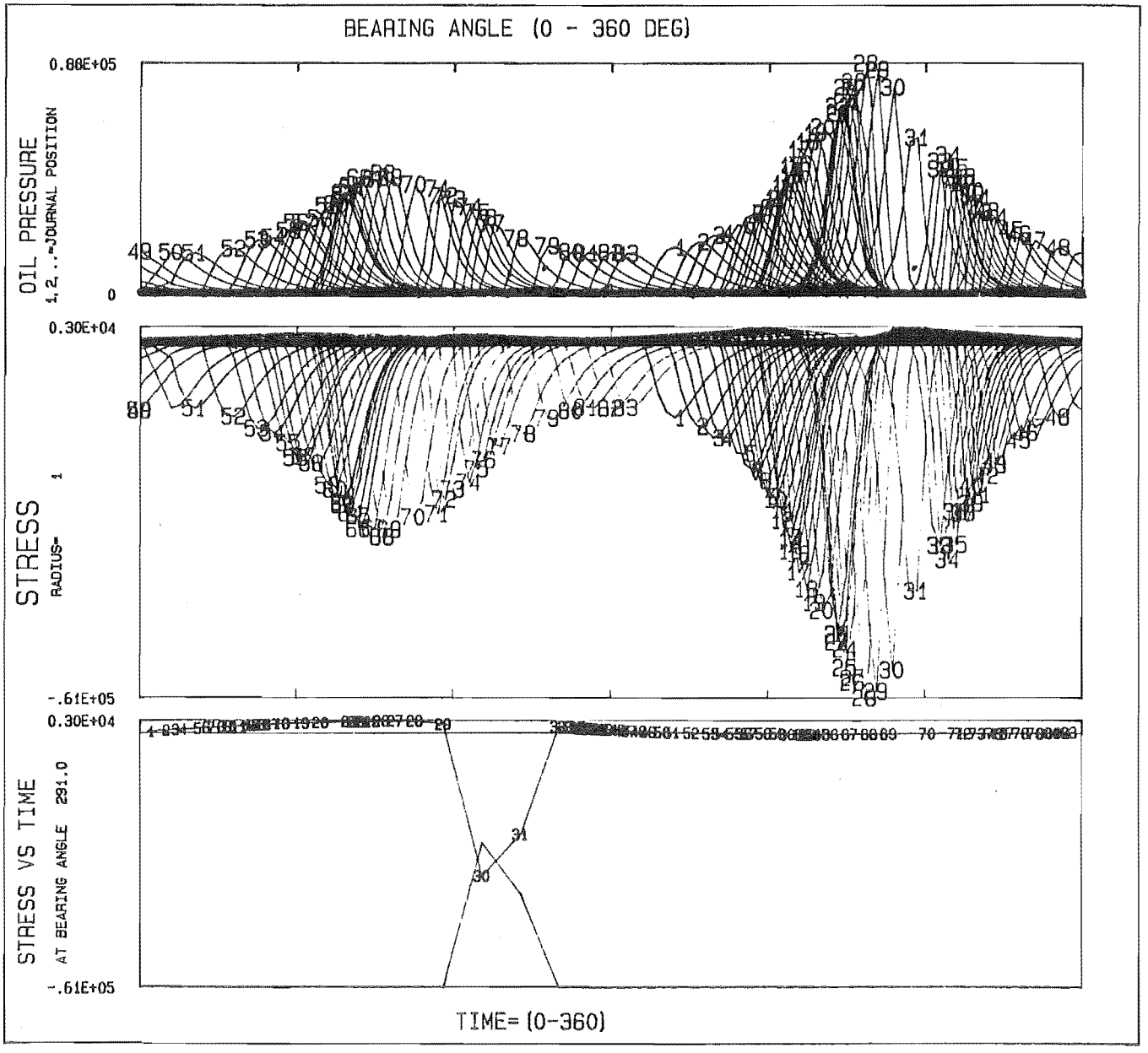

TEST NO 520 CO ROTATIONAL LOAD, 2 LAND BEARING (SENST. TEST)

MAX STRESS = 0.305E+04 , AT ANGLE= 291.0

MIN STRESS = -0.607E+05 , AT ANGLE= 277.6 STRESS TYPE= TANGENTIAL

Fig.6.26

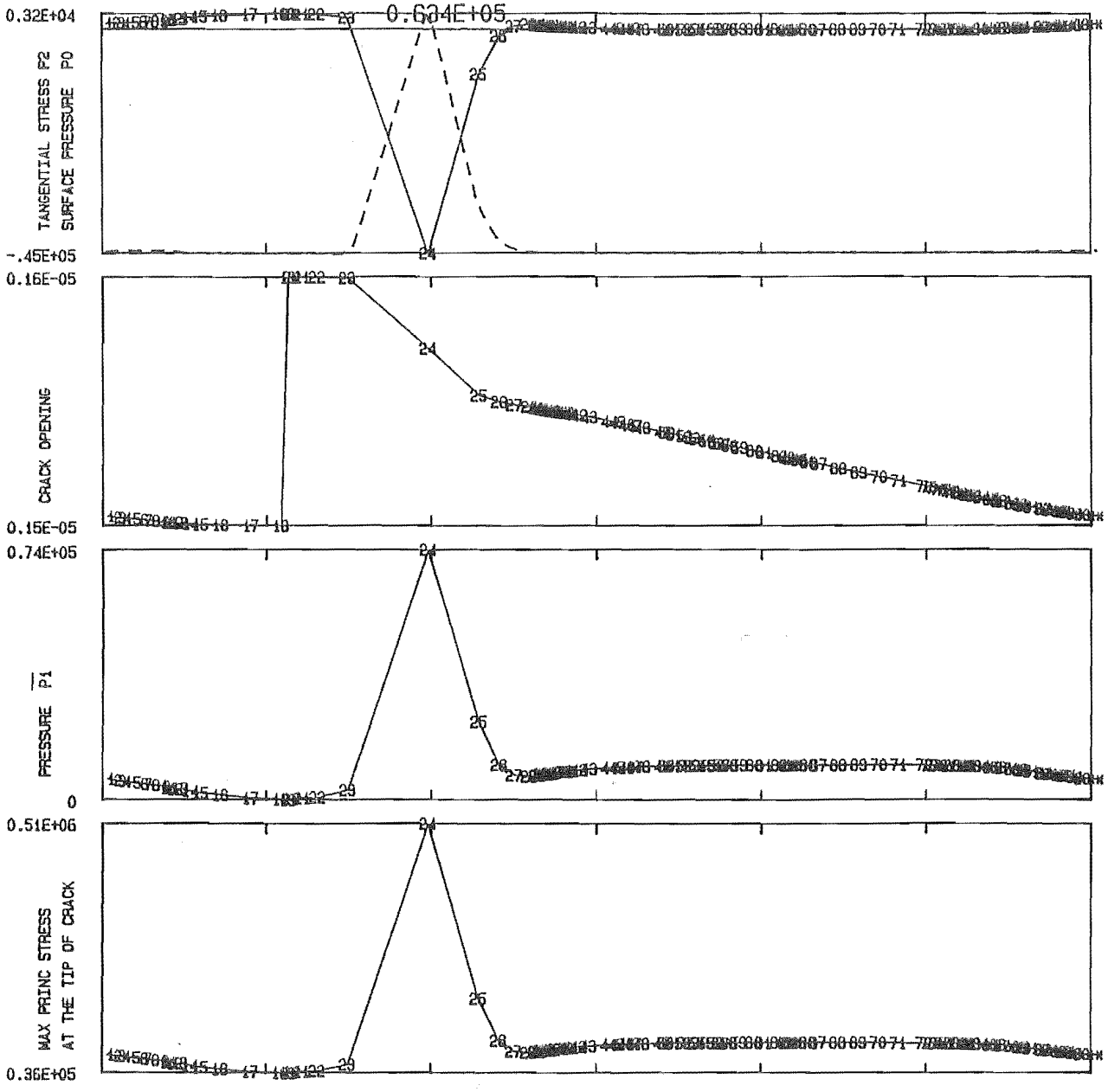

TEST NO 518 CO ROTATIONAL LOAD , 2 LAND BEARING

Fig. 6.27

Test No.	Maximum Principle Stress at the tip of crack x 10^5 PSI	Hours to Failure		
		1	2	3
501	0.88	37	39.5	40
502	2.00	29.5	36	–
503	1.25	16.75	22	–
504	2.50	20	17	–
505	1.10	14	17.5	16
506	1.70	26	37	–
507	2.6	28	41	39
508	0.56	31	57	72
509	1.72	41	36	–
510	1.27	30	39	–
511	1.20	27	31	40
512	1.02	27	25	–
513	2.30	29	14.5	32
514	2.60	42	26	44
515	1.50	26	27	24
516	4.20	21	14	26
517	1.90	12	17	–
518	5.1	6.6	6.	–
519	3.1	6.	5.8	–
520	5.5	24	13	–
521	5.74	30	32	–
522	1.50	28	33	–
523	2.80	14	16.5	–
524	0.89	10	13.	–
525	2.48	9	14.	–
526	1.75	12.	17.	–
527	3.55	35.	27.	–
528	4.38	38	35.	–

Crack shape = V

Table 6.5

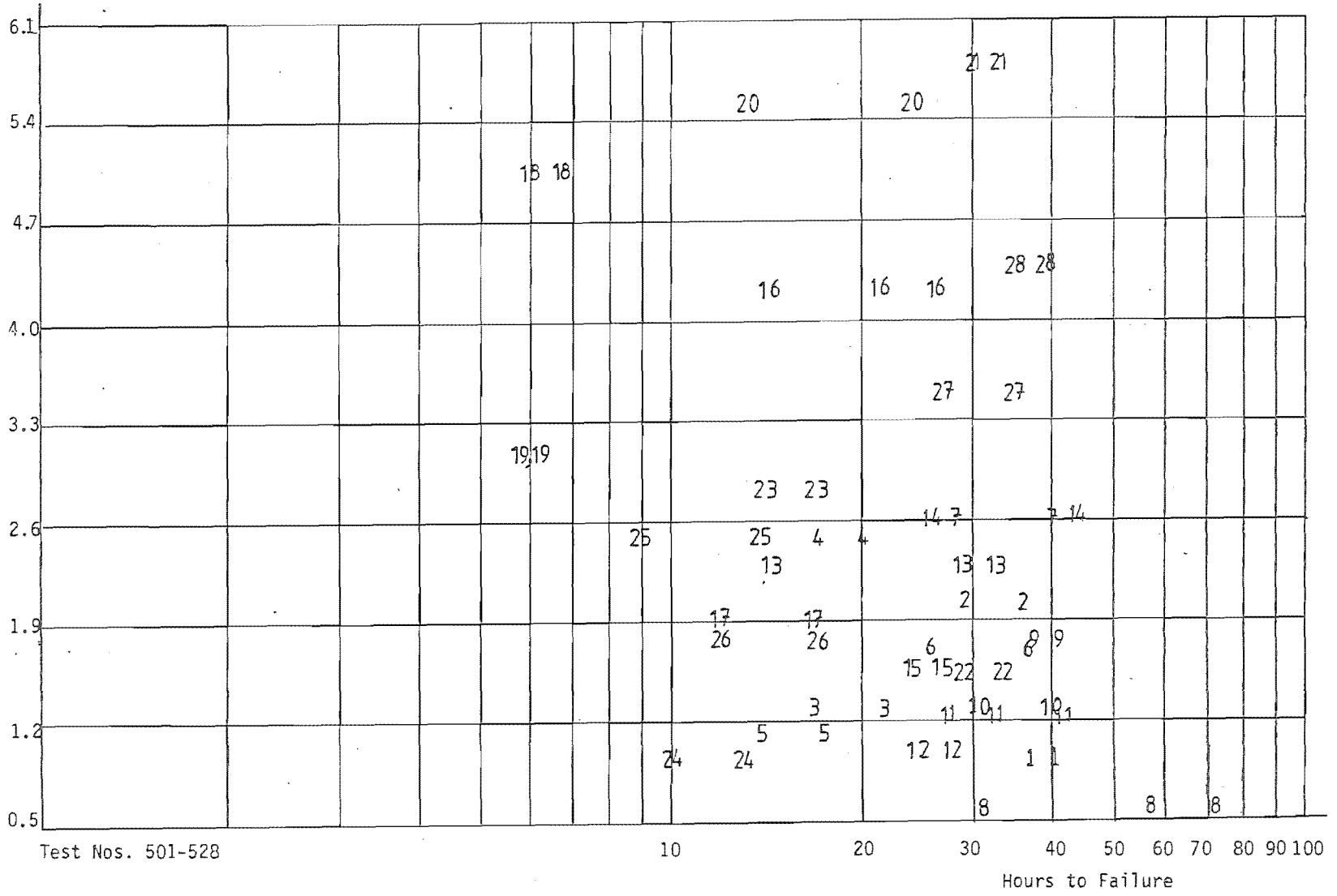

Fig.6.28

(V-crack Assumption)

6.4.2 Application of The Crack Model to Gyde's Test Cases

Gyde's Test Cases (701–748) covered a wide range of mean and amplitude loading (Fig. 5.37). Twelve of these cases, with mean load values ranging between zero to a value much higher than the load amplitude (Tests Nos. 707–744 shown in Figs. 5.38–5.49), were chosen and the crack closure model were applied to them. Figs. 6.29–6.33 show the stress and pressure plot for some of these cases. In Fig. 6.29, the crack opening H was a maximum when the surface tangential stress was in maximum tension (time instant 24). The stresses at the tip of the crack became maximum, when surface stress reached its highest compressisve level (time instant 17). Maximum, minimum and amplitude of the stresses at the tip of the crack for each case, and whether the bearing on that test failed after 10^7 cycles (failures marked with crosses and non–failures with circles) are listed in Table 6.6. To compare Gyde's and Blundell's Test Cases, maximum stresses were plotted on the same S–N diagram (Fig. 6.34). Since Gyde's experiments were performed with lower input loadings than those of Blundell's experiments, the resulting stresses will fall in a narrow band of the diagram (0.11 x 10^5 PSI to 0.42 x 10^5 PSI). The exact times of the failure for Gyde's bearings were not known. All the bearings were checked only once after 10^7 running cycles, hence the failed and unfailed Test Cases were marked respectively with crosses and circles at the left and right side of a line drawn at 10^7 cycles on the S–N diagram (Fig. 6.34).

Among the Gyde's Test Cases shown in Figs. 5.38–5.49, Cases Nos. 707, 710 had zero mean load, hence there were two regions of similar eccentricity ratio and pressure curves around the bearing, which meant the shaft was travelling in similar patterns in these two regions. Tests Nos. 716–721 had mean loads with values much lower than the load amplitude. The shaft was travelling more in

one side of the bearing, making the oil film thinner and the peak pressure higher on that side. Test Nos.. 726, 733, 734 had mean loads equal or slightly higher than the load amplitude. This shifts the eccentricity and pressure curves to one side of the bearing, which meant the shaft was travelling only on that side of the bearing. Test Nos. 732, 736, 744 had mean loads much higher than the load amplitudes. Their eccentricity loci appeared as a point, meaning the rotating shaft was not travelling on a path; it had remained at one point. This was thought to generate some extra heat, which may explain why Test Nos. 732 and 744 with higher maximum stresses than Test Nos. 707, 716, 719 did not fail. The extra heat may induce some compressive stresses in the surface, which could close the crack and prevent the oil from entering. Fig. 5.37 shows that Test No. 736 was an odd case, failing under low amplitude loading.

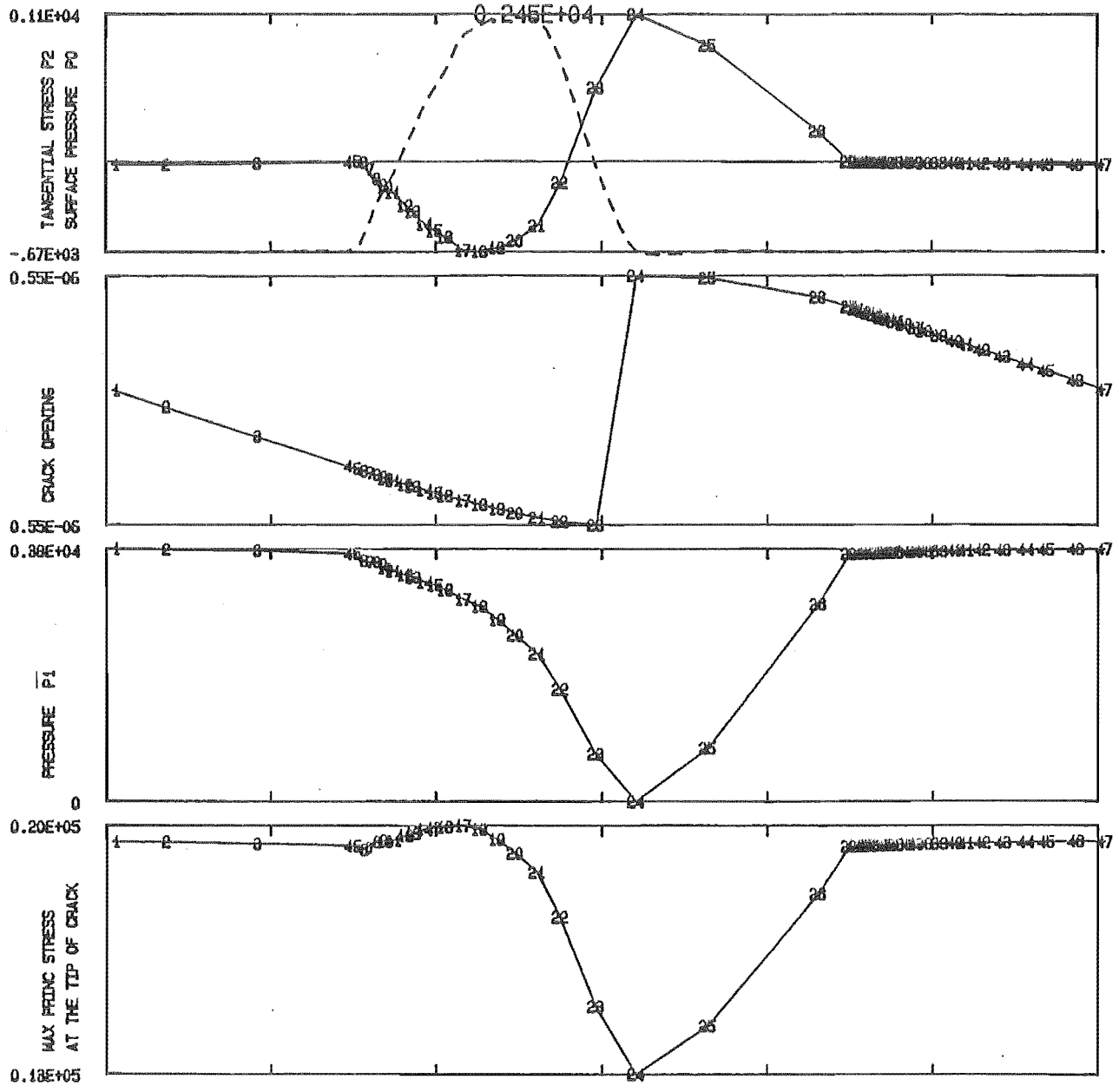

TEST NO 707 CO ROTATIONAL LOAD , 1 LAND BEARING

Fig.6.29

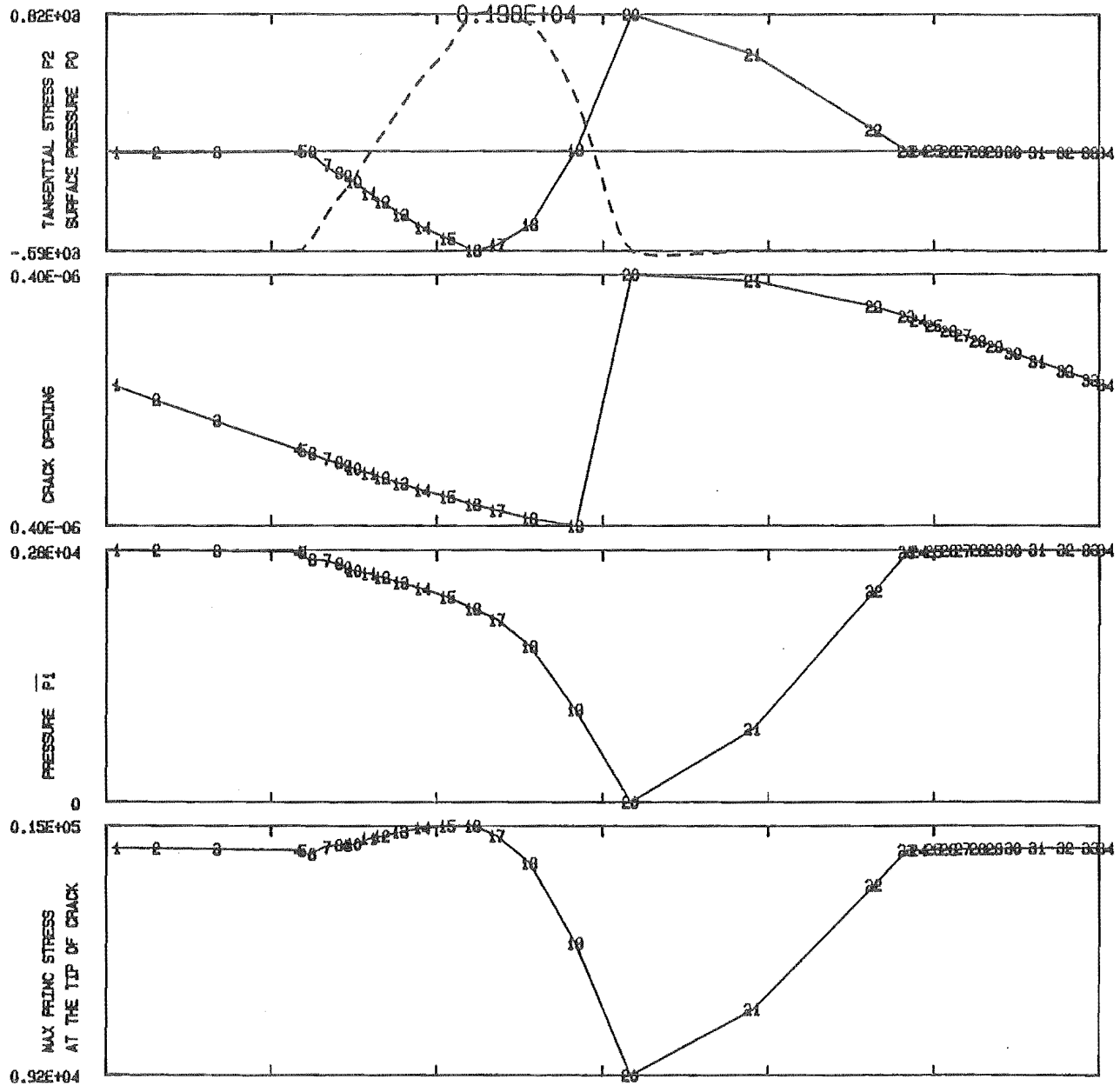

TEST NO 716 CO ROTATIONAL LOAD , 1 LAND BEARING

Fig. 6.30

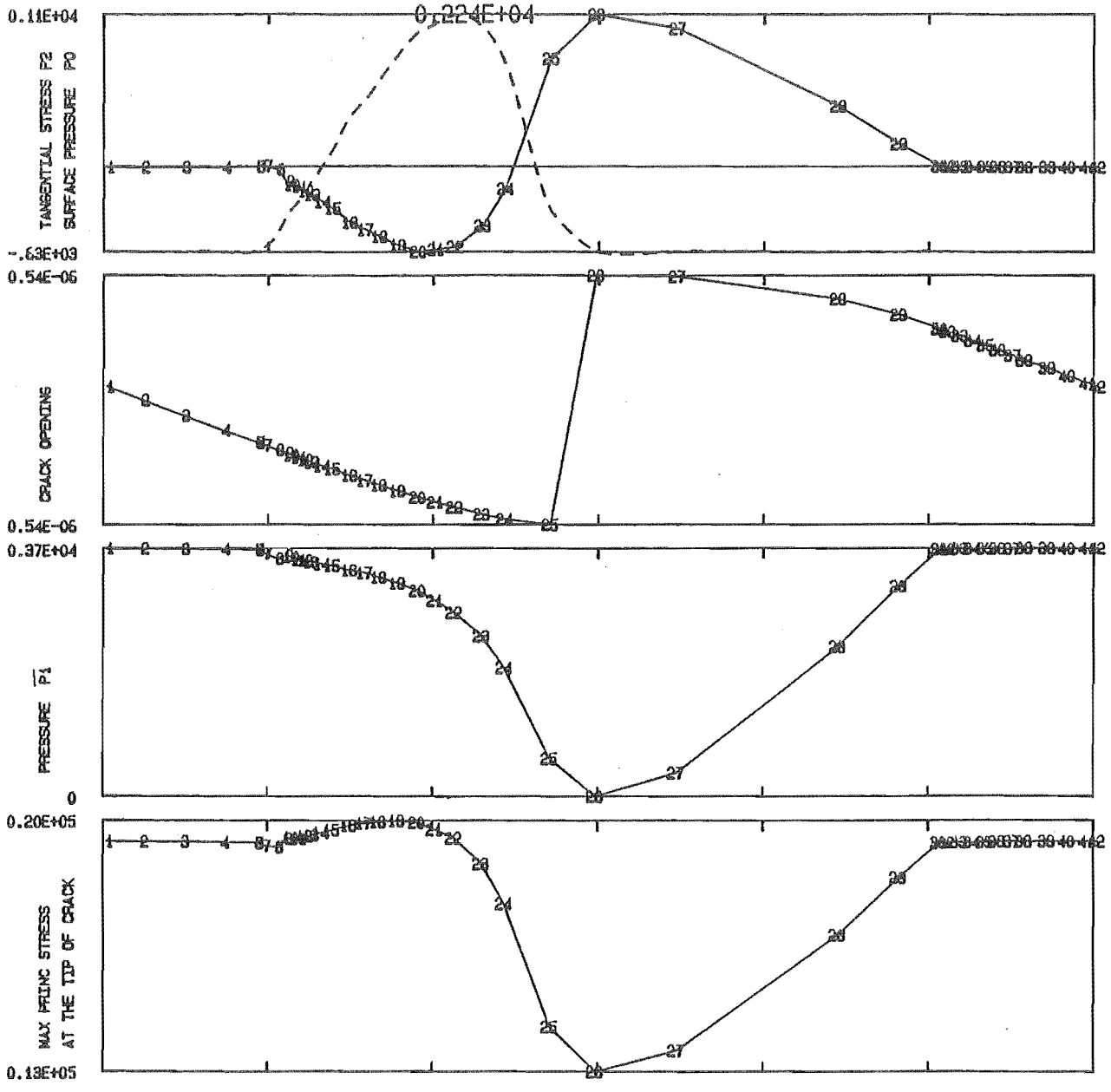

TEST NO 719 CO ROTATIONAL LOAD , 1 LAND BEARING

Fig.6.31

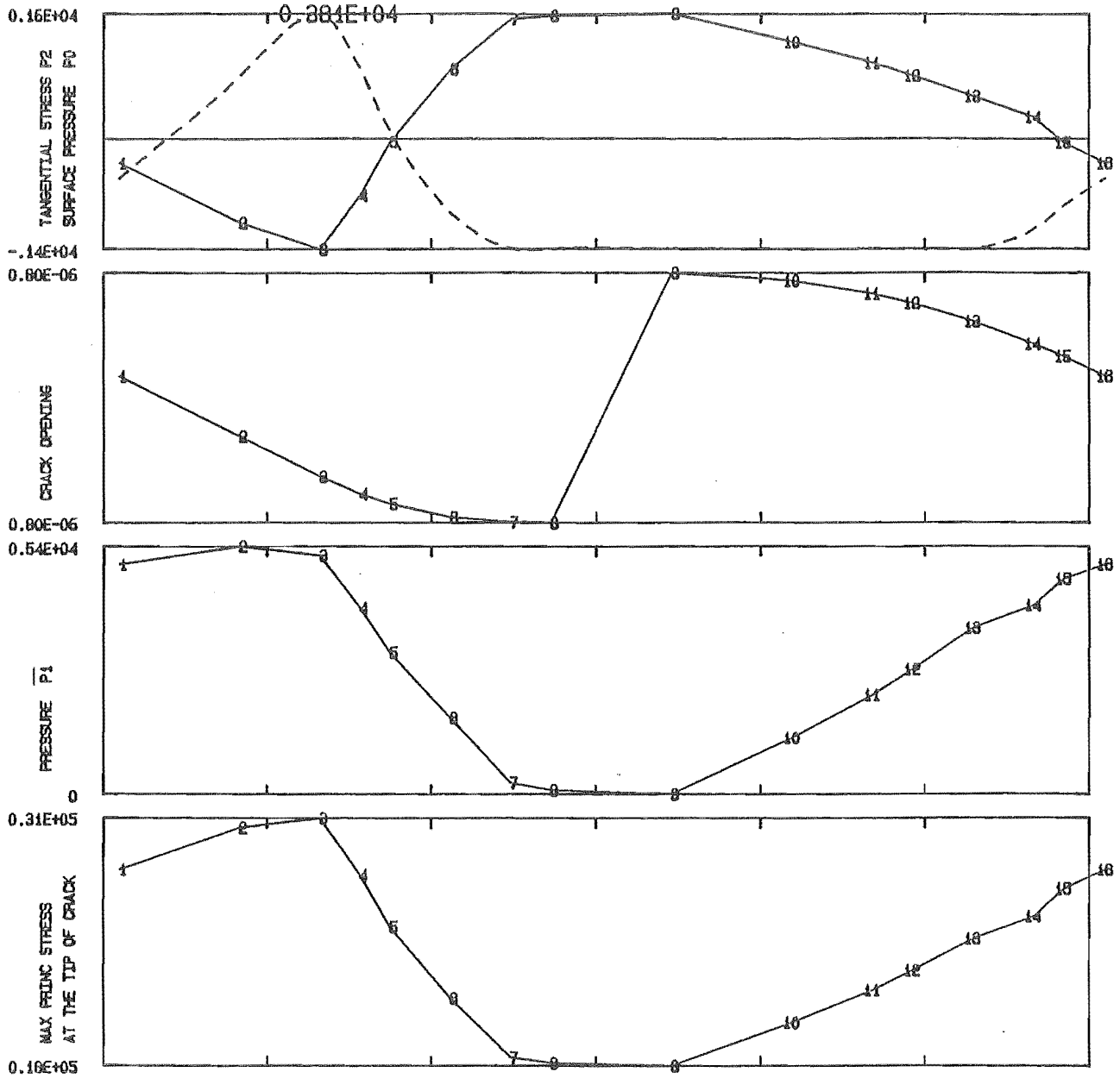

TEST NO 732 CO ROTATIONAL LOAD , 1 LAND BEARING

Fig.6.32

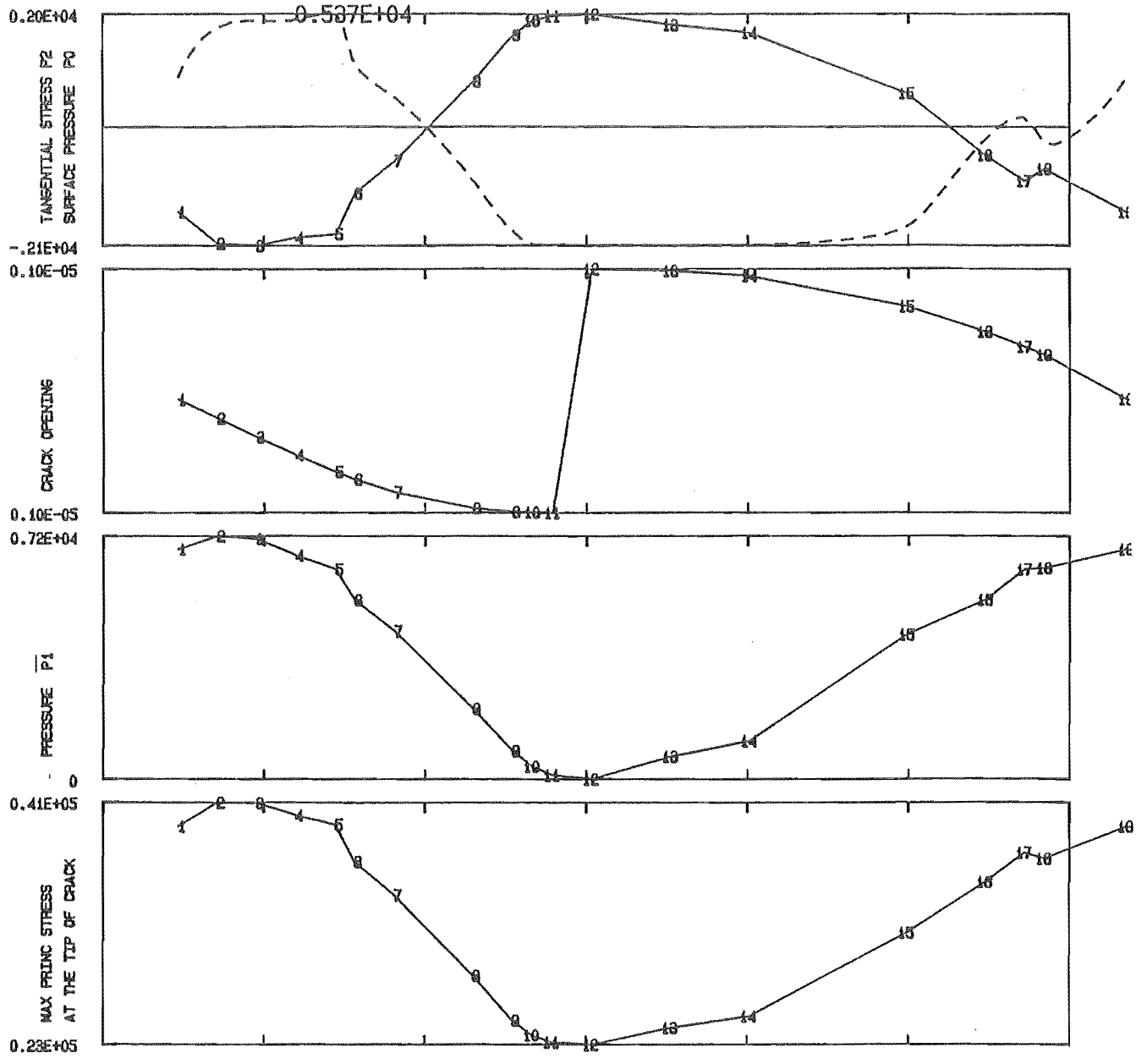

TEST NO 744 CO ROTATIONAL LOAD , 1 LAND BEARING

Fig.6.33

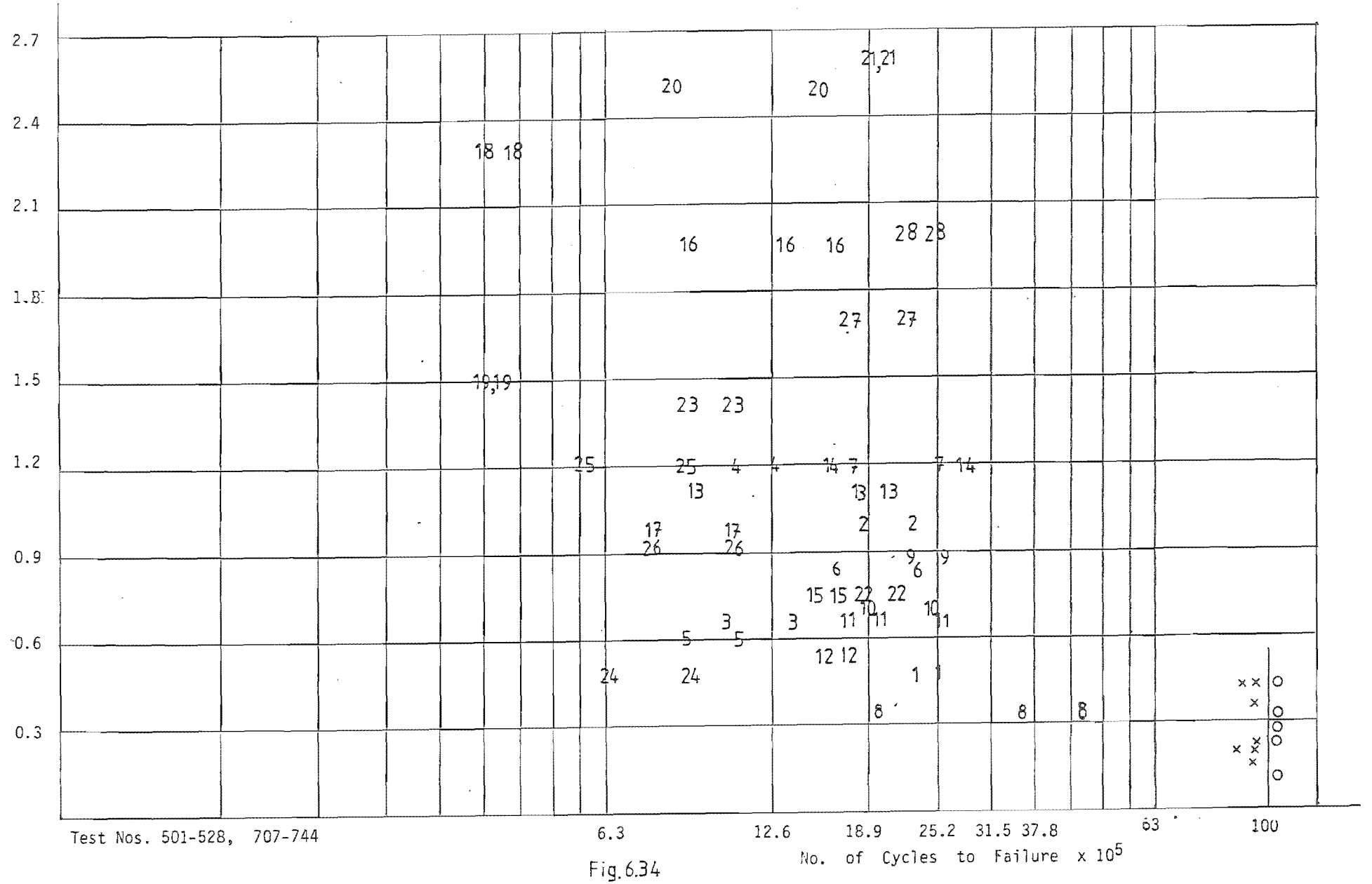
Maximum principal stress at the tip of crack - PSI x 10^5
2.7
2.4
2.1
1.8
1.5
1.2
0.9
0.6
0.3
Test Nos. 501-528, 707-744
6.3
12.6
18.9
25.2
31.5
37.8
63
100
No. of Cycles to Failure x 10^5

Fig. 6.34

6.4.3 Stress Amplitude versus the Number of Cycles to Failure

Gyde showed that the loading amplitude was an important factor in bearing failure (Fig. 5.37). Except for Test No. 736 (marked 36), the rest of the failed Test Cases were outside or on the boundary of an approximately constant load amplitude lines. Hence, it was decided to use the stress amplitude at the tip of the crack to plot the S–N diagram. Maximum, minimum and amplitude value of the stresses at the tip of the crack for all of the Blundell's Test Cases (501–528) and the twelve chosen Gyde's Test Cases (707–744) mentioned in Section 6.4.2 are listed in Tables 6.6, and 6.7. Since the actual time of failure for Gyde's Test Cases were not known, they were distinguished with crosses and circles at 10^7 cycles, while Blundell's Test Cases with known failure times were marked with numbers 1–28. A comparison between the two diagrams (Figs. 6.34, 6.35) shows the same general pattern. The crack shape and sensitivity of input load data mentioned in Section 6.4.1 should bring similar effects to the S–N diagram (Fig. 6.35). It should be noted that the above method of calculating the stresses at the tip of a crack, was only an approximation to show the order of magnitude of expected stresses, during a complete loading cycle.

Test No.	Maximum principle stress at the tip of crack x 10^5 PSI			Failed X Unfailed O
	Maximum	Minimum	Amplitude	
707	0.20	0.13	0.07	X
710	0.34	0.21	0.13	X
716	0.15	0.09	0.06	X
717	0.11	0.07	0.04	O
719	0.20	0.13	0.07	X
721	0.23	0.14	0.09	O
726	0.28	0.16	0.12	O
732	0.31	0.18	0.13	O
733	0.41	0.23	0.18	X
734	0.42	0.24	0.18	X
736	0.22	0.16	0.06	X
744	0.41	0.23	0.18	O

Table 6.6

Test No.	Maximum principle stress at the tip of crack x 10^5 PSI		
	Maximum	Minimum	Amplitude
501	0.47	0.21	0.26
502	1.00	0.31	0.69
503	0.67	0.30	0.37
504	1.20	0.28	0.92
505	0.61	0.31	0.30
506	0.84	0.26	0.58
507	1.20	0.28	0.92
508	0.33	0.19	0.14
509	0.88	0.31	0.57
510	0.70	0.32	0.38
511	0.66	0.31	0.35
512	0.53	0.20	0.33
513	1.10	0.27	0.97
514	1.20	0.30	0.90
515	0.76	0.23	0.53
516	2.00	0.41	1.59
517	0.97	0.38	0.59
518	2.30	0.36	1.94
519	1.50	0.43	1.07
520	2.50	0.35	2.15
521	2.60	0.36	2.34
522	0.74	0.24	0.50
523	1.40	0.37	1.03
524	0.49	0.24	0.25
525	1.20	0.33	0.87
526	0.92	0.38	0.54
527	1.70	0.36	1.34
528	2.00	0.38	1.62

Table 6.7

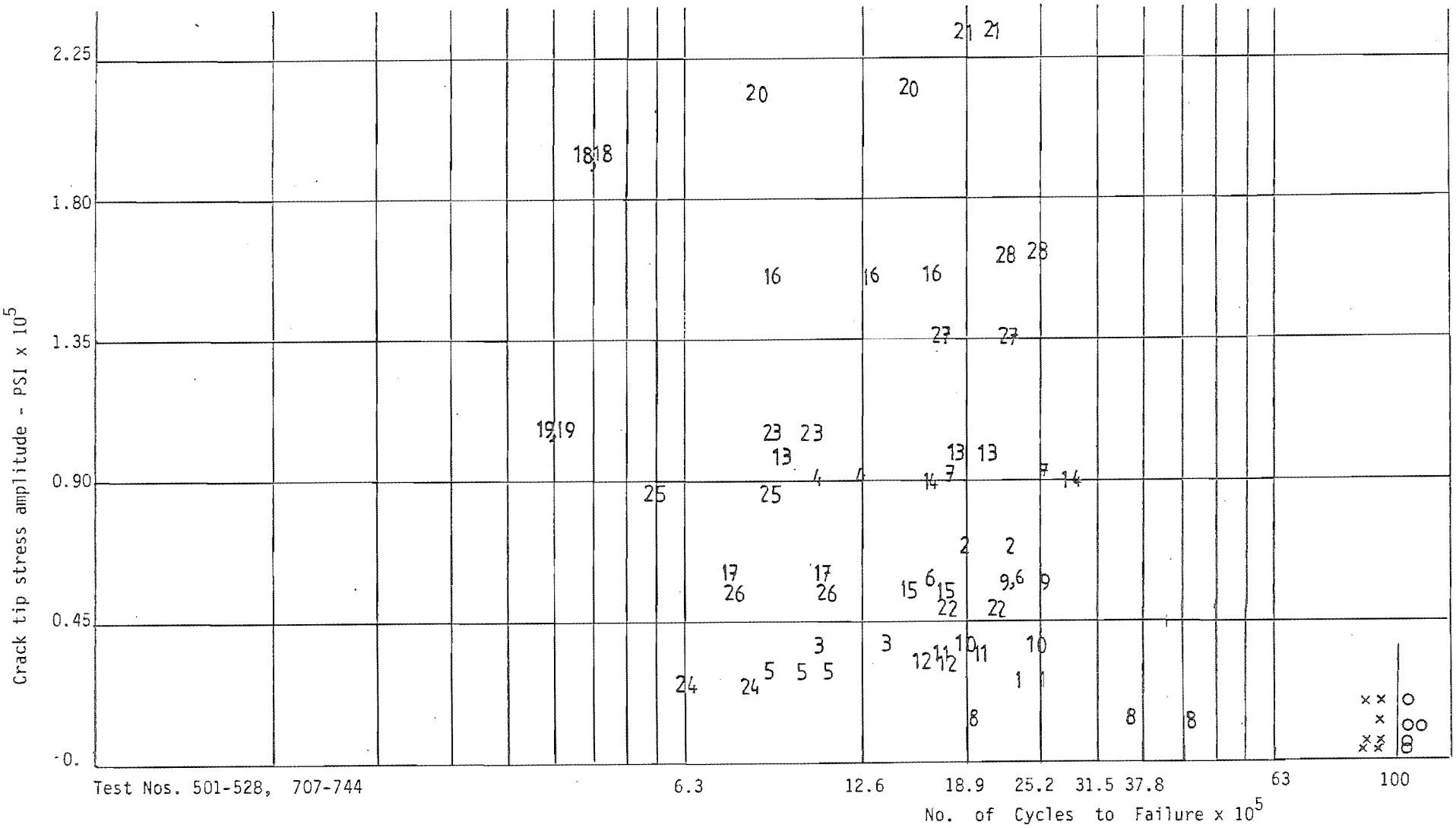
Crack tip stress amplitude - PSI x 10^5
2.25
1.80
1.35
0.90
0.45
0.
Test Nos. 501-528, 707-744
6.3
12.6
18.9
25.2
31.5
37.8
63
100
No. of Cycles to Failure x 10^5

Fig.6.35

CHAPTER SEVEN

SUMMARY AND CONCLUSIONS

In this thesis, the results of a detail investigation into the fatigue stress analysis of journal bearings based on simultation of experimental tests performed by other workers is presented. For this purpose, a computer program developed by Lloyd and McCallion was modified to generate the centreline pressure distribution at very finely graded and constant meshes, which may be used by the finite element program for calculating the stresses. Great care was taken in generating a wide range of different input load diagrams as close as possible to those reported by Blundell.

The results of temperature and diametral clearance tests of the program showed that, under the same loading conditions, bearings operating at a higher temperature or with a higher diametral clearance will generate a higher peak pressure and a greater maximum eccentricity ratio. These eventually decreases bearing life. Similarly increasing the bearing's land length lowers both the maximum peak pressure and the maximum eccentricity ratio, giving a longer life to the bearing, but space limitation in the internal combustion engines does not usually permit using longer length bearings. Surface distortion, neglected in the Lloyd and McCallion's program, has an effect on the pressure curves. Allen [22] showed that surface distortion makes the pressure curves of connecting rod bearings less steep, however the very thick housing used in the test rigs lowers this effect.

For calculating the stresses in the bearing shell, a finite element program capable of working in Cartesian form was extensively modified to also work in polar coordinates. This made it possible to compute the stresses in the radial and tangential directions, due to a centreline pressure distribution or the stresses

in the axial direction due to a parabolic variation of pressure. An automatic mesh generating program capable of generating the meshes for both geometries (rectangular and circular) was written and found to be very advantageous in saving time and in reducing the possibility of errors. Further modification to the FEM program enabled it to handle multiple loading cases, giving considerable savings in the calculation of the stiffness matrix. Extensive work done in writing codes for plotting routines proved to be extremely useful in presenting the results clearly. For the purpose of verification and illustration, an application to a bimetalic strip, of white metal on a steel backing, subjected to a parabolic pressure distribution, was presented. Contour plots of stresses showed that the two normal stresses σ_x, σ_y were uniform in the white metal layer. σ_x at the interface to two metals became discontinuous. This was due to the fact that although both metals underwent the same strain, their material properties were different. The shear stress τ_{xy} had its maximum value on the interface closer to the free edge.

In a search to find the type of stress responsible for the fatigue, all the different stresses in the white metal layer including the radial, tangential, shear, maximum principal, maximum shear and maximum distortion energy, which were suspected to cause the failure were investigated. Radial stress had the same magnitude as the applied pressure but in compression. Maximum shear and maximum distortion stresses had similar plot shapes with their highest point under the peak pressure away from the point of failure. Blundell chose τ_{xy} at the interface of two metals for his stress analysis, but it had been shown that the crack starts from the surface and then advances toward the interface. Therefore τ_{xy}, which was zero at the surface and has a value lower than maximum shear stress at the interface may not be responsible for the failure. The tangential stress σ_θ which had repetitive tension to compression changes at points closer to the failure position reported by Blundell and Gyde was more likely to be

responsible for the failure.

The results obtained from calculating the stresses in a bearing shell supported on a rigid surface did not show any tensile tangential stress. This indicates that although the steel housing supporting the bearing shell was designed very thick to make the bending effects negligible, tensile tangential surface stresses of sufficient magnitude to cause failure were still induced. This shows how important the bending effect could be in a connecting rod bearing, which lacks a thick support.

Since there was no shear stress at the surface of white metal, the radial and tangential stresses were the two principal stresses. The third principal stress σ_3 was found to be equal or slightly higher than the tangential stress in a region under the pressure curve. Outside the pressure curve in the critical region, σ_3 was less than half the maximum principal stress (tangential stress). Maximum and mean value of tangential stresses were plotted on a modified Goodman diagram. Boundary lines connecting the endurance limits to the ultimate strength on the diagram of Gyde's results did not separate the failed and unfailed bearing Test Cases. This indicates that the Modified Goodman diagram cannot be used as a criterion of failure in dynamically loaded journal bearings, which requires a more complex stress analysis. However, the diagram showed that all the failed bearing cases were under repetitive tension to compression changes. The plot of maximum principal stresses versus the number of running cycles to failure (S–N diagram) showed some scattered results.

A more careful investigation of the stresses at their maximum point (the critical region) for the CO and antirotational loading cases showed that the time period between the maximum tensile stress to minimum compressive stress of co–rotational loading cases was a lot shorter than for antirotational loading cases. The bearings under the first type of loading failed quicker than those under the second type. Experimental work by Crossland and others showed that covering

the surface of fatigue specimens tested under hydrostatic pressure with a rubber type coating increased the life of specimens.

A full investigation of a crack behaviour at the point of maximum tangential stress was planned in the following steps :

Analysing the fluid in a parallel and V–shape crack.

Finite element representation of the crack.

Numerical analysis of the crack closure.

Application of the crack closure model.

Effect of changing the crack shape.

Results of the above investigation showed that the pressure in a parallel shaped crack gives surface displacement close to that of a V–shaped crack, but the principal stress at the tip of the later type crack was considerably higher. The tangential stress at the surface of a bearing produced the highest stress at the tip of the crack and the highest displacement on the surface compared to other types of loading. The slow rate of crack closure was found to be related to the oil viscosity. Application of the crack model on different cases showed a rapid rise of pressure inside the crack due to a sudden drop in magnitude of tangential stress, which increased the principal stress at the tip considerably. This increase for the V–shaped crack assumption was higher due to a higher stress factor obtained by the FEM method. The above approximate method of calculating stresses at the tip of the crack, which was based on the parallel and V–shaped crack assumptions, gave the order of magnitude of stresses that may be expected at the tip of the crack during a complete loading cycle.

Application of a crack model on Blundell's Test Cases and plot of maximum principal stress at the tip of the crack versus the number of running cycles to failure (a new S–N diagram compared to a previous one based on surface stresses) showed some shifting of points due to pressure build up inside the crack. The shift spreads the points in a wider stress range, but the points on the new

diagram still have considerable scatter. Sensitivity of bearing performance to the uncontrollable variation of input load, as reported by Blundell, was found to be an important parameter in altering the final results calculated at the position of maximum tangential stress. A 600 LbF increase of load amplitude for Test No. 519 and 600 LbF reduction of load amplitude for Test No. 520 resulted in considerable change of maximum principal stress at the tip of the crack (points 19 and 20 in Fig. 6.24). A 600 LbF variation of mean load in direction of A axis shifts the angular position of maximum peak pressure by 4^0. Smoothness of the theoretically generated input load diagrams compared to the actual experimental load diagrams may also affect the final results. The plane strain assumption in the finite element stress analysis of the cracks, which considers infinite crack length in axial direction, may also be very important in scattering points on the S–N diagram. Other workers [29] have shown the stress at the tip of a crack having part circular shape in the axial direction may be as low as 47% of plane strain assumption.

Application of the crack model to Gyde's Test Cases, which covered a wide range of mean load and of load amplitude (zero mean load to mean load much higher than the amplitude) showed some interesting results. Since Gyde's experiments were performed with lower input loading than those of Blundell's experiments, and since all his tests were left to run for longer time periods (10^7 cycles), the resulting stress points fall in a very narrow band of stresses on the S–N diagram compared with those of Blundell. A comparison of unfailed Test Cases 732 and 744 with failed Cases 707, 716 and 719 showed that 732 and 744 had higher maximum principal stresses at the tip of the crack than failed Cases 707, 716, 719. Due to the high mean load compared to amplitude, the journal in 732 and 744 hardly moved in the clearance, whereas 707, 716 and 719 had large journal movements (Figs. 5.45, 5.49, 5.38, 5.40, 5.42). This lack of

movement may have generated some extra heat at the failure point, inducing compressive stresses which may have closed the crack and prevented the oil from entering.

Since Gyde had shown the load amplitude to be an important factor in bearing failure, a new S–N diagram based on the calculated crack tip stress amplitude was plotted. A comparison between this diagram and the diagram based on maximum stress showed the same general pattern.

REFERENCES

1. Blount, E.A.
Design factors influencing the fatigue resistance of connecting–rod big–end bearings. Proc. Inst. Mech. Engrs., 1961, 175, 513.

2. Gyde, N.
Fatigue fracture in babbitt lined journal bearings. Thesis 1969, Laboratory of Internal Combustion Engines, Technical University of Denmark Copenhagen.

3. Roach, A.E. and Johnson, L.G.
What is bearing fatigue? Journal of American Society of Lubrication, 7th Annual Meeting, April, 1952.

4. Ibrahim, S.M., McCallion, H.
Stresses in oil lubricated bearings. Proc. Inst. Mech. Engrs., 1970, 184, 69.

5. Hassan, H.A.H.
Fatigue cracking of dynamically loaded plain bearings. M. Phil. thesis 1971, University of Nottingham.

6. Lloyd, T. and McCallion, H.
A computer program for the design of reciprocating engine bearings. Symposium on computers in internal Combustion Engine Design, Inst. Mech. Engrs., 1967–1968, Paper 20.

7. Blundell, J.K.
The fatigue of dynamically loaded journal bearings. Ph.D. thesis, 1977, University of Nottingham.

8. Martin, F.A., Garner, D.R., Adams, D.R.
Hydrodynamic aspects of fatigue in plain journal bearings. T.A.S.M.E., Journal of Lubrication Technology, 1980, p.1.

9. Tower, B.
First report on friction experiments. Proc. Inst. Mech.Engrs., 1883, **34**, p.632.

10. Reynolds, O.
On the theory of lubrication and its application to Mr Beauchamp Tower's experiments. Phil. Trans. Roy. Soc. Lond., 1886, **177**, Part 1, p.157.

11. Sommerfeld, A.
Zur hydrodynamicschen theorie der schmiermittelreibung. Z. Math. U. physik, 1904, **50**, p.79

12. Swift, H.W.
The stability of lubricating films in journal bearings. Proc. Inst. Civil Engrs., 1931–32, **233**, p.267.

13. Southwell, R.V.
Relaxation methods in engineering science. Oxford U. Press.

14. Christopherson, D.G.
A new mathematical method for the solution of film lubrication problems. Proc. Inst. Mech. Engrs., 1941, **146**, p.126.

15. Floberg, L., Jakobseen, B.
The finite journal bearing considering vapourisation. Report No.3 (Institute of M/c elements, Chalmers University of Technology), 1957.

16. McCallion, H., Horsnell, R.
Prediction of some journal bearing characteristics under static and dynamic loading. Proc. Inst. Mech. Engrs. 1963, Lubrication and Wear Conference.

17. Gumbel, L., Everling, E.
Reibung und Schmierung im Maschinenbau. M. Krayn, Berlin.

18. Lloyd, T.
Dynamically loaded journal bearings. Ph.D. thesis, 1966, University of Nottingham.

19. Patrick, J.K.
An experimental investigation into the performance of sleeve bearings subjected to a range of alternating loads. Proc. Inst. Mech. Engrs. 1967, 182, Part 3N.

20. NCAR (National Center for Atmospheric Research), May 1983, Boulder, Colorado, USA.

21. Hinton, E., Owen, D.R.J.
Finite element programming. London, Academic Press, 1977.

22. Allen, D.G.
A theoretiucal investigation of the effects of housing distortion on journal bearing performance. Ph.D. thesis, 1972, Univeristy of Nottingham.

23. Rees, H.D.
The development of test facilities for dynamically loaded plain journal bearings. M.Phil. Degree, University of Nottingham, May, 1976.

24. Crossland, B.
Effect of large hydrostatic pressures on the torsional fatigue strength of an alloy steel. ASME, Proceedings of the International Conference on Fatigue of Metals, 1956, p.138.

25. Parry, J.S.C.
Further results of fatigue under triaxial stress. ASME, Proceedings of the International Conference on Fatigue of Metals, 1956, p.132.

26. White, D.G., Crossland, B., Morrison, J.L.M.
Effect of hydrostratic pressure on the direct stress fatigue strength of an alloy steel. Journal Mechanical Engineering Science, 1959, 1, No. 1, p.39.

27. Morrison, J.L.M., Crossland, B., Parry, J.S.C.
Strength of thick cylinders subjected to repeated internal pressure. Proc. Inst. Mech. Engrs., 1960, **174**, No. 2, p.95.

28. Sih, G.C.
Methods of analysis and solutions of crack problems. 1973, p.49, Noordhoff International Publishing.

29. Rooke, D.P., Cartwright, D.J.
Compendium of stress intensity factors, 1974, London, Her Majesty's Stationery Office.